On the Adequacy of Global Pressure Gain as the Performance Metric for Rotating Detonation Combustors

by

Alexander D. Feleo

A dissertation submitted in partial fulfillment
of the requirements for the degree of
Doctor of Philosophy
(Aerospace Engineering)
in the University of Michigan
2024

Doctoral Committee:

Associate Professor Mirko Gamba, Chair
Professor James Driscoll
Professor Venkat Raman
Professor Margaret Wooldridge

Alexander D. Feleo
afeleo@umich.edu
ORCID iD: 0000-0002-7232-2135

DEDICATION

For my Lord and Savior. For from Him and through Him and to Him are all things. To Him be glory forever. Romans 11:36 ESV

To Erica, my best friend, my love, and my world. Without your endless love, support, and encouragement none of this would have been possible.

ACKNOWLEDGEMENTS

First and foremost I would to extend a thank you to my amazing wife, Erica; my parents, Rebecca and David; and everyone else in my family, both biological and chosen. Through every hardship and every triumph, their loving support never faltered. This final triumph of the Ph.D. is the culmination of many, many years of encouragement and pushing me to strive further in my education. All of those little reminders, messages, or pep talks have kept me going. Now I get to stand at the summit of my education and appreciate everything that they have provided for me.

Thank you as well to Professor Mirko Gamba for these many years of tutelage and guidance. My very first Aerospace Engineering course that I took at Michigan, Introduction to Gas Dynamics, was taught by you. You would then take me on as an undergraduate research which ultimately led to you convincing me to stay at Michigan to pursue a Ph.D. after graduation. Without your influence, I would likely not be writing this dissertation. While the process has been undoubtedly challenging, you have imparted your knowledge, skills, and wisdom throughout the journey. Thank you for helping to develop how to approach these problems and pushing me to keep asking questions so that I became the scientist/engineer that I am now.

The story of my Ph.D. would be incomplete without acknowledging Dr. Fabian Chacon. The Rotating Detonation Combustor research at Michigan would not exist without you, and I was exceedingly fortunate to inherit an experiment that you built up. Even more than that, you gave me an example to strive towards and passed along the lessons you have learned. Through your mentorship, I was able to go from an uppity undergrad to a proper researcher, so I thank you for that.

A special thank you is extended to Dr. Josh Shepard, for being my partner over three years. All of those long hours in the lab or the office were made enjoyable by having someone to share the burden with. We were a tag team in that almost all the theories, discoveries, setbacks, and triumphs were done together even if you were able to get out before me. Much of this work wouldn't exist without Josh, so thank you.

I also want to thank all of my other labmates whom I have had the pleasure of sharing time with, Dr. Jacob France, Dr. Logan White, and future Drs. Rahul Ramesh, Jose Guerrero, Riley Huff, and Ben Bates. The discussions and camaraderie that I shared with you have been a highlight of the time during my Ph.D. This thank you also extends to future Dr. Yunseok Choi, who has

been one of my best friends through all of the years dating back to being a freshman. Who would have guessed that a bond formed by realizing that we shared three of the same classes would have persisted through the Ph.D. program, but I am glad that we happened to find each other in those classes. As the saying goes, “iron sharpens iron” and I know that studying and working with you all those years has made me significantly more knowledgeable.

None of this work would have been possible without the invaluable support from the technical staff in the Aerospace Engineering department at Michigan. Aaron Borgman was always willing to chase down the gremlins running rampant in the electronics. David McLean handled all of the IT that went over my head. Doug Barr was there to help set up the facilities. Tom Griffin and Chris Chartier kept the building running. Last but certainly not least is Terry Larrow, our expert machinist. A significant portion of hardware was made by him and his high standards pushed me to become a better designer. It was a pleasure interacting with everyone as they always had a smile and/or story to tell. For everything that you have done for me, I’m forever grateful to each of you.

I have been exceedingly fortunate to have been fully financially supported throughout the Ph.D. by fellowships. Funding was provided by the Department of Defense (DoD) through the National Defense Science and Engineering Graduate Fellowship (NDSEG) Program. Additional funding was given through the Rackham Predoctoral Fellowship program. Being able to focus on my work without worry of financial support was certainly a blessing. Finally, the research work was supported by the DOE/NETL University Turbine Systems Research awards No. DOE FE0031228 and DE-FE0031773 with Dr. Mark Freeman as Program Monitor (DOE NETL/UTSR program).

PREFACE

The present work consists of several independent studies and papers, all pertaining to the definition of the thermodynamic gain of Rotating Detonation Combustors (RDCs). These papers are integrated into an overarching evaluation of the experimental "pressure gain," or increase in total pressure across the combustor, frequently promised when discussing RDCs. There are theoretical and experimental explorations of said "pressure gain" and the list below highlights several critical points from each chapter that connect the entire story of "pressure gain".

- **Chapter 1:** Introduction to the RDC concept, including a historical investigation into how they became known as pressure gain devices, and the prerequisite thermodynamic background into the potential gain.
- **Chapter 2:** The impact of the flow non-uniformity on defining a singular value of pressure gain is addressed by theoretically considering different averaging procedures. The experimental methods to measure pressure gain are contrasted with the theoretical analysis, highlighting the deficiencies in the experimental techniques.
- **Chapter 3:** The work shifts into the experimental portion despite the concerns listed in Chapter 2, which describes the experimental setup and geometry. Specifically, the thrust stand needed to estimate total pressure is detailed.
- **Chapter 4 & 5:** A detailed uncertainty analysis into the experimental method for measuring "pressure gain" using thrust is given. The required assumptions and the overall experimental method result in large uncertainties, thereby limiting the precision of the measurement.
- **Chapter 6:** The length of an experimental RDC was varied to induce changes to speed, strength, and number of detonation waves. These changes were then compared to the measured pressure gains to demonstrate that the experimental pressure gain is effectively insensitive to the details of the detonation wave(s).
- **Chapter 7:** Despite the significant uncertainties presented in Chapters 4 and 5 and the insensitivity to the detonation wave(s) in Chapter 6, a measurable difference in the pressure gain was observed as the inlet was modified to augment backflow and blockage. An increase

in backflow/blockage results in a significant decrease in “pressure gain”, illustrating that the experimental “pressure gain” can measure large-scale changes to the flow.

- **Chapter 8:** Conclusions and final remarks/discussion on the usefulness of “pressure gain” as performance metric of RDCs.

TABLE OF CONTENTS

DEDICATION ii

ACKNOWLEDGEMENTS iii

PREFACE v

LIST OF FIGURES xi

LIST OF TABLES xvi

LIST OF APPENDICES xvii

LIST OF ACRONYMS xviii

LIST OF SYMBOLS xx

ABSTRACT xxiv

CHAPTER

1 Introduction 1

1.1 Motivation 1
1.2 Detonation Waves 2
1.2.1 One-Dimensional Theory 3
1.2.2 Zel'dovich-von Neuman-Döring Model 9
1.2.3 Three-Dimensional Structure of Detonations 12
1.3 Thermodynamic Benefit of Detonation 13
1.4 Combustor Performance Metrics 17
1.4.1 Combustion Efficiency 18
1.4.2 Total Pressure Ratio 18
1.4.3 Total Pressure and Irreversible Processes 19
1.5 Literature Review 20
1.5.1 Rotating Detonation Combustor Overview 20
1.5.2 History of Detonation Engines 24
1.5.3 Non-Ideal Detonation Waves and Flow Features 26
1.5.4 Non-Uniform Exit Flow 29
1.5.5 Performance Measurements 30

1.5.6 Influence of Geometric Parameters on Performance . . . 33
1.5.7 Detonation Channel and Plena Coupling . . . 34
1.6 Dissertation Objectives and Contributions . . . 36

2 Defining a Singular Value of Pressure Gain . . . 40

2.1 Introduction . . . 40
2.2 Why Averaging is Desirable . . . 41
2.3 Averaging the Non-Uniform Flow . . . 42
2.3.1 Thermodynamic States and Naming Convention . . . 42
2.3.2 General Considerations on the Averaging Process . . . 43
2.4 Types of Averaging Procedures . . . 46
2.4.1 Area-Averaging . . . 46
2.4.2 Thrust Averaging and Ideal EAP . . . 49
2.4.3 Work Averaging . . . 53
2.4.4 Entropy Averaging . . . 55
2.5 Demonstration using RDC Simulations . . . 57
2.5.1 Description of RDC Simulations . . . 57
2.5.2 Different Equivalent Total Pressures . . . 57
2.5.3 Difference Between Thrust and Work-Averages . . . 61
2.5.4 Dependence on Exit Conditions . . . 62
2.6 Alternative Experimental Pressure Gain Methods . . . 64
2.6.1 Area-Mach Relation Method . . . 65
2.6.2 Direct Measurement Method . . . 67
2.6.3 Similarity of the Methods . . . 68
2.7 Discussion . . . 70

3 Description of Experimental Setup . . . 72

3.1 Overview . . . 72
3.2 RDC Geometries . . . 72
3.2.1 General Description of the RDC . . . 73
3.2.2 Injection Geometries . . . 73
3.2.3 Combustor Length . . . 75
3.3 General System Description . . . 76
3.3.1 Control System and Data Acquisition . . . 76
3.3.2 Gas Delivery Systems . . . 78
3.3.3 Coupled Exhaust and Afterburner . . . 79
3.3.4 Pre-Detonator . . . 81
3.3.5 Testing Sequence . . . 82
3.4 Measurements . . . 83
3.4.1 Channel and Plenum Pressure Measurements . . . 83
3.4.2 Aft High-Speed Video . . . 84
3.4.3 Thrust Measurement System . . . 86
3.5 Sensor Calibration and Uncertainty . . . 88
3.5.1 Thrust System Uncertainty . . . 88
3.5.2 Flow Rate Uncertainty . . . 90

4 Improving Base-Drag Corrections for Rotating Detonation Combustor Gross Thrust Measurements . . . 93

4.1 Introduction . . . 93
4.2 Geometry and Tested Operating Conditions . . . 95
4.3 Sample Pressure Measurements . . . 96
4.4 Numerical Integration for the Base Drag . . . 98
4.4.1 Newton-Cotes Method . . . 99
4.4.2 Gauss-Kronrod Method . . . 103
4.4.3 Axisymmetric Evaluation . . . 108
4.5 Exit Flange Aside . . . 110
4.6 Discussion . . . 110

5 Evaluation of Uncertainties of Pressure Gain Measurements . . . 113

5.1 Introduction . . . 113
5.2 Thrust Measurements and Analysis . . . 114
5.2.1 Quasi-Steady Measurements . . . 114
5.2.2 Different Contributions to Gross Thrust . . . 116
5.3 Thrust Uncertainty Analysis . . . 117
5.3.1 Resultant Force Uncertainty . . . 118
5.3.2 Base Drag Uncertainty . . . 119
5.3.3 Combined Thrust Uncertainty . . . 122
5.4 Pressure Gain Measurements and Analysis . . . 124
5.4.1 Exit Gas Composition . . . 124
5.4.2 EAP and Pressure Gain Calculations . . . 125
5.4.3 Pressure Gain Uncertainty . . . 127
5.5 Some Considerations on Exit Mach Number Assumption . . . 131
5.5.1 Exit Mach Number Estimation . . . 131
5.5.2 Impact of Non-Choked Exit Conditions . . . 137
5.6 Discussion . . . 140

6 Pressure Gain Invariant to Changes to Detonations Caused by Combustor Length . . . 143

6.1 Introduction . . . 143
6.2 Geometry and Tested Operational Conditions . . . 144
6.3 Classification of Wave Mode with Respect to Length . . . 145
6.3.1 Two Indistinguishable Co-Rotating Waves (2WI) . . . 147
6.3.2 Two Distinguishable Co-Rotating Waves (2WD) . . . 149
6.3.3 Transient Super-Cycle (TSC) in Wave Dynamics . . . 152
6.3.4 Chaotic Operation (CH) . . . 157
6.4 Change in Wave Properties Induced by Length . . . 159
6.4.1 Speed of Individual Waves . . . 160
6.4.2 Pressure Ratio across Waves . . . 162
6.5 Minimal Performance Changes from Length . . . 163
6.5.1 Gross Thrust . . . 163
6.5.2 Fluidic Blockage . . . 163
6.5.3 Pressure Gain . . . 165

6.5.4 Relating Pressure Gain to Wave Dynamics . . . 166
6.6 Discussion . . . 168

7 Impact of Detonation-Induced Blockage on the Pressure Gain . . . 169

7.1 Introduction . . . 169
7.2 Geometry and Tested Operating Conditions . . . 170
7.3 Change in Wave Mode from Modified Inlet . . . 171
7.4 Change in Wave Properties from Modified Inlet . . . 173
7.4.1 Speed of Individual Waves . . . 173
7.4.2 Pressure Ratio across Detonation Waves . . . 174
7.5 Coupling Between Detonation Channel and Plenum . . . 181
7.5.1 Pressure Disturbances Upstream of Inlet . . . 181
7.5.2 Blockage Fraction Measurements . . . 184
7.6 Performance Analysis . . . 184
7.6.1 Gross Thrust Measurements . . . 184
7.6.2 Pressure Gain Measurements . . . 186
7.7 Blockage as a Loss Mechanism . . . 188
7.8 Discussion . . . 194

8 Conclusions and Final Discussion . . . 197

8.1 Summary of Work . . . 197
8.1.1 Theoretical Analysis of Pressure Gain . . . 197
8.1.2 Experimental Method to Measure Pressure Gain . . . 198
8.1.3 Relating Pressure Gain to Detonation Wave Properties . . . 202
8.1.4 Detrimental Impact of Blockage on Pressure Gain . . . 203
8.2 Conclusions . . . 204
8.3 Final Discussion . . . 206
8.3.1 Concluding Remarks on Pressure Gain . . . 206
8.3.2 Alternative Benefits of RDCs . . . 209
8.4 Future Work . . . 209
8.4.1 Combustion Efficiency Measurements . . . 209
8.4.2 Pressure-Fed System . . . 210

APPENDICES . . . 212

BIBLIOGRAPHY . . . 241

LIST OF FIGURES

FIGURE

1.1 One-dimensional representation of infinitely thin detonation wave in a) lab and b) wave frame of reference. . . . 3
1.2 A p-ν diagram with Hugoniot curve and Rayleigh lines; the different combustion regimes are labeled. . . . 6
1.3 a) The detonation structure according to ZND theory with notional changes in pressure, temperature, specific volume, and Mach number in wave frame. b) Notional changes of total pressure in both wave and lab frames. . . . 10
1.4 A p-ν diagram including the Von-Neumann spike present in the ZND model. . . . 11
1.5 Two-dimensional representation of detonation front consisting of triple point interactions of Mach stems and incident waves. Reproduced from a) Liu and Zhang [1] and b) Porowski and Teodorczyk [2]. . . . 12
1.6 Sample left) p-ν and right) T-s diagrams of the Brayton (isobaric), Humphrey (isochoric), and Fickett-Jacobs (detonation) cycles. Figure reproduced from [3]. . . . 15
1.7 Ideal thermal efficiency of the different cycles for different left) compression ratios and right) combustion pressure. Figure reproduced from [4]. . . . 16
1.8 Energy conserved T-s diagram of detonation cycle analysis. Figure reproduced from [5]. . . . 17
1.9 Schematic representation of a) annular RDC and b) unwrapped RDC flowfield with primary flow features. Figure reproduced from [6] and [7]. . . . 21
1.10 In descending order: pressure, temperature, and equivalence ratio of RDC flowfield from an unwrapped three-dimensional simulation. Figure reproduced from [8]. . . . 22
1.11 Schematic representation of differences between a) annular and b) disk RDC. Figure reproduced from [9]. . . . 23
1.12 OH chemiluminescence highlighting contact burning (CB) and auto-ignition kernels (white circle). The detonation wave is a the right edge of the image and moves to the left. Figure reproduced from [10]. . . . 27
1.13 Representative phase-averaged cycle of OH* emission detailing the different combustion regions. Figure adapted from [11]. . . . 28
1.14 Pathlines through time-averaged RDC flowfield, where the color gives changes in stagnation enthalpy. Figure adapted from [12]. . . . 29
1.15 The variations of stagnation enthalpy and entropy along the different pathlines at the exit of the RDC. Figure adapted from [12]. . . . 30

2.1 Definition of state naming along flowpath for RDC. . . . 42

2.2 Variation of total pressure at the exit of RDC for a) full two-dimensional annulus and b) discrete radial locations. Plots are for a single instance in time. 59
2.3 The different averaging techniques produce different measures of the "average" total pressure for a) Case 1, b) Case 2, and c) Case 3. Values relative to experimental EAP equivalent. 60
2.4 Static and total pressure at a) outlet of RDC, b) after thrust-averaging, and c) after work-averaging. Assumed outlet states in b) and c) are shown as flat lines. 61
2.5 Changes in a) thrust-averaged total pressure and b) work-averaged total pressure with variable assumed exit conditions. 64
2.6 Kiel probes to measure the outlet total pressure. Figure reproduced from [13]. 67
2.7 Comparison of published pressure gain (y-axis) measurements with respect to the ratio of outlet and inlet throat areas. Figure reproduced from [14]. 69

3.1 Air inlets considered in this work. Left) Baseline geometry used throughout this work and right) modified inlet to study inlet diodicity. 74
3.2 Combustor length defined from inlet throat (end of constant area portion) to exit throat. 75
3.3 Coupled exhaust vessel and afterburner. The RDC is not shown but would be to the left of the image. 80
3.4 Automated timing sequence for a four-second duration RDC test. Start and end times are user inputs in the LabVIEW control program. 82
3.5 A schematic diagram of the assembled thrust stand integrated with a round RDC. Air/fuel feed lines and accessories are not shown for clarity. The radial seal for the exit flange is highlighted in the blue circle. 85
3.6 Diagram of instrumentation of center body (inner gray circle) and exit flange (outer gray ring) for base drag corrections. Red circles and blue circles denote pressure transducers with a range of 2.04 atm and 13.6 atm respectively. 87
3.7 Uncertainty in pressure measurements on the a) center body (truncated nozzle) and b) exit flange. 91

4.1 Definition of control volume and conditions at boundaries used to determine the thrust produced by the combustor. The truncated converging nozzle is shown. 94
4.2 Summary of test conditions tested in this study. The number of detonation waves and their normalized wave speed are given by marker shape and coloration, respectively. . 96
4.3 Pressure at different radial and circumferential locations for a) $\dot{m}''_a = 330$ kg s^{-1} m^{-2} and $\phi = 0.55$ b) $\dot{m}''_a = 329$ kg s^{-1} m^{-2} and $\phi = 1.01$ c) $\dot{m}''_a = 507$ kg s^{-1} m^{-2} and $\phi = 0.61$. An asymmetry is observable in most cases. 97
4.4 Normalized weights of nodes used for midpoint rule. The last effective area extends to the edge of the center body. 100
4.5 Nozzle edge pressure is either equivalent to the last measurement (red triangle) or from extrapolated cubic fit (blue triangle) of measurements (black circles). Case where $\dot{m}''_a = 330$ kg s^{-1} m^{-2} and $\phi = 0.55$. 101
4.6 Computing the base drag with an edge pressure that is either a) constant or extrapolated gives b) different values that are c) contextualized against gross thrust. 102

4.7 a) Comparing the trapezoidal rule and Gauss scheme, where the b) numerical integration error in the Gauss-Kronrod scheme c) typically captures the differences between the two. 106
4.8 Simulated Gauss-Kronrod error compared to gross thrust. 108
4.9 The base drags with ($D_{cb,N}$) and without ($D_{cb,2D}$) axisymmetric assumption are a) different which is b) contextualized against the gross thrust. 110
4.10 By utilizing two-dimensional integration a) the gross thrust decreases compared to previously using the midpoint rule ($F_{G,old}$), which is shown b) relative to the gross thrust. 111

5.1 a) Time history of load cell measurement (resultant force) and base drag forces. b) Variation of the gross thrust relative to the quasi-steady state value. c) Average over the last 0.5 seconds of the run to produce a quasi-steady value; the time variation over this region in time is comparable to the noise. The operating condition is $\dot{m}''_a = 524$ kg s^{-1} m^{-2} and $\phi = 0.97$. 114
5.2 a) The resultant force increases more rapidly than drag forces. b) center body drag has a non-monotonic relationship with mass flux. c) Flange drag comparable to center body drag despite smaller area. 116
5.3 Gross thrust values for tested conditions; increases linearly with mass flux, and increases with increasing equivalence ratio. 118
5.4 a) The total uncertainty of resultant force (F_L) for tested conditions; the maximum is about 1.4% of the full scale of the load cell. b) The total uncertainty in F_L relative to gross thrust for tested conditions; largest values at low mass fluxes. 119
5.5 The a) total and b) relative uncertainty in base drag along the center body (D_{cb}) due to pressure sensors and unknown edge pressure for tested conditions. 121
5.6 The a) total and b) relative uncertainty in gross thrust for tested conditions. The relative uncertainty decreases with increasing flux, going from over 30% down to 5%. c) Relative uncertainty in thrust if the edge pressure is measured instead of estimated. . 123
5.7 a) Change in ratio of specific heats (γ_8) over expected range of η_c and T_8 for $\phi = 1$; variation of γ_8 within ±4% of 1.3 (red dotted curve). b) Gas constant (R_8) decreases with both ϕ and η_c; variation of R_8 due to η_c is ±6% of mean value. 125
5.8 Pressure gain measurements for tested conditions; large error bars span all variations in the data. 127
5.9 Pressure gain uncertainty introduced by a) gross thrust and b) plenum pressure measurements. The c) total and d) relative uncertainty in PG for tested conditions; higher fluxes exhibit less uncertainty. 129
5.10 Systematic uncertainty in pressure gain introduced by a) exit area uncertainty and b) choked Mach number assumption. Exit area can increase or decrease PG while Mach number can only increase PG. 131
5.11 a) Comparison between measured static pressure (p_8) and the estimated static pressure ($\widetilde{p}_8$) from the thrust balance equation. Discrepancy implies subsonic Mach numbers. b) Relative uncertainty in $\widetilde{p}_8$ across tested conditions. c) Cycle-averaged exit Mach number computed by matching p_8 and $\widetilde{p}_8$. All Mach numbers are subsonic. 133
5.12 a) Cycle-averaged exit temperature across tested conditions. b) Cycle-averaged exit Mach number across all operating conditions is subsonic. c) Comparison between different methods for estimating exit Mach number. 136

5.13 Modified PG with estimated exit Mach number correction for tested conditions. The best performance of RDC at lowest tested mass fluxes. 138
5.14 a) Comparison between modified pressure gain with Mach number correction (PG_M) and pressure gain with the choked assumption (PG). Subsonic flow causes PG_M to be larger when the exit Mach number is below 0.8. b) Ratio of PG_M and PG across test conditions. c) Uncertainty comparison of PG_M and PG with choked assumption. . . . 140

6.1 Map of operational modes for Configurations. a) A, b) B, c) C, and d) D. 146
6.2 The channel pressure a) trace, b) time-varying spectrum, and c) time-averaged spectrum of a 2WI operation. Data from $\dot{m}''_a = 513$ kg s^{-1} m^{-2} with $\phi = 0.6$ in Configuration C. 147
6.3 Probability density function of cycle-to-cycle pressure ratio across detonation waves for 2WI. 148
6.4 The channel pressure a) trace, b) time-varying spectrum, and c) time-averaged spectrum of a 2WD operation. Data from $\dot{m}''_a = 451$ kg s^{-1} m^{-2} with $\phi = 0.6$ in Configuration C. 150
6.5 Probability density function of cycle-to-cycle pressure ratio across detonation waves for 2WD. 151
6.6 The channel pressure a) trace, b) time-varying spectrum, and c) time-averaged spectrum of a TSC operation. Data from $\dot{m}''_a = 522$ kg s^{-1} m^{-2} with $\phi = 0.98$ in Configuration D. 153
6.7 a) The time variation of multiplicity (N), speed (v), and direction of the wave systems mid-run. b) Simplified representation of the super-cycle. Data from $\dot{m}''_a = 522$ kg s^{-1} m^{-2} with $\phi = 0.98$ in Configuration D. 155
6.8 Probability density function of super-cycle period. 156
6.9 Distributions along the super-cycle phase of multiplicity (a and c) and normalized velocity (b and d) in the positive (a and b) and negative (c and d) directions. 157
6.10 The channel pressure a) trace, b) time-varying spectrum, and c) time-averaged spectrum of a CH operation. Data from $\dot{m}''_a = 193$ kg s^{-1} m^{-2} with $\phi = 1.23$ in Configuration B. 158
6.11 The time variation of multiplicity (N), speed (v), and direction of the wave systems mid-run. Data from $\dot{m}''_a = 193$ kg s^{-1} m^{-2} with $\phi = 1.23$ in Configuration B. 159
6.12 Normalized speed of individual detonation wave(s) for a) $\dot{m}''_a = 327$ kg s^{-1} m^{-2} b) $\dot{m}''_a = 393$ kg s^{-1} m^{-2} and c) $\dot{m}''_a = 520$ kg s^{-1} m^{-2}. 161
6.13 Normalized pressure ratio of individual detonation waves for a) $\dot{m}''_a = 327$ kg s^{-1} m^{-2} b) $\dot{m}''_a = 393$ kg s^{-1} m^{-2} and c) $\dot{m}''_a = 520$ kg s^{-1} m^{-2}. 162
6.14 Gross thrust output for a) $\dot{m}''_a = 327$ kg s^{-1} m^{-2} b) $\dot{m}''_a = 393$ kg s^{-1} m^{-2} and c) $\dot{m}''_a = 520$ kg s^{-1} m^{-2}. 164
6.15 Change in gross thrust output relative to Configuration A ($F_{G,A}$) for a) $\dot{m}''_a = 327$ kg s^{-1} m^{-2} b) $\dot{m}''_a = 393$ kg s^{-1} m^{-2} and c) $\dot{m}''_a = 520$ kg s^{-1} m^{-2}. 164
6.16 The fluidic blockage fraction for a) $\dot{m}''_a = 327$ kg s^{-1} m^{-2} b) $\dot{m}''_a = 393$ kg s^{-1} m^{-2} and c) $\dot{m}''_a = 520$ kg s^{-1} m^{-2} across tested configurations. 165
6.17 The pressure gain for a) $\dot{m}''_a = 327$ kg s^{-1} m^{-2} b) $\dot{m}''_a = 393$ kg s^{-1} m^{-2} and c) $\dot{m}''_a = 520$ kg s^{-1} m^{-2}. 166

6.18 A comparison between changes in the individual wave speed and measured pressure gain for a) ϕ =0.6, b) ϕ = 0.8 and c) ϕ =1.0. 167

7.1 Air inlets considered in this work. Left) Baseline geometry used throughout this work and right) modified inlet to study inlet diodicity. 171
7.2 Map of operational modes for a) AAI and b) AAI-M for the same combustor length, inlet area, and outlet areas. 172
7.3 a) Evolution of wave speed across the operating map. b) Direct comparison of wave speed between inlets. 173
7.4 a) Evolution of detonation pressure ratio across the operating map. b) Direct comparison of pressure ratio in the channel between inlets. 175
7.5 PDFs of the channel a) peak pressure, b) base pressure, and c) normalized pressure ratio across detonation wave. Data from $\dot{m}''_a = 513$ kg s^{-1} m^{-2} with $\phi = 0.6$. 177
7.6 PDFs of the relative change in the channel a) peak pressure, b) base pressure, and c) normalized pressure ratio across detonation wave. Data from $\dot{m}''_a = 513$ kg s^{-1} m^{-2} with $\phi = 0.6$. 178
7.7 Probability that the relative change in a) peak pressure, b) base pressure, and c) normalized pressure ratio across detonation wave in the channel. 180
7.8 a) Direct comparison of pressure ratio across the oblique shocks in the plenum between inlets. b) The reduction in pressure ratio between the plenum and channel. 181
7.9 Probability that the relative change in a) peak pressure, b) base pressure, and c) pressure ratio across oblique shock wave in the inlet. 182
7.10 a) Blockage fraction decreases with increasing mass flux. b) Direct comparison of blockage fraction between the two inlets. 185
7.11 a) Gross thrust still decreased with increasing flux. b) Direct comparisons of F_G appear to fall along the 1:1 line. c) There is an insignificant probability of a worse F_G due to the large uncertainties. 186
7.12 a) Pressure gain still decreased with increasing flux. b) Direct comparisons of PG suggest worse performance from AAI-M. c) There is a high probability of a worse PG despite the large uncertainties. 187
7.13 Comparing the mass-based blockage fraction to pressure gain. 189
7.14 a) Pressure gain if the plenum pressure increase caused by fluidic blockage is neglected. b) Direct comparison of hypothetical pressure gain between inlets. c) Changes in the hypothetical pressure gain are insignificant. 191
7.15 Comparing pressure-based blockage fraction to a) hypothetical PG without plenum pressure increase and b) change in PG from measured to hypothetical value. 192
7.16 Comparing the mass-based blockage fraction to pressure gain decrease. 193

LIST OF TABLES

TABLE

1.1 Description of location notation in air-breathing engines. 8
1.2 Representative values of change in velocity and thermodynamic properties for detonation and deflagration [15]. 9

2.1 Description of location notation in air-breathing engines. 43
2.2 Total pressure averaging procedures considered for their applications to RDC and the conserved quantities associated with each procedure. 46
2.3 Summary of the geometry and operating condition of the hydrogen/air numerical simulations used in this study. [16, 17] 58
2.4 Summary of the different average total pressures across the simulated cases. Results assume: $M_{z,8} = 1$ for $\mathrm{EAP_e}$, $p_0 = 0.1$ atm for $\left\langle p_{tz,8} \right\rangle_F$, and $p_{tz,5} = 1$ atm for $\left\langle p_{tz,4} \right\rangle_W$. 59

3.1 A summary of which geometric properties varied during the different studies outlined in the following chapters. 73
3.2 Relevant geometric parameters of tested RDC configurations. Variables (in order are): L, combustor length; d_i, inner diameter of annulus; d_o, outer diameter of annulus; $A_8/A_{3.2}$, ratio between exit throat and annulus areas; $A_{3.2}/A_{3.1}$, ratio between annulus and air inlet throat areas; $d_m = {}^1/_2\,(d_i + d_o)$, mean annulus diameter 76
3.3 Linear calibration and calibration uncertainties of key measurements used in this work. 89

4.1 Nodes and weights of Gauss-Kronrod scheme with $n = 2$ and $r_{CB} = 7.33$ cm. 105

6.1 Relevant geometric parameters of tested RDC configurations. Variables (in order are): L, combustor length; d_i, inner diameter of annulus; d_o, outer diameter of annulus; $A_8/A_{3.2}$, ratio between exit throat and annulus areas; $A_{3.2}/A_{3.1}$, ratio between annulus and air inlet throat areas; $d_m = {}^1/_2\,(d_i + d_o)$, mean annulus diameter 144

7.1 Parameters for the quadratic fits that satisfy Eqn. 7.12 193

F.1 Position and sensor range for CTAP measurements taken for base drag correction. . . . 237

LIST OF APPENDICES

A Unsteady Terms in Control Volume for Periodic Flows 212

B Inequality within Experimental EAP 215

C Ideal Equivalent Available Pressure Derivation 217

D Work-Averaged Extended Derivation 220

E Equating Time-Average to Area-Average Quantities in Periodic Flowfields 223

F Sensor Positions for Base Drag Correction 237

G Pressure Gain Uncertainty Sensitivity Coefficients 238

LIST OF ACRONYMS

AAI Axial Air Inlet

AAI-M Modified Axial Air Inlet

CDF Cumulative Density Function

CFD Computational Fluid Dynamics

CH Chaotic operation of multiple waves

CJ Chapman-Jougeut

CTAP Capillary Tube Averaged Pressure

CPG Calorically Perfect Gas

CV Control Volume

CWA Circuit Wave Analysis

DNS Direct Numerical Simulation

DTD Deflagration-to-Detonation

EAP Equivalent Available Pressure

FJ Fickett-Jacobs

NPS Naval Postgraduate School

PDE Pulsed Detonation Engine

PDF Probability Density Function

PG Pressure Gain

PGC Pressure Gain Combustion

PSD Power Spectral Density

RDC Rotating Detonation Combustor

RDE Rotating Detonation Engine

TSC Multiple waves that follow a transient super cycle

ZND Zel'dovich-von Neuman-Döring

1W Single wave

2WI Two co-rotating, *indistinguishable* waves

2WD Two co-rotating, *distinguishable* waves

LIST OF SYMBOLS

a speed of sound [m s^{-1}]

A geometric area [m^2]

B_m mass-based inlet blockage fraction

B_p pressure-based inlet blockage fraction

c_d discharge coefficient

c_p specific heat at constant pressure [J kg^{-1} K^{-1}]

d_i inner diameter of annulus [mm]

d_o outer diameter of annulus [mm]

D detonation wave speed [m s^{-1}]

D_{cb} base drag from center body [N]

D_{fl} base drag from flange [N]

$\hat{\mathbf{e}}_\mathbf{z}$ unit vector in axial direction

f frequency [Hz]

F_G gross thrust [N]

F_L resultant force from load cell [N]

h specific enthalpy [J kg^{-1}]

L combustor length [mm]

$\dot{m}$ mass flow rate [kg s^{-1}]

$\dot{m}''_a$ air mass flux defined at geometric inlet throat, $\dot{m}_a/A_{3.1}$ [kg s^{-1} m^{-2}]

M Mach number, u/a

$\hat{\mathbf{n}}$ unit vector normal to surface

N_{D} number/multiplicity of detonation waves

p pressure [Pa]

p^{+} peak pressure in detonation cycle [atm]

p^{-} base pressure in detonation cycle [atm]

p_{r} pressure ratio across detonation wave

PG pressure gain from EAP methodology

PG_{M} Mach number corrected pressure gain

q added specific heat [J kg^{-1}]

r radius [m]

R gas constant of mixture [J kg^{-1} K^{-1}]

$\bar{R}$ universal gas constant [J mol^{-1} K^{-1}]

s specific entropy [J kg^{-1} K^{-1}]

t time [s]

T temperature [K]

u speed, $|\mathbf{u}|$ [m s^{-1}]

$\mathbf{u}$ velocity vector [m s^{-1}]

w numerical integration weight

w_{net} net specific work of cycle [J kg^{-1}]

$\dot{W}$ rate of extracted work [J s^{-1}]

$\mathbf{x}$ position vector

$\mathcal{M}$ molar mass [g mol^{-1}]

$\mathcal{O}\left(10^{n}\right)$ order of n

$\mathcal{P}_{n}$ monic polynomial of order n

$\mathcal{Q}$ arbitrary thermodynamic/fluid quantity

γ ratio of specific heats

δ uncertainty according to 95% confidence interval

Δp gauge pressure, $p - p_{\infty}$ [atm]

ϵ numerical integration error

η_c combustion efficiency

η_n nozzle efficiency

η_T turbine efficiency

η_{th} thermal efficiency

θ circumferential position [radian]

ν specific volume, $1/\rho$ [m^3 kg^{-1}]

π_b total pressure ratio across burner/combustor

ρ density [kg m^{-3}]

σ standard deviation

τ period

ϕ equivalence ratio

χ mole fraction

ψ position relative to detonation wave

ω rotational speed

$\langle\cdot\rangle_A$ area-averaged quantity

$\langle\cdot\rangle_F$ thrust-averaged quantity

$\langle\cdot\rangle_M$ mass-averaged quantity

$\langle\cdot\rangle_S$ entropy-averaged quantity

$\langle\cdot\rangle_t$ time-averaged quantity

$\langle\cdot\rangle_W$ work-averaged quantity

Subscripts

3 air plenum/start of combustor state

3.1 air inlet throat state

3.2 detonation channel state

4 end of combustor state

8 nozzle throat state

9 exit plane of nozzle state

a air

cb end face of center body

C quantity from non-reacting test

C|$\dot{m}$ quantity from non-reacting test at given mass flow rate

C|p quantity from non-reacting test at given plenum pressure

CJ ideal Chapman-Jougeut quantity

e experimental

f fuel

fl exit flange

H quantity from test with detonative operation

i ideal quantity

K Gauss-Kronrod

N Newton-Cotes

o orifice

t total/stagnation quantity

z axial direction component, $\mathbf{u} \cdot \hat{\mathbf{e}}_\mathbf{z}$

∞ ambient condition

Superscripts

$\tilde{}$ EAP equivalent condition

$\prime$ deviation from a mean value

o reference value for NASA polynomial

ABSTRACT

Detonation-based combustors are attractive for potential increases in thermodynamic efficiency, leading to improved thrust or work production. Fundamentally, a detonation produces less entropy at the flame front. Rotating detonation combustors (RDCs) are designed to provide this gain in a compact form. However, experimentally evaluating this is challenging due to the unsteady, non-uniform, and complex flow within RDCs along with being incapable of measuring entropy. Thus, in the RDC literature, the thermodynamic gain is equated to an increase in total pressure globally across the RDC, termed "pressure gain" (PG). The RDC community widely accepts PG as a preferred performance metric. This work comprehensively evaluates experimental measurements of this global PG metric.

One must average the non-uniform exit flow to define a singular exit total pressure for an RDC. Experimentally, this is done through the Equivalent Available Pressure (EAP) methodology. This work demonstrates that the EAP is equivalent to area-averaging and does not conserve the exiting flow's momentum, energy, or entropy. Additionally, the concept of PG is not unique, as shown by applying various averaging methods to high-fidelity, three-dimensional RDC simulations. For instance, the average total pressure varies by 10-20% depending on the assumed outlet state and whether one uses the RDC for work or thrust production. Perhaps even more importantly, the EAP significantly under predicts, by 2.5-38%, the other average total pressures. Therefore, the experimental PG has limitations from a theoretical perspective.

Nevertheless, the EAP method of experimentally measuring PG is adapted and applied to an axial-air inlet RDC with a nozzle, with $A_8/A_{3.1} = 2.31$. A parametric study of air mass fluxes, from 193 kg s^{-1} m^{-2} to 773 kg s^{-1} m^{-2}, and equivalence ratios, from 0.6 to 1.2, of hydrogen/air chemistry was investigated. No positive PG was measured, with the best performance being a total pressure loss of 20%. A detailed uncertainty analysis reveals that the experimental PG method is prone to significant experimental uncertainties, such as resolving the base drag acting upon the bluff nozzle. When combined, the uncertainties in the PG result are ±6%, a 30% relative change of the measured -20%. Such precision limitations pose practical challenges for future demonstrations of a definitive positive PG. Additionally, further improvements to the accuracy and precision of EAP and PG come from evaluating the area-averaged exit Mach number using a static pressure measurement.

This work also varied the combustor length from 79 mm to 137 mm, to induce significant changes to the properties of the detonation wave(s). The PG only changed by at most 5% despite the wave speed changing by 38%. Furthermore, the changes in PG are less than the uncertainty; thus, the PG is invariant to such changes. Conversely, a change to the injection geometry investigated in this work exhibited a measurable decrease in PG (greater than 6%), which is attributed to an augmentation of the backflow in the system from intentionally worsening the injector diodicity. Overall, there are many competing physics within a RDC (e.g., wave strength, backflow, secondary combustion, secondary waves, etc.), and the global PG has different sensitivities to the individual processes, limiting the metric's usefulness. Ultimately, while PG can readily assess the impact of inlet performance on the overall performance of RDC, the concerns about not conserving any thermodynamic quantity, high experimental uncertainty, and insensitivity to several key features of the RDC flowfield limits PG as an all-inclusive performance metric.

CHAPTER 1

Introduction

1.1 Motivation

Detonation-based devices, such as a Rotating Detonation Engine (RDE) or a Rotating Detonation Combustor (RDC), are attractive technologies for overcoming the efficiency plateau that shackles modern-day combustion devices. Modern-day gas turbine engines are marvels of engineering that have achieved exceptional levels of efficiency, reaching up to 65%. However, the iterative increases in efficiency have grown less and less significant; such deflagrative devices have efficiencies that have reached an asymptotic value due to sizing and material considerations. Research into RDCs holds promise for a step-change in efficiency by several percent [4]. Such efficiency increases are imperative as the need for increasingly better performance from combustion devices (either energy generation or propulsive applications) to meet sustainability goals outgrows the possible efficiencies that the traditional, constant-pressure devices are capable of.

A RDC achieves this thermodynamic gain through an unsteady combustion front, producing less entropy for the same heat input than the traditional deflagration. The archetypal RDC design is geometrically simple, composed of two concentric cylinders. A fuel/oxidizer injection system continuously feeds fresh reactants into the annular gap between the cylinders, called the combustion or detonation chamber. As the fuel and oxidizer mix in the combustion chamber and travel axially through the combustor, one or more detonation waves consume the fresh mixture as it continuously rotates in the circumferential direction at a frequency of several kHz, resulting in quasi-steady exhaust conditions [18]. This process is self-sustaining as the passage of the detonation wave modulates the passive reactant injection, which recovers before providing a fresh mixture to the next passage of the wave. The high-temperature and pressure products from the detonation(s) are then exhausted axially to produce either work or thrust. While accurate, this concise description belies the complexity of the flowfield, which is intrinsically three-dimensional, unsteady, compressible, viscous, reactive, and has high heat fluxes and pressures, making measurements challenging. Additionally, all these phenomena couple together across multiple scales that are not yet fully

understood. The ongoing research in this field seeks to understand the complex flowfield and to demonstrate whether there is a tangible benefit to utilizing such a device in a practical setting, which is the focus here.

Demonstrating the purported increase in thermodynamic efficiency quantitatively experimentally has proven challenging. One such challenge arises from the difficulties in directly measuring the thermodynamic state (pressure, temperature, and velocity) at the exit of the RDC. Another challenge arises from the spatio-temporal non-uniformity of the flow around the annulus in the RDC. This non-uniformity is caused by the unsteady, albeit periodic, propagation of the detonation wave about the annulus. In contrast, deflagrative combustors typically have a uniform and steady flow throughout the combustor. A figure of merit that captures the non-uniformity of RDCs while allowing for direct comparisons to deflagration devices is desirable in quantifying and demonstrating the usefulness of such devices. The label of Pressure Gain Combustion (PGC) has been given to RDCs; thus, the current figure of merit compares an "average" total pressure at the outlet to the incoming total pressure. An increase in the total pressure, which is a surrogate measure of entropy, would then demonstrate a benefit over deflagrative devices with a total pressure loss of several percent. The definition, measurement, and validity of this global total pressure ratio, or Pressure Gain (PG), as the figure of merit for RDCs is the motivation of this work.

1.2 Detonation Waves

As the name suggests, the combustion within RDCs are detonation waves instead of the traditional deflagration. A detonation wave is the least well-known of the combustion modes, and it has had limited application in a broad engineering setting compared to the other combustion modes (explosions and deflagrations). In total, there are three categories for the combustion of a premixed mixture:

1. *Explosion*: reactions occur nearly instantaneously and simultaneously throughout the mixture without a wavefront.

2. *Deflagration*: a combustion wave propagating at subsonic speeds.

3. *Detonation*: a combustion wave propagating at supersonic speeds.

While explosion calls to mind militaristic applications, the most commonly encountered explosion is within the internal combustion engine. After the compression stroke, the fuel/air mixture is ignited, with the piston maintaining a nearly constant volume during ignition. Meanwhile, deflagration covers a range of devices, including but not limited to jet engines, rocket engines, and gas turbines for power generation. While all of these applications are not premixed, the speeds at which chemical

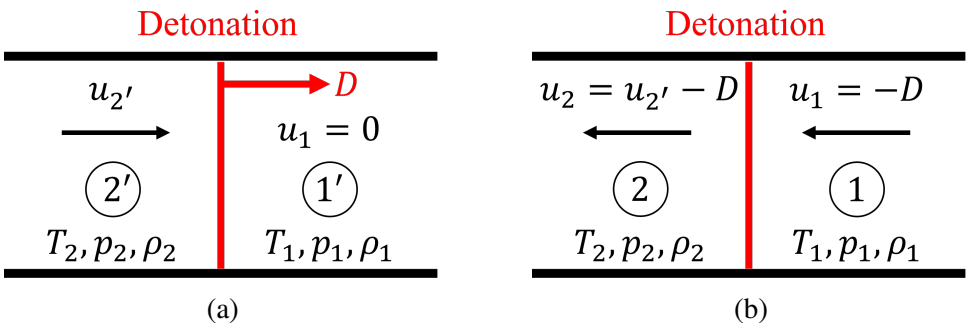

Figure 1.1: One-dimensional representation of infinitely thin detonation wave in a) lab and b) wave frame of reference.

reactions occur are relatively slow. These are well-known and have seen extensive use in wide applications.

Nevertheless, for reasons discussed later in this section, detonation-based propulsion or energy conversion devices are of great interest for potential efficiency gains. The remainder of this section is to provide the background theory of detonation waves and their associated physics. Then, in the following section, Section 1.3, the source of interest in detonations, which comes in the form of an observable benefit in thermodynamic cycle analysis, is explored in detail.

1.2.1 One-Dimensional Theory

While the overall structure of detonation waves is complex and three-dimensional, one-dimensional theory is applied to gain insight into the processes as it presents an idealized version of detonation waves. Chapman [19] and Jouguet [20] were the first to apply one-dimensional theory to detonations, leading to the development of Chapman-Jougeut (CJ) theory, named after them. A Control Volume (CV) approach is adopted, which encompasses the upstream, unburnt state (①) and the downstream, burnt state (②). A visual of the CV in the laboratory frame of reference is given in Figure 1.1a, while the same CV in the wave frame of reference is given in Figure 1.1b. The wave frame of reference is adopted to simplify the following analysis. The variable D is the propagation velocity of the detonation wave. Further simplifications occur by assuming the following: [15]

1. The flow is steady (in the wave frame) and one-dimensional, with no area changes.
2. States 1 and 2 are uniform with no gradients in composition or properties.
3. The detonation wave front is a discontinuous plane where all variations in flow properties occur. Thus, infinitely fast chemical reactions are implicitly assumed.

4. The working gas is a Calorically Perfect Gas (CPG). That is to say that the perfect gas law is the appropriate equation of state for the gases, and both specific heats are constant and remain unchanged through the detonation.

5. Viscous and other body forces are negligible and are neglected.

6. There is no heat transfer to the wall.

With the assumptions and simplifications discussed above, the integral form of the conservation of mass reduces to the following,

$$\rho_1 u_1 A_1 = \rho_2 u_2 A_2 \tag{1.1}$$

where ρ denotes density, u denotes velocity, and A denotes area. The areas were assumed to be constant and equal ($A_2 = A_1$); thus, the Eqn. 1.1 states that the mass flow rate per unit mass, i.e., the mass flux ($\dot{m}''$), is a constant.

$$\dot{m}'' = \rho u = \text{const.} \tag{1.2}$$

Likewise, the integral form of the conservation of momentum reduces to,

$$p_1 + \rho_1 u_1^2 = p_2 + \rho_2 u_2^2 \tag{1.3}$$

where p denotes pressure. Finally, the integral form of the conservation of energy becomes,

$$c_p T_1 + \frac{1}{2} u_1^2 + q = c_p T_2 + \frac{1}{2} u_2^2 \tag{1.4}$$

where c_p indicates the specific heat at constant pressure, T indicates temperature, and q is the specific (per unit mass) heat added to the CV from the chemical reactions. Recall that despite the chemical reactions within the detonation wave, the specific heat (c_p) does not change between the states under the CPG assumption. Likewise, the CPG assumption leads to the equation of state being the perfect gas law.

$$p = \rho R T \tag{1.5}$$

The gas constant, R, is defined as the universal gas constant divided by the mean molecular weight of the mixture.

There are five unknowns in this description: u_1, u_2, ρ_2, T_2, and p_2. However, the conservation equations and state equation total four unique relationships, thereby making the problem under-defined. An additional constraint based on physical processes is required to address the under-defined problem.

Determining the additional constraint starts by finding the simultaneous solution of the conservation of mass and momentum equations. Plugging Eqn. 1.1 into Eqn. 1.3, and re-arranging

results in the following,

$$\frac{p_2 - p_1}{\nu_2 - \nu_1} = -\rho_2^2 u_2^2 \tag{1.6}$$

$$= -\left(\dot{m}''\right)^2 \tag{1.7}$$

where ν denotes specific volume ($1/\rho$). This relationship is referred to as the Rayleigh line since for a given mass flux and initial condition (p_1 and ρ_1), Eqn. 1.6 is a linear line when plotted on a p-ν diagram. The slope of the line is equivalent to the square of the mass flux through the combustion event.

$$p_2 = \left(\dot{m}''\right)^2 (\nu_1 - \nu_2) + p_2 \tag{1.8}$$

Any physical processes, subject to the assumptions made, would follow this relationship. However, the Rayleigh line is insufficient in providing the additional constraint since it does not provide a unique solution.

The energy equation used in conjunction with the Rayleigh line can provide the desired unique solution; however, it is advantageous to transform Eqn. 1.4 to be a function of pressure and specific volume similar to the Rayleigh line. Invoking the perfect gas law, Eqn. 1.5, the temperature dependence is removed to get the following intermediate result after some re-arranging.

$$\frac{c_p}{R}(p_2\nu_2 - p_1\nu_1) - \frac{1}{2}\left(u_1^2 - u_2^2\right) = q \tag{1.9}$$

Recall that for a CPG, the specific heat at constant pressure is related to the gas constant and the ratio of specific heats (γ).

$$c_p = \frac{\gamma}{\gamma - 1}R \tag{1.10}$$

The Rayleigh line equation, Eqn. 1.6, then replaces the velocity squared terms in Eqn. 1.9. Doing so incorporates solving the mass and momentum equation simultaneously with the energy equation. Thus, combining the modified energy equation with the Rayleigh line and the definition of c_p gives the final result, the Hugoniot curve.

$$\frac{\gamma}{\gamma - 1}(p_2\nu_2 - p_1\nu_1) - \frac{1}{2}(p_2 - p_1)(\nu_1 + \nu_2) = q \tag{1.11}$$

The Hugoniot curve gives the possible solutions to the energy, momentum, and state equations in the p-ν plane for a given amount of added heat, q, to some initial state.

Figure 1.2, a p-ν diagram, shows the Rayleigh line and the Hugoniot curve for an arbitrary mass flux, added heat, and initial conditions. The initial conditions (①) are point A; all possible Rayleigh lines must pass through this point. Non-physical results result from solutions that cannot

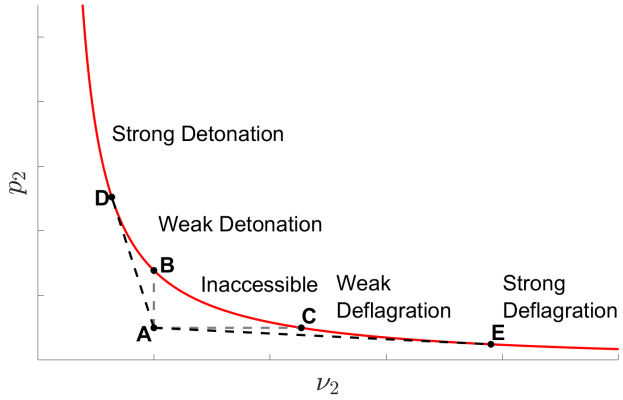

Figure 1.2: A p-ν diagram with Hugoniot curve and Rayleigh lines; the different combustion regimes are labeled.

simultaneously satisfy the Rayleigh line and the Hugoniot curve. For instance, an infinite mass flux would result in a vertical Rayleigh line originating from point A, while zero mass flux would result in a horizontal Rayleigh line. These scenarios give points B and C, respectively. A Rayleigh line can not pass through A and intersect with the Hugoniot curve between points B and C due to the negative slope and negative mass fluxes being impossible, see Eqn. 1.6. Therefore, the solutions region between points B and C is completely inaccessible.

The possible physical solutions are then further separated into a region where the combustion causes the pressure to increase and a region where the pressure causes the pressure to decrease. These are classified as detonation and deflagration, respectively. Two additional points of interest are defined to characterize these combustion regimes further. The Hugoniot curve is a hyperbola. Thus, two tangent Rayleigh lines exist, further segmenting the Hugoniot curve. The upper tangent point is point D, while the lower tangent point is point E. These points are the upper and lower CJ points. Chapman recognized that at the point of tangency, the slope of the Hugoniot curve must be equal to that of the Rayleigh curve. Chapman [19] demonstrated using Gibb's relation that the slope of the Hugoniot curve at these points is,

$$T_2 \left[\frac{ds_2}{d\nu_2}\right]_{\mathrm{D}} = \frac{1}{2}(\nu_1 - \nu_2)\left(\frac{p_2 - p_1}{\nu_1 - \nu_2} + \left[\frac{dp_2}{d\nu_2}\right]_{\mathrm{D}}\right) \tag{1.12}$$

where s denotes the specific entropy. However, the slope must also be equivalent to the Rayleigh

line. Differentiating the Rayleigh line, Eqn. 1.8, gives,

$$\left[\frac{dp_2}{dv_2}\right]_{\mathrm{D}} = -\rho_2^2 u_2^2 \tag{1.13}$$

$$= \frac{p_2 - p_1}{v_2 - v_1} \tag{1.14}$$

For both Eqns. 1.12 and 1.14 to be true, ds_2/dv_2 must be zero at the CJ point. Thus, an isentrope is tangent to the Rayleigh line and Hugoniot curve at the CJ point [21]. From this, Eqn. 1.14 then reduces to the following.

$$\left[\left(\frac{dp_2}{dv_2}\right)_s\right]_{\mathrm{D}} = -\rho_2 u_2^2 \tag{1.15}$$

The subscript "s" is appended to the derivative to indicate that the derivative is evaluated at constant entropy. A similar process can done for point E, and Glassman details the proof of this [22].

Now recall the definition of the speed of sound (a),

$$a_2^2 = \left(\frac{\partial p_2}{\partial \rho_2}\right)_s \tag{1.16}$$

$$= -\frac{1}{\rho_2^2}\left(\frac{\partial p_2}{\partial v_2}\right)_s \tag{1.17}$$

After combining Eqns. 1.15 and 1.17, it is found that the post-combustion velocities at the CJ points are the local speed of sound.

$$u_{2,\mathrm{CJ}} = a_2 \tag{1.18}$$

The sonic velocity in the post-combustion state is a crucial result from CJ theory.

With the CJ points, further segmentation of the Hugoniot curve in Figure 1.2 is possible, and these are summarized in Tab. 1.1. The region of the Hugoniot curve between C-E is called weak deflagration. In this regime, p_2 is greater than the lower CJ pressure ($p_{\mathrm{CJ,E}}$), thus, $u_2 < a_2$. Thus, for weak deflagration, the burnt gas travels at subsonic speeds. The burned gas velocity would become supersonic for a further reduction in pressure from point E. This regime is called strong deflagration. Since heat addition in a constant area without viscosity and turbulence cannot accelerate subsonic flow to supersonic flow, strong deflagration is deemed physically impossible to achieve. Thus, only weak deflagration is possible. With deflagration causing an acceleration of the flow away from the flame front, deflagration is a subsonic flame front with a small pressure decrease.

Likewise, the region above the upper CJ point (point D) is referred to as strong detonation, while the region below the CJ point, between D and B, is referred to as weak detonation. Jougeut [20] argued that strong detonation, while physically achievable, is unstable and only exists in a

Region of Hugoniot Curve	**Classification**	**Possible?**	Burned Gas Velocity
Above D	Strong Detonation	Transient	Subsonic
D	C-J Detonation	Yes	Sonic
D-B	Weak Detonation	No	Supersonic
B-C	Inacessible	No	N/A
C-E	Weak Deflagration	Yes	Subsonic
E	C-J Deflagration	Yes	Sonic
Below E	Strong Deflagration	No	Supersonic

Table 1.1: Description of location notation in air-breathing engines.

transient state. In the case of strong detonation, the velocity behind the wave would be subsonic. If a rarefaction wave were to form in this post-combustion state, the subsonic speeds would enable this wave to propagate to the flame front. Several realistic processes, including heat loss, friction, turbulence, etc, could cause the rarefaction wave. The wave would cause the pressure to decrease and approach the CJ pressure. This process would repeat until the detonation wave decays to the CJ condition. Once at the CJ state, the sonic speeds post-combustion would isolate the flame front from downstream perturbations. Overall, strong detonations are observable in reality, but they exist as a transient state and will eventually decay to a CJ detonation without external forcing. Additional information about the structure of the detonation wave is required to assess the possibility of weak detonation waves. The following section will discuss that the Zel'dovich-von Neuman-Döring (ZND) model prohibits weak detonations from existing.

In the ZND model, only the CJ detonations are physically possible and stable. Thus, the condition of sonic burnt gas velocity, Eqn. 1.18, provides a constraint to the conservation of mass, momentum, and energy in such a manner that a unique solution for ② exists for a given ①. Thus, in the CJ theory, the properties of the detonation wave are uniquely determined by the upstream mixture and state. An iterative approach is required to solve for this state, and in this work, NASA Chemical Equilibrium Applications [23] was used to perform such calculations. Thus, it is now possible to determine the change in properties caused by detonation. Table 1.2 provides representative values for the velocity and thermodynamic variables for detonations and contrasts them with deflagration. Detonations propagate into the fresh mixture at supersonic speeds, with the post-combustion gases traveling at sonic speeds. Unlike deflagration, the static pressure increases across detonations, and detonations achieve higher overall static temperatures. The increase in static pressure and temperature is particularly interesting for improving efficiency, as discussed in Section 1.4.

Quantity	Detonation	Deflagration
u_1/a_1	5-10	0.0001-0.03
u_2/u_1	0.4-0.7	4-16
p_2/p_1	13-55	0.98-0.976
T_2/T_1	8-21	4-16
ρ_2/ρ_2	1.4-2.6	0.006-0.25

Table 1.2: Representative values of change in velocity and thermodynamic properties for detonation and deflagration [15].

1.2.2 Zel'dovich-von Neuman-Döring Model

The above one-dimensional analysis assumed that the detonation wave is infinitely thin by having infinitely fast chemistry. However, finite-rate chemistry, indicative of reality, thickens the combustion region. A model of a one-dimensional but finite-width detonation wave was proposed independently by Zel'dovich [24], von Neumann [25], and Döring [26] in the 1940s. This model is named ZND model after them, and it serves as the most common representation of the detonation wave structure.

The explicit assumptions that are made for the ZND model are as follows: [21]

1. The flow is one-dimensional and steady in the shock-frame.

2. The shock is a jump discontinuity such that transport effects within the shock are negligible, and the shock is infinitely thin.

3. The reaction rate before the shock is zero and is finite after the shock. Additionally, only the forward reactions occur.

4. Except for the chemical composition, the thermodynamic variables are in local thermal equilibrium at every point. The relaxation of the internal modes after the shock is instantaneous.

A graphical representation of the ZND model is in Figure 1.3, which qualitatively shows the rise and fall of thermodynamic properties throughout the different regions within the detonation wave. Note that Figure 1.3a is in the moving shock frame, and this is the frame where the detonation is steady. The ZND model describes a detonation wave as a discontinuous planar shock front that compresses and heats the mixture before the finite rate chemistry begins. As shock waves are several molecular mean-free paths thick, it is improbable for chemical reactions to occur within the shock. The post-shock state is the von-Neumann state, and the changes in properties are comparable to those across a normal shock. Following the shock, there is an induction region/zone as there is a delay time before the elevated temperature and pressure cause auto-ignition of the mixture.

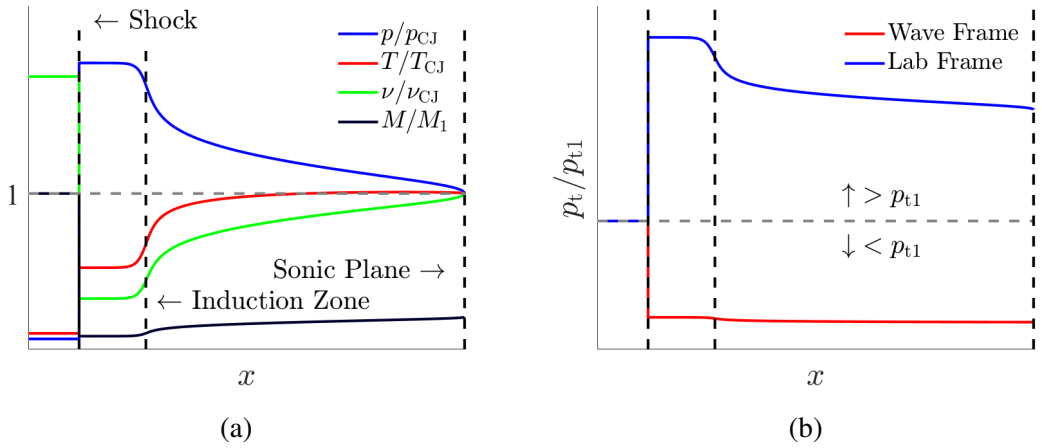

Figure 1.3: a) The detonation structure according to ZND theory with notional changes in pressure, temperature, specific volume, and Mach number in wave frame. b) Notional changes of total pressure in both wave and lab frames.

The induction region's temperature, pressure, and density remain effectively constant. Heat release from the chemical reactions occurs over a finite region in space/time, aptly named the reaction region. As the exothermic reactions progress, the temperature, specific volume, and Mach number in the wave frame increase while the pressure and density decrease within the reaction region as the distance from the shock increases. However, the heat release occurs at a pressure (blue line) significantly larger than the starting pressure in Figure 1.3a, which is advantageous since entropy production is less at elevated pressures. Eventually, the flow reaches the sonic plane, and the properties at this plane match those defined in the above CJ theory. The thickness of the different regions depends upon the reactivity of the mixture. The detonation wave is thus defined to be the distance between the leading shock and the sonic plane.

Much of the discussion of this work focuses on total pressure; thus, Figure 1.3b gives the total pressure across the detonation wave. In the wave frame of reference (red line), the detonation wave is a steady process; therefore, the total pressure decreases across the shock and from the heat addition between the induction zone and sonic plane. However, when the detonation wave is observed in the lab frame of reference (blue line) propagating into a quiescent mixture, the total pressure increases across the wave (i.e., above the dashed gray line). The total pressure increase is due to the detonation wave being an unsteady process in the lab frame, which induces a velocity behind the wave. The heat release between the induction zone and the sonic plane still decreases the total pressure, but overall, the detonation wave causes a local increase in total pressure. The term *pressure gain combustion* (PGC) is often used to describe detonation waves due to this increase in total pressure across the unsteady combustion front.

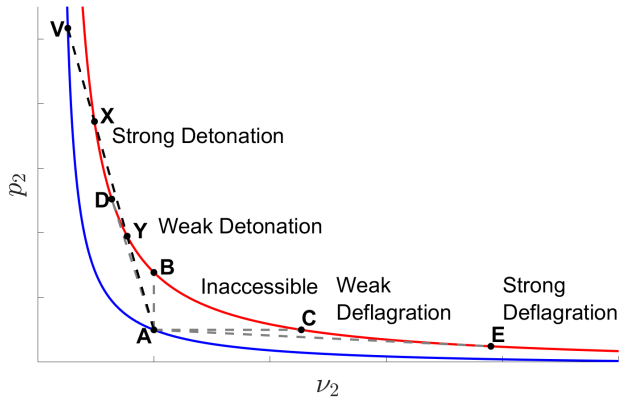

Figure 1.4: A p-ν diagram including the Von-Neumann spike present in the ZND model.

As mentioned previously, the ZND model also prohibits the existence of weak detonations. The ZND model in a p-ν diagram, Figure 1.4, is considered to demonstrate this. The initial state is point A, the upper CJ point is point D, and the bounds of the weak detonation region is point B to be consistent with Figure 1.2. The second, blue Hugoniot curve is the adiabatic curve ($q = 0$), which gives the jump conditions across a normal shock. The von-Nueman spike is located on this curve and is point V. A Rayleigh line connects A and V to ensure the solution is physical. This Rayleigh line intersects the Hugoniot curve twice, with the points labeled X and Y for the strong and weak detonation solutions. Recall that the fluid particles would first go to point V; thus, the initial trajectory is from A to V. Once at V, the pressure would decrease to X as heat release occurs, resulting in a strong detonation solution. For the weak detonation solution, point Y, to be achieved, additional energy is required to go from X to Y. However, all the energy was released going from V to X, making it impossible to reach Y. Therefore, it is impossible to have weak detonations if the detonation wave is a shock followed by chemical reactions. Alternatively, the velocity must be subsonic in the wave frame after the assumed shock front within the detonation wave. Then, the heat release within the reaction zone can only accelerate the flow to sonic speeds in this frame. Thus, the supersonic post-combustion speeds required for weak detonations are impossible, thereby eliminating the possibility of weak detonations in the ZND model. In the case presented in Figure 1.4, a strong detonation would occur, but since these are unstable, the wave would gradually slow until the CJ velocity. This analysis again reaffirms that in most instances, the CJ state uniquely defines detonations for a given mixture and is the most appropriate state to compare observed detonations to.

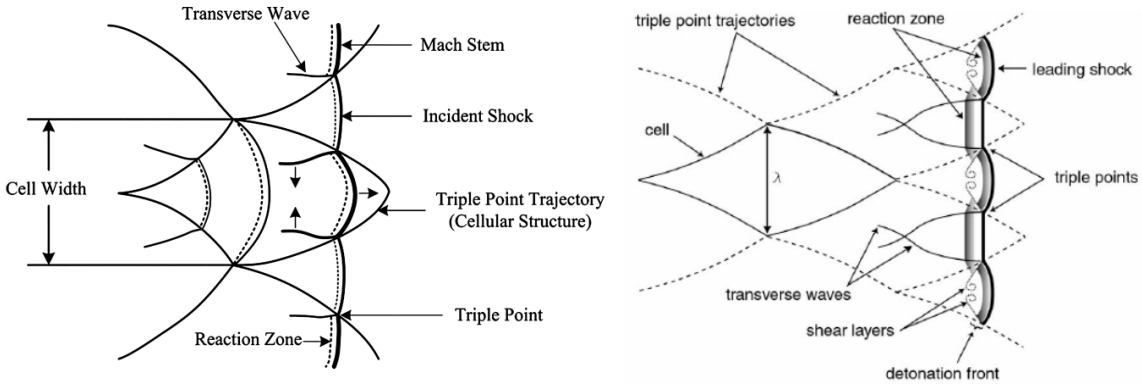

(a) (b)

Figure 1.5: Two-dimensional representation of detonation front consisting of triple point interactions of Mach stems and incident waves. Reproduced from a) Liu and Zhang [1] and b) Porowski and Teodorczyk [2].

1.2.3 Three-Dimensional Structure of Detonations

In reality, the structure of a detonation wave is much more three-dimensional and complex than what the ZND model describes. Experimental observations show that a detonation consists of many intersecting shocks interacting along the wave's surface instead of a planar wave, giving it a wrinkly or corrugated appearance [27]. This two-dimensional visualization is shown in Figure 1.5a, reproduced from Liu and Zhang [1]. The two-dimensional visualization is the projection of the three-dimensional phenomenon onto a single plane. The leading shock front consists of incident shocks and Mach stems that interact and give off transverse waves that trail the leading front. The intersection points of these shocks are the triple points, and the leading front typically consists of multiple such triple points. The transverse waves given off at the triple points propagate at the acoustic speed of the post-combustion state and eventually collide with one another downstream of the shock front. After a triple point interaction, a local high-pressure region with a thin reaction region generates a new Mach stem. The previous Mach stem decays in strength, thereby becoming the incident shock that interacts with the Mach stem. This interchange occurs in a cyclical pattern, causing the detonation surface to be dynamic and vary in time. The local speed of the front varies in time as a part of this dynamic structure, as evidenced by the curvature of the Mach stems, which suggests they are locally propagating faster than the incident shocks. Nevertheless, the time-average speed closely matches the CJ speed from one-dimensional analysis.

Due to this periodic behavior, the trajectory of the triple points in space forms a fish-like or cell-like structure. While this is indicated in Figure 1.5a, it is more clearly seen in Figure 1.5b, reproduced from Porowski and Teodorczyk [2], as the dashed lines. The detonation cells are commonly observed on soot foils in experiment [28], and the resulting structures are called

detonation cells. It is important to note that, in general, the chemical reactions are complete within one of these cells [27]. The size and distribution of the cells depend on the mixture, although the bounding geometry may impact the formation of these cells.

Current theory believes regular detonation cells are necessary for the continued propagation of a detonation wave. In particular, the detonation cell width (λ), the distance between the triple points orthogonal to the direction of wave propagation, has been shown to be a critical length scale in determining the limit of wave propagation. For instance, the ratio between the tube diameter of a detonation tube and the detonation cell size determines whether the detonation becomes planar and can continuously propagate. Knystautas et al. empirically found that the critical tube diameter was 13 times the cell size, and diameters smaller than this critical value cause the detonation to fail as the heat release and shock become decoupled [29]. Likewise, Bykovskii theorized that there exists some relationship between the cell size and geometric parameters of the RDC [30] that influences the operability and stability of a RDC. However, a conclusive demonstration of this is still absent from the literature. Some studies have looked at the detonation structure as it passes around a confined curve that is more representative of the geometries of a RDC since the wave becomes curved and diffraction of the transverse waves occurs along the walls [31, 32]. However, there is currently no established means of predicting continuous detonative operation of a RDC, nor is there a well-described mechanism that causes detonations to fail or not establish within a RDC. In contrast to detonation tubes, there is likely a balance between the local structure of the detonation wave and the macroscopic processes involved with mixing, injection, bulk flow, etc., that prevents the analysis of RDCs from being solely in terms of cell size. Regardless, it is highly probable that the three-dimensional structure of the detonation wave within a RDC is of great importance, although the current work does not investigate this.

1.3 Thermodynamic Benefit of Detonation

Instead of comparing detonation to deflagration in isolation, an integrated thermodynamic cycle approach better demonstrates the benefit of detonation waves. Recall that the ultimate goal of a detonation-based thermodynamic cycle is to supplant the Brayton (deflagration) cycle in current devices commonly used in many aerospace applications. When considering the thermodynamic benefit of detonations, three thermodynamic cycles are compared:

1. *Brayton* cycle: The ideal Brayton cycle consists of an isentropic compression, an isobaric combustion (heat addition), and finally, an isentropic expansion. The isobaric combustion is in the form of deflagration.

2. *Fickett-Jacobs (FJ)* cycle: Describes the thermodynamic cycle of a propagating detonation

wave. The ideal FJ also consists of isentropic compression, combustion, and isentropic expansion like the Brayton cycle; however, the combustion consists of a propagating detonation wave instead of the isobaric deflagration. In the model, two pistons bound the detonation wave, and the displacement of the pistons produces the extracted work. The FJ cycle is named after Jacobs, who originated the concept [33], and after Fickett, who, with Davis, expounded upon the concept [21]. The work of Wintenberger and Shepherd popularized the term, and they give a more detailed description [4].

3. *Humprhey* cycle: The ideal Humphrey cycle is typically also considered when discussing the FJ cycle due to it resulting in similar results to the FJ cycle [34]. The ideal Humphrey is, once again, comprised of isentropic compression, combustion, and isentropic expansion like the Brayton cycle; however, the combustion is isochoric (constant volume) instead of isobaric.

These three different cycles are plotted on the left in Figure 1.6, reproduced from Xie et al. [3], in the p-v space, where v is the specific volume.

The thermal efficiency of the cycle is the net work output for a given heat input.

$$\eta_{\text{th}} = \frac{w_{\text{net}}}{q_{\text{in}}} \tag{1.19}$$

In the case of Figure 1.6, all the cycles are shown with the same heat input. The net work output is the area encapsulated by the closed thermodynamic cycle,

$$w_{\text{net}} = \oint p \mathrm{d}v \tag{1.20}$$

Therefore, if the FJ cycle is more efficient than the Brayton cycle, it is from the additional extractable work due to the elevated pressure, $p_{3.5} > p_3$. Recall that this elevated pressure is a consequence of the supersonic flame front.

On the right side of Figure 1.6, the same cycles are plotted in T-s space instead (i.e., a Mollier diagram). Instead of seeing the elevated pressure, the elevated temperature and overall lower entropy of the FJ cycle are readily observable. Again, the different cycles had the same amount of heat input. Therefore, for the same supplied energy input, the lower final entropy directly results in more usable energy that can be extracted, thereby increasing efficiency. In this way, the T-s diagram more clearly shows the improved thermal efficiency of the FJ cycle over the p-v diagram. Thus, it is most appropriate to say that the actual "gain" or benefit of using detonation in a thermodynamic cycle is less entropy production.

One work performed by Kailasantah showed ideal cycle efficiencies of 27%, 47%, and 49% for the Brayton, Humphrey, and FJ cycles, respectively [35]. Kailasantah performed those idealized calculations by assuming an adiabatic compression from 1 atm to 3 atm before the heat release

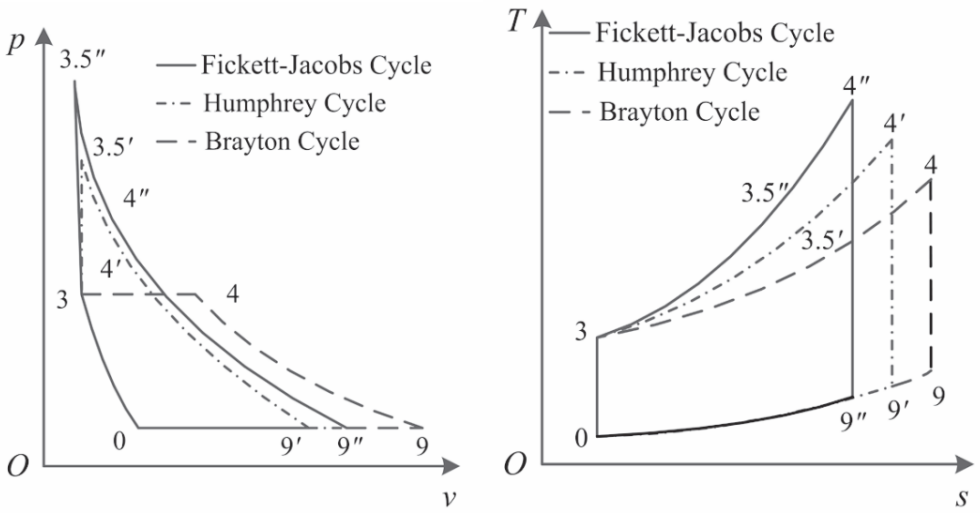

Figure 1.6: Sample left) p-v and right) T-s diagrams of the Brayton (isobaric), Humphrey (isochoric), and Fickett-Jacobs (detonation) cycles. Figure reproduced from [3].

and then having the same amount of heat addition for each of the three cycles. An isentropic expansion down to 1 atm was assumed to occur after the heat release. The similarity between the FJ and Humphrey cycles is evident, as is the increase in the efficiency of FJ over the Brayton cycle. The exact percentages of the cycle will depend on various factors such as the initial conditions, compression ratio, fuel-oxidizer chemistry, equivalence ratio of the mixture, and practical losses. For instance, Kindracki and Wolanski computed the thermal efficiency of the FJ cycle to be 59.3%, 53.2%, and 61.4% for hydrogen-air, methane-air, and acetylene-air combustion at a compression ratio (π_c) of 5 [18]. Meanwhile, the Brayton cycle at the same conditions had respective thermal efficiencies of 36.9%, 31.4%, and 36.9%.

Wintenberger and Shepherd performed similar efficiency calculations for stoichiometric propane-air mixtures at standard temperature and pressure but with varying compression ratios (π_c) [4]. The results from that study are reproduced in the figure on the left in Figure 1.7. For every compression ratio, the FJ cycle had a greater thermal efficiency, which is a direct result of the lower entropy generation throughout the thermodynamic cycle through the pre-compression that the detonation wave provides. However, the gap between the Brayton and FJ cycles narrows with an increasing compression ratio. When the thermal efficiency is instead plotted against the peak combustion pressures, as is the case of the left figure in Figure 1.7, the Brayton cycle is observed to be more efficient than the FJ cycle. This result is essentially a byproduct of needing less compression ratio (π_c) to achieve high pressure in the FJ cycle compared to the Brayton cycle. Thus, depending on the design constants, there may be instances where the Brayton cycle may still be favorable. Still, regardless, there are clear potential advantages to using the FJ cycle.

The FJ cycle analysis described above all originally pertained to Pulsed Detonation Engine

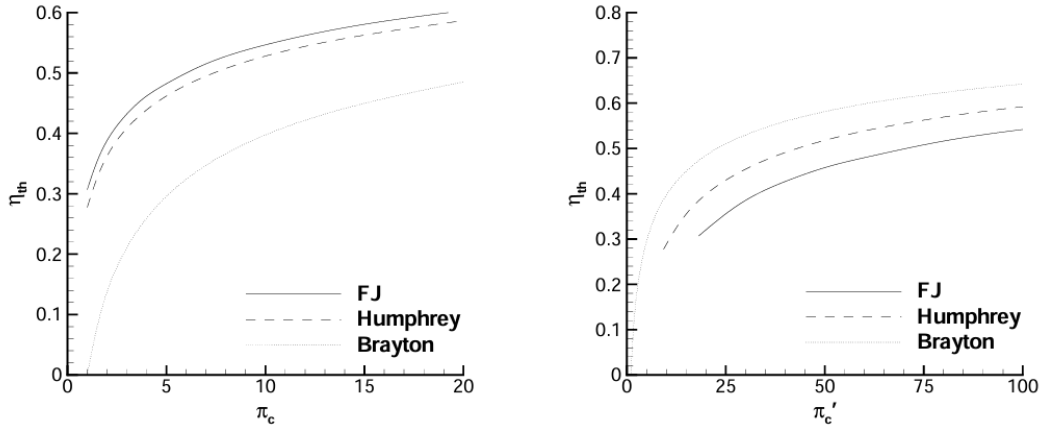

Figure 1.7: Ideal thermal efficiency of the different cycles for different left) compression ratios and right) combustion pressure. Figure reproduced from [4].

(PDE)s since PDEs more closely follow the traditional planar detonation wave propagating through a quiescent mixture. In the lab frame, the detonation wave propagation is unsteady, resulting in a local gain in kinetic energy immediately following the detonation wave (i.e., the CJ state). Due to this kinetic energy gain, the total enthalpy of the products at the CJ state exceeds the combination of the total enthalpy of the reactants and the chemical energy released. In the above cycle analysis, the work/thrust was computed from this local CJ state, thereby giving the favorable comparisons detailed above. However, such analysis is disingenuous as the CJ is a temporary local state trailed by expansion waves. In the case of a PDE, the expansion waves are to satisfy the wall boundary condition of zero velocity. For RDCs, the expansion waves arise from the boundary between the detonation wave and inert gases [36].

Zel'dovich theorized that since the total energy (chemical, kinetic, and thermal) cannot exceed the initial amount, the additional kinetic energy comes from work exerted on the fluid by the fluid to keep the detonation wave propagating [37, 38]. In other words, not all the energy in the CJ state can provide external work since sustaining the CJ state requires using some of the energy. Thus, the promised thermodynamic gains may be overly optimistic, although Zel'dovich noted that the detonation process is still more efficient than a constant volume explosion [37].

Dyer and Kaemming considered this by modifying the cycle analysis by limiting the total enthalpy increase to equal the heat added [5]. Figure 1.8 is a reproduction of their modified T-s diagram, where the T on the y-axis denotes total temperature in their notation. They assumed that the expansion process trailing the detonation wave is isentropic. Therefore, the known CJ entropy, s_4, combined with the possible total enthalpy given by the gray band, to calculate ④′, which is the state they claim the system can extract work from. Even accounting for nozzle losses, dashed purple line, less entropy is produced through the detonation cycle than the Brayton cycle (RJ in

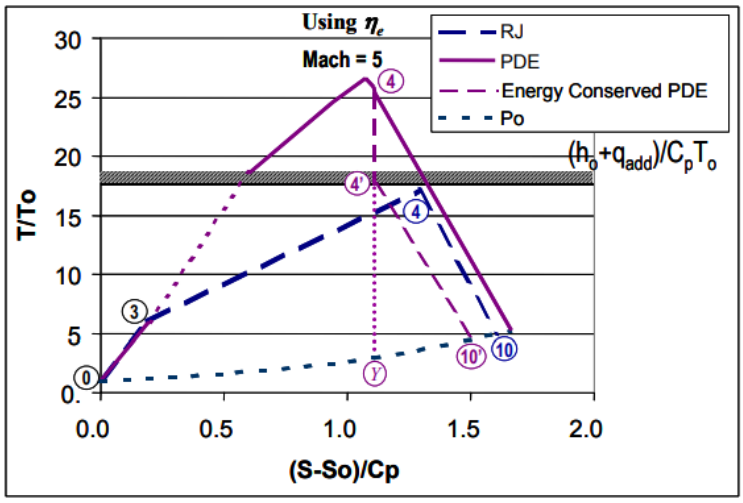

Figure 1.8: Energy conserved T-s diagram of detonation cycle analysis. Figure reproduced from [5].

Figure 1.8). Again, lower entropy for the same heat input would increase thermodynamic efficiency, although Dyer and Kaemming did not directly make that calculation [5].

Overall, while some of the initial modeling efforts may have overestimated the efficiency gains by extracting work from the CJ state, Dyer and Kaemming demonstrated that gains are still possible. Even if the potential gain is only several percent, this several percent will still mark a step-change in technological development as current devices have effectively reached the limit of the Brayton cycle efficiency due to sizing and material considerations. Finally, to reiterate, the cycle modeling here is for PDEs, and no equivalent work for RDEs is in the literature. The lack of similar analysis for RDEs is mainly due to the increased complexity of no longer having easily defined thermodynamic states. Nevertheless, it has been assumed in the literature the detonations in RDEs transfer the same thermodynamic gains as the FJ cycle discussed here.

1.4 Combustor Performance Metrics

From the prior discussion, detonation waves theoretically increase the thermal efficiency of a thermodynamic cycle; however, thermal efficiency only applies to the entire engine, i.e., RDEs. In the case of the RDC considered throughout this work, component level performance metrics are the most appropriate considering this work studies the combustor isolated from up- and down-stream components. In the context of a traditional combustor, two such metrics are prevalent: the combustion efficiency and total pressure ratio across the combustor. Combustion efficiency will be briefly addressed in this section, while the total pressure ratio is the focus of the remainder of the work.

1.4.1 Combustion Efficiency

The purpose of a combustor is to release energy, in the form of heat, from the chemical bonds of the reactants. Any unreacted mixture, therefore, serves as a loss on account of the reduction of thermal energy added to the flow. The combustion efficiency is the ratio of the actual change in total enthalpy over the ideal change in total enthalpy across the combustor. If the pre-combustor state is ③ and the post-combustor state is ④, the combustion efficiency, η_c, can be expressed as,

$$\eta_c = \frac{(\dot{m}_\mathrm{a} + \dot{m}_\mathrm{f}) h_{\mathrm{t}4} - \dot{m}_\mathrm{a} h_{\mathrm{t}3}}{\dot{m}_\mathrm{f} h_\mathrm{PR}} \tag{1.21}$$

Where h_PR is the thermal energy released per unit mass of added fuel. Although combustion efficiency is a crucial performance metric, it is also challenging to measure experimentally as it requires either measurements of the gas composition at the exit or measurements of the temperature and velocity to get the total enthalpy.

1.4.2 Total Pressure Ratio

The second parameter typically used to quantify the performance of a gas turbine combustor is the total pressure ratio across the device (π_b). Again, if the pre-combustor state is ③ and the post-combustor state is ④, this ratio is expressed as,

$$\pi_\mathrm{b} = \frac{p_{\mathrm{t}4}}{p_{\mathrm{t}3}} \tag{1.22}$$

The quantity called Pressure Gain (PG) will be referenced extensively throughout this work. The PG is defined to be the increase in total pressure across the device relative to the incoming total pressure. As such, the relationship between PG and the total pressure ratio (π_b) is as follows.

$$\mathrm{PG} = \pi_\mathrm{b} - 1 \tag{1.23}$$

This work focuses on either the reduction of the total pressure loss or, ideally, an increase in total pressure across the combustor. As such, a discussion of why total pressure is the quantity of interest is warranted. From an end-to-end perspective, a performance metric, such as thrust, specific thrust, thermodynamic efficiency, etc., may seem preferable to the total pressure ratio. However, as will be demonstrated later, the total pressure is used as a surrogate measurement of the irreversibility (entropy generation) of the processes that occur within the combustor.

By defining the CV around the combustor to be rigid and fixed in space relative to the combustor, no work is imparted on the fluid by the viscous shear acting along the walls since the displacement of the control surface is zero. Thus, the integral energy equation contains no frictional (irreversible)

terms, making the total enthalpy independent of how the flow stagnates (i.e., reversibly or irreversibly). Therefore, the change in total enthalpy (temperature) from adding heat is equal solely to the amount of heat added with no dependence on whether that heat was added irreversibly, as in the case of combustion.

The same is not valid for the total pressure. The familiar formulation of total pressure,

$$p_{\mathrm{t}} = p\left(1 + \frac{\gamma - 1}{2}M^2\right)^{\gamma/(\gamma-1)} \tag{1.24}$$

is explicitly defined when the flow is isentropically (e.g. reversibly and adiabatically) brought to rest. The resulting total pressure would be different than Eqn. 1.24 if the flow did not isentropically stagnate. The dependency on the process of stagnation originates from Gibb's equation. If the flow in ① is slowed to rest adiabatically, but irreversibly to ② such that ② is the stagnation state, Gibb's equation becomes,

$$s_2 - s_1 = c_p \ln\frac{T_{\mathrm{t}2}}{T_{\mathrm{t}1}} - R\ln\frac{p_{\mathrm{t}2}}{p_{\mathrm{t}1}} \geq 0 \tag{1.25}$$

$$\frac{p_{\mathrm{t}2}}{p_{\mathrm{t}1}} \leq 1 \tag{1.26}$$

Therefore, for the final pressure at ② to be equivalent to the pressure defined in Eqn. 1.24, the process must be isentropic. Thus, increasing entropy would directly decrease the total pressure for non-reacting flows, given a stagnation temperature. This link to the entropy is the main reason for focusing on total pressure. A side benefit of total pressure is that it fully defines the thermodynamic state in conjunction with a total temperature and static pressure measurement.

1.4.3 Total Pressure and Irreversible Processes

In traditional combustors, the total pressure always decreases across the combustor. For steady, quasi-one-dimensional flow with heat addition and viscous forces but no chemical reactions, the conservation of momentum and energy equations, along with Gibb's equation, results in the following formula for the change in total pressure,

$$\frac{dp_{\mathrm{t}}}{p_{\mathrm{t}}} = \frac{-\gamma M^2}{2}\left(\frac{dT_{\mathrm{t}}}{T_{\mathrm{t}}} + C_{\mathrm{f}}\frac{c}{A}dx\right) \tag{1.27}$$

where c is the circumference of the volume and C_{f} is the friction coefficient, which accounts for shear forces acting along the walls. Oates presents a detailed derivation of the above equation [39]. Note that in a *steady* combustor, the total pressure cannot increase across the combustor without violating the Second Law of Thermodynamics.

Therefore, the total pressure decreases due to the combustion at a finite Mach number and

viscous losses. The former is unavoidable, as adding energy to a steady system will always reduce the total pressure, e.g., Rayleigh flow. The latter is from friction along the wall and turbulence losses. In reality, the losses due to turbulence in gas turbine engines are typically an order of magnitude greater than those from the heat addition [40]. However, this may be due to the low Mach numbers within the combustor. In total, the irreversibilities within the engine decrease the exhaust kinetic energy for the same total enthalpy as more energy transfers into the internal structure of the molecules. In turn, the reduction of the kinetic energy reduces thrust production and the amount of extractable work. Using entropy to define the irreversibilities would be more advantageous since it is a thermodynamic state variable independent of the frame of reference, unlike stagnation/total properties; however, experimental entropy measurements are impossible. Thus, total pressure measurements are the best alternatives for RDCs at the time of writing.

1.5 Literature Review

With the background of detonations established and a brief exploration of the theoretical performance gain they promise, an overview of existing literature on Rotating Detonation Combustors (RDCs) is presented.

1.5.1 Rotating Detonation Combustor Overview

On the left in Figure 1.9 provides a visual aid of the general features of a RDC, with the figures reproduced from [6, 7]. As in Figure 1.9, the most common version of a RDC is an annular channel formed by two concentric cylinders. Fresh fuel and oxidizer are constantly and passively injected into the annular gap at the base of the annular channel from one or more plena, depending on whether the device is premixed [41, 42] or non-premixed, like most experimental RDCs [43]. Various fuel/oxidizer injection geometries have been tested, including discrete and continuous injection elements [44, 45, 46, 47, 48]. Passive injection here directly refers to the lack of valves for either reactant. Once the reactants are within the annular channel, turbulent mixing occurs before the continuously propagating detonation wave(s) consumes the mixture. The detonation wave(s) is the coalescence of the reactions initiated by a single ignition event, after which the detonation becomes self-sustaining. The ignition process is poorly understood, although Deflagration-to-Detonation (DTD) appears to occur within the channel. As alluded to previously, there are a significant number of studies into different injector geometries since they must provide adequate mixing at the short time scales between detonation waves (under a millisecond). Finally, the high pressure and temperature products or burnt gases post-detonation wave then expand through a nozzle to either produce work when integrated with a turbine or to produce thrust if exhausted to

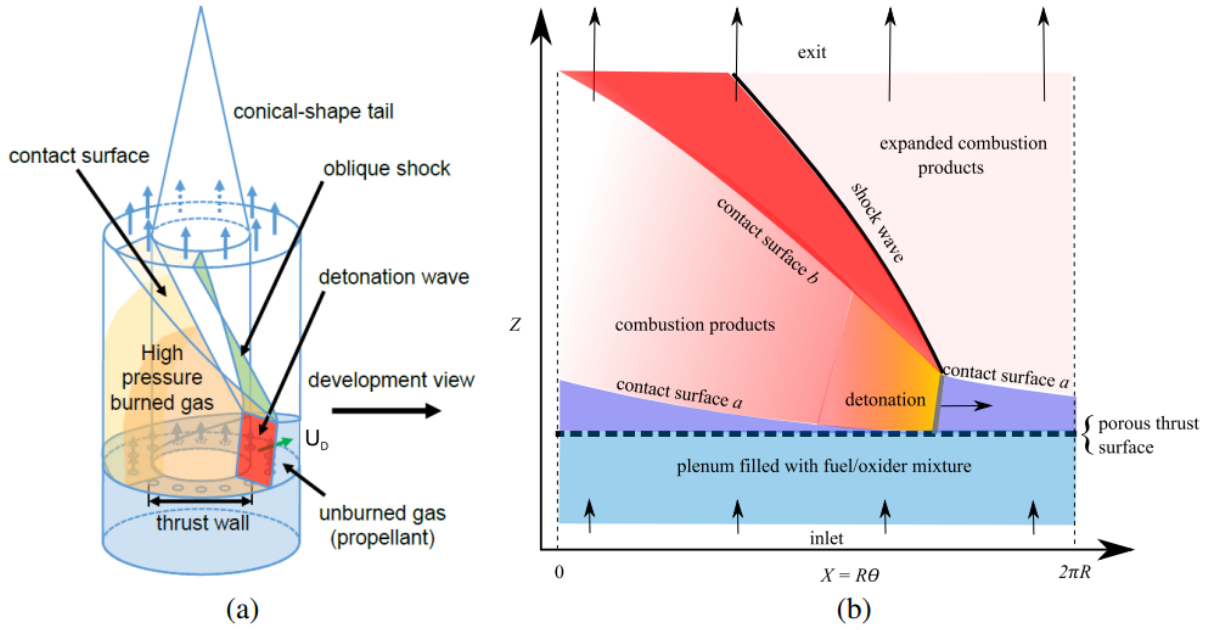

Figure 1.9: Schematic representation of a) annular RDC and b) unwrapped RDC flowfield with primary flow features. Figure reproduced from [6] and [7].

ambient. Overall, the bulk fluid motion through the RDC is in the axial direction, i.e., upwards in Figure 1.9. However, the circumferential propagation of the detonation wave(s) may induce some local swirl [49, 50, 51].

It is often easier to consider the flowfield in an "unwrapped" sense or along the θ plane at a fixed r. Figure 1.9 also contains a simplified representation of the unwrapped flowfield on the right. Once again, the bulk of the flow is axially upwards in this figure, starting from the upstream plenum (light blue). For simplicity, in this figure, the reactants are premixed in the plenum; non-premixed configurations would consist of two separate plenums and injection elements. The fresh reactants (dark blue shading) terminate at the detonation wave, which moves from left to right. Immediately after the detonation wave is a region of high-pressure products that prevents fresh fuel reactants from being injected [52], and flow reversal or backflow can occur depending on the severity of the pressure gradient. While not shown, an expansion wave trails the detonation wave [36] that lowers the pressure until the injectors can recover and inject fresh reactants into the channel again. A contact surface (a) separates the fresh reactants from the combustion products. The height of the detonation wave is dependent upon the fill region and the response time of the injectors. At the intersection of contact surface (a) and the top of the detonation, a downstream propagating oblique shock forms to handle the discrepancy between the higher pressure gases behind the detonation wave and the gases that bound the detonation [36]. A new contact surface (b) forms to differentiate between the products that have or have not interacted with the oblique shock. All the while, the

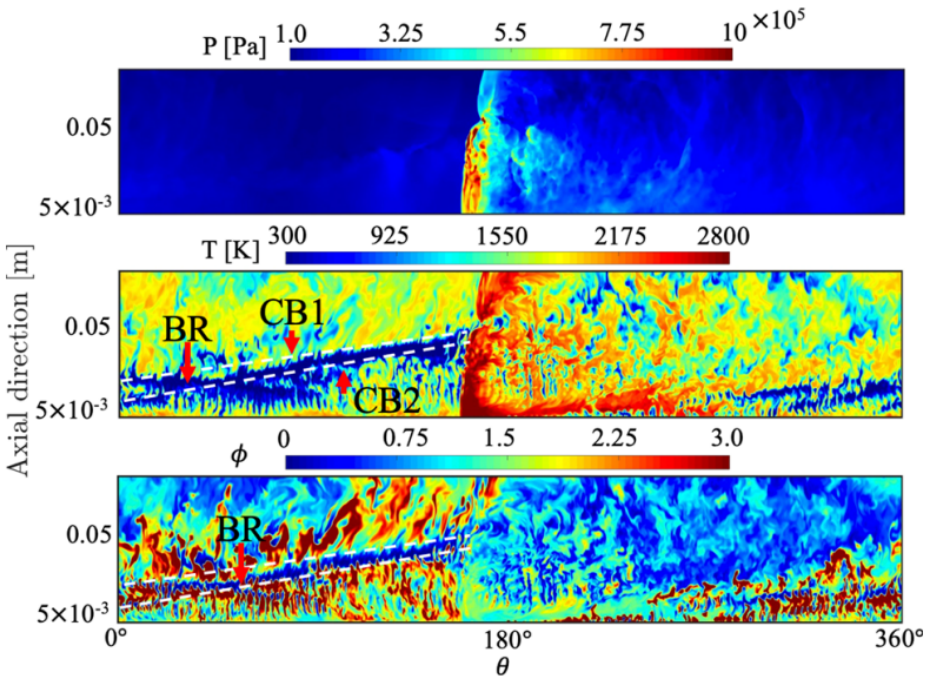

Figure 1.10: In descending order: pressure, temperature, and equivalence ratio of RDC flowfield from an unwrapped three-dimensional simulation. Figure reproduced from [8].

fluid is being expanded in the axial direction to be exhausted from the exit (top). While not shown in Figure 1.9, a similar oblique shock and contact surface can form at the bottom of the detonation, which propagates upstream into the plenum [53, 54, 55].

The flowfield for non-premixed RDCs is similar but typically has additional flow features. Namely, if either the fuel or oxidizer injectors recover faster than the other, there would be a buffer region of pure fuel or oxidizer. Such a bugger region would introduce two contact surfaces, one that separates the pure fuel or oxidizer from the products and another that separates the pure fuel or oxidizer from the mixture that starts after both injectors have recovered [45, 56]. Figure 1.10, which contains the unwrapped results from a high-fidelity, three-dimensional Direct Numerical Simulation (DNS) simulation from Sato et al. [8]., illustrates the existence of said buffer region. The pressure, temperature, and local equivalence ratio are shown in Figure 1.10, and the wave moves from left to right. There is an increase in complexity when the simplified flowfield of Figure 1.9 is compared to Figure 1.10, although Figure 1.10 is likely more indicative of physical experiments. The spatial variations intrinsic to the RDC flowfield complicate interpreting point measurements and defining an average state across the annulus at a given axial (vertical) location. The latter is particularly significant to this work, as discussed later in Chapter 2.

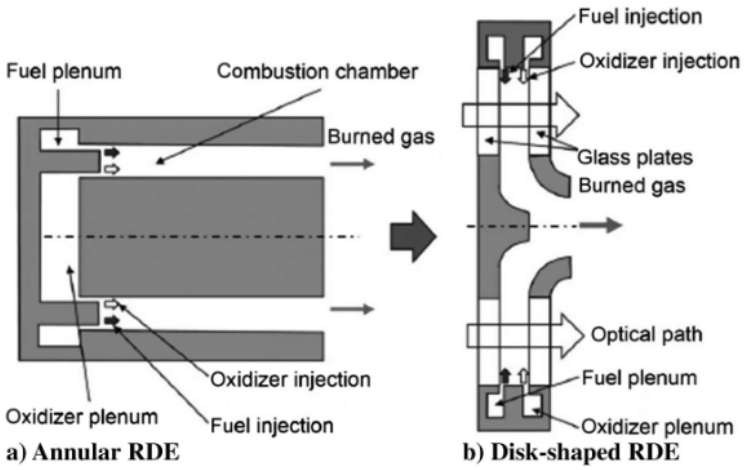

Figure 1.11: Schematic representation of differences between a) annular and b) disk RDC. Figure reproduced from [9].

1.5.1.1 Alternative Designs

Although this work exclusively utilizes the traditional cylindrical annulus design discussed above, several variations of RDCs that serve as alternatives to the traditional cylindrical annulus have also been explored. The commonality between all the designs is the continuous, circumferential propagation of detonation waves, and all seek to gain the thermodynamic benefit of using the detonation wave. Non-circular annular designs have been tested, with the most common shape being the "racetrack" design, which consists of two semi-circles connected by linear sections [57, 58, 59]. At this point, such devices are constructed solely for use within laboratories instead of with practical applications in mind. This design's primary feature is having optical access to the linear section, which is well suited for planar-laser diagnostics [60]. The hollow cylinder design is another variation of the RDC concept, and it is quite similar to the cylindrical annulus, except no inner body confines the detonation wave(s) [61, 62, 63]. This variation has garnered extra interest from the rocket community since the resulting shape resembles traditional rocket combustors. Nevertheless, both the air-breathing and rocket communities may be interested in further research as the hollow geometry removes the inner body's additional weight and the need for cooling said inner body.

The final variation considered thus far in the literature is the radial disk [9, 64]. Figure 1.11, reproduced from Huff et al. [9], highlights the differences from the radial/disk RDC. The overall flow is still constrained to a slot (like an annulus); however, whereas the other designs have the bulk motion in the axial direction, the reactants are injected radially inwards towards the center of the device. The detonation wave still rotates in the circumferential direction within the chamber (i.e., in and out of page in Figure 1.11), consuming the mixture. The hot products are then turned in the

axial direction and exhausted axially. Overall, the form factor of the disk RDCs reduces to leverage the high energy density for potential use in compact auxiliary power generation applications when integrated with a radial turbine. Overall, the methodologies presented and developed in this work are also applicable to such alternative designs, as the results from this work are irrespective of the particular design since the general concept of the RDC remains intact across the designs.

1.5.2 History of Detonation Engines

Now that a general description of RDCs has been established, a brief history of their development is presented. Detonation engines are frequently touted as using pressure gain combustion (PGC); thus, a brief history of the term PGC is given in parallel to the history of RDCs. As will be discussed, the original concept of RDCs did not discuss an increase in total pressure across the device (PGC); therefore, tracking the evolution of term PGC will provide insight as to when RDCs adopted the moniker.

1.5.2.1 Pressure Gain Combustion

As shown in the previous section, in a steady combustion system, the total pressure must decrease due to the laws of thermodynamics. However, if an unsteady combustion process is used and constrained (i.e., detonation or constant volume), it is theorized that an increase in total pressure is possible. This unsteady combustion process is now referred to as PGC since,

$$\pi_b > 1 \tag{1.28}$$

$$\mathrm{PG} > 0 \tag{1.29}$$

By this definition, reciprocating engines constitute PGC as combustion after the piston strokes are approximately at constant volume [65]; however, reciprocating engines are impractical for aerospace applications due to physical complexity (moving parts) and being ill-suited to produce thrust. However, the reciprocating engine is not the only conceived constant volume device. One of the earliest designs for a gas turbine, the explosion gas turbine, made around 1908 by Holzwarth, made use of constant volume combustion [66]; thus, the concept of trying to integrate PGC into gas turbines dates back over a century predating the concept of the modern gas turbine. Due to the materials and cooling processes at the time, the developers of the gas turbine dropped the concept in favor of the Brayton cycle, which allowed for more work given the limited combustor temperature/pressure (refer back to Figure 1.7).

A valveless version of the explosion gas turbine, a pulse combustor, was discussed by Porter in 1958 as having the potential for pressure gain [67]. Porter was one of the literature's first direct

mentions of pressure gain. The pulse combustor has seen on-and-off research since, though there are some active groups to this day [68, 69, 70, 71]. Perhaps most important to this current work was the work done by Kentfield on pulse combustors in the 1960-1980s [72, 73, 65], since the popularity of the term PGC can be seemingly directly traced back to Kentfield and his collaborators. At the time, little work looked into detonation engines (discussed in the following section); therefore, for nearly two decades, PGC almost exclusively referred to constant volume combustion. The exclusivity of PGC changed in 1988 as Kentfield, recognizing the work of Helman et al. on early versions of PDEs [74], began to classify unsteady, pulsed detonation waves as PGC well [65] based on the ZND structure in the lab frame (see Figure 1.3b).

1.5.2.2 Detonation Engines

The earliest recorded works in harnessing unsteady detonation wave propagation for propulsion were by Voitsekhovsky in 1960 at the Moscow Institute of Physics and Technology [75] and Nicholls in 1957 at the University of Michigan [76]. Nicholls noted the similarity between rotating detonation waves and circumferentially rotating combustion instabilities observed in rockets at the time and theorized that the pressure rises could be potentially harnessed [77]. The term PGC did not appear at the time. However, Nicholls theorized that rotating detonations may offer a potential increase in specific impulse for rocket combustors [76] or alter the scaling parameters of rocket combustor [77]. However, due to being unsuccessful at maintaining a continuously propagating rotating detonation wave (operation) and concerns over heat management, research into RDCs seemingly stopped in the US after the 1960s. After a brief lull, Bykovskii and his research group at Lavrentyev Institute of Hydrodynamics in the USSR recommenced the research into RDCs starting around 1980 [78] and has continued even to the time of writing. It was this group that demonstrated continuous and stable rotating (spinning) detonation waves of gas-gas [79] and liquid-gas mixtures [80]. Additionally, various geometries were considered, including the now pervasive annular geometry [81] and design parameters being introduced [30]. Overall, while Bykovskii may not have originated the RDE concept, his vast body of collective work forms the foundation of the RDE literature as a whole from which more modern studies build. Importantly, Bykovskii never mentioned an increase in total pressure (i.e., PGC) as the benefit of RDEs.

A resurgence in interest in detonation engines in the US occurred in the mid-1980s [74] through the 2000s with the rise in popularity of the PDE [82, 83, 84, 85]. A PDE consists of a long tube closed at one and open at the other. Fuel and oxidizer mix within the chamber after being injected from the closed end. The mechanical valves controlling the injectors close once the chamber is adequately filled and mixed. Afterward, ignition occurs, thereby producing a detonation. The wave propagates along the length of the tube before exhausting through the open end. The induced velocity produces thrust through the open end. A trailing expansion wave stagnates the flow within

the tube after some time to satisfy the wall boundary condition; thus, the system must purge the hot products before the following firing sequence. The PDE can be considered an extension of the pulse-jet concept with the caveat that pulse-jet combustion is deflagrative instead of detonative. The PDE was the first detonation-based engine that earned the label of PGC as the unsteady detonation wave and subsequent expansion are in the same direction as the bulk motion [65, 86]. Additionally, as discussed in the previous section, much of the thermodynamic modeling efforts demonstrated that the FJ cycle theorized in PDEs closely matched the Humphrey cycle [34, 4, 35, 5] further connecting PDEs to the constant-volume that originally constituted PGC.

Overall, the research into PDEs culminated with a flight demonstration of Long-EZ aircraft propelled by a PDE in 2008 [87]. But, while there was promise and significant progress in PDEs, there remained substantial technological challenges and limitations [88, 38]. Each pulsed detonation wave required a distinct ignition event and transition, necessitating the continuous provision of activation energy to the system. The re-filling cycle, ignition, and purging sequences, which require physical valves, are limited to approximately 50 Hz firing rates, making the thrust unsteady. Specific length requirements exist to successfully undergo the DTD transition, preventing the device from being compact. The continuous propagation of detonation wave(s) in RDEs mitigate many, if not all, of these problems [38]. As such, around 2010, much of the detonation engine research transitioned to RDEs [89, 90, 91] where the focus remains. Interestingly, in 2006, before the switch to RDEs, Bykovskii published an extensive review of his work on continuous rotating detonations, which included geometric scaling parameters and demonstrations of a variety of mixtures [30], in a Western journal which may have influenced the return to RDE concept which had otherwise been dormant in the US since the 1960s.

By the point that the research focus shifted away from PDEs to RDEs, the concept of unsteady detonation wave propagation and PGC had become intertwined [92, 93]. Thus, even though the unsteady wave propagation was no longer in the same direction as the bulk flow, RDEs were still regarded as PGC devices [91], mainly as a remnant of the previous PDE research.

1.5.3 Non-Ideal Detonation Waves and Flow Features

In the theoretical description of detonation waves presented earlier in this chapter, the CJ point uniquely determined the properties of the detonation wave. Furthermore, the homogenous mixture that the detonation wave propagates into uniquely determines the CJ point. Experiments have confirmed that the ZND theory is a reasonable model of experimental planar waves that travel through a perfect mixture of fuel and oxidizer. However, the detonation wave(s) observed in RDCs are radically different than those predicted by the one-dimensional theory. For instance, the most wave-speeds are typically around 60-80% the ideal CJ velocity (u_{CJ}) [43, 11]. Occasionally, even

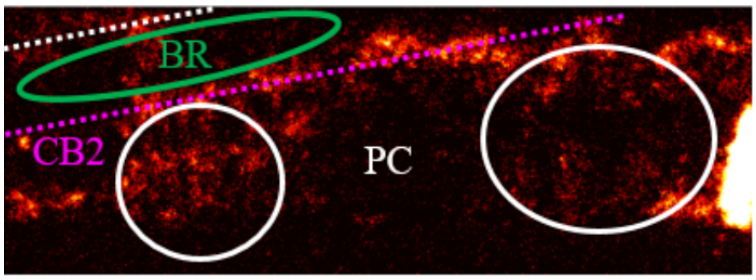

Figure 1.12: OH chemiluminescence highlighting contact burning (CB) and auto-ignition kernels (white circle). The detonation wave is a the right edge of the image and moves to the left. Figure reproduced from [10].

slower waves, around 50% u_{CJ}, arise. These slow speeds are approximately the same as the sound speed in the products. Furthermore, the static pressure ratios across the detonation waves are typically 10-30% of CJ values [43, 11]. While there are some concerns that piezoelectric pressure sensors cannot resolve the sharp pressure rise due to finite response times, the detonation wave(s) are still far from the ideal waves used in modeling.

There are a variety of factors that likely contribute to the decrement in wave properties. Unlike the one-dimensional analysis, detonations propagating through a curved annulus are inherently two-dimensional. In particular, the curvature of the bounding walls can impact the transverse waves that compose the detonation cells by either causing wave reflections or generating additional transverse waves, thereby affecting the stability and structure of the wave [38, 94, 95]. Practical RDCs injects the fuel and/or oxidizer through discrete elements [43, 96], leading to an inhomogeneous mixture before the wave arrival, unlike the assumptions in ideal CJ theory. The inhomogeneous mixture leads to reactant stratification [97, 95] along with incomplete mixing and mixture leakage [98, 99]. Additionally, if the fuel and oxidizer injectors' response times are mismatched, pure oxidizer and fuel buffer regions can form [45, 56]. Many of these factors likely culminate in the increase in wave thickness relative to the ZND model [100, 101], further differentiating the observed detonation wave(s) from those predicted by theory.

On top of thicker, slower, and weaker detonation waves, experiments have also observed deflagration within the RDC [10, 99, 11] and computations [101, 102]. Ultimately, RDCs seek to leverage detonation over deflagration. Thus, this secondary combustion (deflagration) is undesirable since it would produce more entropy than the detonation waves. This deflagration appears as auto-ignition kernels throughout the flowfield or as burning along the contact surface of fresh reactants [10]. Chacon and Gamba visually identified this deflagration in an optically accessible RDC based on the image reproduced in Figure 1.12 [10]. The white circles highlight the auto-ignition kernels labeled parasitic combustion (PC), while the pink line highlights contact burning (CB). Secondary combustion is classified as either parasitic or commensal combustion, depending on

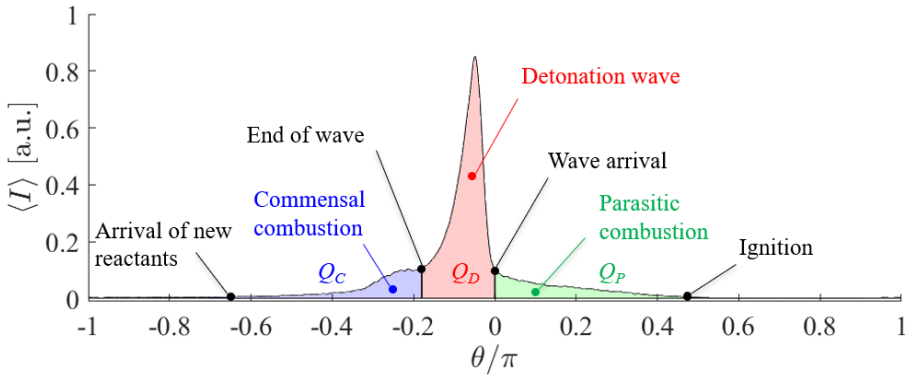

Figure 1.13: Representative phase-averaged cycle of OH* emission detailing the different combustion regions. Figure adapted from [11].

whether it occurs before (parasitic) or after (commensal) the detonation wave [10, 58]. The terms "parasitic" and "commensal" come from biology and describe the relationship each classification of deflagration has with the primary detonation wave [58]. Recirculation regions are theorized to be one of the mechanisms that support parasitic combustion [58]. The recirculation regions within the combustor can temporarily trap hot products, which can feed thermal energy to fresh reactants, causing auto-ignition. Meanwhile, incomplete mixing and mixture leakage are theorized to cause commensal combustion [58]. The unreacted pocket of the mixture passes through the detonation wave and then combusts later. Using point-wise, temporally resolved OH* chemiluminescence measurements, Feleo et al. were able to experimentally estimate the heat release breakdown across an averaged detonation cycle as visualized in Figure 1.13 [103]. The same study presented a correlation between increased amounts of secondary combustion and the velocity and pressure deficits of the detonation wave(s) [11]. In particular, the parasitic combustion is especially detrimental to the propagation of the detonation wave(s) [104, 105, 58].

Overall, the non-ideal detonation waves result from the combination of all of the discussed flow features [96], complicating the traditional understanding of the RDC flowfield. This discussion was not all-inclusive, as there are potentially more unexplored and uncharacterized phenomena since the complexities of the RDC flowfield are not fully understood. The extent of such research is beyond the scope of this work. Nevertheless, the discussion of the non-idealities is critical as they are detrimental to the global performance of RDCs according to the prevailing theories. Several efforts have incorporated secondary combustion, parasitic and commensal, in thermodynamic modeling of detonations and RDCs [104, 105, 58]. In particular, multiple studies have demonstrated that parasitic combustion has a significant impact on the pressure ratio across the detonation wave [104, 58] and on specific impulse [105]. Directly demonstrating the impact of the non-idealities requires suppressing the mechanisms that support them (e.g., suppressing secondary combustion);

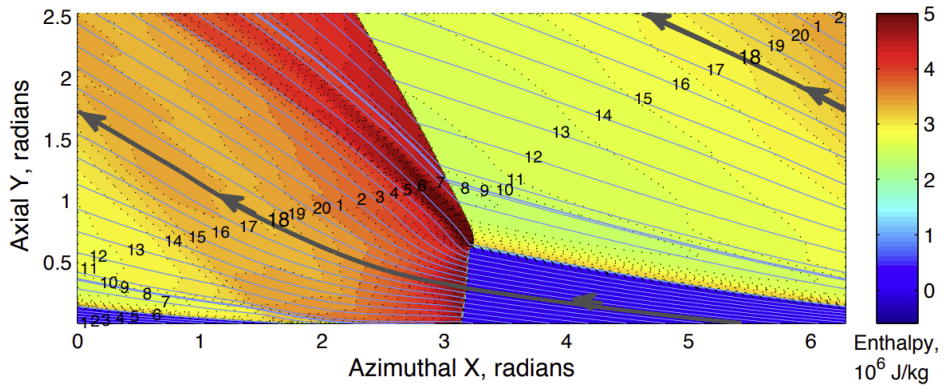

Figure 1.14: Pathlines through time-averaged RDC flowfield, where the color gives changes in stagnation enthalpy. Figure adapted from [12].

however, the entire flow field would become altered, including the detonation wave(s), since the resulting flowfield depends on all the individual processes [58]. Thus, it is impossible to isolate whatever changes to performance may arise after the suppression of the non-ideal phenomenon due to the other changes. Nevertheless, when considering the global performance of RDCs, these local processes likely need to be considered as loss mechanisms that could lower said global performance, especially since the detonation waves are not as ideal as those in PDEs.

1.5.4 Non-Uniform Exit Flow

The flowfield within a RDC is fundamentally three-dimensional. However, assuming that the properties' variations are minimal in the radial direction from the small channel width, the flowfield can be simplified to two dimensions [106, 107]. However, the variations in the circumferential direction at a given axial location can not be easily reduced to a singular value as would be typically done in the quasi-one-dimensional analysis techniques for deflagrative combustors [108]. There are two ways of considering the variations in the thermodynamic states. First, consider an instantaneous snap-shot of the RDC flowfield, like the simulation presented in Figure 1.10. At any moment in time, the velocity, temperature, pressure, etc., are all non-uniform across the exit plane, i.e., around the annulus. Therefore, defining a singular thermodynamic state that accurately captures all the information around the annulus is not possible [108].

Non-uniform exit flow can also be explored by considering pathlines or particle tracking through RDC simulations [109, 110, 90]. The work of Nordeen et al. is an example of this work [109, 110], who tracked the thermodynamic properties in a two-dimensional simulation produced by Schwer and Kailasanath [90] along discrete pathlines. The pathlines are shown in Figure 1.14, reproduced from [12], as light blue lines through the flowfield, where the color gives the stagnation enthalpy. Again, the non-uniformity at a given axial location (Y) is evident. Meanwhile, Figure 1.15, also

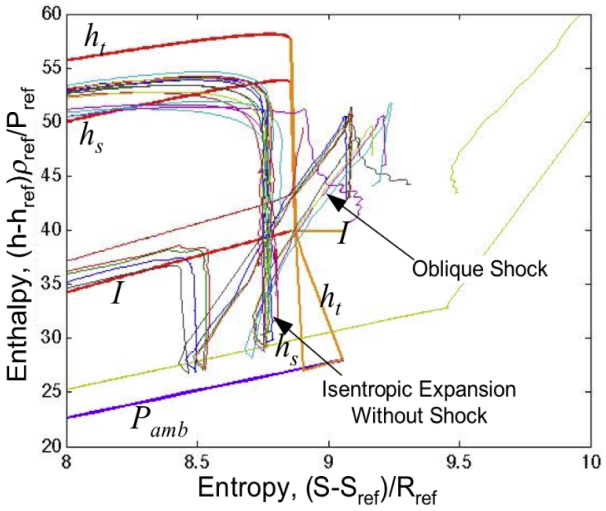

Figure 1.15: The variations of stagnation enthalpy and entropy along the different pathlines at the exit of the RDC. Figure adapted from [12].

reproduced from [12], shows the corresponding stagnation enthalpy (h_s)-entropy diagram that tracks the properties from those pathlines. The pathlines were applied to the flowfield after the flowfield as time-averaged. Based upon the spread in the lines (each giving the path of a fluid particle), the exiting fluid particles each have a unique thermodynamic state. The processes that a fluid particle experiences while traveling through a RDC depend on the injection site of the fluid particle into the RDC. In addition to the detonation wave and expansion after the wave, some particles interact with the downstream propagating oblique shock wave. The shock wave produces more entropy as the particles pass through it, further differentiating the final state of these particles from those that did not interact with the oblique shock wave. Such differences would be exacerbated by secondary combustion as the different particles may undergo varying combinations of deflagration and detonation, further complicating wanting to define a single representative thermodynamic cycle [111]. Finally, in addition to not matching one another, none of the individual pathlines matched the theorized thermodynamic cycle associated with the ZND structure, which is problematic from a modeling perspective [109, 111]. Overall, addressing the non-uniformity of the flow is crucial to generating a unique, combustor-specific performance metric, as will be explored in further detail in Chapter 2.

1.5.5 Performance Measurements

One of the critical challenges RDC literature is currently facing is quantitatively demonstrating the purported thermodynamic benefit. Ideally, the RDC performance metric can be readily compared to the baseline of a comparable deflagrative combustor to demonstrate an increase in that performance

metric. As mentioned previously, such comparisons are complicated because the exit flow is spatially non-uniform about the annulus and unsteady, contrasting the steady and uniform combustion of deflagrative devices. Kaemming and Paxson proposed that the best global performance metric for comparison is defining a *pressure gain*, which the community has broadly accepted. Pressure gain here refers to an increase in total pressure across the RDC, similar to the total pressure ratio used in traditional combustors. If this total pressure is greater than the incoming feed/supply pressure [112], then a thermodynamic gain is considered to have been achieved. Conceptually, this likely originated from the preconceived notion that RDCs are fundamentally PGC devices.

In the same introductory work, Kaemming and Paxson theorized that a quantity called Equivalent Available Pressure (EAP) can estimate the total pressure at the exit of a RDC. EAP is defined as the total pressure that a homogeneous flow would have to achieve the same thrust produced by the RDC if it isentropically expanded down to ambient pressure [113]. Thus, direct comparisons of the non-uniform RDC and the uniform deflagration-based combustor are better enabled. An experimental version of EAP was derived based on gross thrust measurements and some assumptions about the exit velocity. Said thrust measurements would inherently capture the details of the non-uniform flow along the exit plane. In theory, EAP encapsulates many of the losses that may occur through the system (e.g., viscous, non-isentropic heat addition, etc.) while being agnostic to how the losses in total pressure occurred. The number of experimental studies that have characterized the pressure gain through the EAP has dramatically increased over the past several years [114, 115, 116, 117, 118, 13, 119]. Additional work has looked at alternative methods of computing the total pressure, such as utilizing Kiel probes [13, 14] and using area-Mach relations with static pressure measurements [114, 120, 121]. Thus far, all reported pressure gains (relative to plenum pressure) have been negative and significantly less than the values generated from two-dimensional simulations [14, 113]. That said, specific geometries have shown single-digit percent pressure losses [118, 121, 48], suggesting an achievable positive pressure gain with further design iterations. In particular, a recent work by Brophy and Thoeny reported effectively no pressure loss, though information was limited in the work [48].

In the effort to measure the performance of the combustor independent of the nozzle when measuring the PG, a truncated, purely converging nozzle is typically recommended since it eliminates the impact of the nozzle efficiency on the expansion process [113]. However, the lack of a diverging portion can cause a pressure mismatch at the exit plane. The flow will experience a rapid expansion around the corner of the nozzle, which will, in turn, create an expanded recirculation region anchored around the nozzle [122], creating an effective drag force. Accounting for this drag force is necessary for computing the gross thrust from a load cell measurement of the total force produced by the device, making this a necessary correction to compute the EAP and PG. A study by Walters et al highlighted the importance since the contribution to the gross thrust from the base drag can

range from 10-40%. [119]. The common practice is installing flush-mounted pressure transducers on aft-facing surfaces at specific locations. The measurements are then numerically integrated to get the base drag. These pressure measurements are taken at various radial locations while several studies had multiple circumferential locations [114, 119, 123, 124]; however, none of those works addressed the effect of any possible circumferential variations on the integrated value of base drag. In most studies, the numerical integration is performed by assuming an axis-symmetric profile and summing over the area-weighted pressures [115]. Such numerical integration is a Newton-Cotes integration method. Fievioshn et al. proposed an alternative numerical integration method (Gauss-Kronrod) to minimize the number of necessary pressure measurements while maintaining low numerical error [116]. By assuming the radial pressure distribution is continuous, axisymmetric, and follows a monic polynomial, Fievioshn et al. measured the base drag with only five measurements, which is less than what employed by others [114]. More importantly, through the Kronrod extension, the integration error is estimated [116, 125], an often overlooked uncertainty source. However, Fievioshn et al. did not make the comparisons, at the time, to the more common Newton-Cotes integration.

Based on current measurements, the pressure gain of an experimental RDC will likely be on the order of several percent [118, 121, 126]. Thus, the margin of error for a definitive demonstration of pressure gain will have to be small. As estimated by EAP, the experimental pressure gain is a conservative metric due to assuming choked flow at the exit [113]. By being conservative, an experimentally observed positive pressure gain value is considered sufficient to demonstrate an actual gain. However, this reasoning needs to pay more attention to the significant experimental uncertainties in these measurements, which may add additional ambiguity. Reporting uncertainties in mass flow rates, gross thrust measurements, and specific impulse occurs in the RDE literature [115, 119, 127]. Typically, the propagation of the uncertainties follows the guidelines given by the ISO "Guide to Expression of Uncertainty in Measurement" [128]. Still, a demonstration of the propagation of uncertainties in the calibration through the EAP methodology does not exist in the literature. Fievisohn et al. provided an overview of possible sources of uncertainty in EAP to recap the lessons learned by utilizing the method [129]. Some of these sources are controlled through experimental design, such as different instrumentation and numerical integration techniques for accurate base drag measurements [116]. Other considerations were practical considerations, namely the unknown gas properties and possible subsonic Mach number [129]. While again, Fievisohn et al. presented some sensitivity analysis, they did not give a rigorous method of propagating all sources of error into the final pressure gain measurement. Overall, the minimal studies focused on the base drag on the nozzle have left a hole in the literature in assessing the experimental measurement of EAP and PG in terms of its overall precision/uncertainty.

1.5.6 Influence of Geometric Parameters on Performance

Several geometric parameters defining the RDC flow path have been varied in the literature to minimize pressure losses, including the inlet throat area, exit area, and detonation channel width. Many studies have observed that having more open (larger area) inlet throats results in better performance [13, 14, 114, 121, 116]. The prevailing hypothesis is that the total pressure drop across the inlet would decrease with the larger area due to lower flow speeds and less turbulent losses. Lower flow speeds are achievable by lowering the mass flux through the inlet; thus, larger areas reduce the mass flux for a given mass flow rate, theoretically improving performance. One demonstration of the link between the inlet losses and PG was given by Brophy and Theony [48]. In their work, they mitigated regions of possible separation during the area convergence in the inlet, thereby reducing the total pressure loss across the inlet and subsequently observing the PG grew less negative [48]. Overall, this is likely analogous to the loss in dynamic pressure discussed in gas turbine combustors, and more optimized inlets would ideally minimize the loss across the inlet.

Similar to the inlet area, many studies have extensively investigated the relationship between the exit area constriction and PG [13, 14, 114, 121, 116]. Reducing the exit area (i.e., making a more restrictive nozzle) back-pressurizes the detonation channel for a given flow rate, and this correlates with an increase PG by making it less negative. The back-pressurization reduces the static pressure ratio across the inlet, likely reducing the losses associated with the inlet. Additionally, the area convergence better guarantees sonic exit flow, which is required for calculating EAP [113]. In the introductory work, Kaemming and Paxson initially predicted that performance would scale by the ratios of areas between the inlet, channel, and exit; thus, the results were not unprecedented. However, Bach et al. recognized that the results from a wide variety of experimental PG seem to scale with the ratio between the area of the inlet throat and the outlet throat [14]. In other words, as the throat areas that bound the detonation channel approach the same value, the measured PG values approach zero, or no pressure losses occur. The best performing RDC geometries reported with single-digit losses have this area ratio being approximately one [118, 48].

Some recent work by Brophy et al. explored the channel width as an additional geometric parameter that may impact performance [121, 48]. By fixing the inlet and outlet areas and varying the channel width from 7.62 mm to 19.0 mm, they observed that the larger channel width resulted in significantly better performance in less negative values of PG [121]. Many of the previously discussed works [114, 115, 116, 117, 118, 13] had used the same channel width of 7.62 mm (0.3 in) that is commonly used throughout literature [130], marking the study of Brophy et al. a first of its kind to vary the width parametrically. Even after changing the inlet area, the increase in performance with increasing channel width persisted. The increase in channel width theoretically mitigates the heat transfer to the walls, and such heat transfer serves as a loss of energy incapable of producing work or thrust. The increased channel width may also have the benefit of lowering

the overall bulk axial velocity (and mass flux) in the chamber, decreasing the total pressure losses associated with viscosity/turbulence, which is of particular interest for determining the PG.

The combustor length is another alternative geometric parameter for fixed inlet and outlet areas. The combustor length has been previously observed in several studies to significantly change the operating mode of the RDC [131, 132, 133]. For instance, one recent study focused on studying secondary waves within RDCs found that increasing the length leads to a mode transition and stabilization of the detonation wave(s) [132]. Additional work has shown that changing the combustor length can avoid longitudinal pulsing modes [131, 133]. In the context of performance, longer detonation channels allow for more viscous and/or thermal losses to the wall and are typically considered detrimental [134]. Some early work done by Bykovskii et al. reported relationships for the minimum and "optimal" length of the detonation chamber with reference to the detonation height based upon extensive testing, although in those studies, the optimized metric in the "optimal" length is not well-defined [30]. Other computational work suggests changing axial lengths has no significant impact on performance (measured by thrust and specific impulse) [89, 135]. Experimentally, several groups have demonstrated that length changes did not significantly alter the thrust and specific impulse of RDCs with rocket injectors [136, 137, 138]. While thrust and specific impulse are useful performance metrics, they neglect the increase in plenum pressure needed to drive the bulk flow in RDCs [139]. For instance, even if the specific impulse is constant across the combustor lengths, a smaller plenum pressure for the same flow rate for a certain length would be equivalent to better performance. Pressure gain measurements, on the other hand, account for changes in plenum pressure, making it ideal for comparisons between lengths; however, thus far, the pressure gain studies in the literature (e.g., [13, 121]) have had the length fixed.

1.5.7 Detonation Channel and Plena Coupling

Reactants are injected passively and continuously into the detonation channel of the RDC. A consequence of the passive injection is a coupling between the detonation chamber and the plena [140]. The sharp rise in pressure associated with the continuously propagating detonation wave(s) exceeds the plenum pressures, causing a modulation in the reactant injection, potentially arresting or reversing the flow. A transient injector response follows as the chamber pressure steadily decays from the Taylor expansion wave behind the detonation wave(s). The impact of the detonation wave on reactant injection has been the subject of many studies in the literature, both experimentally [140, 141, 142, 143, 144, 145, 146] and computationally [134, 147, 148]. Additionally, an oblique shock attached to the individual detonation waves can propagate upstream through the inlet [53, 54, 55], causing high-frequency pressure variation within the plena. Thus, the resulting coupling is highly

geometry-specific and complex with spatially and temporally varying properties. Furthermore, the coupling also likely depends on the number and strength of the waves in the detonation chamber.

One manifestation of the detonation-induced coupling is an observable increase in the required global plenum pressure for a given reactant mass flow rate (for example, [53]). Driscoll et al. [141] likened the plenum pressure increase to a reduction of the *effective area* since similar pressurization would occur by geometrically reducing the injection area for the given flow rate to pass through. The *effective area ratio*, as they referred to it, was computed by taking the ratio of properties at the throat before and during detonative operation and was plotted against the corrected air mass flow rate. Other groups have proposed other similar experimental measurement methods and metrics [142, 144, 143, 146, 145, 50, 139]. Although various groups use different terminology, the core concept remains consistent. The detonation wave changes the effective flow area of the inlet, and this representation is a distillation of the complex and non-uniform inlet dynamics. In particular, the *mass-based blockage fraction* first introduced by Shepard [50] and then later expanded upon by Feleo and Gamba [139], was validated to adequately capture changes in the inlet area, unlike some of the other metrics [139]. This blockage fraction effectively measures the reduction in the mass flux through the inlet for a given plenum pressure during detonative operation [139]. Importantly, this blockage fraction quantifies the coupling between the plena and detonation channel and will be used extensively throughout this work.

Reverse/backflow at the inlet is an additional phenomenon related to the coupling that has yet to be well characterized experimentally. The local channel pressure after the detonation wavefront may be sufficiently large to create an adverse pressure gradient that reverses the flow direction, thereby creating backflow into the injectors [134]. Matsuoka et al. observed characteristics of reverse flow in their study focused on burned gas backflow with ethylene-oxygen mixtures [143]. In their study, high-speed imagery indicated the presence of burned gas propagating upstream of the RDC inlet. However, the functional dependencies or magnitude of the backflow relative to the bulk inlet flow still needed to be explored. Although not a specific focus of their work, the mixing study of Rankin et al. [44] using acetone planar laser-induced fluorescence (PLIF) imaging has shown a time-dependent mixing profile that is consistent with the presence of burnt gas backflow propagating upstream into the air plenum of a hydrogen-air RDC. Finally, Shepard used an optically accessible outer body around the inlet and high-speed broadband chemiluminescence to confirm the backflow in the RDC configurations evaluated in this work [50].

In a practical system, the plenum/inlet of an air-breathing RDC connects to an upstream component that may be susceptible to back-pressurization events, whether that be a compressor [149, 150] or an isolator [151, 152, 153]. Outside of the interaction with upstream components, a global increase in plenum pressure is also significant as it relates to PG since an increase in required plenum pressure results in a less favorable evaluation of RDC performance. Paxson and Miki [148] and

Kaemming et al. [154] demonstrated the negative relationship between backflow and performance through their computational works. However, as discussed previously, more open inlets and lower pressure drop injectors lead to less negative values of PG. Lower pressure drop injectors, while attractive for performance, can lead to greater backflow and/or fluidic blockage, thereby creating a required trade-off between minimizing backflow and pressure drop across the injector. Several attempts have been made to circumvent this trade-off by explicitly suppressing the backflow by using diodic injection schemes similar to Tesla valves [155, 55, 145, 156]. An ideal diodic injector is one where the flow in the forward direction experiences a minimal pressure drop. At the same time, there is an effectively infinite pressure drop in the reverse direction that prevents flow from traveling backward. Barnouin et al. attempted to demonstrate better performance with a higher diodicity injector experimentally, but the results were inconclusive [156]. Thus, this remains an active area of research.

1.6 Dissertation Objectives and Contributions

This work is a comprehensive overview and evaluation of the experimental global "pressure gain" metric prominent in the RDC literature. While the preexisting works have investigated this quantity both experimentally and computationally, the analysis of this work is unprecedented in scope in both the theoretical description of "pressure gain" and the experimental method to measure "pressure gain." In particular, this work focuses on the experimental EAP method in favor of the other techniques found in the literature. Overall, the evaluation of the PG centers on four critical aspects of the experimental metric:

1. The *theoretical background* and description of how the average total pressure is defined. If the theory supporting the definition of the average total pressure used in PG is flawed, the conclusions drawn from PG may be misleading.

2. The *accuracy* of the experimental EAP method. The accuracy addresses the systematic uncertainty within the method that can alter how close a given measurement is to positive gain.

3. The *precision* of the experimental EAP method. The precision addresses the random uncertainty present within the method that impacts the comparison of PG between tests.

4. The practical *usefulness* of PG in evaluating different RDC geometries since one of the end goals for the PG metric is to determine if changes made to RDCs result in better performance. Additionally, changes in the RDC would ideally reflect as changes in PG to enable more intelligent designs and to determine key loss mechanisms.

This work addresses each of these points in some capacity. For reference, Chapter 2 addresses the theoretical background, while Chapters 4 and 5 address the accuracy and precision of EAP. Chapters 6 and 7 utilize the developed experimental method to assess if changes in the RDC flowfield result in a measurable and significant change in PG. Such changes in the flowfield occur due to targeted geometric modifications to the RDC. Substantial portions Chapters 6 and 7 are dedicated to the characterization and quantification of the changes in the flowfield, and the results from those analyses contextualize the changes, or lack thereof, in PG. Thus, the focus remains solely on the PG.

Several novel technical contributions to the RDC literature occurred while using and evaluating the PG measurement method. The following are some of the critical contributions found interspersed throughout this work, and they are summarized below:

- Based on the definition of the experimental version of EAP, it is easily shown that it is effectively equivalent to an area-averaged of the exit flow. Since EAP is an area-averaged quantity, it cannot preserve the exhausting flow's momentum, energy, or entropy, which may make it ill-suited for integration into a quasi-one-dimensional model.

- The application of various averaging techniques adapted from the literature to sample RDC Computational Fluid Dynamics (CFD) simulation data reveals that the experimental EAP under-predicts all other average total pressures. Additionally, the "average" total pressure is not unique since it depends on the quantity of interest and exit state to which the flow is assumed to expand; therefore, a given RDC flowfield does not provide a unique PG.

- The three primary experimental methods of experimentally measuring pressure gain converge to the same result, which is analytically provable. The mathematical demonstration leverages the equality between the time-average and the area-average in periodic flowfields, which is also explicitly proven here. This result unifies the observations made by independent researchers and the different experimental methods.

- A thrust stand for the University of Michigan RDC test facility that can interface with the coupled exhaust was developed, characterized, and integrated. The thrust stand includes extensive instrumentation to correct for base drags along the exhaust flange and nozzle when measuring the gross thrust output of the RDC.

- The large number of pressure measurements taken along the nozzle identified a pressure asymmetry, the first-of-its-kind observation amongst the RDC literature. The base drag along the nozzle is determined to be a significant source of uncertainty due to the lack of edge pressure measurement and the choice made during the numerical integration. This work

also made a direct experimental comparison between a Gauss-Kronrod and the traditional Newton-Cotes, which was lacking in the literature.

- This work provides the most in-depth detailed uncertainty analysis of the EAP method to date. This analysis propagated the uncertainty from individual measurements into the final PG and considered the assumptions made within the EAP method. The total uncertainty in the PG was more significant than previously believed, indicating that PG may not have adequate precision.

- A novel method is introduced in this work to estimate the area-averaged Mach number at the exit using a static pressure measurement and the EAP method. Since all estimated Mach numbers were subsonic, none matched the assumed Mach number in the EAP method. As such, the introduced Mach-number corrected PG improves the accuracy of the EAP method and eliminates a significant source of systematic uncertainty.

- Two new RDC modes of operation were discovered. One of those modes consisted of two co-rotating detonation waves that were distinguishable with different pressure ratios but the same speed. The other mode is a transient super-cycle where the number, direction, and speed of the detonation and secondary waves vary in a well-defined, periodic manner.

- Statistical methods of measuring and comparing the measured pressure and detonation wave speeds are developed. Traditional RDC analysis techniques do not accurately convey the inherent cycle-to-cycle variability in the detonation properties. The empirical distributions of such properties obfuscate direct comparisons between distinct tests, which this work addresses.

- The combustor length was varied, and the resulting changes in the operating mode, stability, and detonation properties were identified using the statistical methods developed. Despite the changes to the detonation wave, the PG did not significantly change. Thus, the PG measurement is insensitive to changes in the multiplicity, speed, and stability of the detonation wave(s) induced by combustor length.

- Making the inlet diodicity worse allowed for the first experimental demonstration of increased coupling between the detonation channel and plenum with an injector with a worse diodicity for the same inlet throat area. Additionally, a significant decrease in PG occurred due to the modified inlet, illustrating that increased blockage/backflow correlates with worse PG.

The remainder of this work explores and elaborates upon these technical contributions in greater detail. This work concludes with some final recommendations and discussions about using the

global PG as the preferred performance metric and about whatever benefits RDCs have that are independent of PG.

CHAPTER 2

Defining a Singular Value of Pressure Gain

2.1 Introduction

Before discussing the experiments performed to measure the pressure gain of the RDCs, additional theoretical analysis is presented in this chapter to contextualize the experimental methods required to estimate the total pressure at the outlet of the RDC. As discussed previously, the flow exiting a RDC is highly non-uniform in the azimuthal direction due to the dependence on the relative position of the detonation wave(s). Despite this non-uniformity, it is desirable to report a singular value for the performance of the combustor. In the case of reporting a pressure gain or, more specifically, a total pressure at the outlet of a RDC, the two-dimensional, non-uniform flow is reduced into a singular value through some averaging procedure. Presented here is a detailed discussion of the choices of the averaging procedure. Alongside this discussion, the current experimental methods of measuring pressure gain are directly compared to the theoretical averaging performed on CFD data. Finally, the convergence of the different experimental methods in measuring the same pressure gain is explored and explained on a theoretical basis.

The averaging process needed for defining a total pressure ratio is non-trivial, and the "proper" method is not immediately evident. Depending on the severity of the non-uniformities, different averaging procedures (i.e., area-averaged, mass-averaged, etc.) give significantly different results. The problem of averaging in unsteady deflagrative combustors has been examined previously by Cumpsty and Horlock [108], who gave a comprehensive overview of the various averaging types. Likewise, Paxson and Kaemming demonstrated the application of mass-averaging, averaging while conserving entropy, and averaging while preserving thrust output to the unsteady flow of a PDE [157]. One of the critical aspects of the choice in averaging is the effective increase in entropy [157, 158]; the entropy calculated using some averaged state is larger than the mass-averaged entropy. Later in this work, there will be a practical demonstration of this increase in entropy.

This work adapts the averaging procedures presented by Cumpsty and Horlock [108] to RDC applications. The procedures for averaging are determined either over a geometric area or to

maintain a quantity of interest, such as thrust production, work output, or entropy. Each procedure has an independent formulation. This work also shows the contrast between these averaging procedures and the EAP presented by Kaemming and Paxson [113]. The thrust-averaging procedure is an extension of the ideal EAP formulation to accommodate variations in gas composition. At the same time, the detailed analysis reveals that the experimental EAP is effectively equivalent to the area-averaging procedure. Applying the averaging procedures to sample high-fidelity, three-dimensional CFD simulation demonstrated that the experimental EAP significantly underrepresents the "average" total pressure calculated from the other averaging techniques, suggesting it may be an overly conservative metric.

Additionally, the averaging procedures that preserve thrust production and work output result in measurably different total pressures based on the CFD data. The different total pressures contradict the concept of EAP, which is said to preserve both quantities simultaneously. Undergoing a physical process, whether passing through a nozzle or turbine, would increase the entropy of the flow, which may be a concern for practical applications. This work contains a novel sensitivity analysis of the averaging procedures on the outlet conditions, which revealed that the perceived performance could worsen despite no changes to the flow at the outlet of the RDC. Overall, this work illustrates that the outlet total pressure is a non-unique figure of merit as it depends upon both the desired application (propulsion or power generation) and the exit conditions to which the flow is expanding.

2.2 Why Averaging is Desirable

For several reasons, defining a corresponding average state for the unsteady and non-uniform flow is desirable. First, reduced thermodynamic models are based on describing the processes along the RDC through a discrete set of representative states and often adopt a quasi-one-dimensional representation of the flow. Determining the representative states along the axial direction necessitates defining equivalent average properties. Secondly, some of the metrics of performance, such as the pressure gain of Kaemming and Paxson [113] that the community has focused on in the last several years, rely on quantities (i.e., total pressure) that are essentially equivalent to average values. For instance, to determine a singular value of pressure gain to describe the performance of a RDC, a singular value of the outlet pressure is needed that is equivalent to the non-uniform flow. It is essential to note the term "equivalent" in these average states may not be well-defined. Finally, total temperature, total pressure, and static pressure are regularly measured in-flight using pitot-static and total temperature probes to provide information about the aircraft subsystems. If RDCs are then to be used for flight, converting the limited amount of measurements with limited spatial information into useful information regarding the performance of the RDC is imperative. Likewise, current experiments seek to build a comprehensive knowledge of the flowfield based on

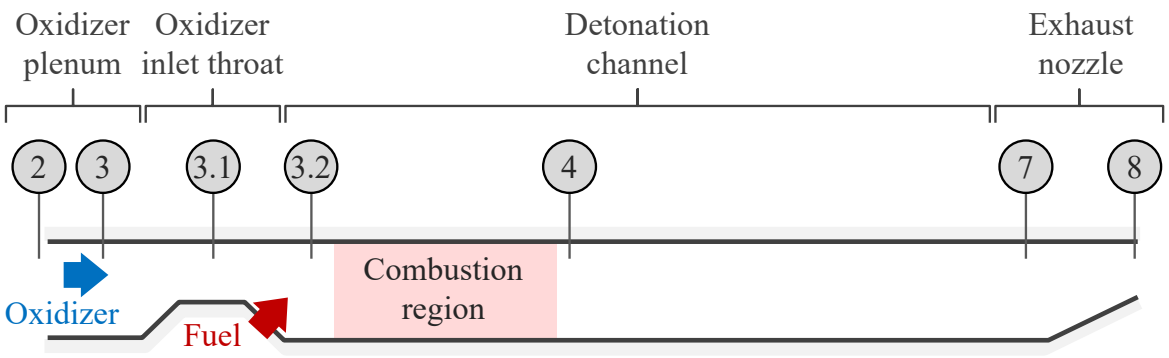

Figure 2.1: Definition of state naming along flowpath for RDC.

such limited information. Overall, one of the purposes of this work is to clarify the different means of defining an average state and how said average states can be "equivalent" to some aspect of the non-uniform flow.

2.3 Averaging the Non-Uniform Flow

2.3.1 Thermodynamic States and Naming Convention

Throughout this work, thermodynamic state notation is based upon the naming convention from the air-breathing propulsion community, although the notation easily translates to rocket applications. The definition of states along a conceptual flow path is given in Figure 2.1. For deflagration-based devices, the individual states effectively correspond to a physical location within the device (e.g., combustor exit, nozzle throat, etc.) because the flowfield and states are essentially uniform and stationary across cross-sectional areas. For detonation-based systems, the propagating detonation introduces spatial and temporal non-uniformity that breaks the relation between spatial location and corresponding states. Thus, in our context, the definition of states should be considered as a steady equivalent representing the state at a particular location or component of the device (e.g., inlet, nozzle, etc.). The definition of this steady-equivalent state is a challenge in itself, however. Table 2.1 summarizes the different location descriptions for ramjet/scramjet and turbojet/turbofan applications. A variable's subscript number denotes its defined location. For example, consider an arbitrary thermodynamic/fluid quantity (Q), then Q_8 indicates that quantity evaluated at the nozzle throat plane (⑧).

These physical locations will have corresponding thermodynamic states for the uniform and steady flows of deflagrative combustors. For a RDC, the flow is inherently three-dimensional, non-uniform, and unsteady from the wave propagation. Again, consider an arbitrary thermody-

State/Location	Ramjet/Scramjet	Turbojet/Turbofan
⓪	Ambient	Ambient/Diffuser Inlet
①	End of External Compression	Compressor Inlet
②	End of Inernal Compression	Compressor Outlet
③	Combustor Plenum/Isolator	Combustor Plenum
③.1	Oxidizer Inlet Throat	Oxidizer Inlet Minimum Area
③.2	Combustor Channel	Combustor Channel
④	Combustor Outlet	Combustor Outlet
⑤	–	Turbine Outlet
⑥	–	Afterburner Inlet
⑦	Start of Nozzle	Afterburner Outlet/Start of Nozzle
⑧	Nozzle Throat	Nozzle Throat
⑨	Nozzle Outlet	Nozzle Outlet
⑩	Expanded air	–

Table 2.1: Description of location notation in air-breathing engines.

namic/fluid quantity (Q) within the RDC, which can be expressed in the following form using cylindrical coordinates,

$$Q = f(\mathbf{x}, t) \tag{2.1}$$

$$= f(r, \theta, z, t) \tag{2.2}$$

Since the bulk of the fluid motion is in the axial (z) direction, tracking the properties at discrete axial locations is still desirable. The desired axial planes correspond to the engine locations in Table 2.1. Thus, the above naming convention will still denote locations within the RDC. This work focuses on the r and θ variations of Q at a fixed z and t. Henceforth, the notation will be simplified to be $Q(\mathbf{x})$ in the following manner,

$$Q_i(\mathbf{x}) = f(r, \theta | z_i, t) \tag{2.3}$$

For example, whenever $p_8(\mathbf{x})$ is referred to in the context of RDCs, the notation implicitly refers to the radial and circumferential variation of pressure at the nozzle throat axially location (z_8) at some arbitrary time, t.

2.3.2 General Considerations on the Averaging Process

The ultimate goal of the averaging is to relate the non-uniform and unsteady flow from RDCs to an "equivalent" uniform flow with reduced dimensionality that preserves some quantity of the

non-uniform flow. In this case, the three-dimensional flow field reduces to a quasi-one-dimensional representation along the center-line axis. Specifically, two-dimensional integrals performed across cross-sectional areas of the annulus reduce the information in each axial plane into a single number. The integrand of the integrals varies according to the specific averaging procedure. The quasi-one-dimensional flow created by the averages preserves some particular information about the flow; however, the averaging cannot conserve all quantities simultaneously. For instance, either the entropy of the quasi-one-dimensional flow artificially increases [157, 158] or one of the conservation equations cannot be enforced along the quasi-one-dimensional flow [159]. The various averaging procedures exist based on what quantities are conserved, with different quantities having greater relative importance in different applications.

This work considers four types of averaging:

1. **Area-averaged** – When a limited amount of information is known, as in the case of physical experiments, geometric averaging across the plane requires the fewest assumptions. The geometric mean, also known as the *area-averaged*, can be applied to the total pressure distribution at the outlet.

2. **Thrust-averaged** – If the flow leaving the RDC passes through a nozzle to produce propulsion, the quantity of interest is the ideal gross thrust (F_{Gi}) production. The *thrust-averaged* total pressure is subsequently defined to be the total pressure that provides the same gross thrust as the non-uniform flow given the same mass-averaged total enthalpy ($\langle h_{\mathrm{t}} \rangle_{\mathrm{M}}$) and mass-averaged gas composition ($\langle \boldsymbol{\chi} \rangle_{\mathrm{M}}$).

3. **Work-averaged** – If the flow leaving the RDC passes through a turbine for power generation, the quantity of interest is the ideal work extracted ($\dot{W}_{\mathrm{i}}$). The *work-averaged* total pressure is subsequently defined to be the total pressure that provides the same work output as the non-uniform flow given the same mass-averaged total enthalpy ($\langle h_{\mathrm{t}} \rangle_{\mathrm{M}}$) and mass-averaged gas composition ($\langle \boldsymbol{\chi} \rangle_{\mathrm{M}}$).

4. **Entropy-averaged** – The primary benefit of using detonation waves is reduced entropy production during combustion. If entropy is the quantity of interest, an *entropy-averaged* total pressure can be defined that satisfies the Gibbs relation for the given mass-averaged enthalpy ($\langle h_{\mathrm{t}} \rangle_{\mathrm{M}}$), gas composition, ($\langle \boldsymbol{\chi} \rangle_{\mathrm{M}}$) and entropy ($\langle s \rangle_{\mathrm{M}}$).

These are also summarized in Table 2.2. The different averaging procedures presented here will all denote averaging of quantity Q by $\langle Q \rangle$, with the different subscripts on the averaging brackets indicating the averaging employed. Each averaging procedure corresponds to a reduction in dimensionality that preserves some specific quantity about the flow, except for the area-averaging procedure. The following sections further develop each type of averaging.

In addition to the aforementioned averaging procedures, the method of computing EAP as proposed by Kaemming and Paxson is considered since it is widely accepted in RDC literature [113]. The formulation of the *experimental equivalent available pressure* and *ideal experimental available pressure* are compared and contrasted to the other averaging procedures. Specifically, the experimental EAP is found to be effectively equivalent to area-averaging. Meanwhile, the ideal EAP is virtually identical to thrust-averaging, albeit with some subtle differences.

Mass-averaged of select extensive properties (properties defined per unit mass) are repeatedly used when defining an "equivalent" uniform flow that conserves some quantity of interest of the non-uniform flow. Both Table 2.2 and the brief descriptions above have already referred to mass-averaging. Mass-averaging can also be referred to as preserving the flux of the quantity [108, 159]. For a generic, extensive quantity Q, the mass averaging procedure is given by,

$$\langle Q \rangle_{\mathrm{M}} = \frac{1}{\iint_A \rho u \mathrm{d}A} \iint_A \rho u Q \mathrm{d}A \tag{2.4}$$

$$= \frac{1}{\dot{m}} \iint_A Q \mathrm{d}\dot{m} \tag{2.5}$$

where,

$$\mathrm{d}\dot{m} = \rho u \mathrm{d}A \tag{2.6}$$

The definition of $\mathrm{d}\dot{m}$ will commonly be used to simplify expressions later in this work.

The important extensive properties for our consideration are the total enthalpy (which is substituted with $c_p T_{\mathrm{t}}$ by assuming a calorically perfect gas) and specific heat at constant pressure and volume, c_p and c_v, respectively. The different specific heats then define a mass-averaged ratio of specific heats (γ), thereby preserving information about the gas composition. Similarly, the specific entropy is mass-averaged for use in the entropy-averaging procedure. While it may seem helpful to perform mass-averaging on the total pressure, such a procedure does not have a physical justification as it is an intensive property [108].

Since spatial locations are the primary concern, the averaging procedures presented here do not average over time but are applied to single instances of time. Thus, the average quantities can vary over time. Finally, while additional averaging procedures exist [108], the ones chosen in this work have either direct applications to practical RDCs (area, thrust, and work-averages) or serve as the idealistic value that is useful for comparison (entropy-average).

Averaging Procedure	Notation	Conserved Quantities				
		$\langle h_t \rangle_M$	$\langle \chi \rangle_M$	F_{Gi}	$\dot{W}_i$	$\langle s \rangle_M$
Area-averaged	$\langle p_t \rangle_A$	×	×	×	×	×
Experimental Equivalent Available Pressure	EAP_e	×	×	×	×	×
Thrust-averaged	$\langle p_t \rangle_F$	✓	✓	✓	×	×
Ideal Equivalent Available Pressure	EAP_i	✓	✓	✓	×	×
Work-averaged	$\langle p_t \rangle_W$	✓	✓	×	✓	X
Entropy-averaged	$\langle p_t \rangle_S$	✓	✓	×	×	✓

✓ indicates quantity is conserved.

× indicates quantity is not conserved.

Table 2.2: Total pressure averaging procedures considered for their applications to RDC and the conserved quantities associated with each procedure.

2.4 Types of Averaging Procedures

2.4.1 Area-Averaging

2.4.1.1 Basis of Area-Averaging

Assuming that the exit of the RDC is a plane, *area-averaging* defines the mean across that plane. Specifically, the definition of an area-averaged value of total pressure ($\langle p_t \rangle_A$) is:

$$\langle p_t \rangle_A = \frac{1}{A} \iint_A p_t(\mathbf{x}) \mathrm{d}A \tag{2.7}$$

In the application to RDCs with a cylindrical geometry $\mathrm{d}A = r\mathrm{d}r\mathrm{d}\theta$.

No theoretical basis exists for area-averaging non-uniform thermodynamic quantities (i.e., total pressure, total temperature, etc.) in that no physical meaning can be associated with these area-averaged quantities [108]. However, due to the limited number of experimental measurements, area-averaged quantities are often used in experiments since they require the fewest assumptions. The other averaging techniques require knowledge about the velocities and the local thermodynamic state, found only in CFD solutions.

2.4.1.2 Experimental EAP

As mentioned previously, the method of measuring the *experimental equivalent available pressure* (EAP_e) is the most widely accepted method of determining the total pressure at the outlet of an experimental RDC. Thus, EAP_e will be used as the base comparison for the other averaging methods presented in this work. To compare and contrast EAP_e with other averaging methods, the

derivation, initially proposed by Kaemming and Paxson [113], is reproduced here.

The starting point for the $\mathrm{EAP_e}$ derivation is the basic gross thrust equation:

$$F_\mathrm{G} = \dot{m} u_{\mathrm{z},8} + A_8(p_8 - p_0) \tag{2.8}$$

$$= A_8 \rho_8 u_{\mathrm{z},8}^2 + A_8(p_8 - p_0) \tag{2.9}$$

Using the ideal gas law and the speed of sound by assuming a CPG, this equation becomes:

$$F_\mathrm{G} = \widetilde{p}_8 A_8 (1 + \gamma_8 M_{8,\mathrm{z}}^2) - p_0 A_8 \tag{2.10}$$

It is this form of the thrust equation that is used in the $\mathrm{EAP_e}$ methodology since the $\widetilde{p}_8$ is solvable by measuring thrust and assuming a Mach number [113]. Note that this Mach number only accounts for the axial velocity ($u_{\mathrm{z},8} = \mathbf{u}_8 \cdot \hat{\mathbf{e}}_\mathbf{z}$) and neglects any non-axial velocity ($M_{8,\mathrm{z}} = u_{\mathrm{z},8}/a_8$). When solving for p_8 in this manner, it is typically denoted with a tilde (i.e., $\widetilde{p}_8$) to indicate the $\mathrm{EAP_e}$ methodology. The isentropic relationship then gives the associated total pressure,

$$\mathrm{EAP_e} = \widetilde{p}_{\mathrm{tz},8} = \widetilde{p}_8 \left(1 + \frac{\gamma_8 - 1}{2} M_{8,\mathrm{z}}^2\right)^{\frac{\gamma_8}{\gamma_8 - 1}} \tag{2.11}$$

The flow is assumed to be isentropic from the end of the combustor (④) to the nozzle throat (⑧), such that the total pressure does not change ($p_{\mathrm{tz},8} = p_{\mathrm{tz},4}$). Here, the focus is on ⑧ since nozzles that terminate at the throat are commonly used experimentally [114] to accelerate the flow and provide back-pressurization while also not introducing a dependence on the nozzle performance for the expansion. In reality, there is no way to distinguish ④ and ⑧ as reactants can theoretically leak through the detonation and deflagrate while expanding towards the nozzle. Nevertheless, the definition of $\mathrm{EAP_e}$ presented by Kaemming and Paxson [113] has been recovered.

2.4.1.3 Experimental EAP as an Area-Averaged Quantity

While it is not immediately evident from the definition of the experimental EAP ($\mathrm{EAP_e}$), $\mathrm{EAP_e}$ is effectively an area-averaged total pressure (i.e., averaged across the annulus for a given instance in time). According to Eqn. 2.10, the thermodynamic variables and gas velocity are implicitly assumed to be area-averaged. Once again, this would be adequate for nearly uniform flows found in deflagrative devices; however, RDCs have a non-uniform flow that Eqn. 2.10 poorly captures.

Consider the integral form of the conservation of momentum for the CV of a generic jet propulsion device,

$$\iiint_V \frac{\partial(\rho \mathbf{u})}{\partial t} \mathrm{d}V + \iint_S \mathbf{u}(\rho \mathbf{u} \cdot \hat{\mathbf{n}}) \mathrm{d}S = \mathbf{F}_\mathrm{T} - \iint_S p \hat{\mathbf{n}} \mathrm{d}S \tag{2.12}$$

where $\mathbf{F}_\mathrm{T}$ is the thrust force vector, which is the resultant force (excluding pressure forces) acting upon the CV. By imposing that the flowfield is periodic about the circumference, as done in Appendix A, the unsteady terms disappear. After re-arrangement, the resultant force (thrust) in the axial direction ($\hat{\mathbf{e}}_\mathbf{z}$) is:

$$F_\mathrm{G} = \iint_S \mathbf{u} \cdot \hat{\mathbf{e}}_\mathbf{z} \left(\rho \mathbf{u} \cdot \hat{\mathbf{n}}\right) \mathrm{d}S + \iint_S p \left(\hat{\mathbf{e}}_\mathbf{z} \cdot \hat{\mathbf{n}}\right) \mathrm{d}S \tag{2.13}$$

$$= \iint_S u_\mathrm{z} \left(\rho \mathbf{u} \cdot \hat{\mathbf{n}}\right) \mathrm{d}S + \iint_S (p - p_0) \left(\hat{\mathbf{e}}_\mathbf{z} \cdot \hat{\mathbf{n}}\right) \mathrm{d}S \tag{2.14}$$

where, $F_\mathrm{G} = \mathbf{F}_\mathrm{T} \cdot \hat{\mathbf{e}}_\mathbf{z}$ and $u_\mathrm{z} = \mathbf{u} \cdot \hat{\mathbf{e}}_\mathbf{z}$. The CV extends into the ambient conditions; thus, the pressure integral is relative to the ambient pressure (p_0). Assuming no momentum enters axially into the propulsion device (CV) by design, the equation for thrust simplifies to:

$$F_\mathrm{G} = \iint_{A_8} \rho_8 u_{\mathrm{z},8}^2 \mathrm{d}A + \iint_{A_8} (p_8 - p_0) \mathrm{d}A \tag{2.15}$$

$$= \iint_{A_8} (\rho_8 u_{\mathrm{z},8}^2 + p_8) \mathrm{d}A - \iint_{A_8} p_0 \mathrm{d}A \tag{2.16}$$

The above equation is also the formulation of the gross thrust of an air-breathing engine, hence, the subscript "G".

Applying the area-averaging process given in Eqn. 2.7 to Eqn. 2.16 results in the following,

$$F_\mathrm{G} = A_8 \left\langle \rho_8 u_{\mathrm{z},8}^2 + p_8 \right\rangle_\mathrm{A} - A_8 \left\langle p_0 \right\rangle_\mathrm{A} \tag{2.17}$$

Utilizing the ideal gas law and the speed of sound for a CPG, Eqn. 2.17 is rewritten as,

$$F_\mathrm{G} = A_8 \left\langle p_8 \gamma_8 M_{8,\mathrm{z}}^2 + p_8 \right\rangle_\mathrm{A} - A_8 \left\langle p_0 \right\rangle_\mathrm{A} \tag{2.18}$$

$$= A_8 \left\langle p_8 (1 + \gamma_8 M_{8,\mathrm{z}}^2) \right\rangle_\mathrm{A} - A_8 \left\langle p_0 \right\rangle_\mathrm{A} \tag{2.19}$$

Equation 2.19 and Eqn. 2.10 are very similar, except for an important distinction. The p_8 can factor out of the first term in Eqn. 2.10, but not for the first term in Eqn. 2.19 due to the averaging procedure. In other words, the following is true,

$$\left\langle p_8 (1 + \gamma_8 M_{8,\mathrm{z}}^2 \right\rangle_\mathrm{A}) \neq \left\langle p_8 \right\rangle_\mathrm{A} \left(1 + \left\langle \gamma_8 \right\rangle_\mathrm{A} \left\langle M_{8,\mathrm{z}} \right\rangle_\mathrm{A}^2\right) \tag{2.20}$$

Appendix B proves the above inequality results from the coupling of the non-uniform properties, which is analogous to the Reynold's stress term that appears when averaging the Navier-Stokes equations. Thus, although $\mathrm{EAP_e}$ requires an area-integrated measure (thrust), its formulation nevertheless neglects the non-uniformities (circumferential variations) of the thermodynamic state

variables. For Eqn. 2.20 to be invalid, the non-uniformities either do not exist or are negligible. However, this neglects the local flow variables' dependence on relative position to the detonation wave(s) within a RDC. By neglecting the non-uniform coupling (ignore Eqn. 2.20), the resulting EAP_e merely approximates the area-averaged quantity. Hence, the analogy between the EAP_e measurement and an area-averaged quantity, despite it often being referred to as preserving the ability of the flow to produce thrust and/or work. This discrepancy will be considered further in the following sections.

2.4.2 Thrust Averaging and Ideal EAP

In many aerospace applications, such as rockets, ramjets, and scramjets, the thrust output of the engine is paramount. Thus, the total pressure is defined such that a uniform flow with the same mass-averaged enthalpy (total temperature) would have the same potential thrust production as the non-uniform flow. This averaging is *thrust-averaging*. Kaemming and Paxson utilize the concept of thrust-averaging in their *ideal equivalent available pressure* (EAP_i) measurement [113]. The method for thrust-averaging presented by Cumpsty and Horlock [108] varies from the derivation of EAP_i in some minor ways. What follows is the derivation for thrust-averaging from Cumpsty and Horlock [108] as applied to RDCs along with a discussion of how it mirrors EAP_i [113].

2.4.2.1 Thrust Averaging

Again the flow is assumed to be isentropic from the end of the combustor (④) to the nozzle throat (⑧), such that the total pressure does not change ($p_{tz,8} = p_{tz,4}$), for the reasons given in Section 2.4.1 2.4.1.2.

The derivation starts by computing the ideal axial exit velocity ($u_{z,9i}$) of expanding the flow through an isentropic nozzle to the ambient static pressure p_0. This velocity is commonly given by,

$$u_{z,9i} = \sqrt{2\eta_n c_{p,8} T_{tz,8} \left[1 - \left(\frac{p_0}{p_{tz,8}}\right)^{\frac{\gamma_8 - 1}{\gamma_8}}\right]} \tag{2.21}$$

where η_n is the nozzle efficiency that captures practical losses. Any non-axial velocity is a loss; hence, the above equation considers only the axial velocity. Throughout this work, the total temperatures and pressures based on the Mach number of the axial velocity component are,

$$T_{tz,8} = T_8 \left(1 + \frac{\gamma_8 - 1}{2} M_{8,z}^2\right) \tag{2.22}$$

$$p_{\mathrm{tz},8} = T_8 \left(1 + \frac{\gamma_8 - 1}{2} M_{8,\mathrm{z}}^2\right)^{\frac{\gamma_8}{\gamma_8 - 1}} \tag{2.23}$$

The flow isentropicaly expanded to ambient pressure (p_0), by assumption; thus, the resulting ideal gross thrust (F_{Gi}) is generated solely by the exiting momentum,

$$F_{\mathrm{Gi}} = \dot{m} u_{\mathrm{z},9\mathrm{i}} \tag{2.24}$$

$$= \dot{m} \sqrt{2\eta_n c_{p,8} T_{\mathrm{tz},8} \left[1 - \left(\frac{p_0}{p_{\mathrm{tz},8}}\right)^{\frac{\gamma_8 - 1}{\gamma_8}}\right]} \tag{2.25}$$

This ideal thrust is treated as the ability of the flow to produce thrust, and this is what is preserved from the non-uniform flow. Importantly, there is a distinction between ideal thrust and experimentally measured thrust.

This formulation of the ideal thrust is for uniform properties across the reference location, which is not the case across the RDC annulus. To address this, first consider an infinitesimally small portion of the annulus, whose area is given by,

$$\mathrm{d}A_8 = r \mathrm{d}r \mathrm{d}\theta \tag{2.26}$$

The state variables are approximately uniform across an infinitesimal area, although variations exist between the areas (i.e., variation in $\mathbf{x}$). Thus, the corresponding mass flow rate through any given infinitesimal area is,

$$\mathrm{d}\dot{m}_8(\mathbf{x}) = \rho_8(\mathbf{x}) u_{\mathrm{z},8}(\mathbf{x}) \mathrm{d}A_8 \tag{2.27}$$

Each area's flow independently passes through an isentropic nozzle to a uniform outlet *static* pressure of p_0 to produce thrust. Utilizing the form of Eqn. 2.25, the gross thrust is given by the following,

$$\mathrm{d}F_{\mathrm{Gi}}(\mathbf{x}) = \mathrm{d}\dot{m}_8(\mathbf{x}) \sqrt{2\eta_n c_{p,8}(\mathbf{x}) T_{\mathrm{tz},8}(\mathbf{x}) \left[1 - \left(\frac{p_0}{p_{\mathrm{tz},8}(\mathbf{x})}\right)^{\frac{\gamma_8(\mathbf{x}) - 1}{\gamma_8(\mathbf{x})}}\right]} \tag{2.28}$$

Adding all the individual thrust contributions together and assuming that none of them interact

while being expanded through the nozzle provides the following expression for F_{Gi}:

$$F_{\text{Gi}} = \int \mathrm{d}F_{\text{Gi}}(\mathbf{x}) \tag{2.29}$$

$$= \iint_{A_8} \left(\sqrt{2\eta_n c_{p,8}(\mathbf{x}) T_{\text{tz},8}(\mathbf{x}) \left[1 - \left(\frac{p_0}{p_{\text{tz},8}(\mathbf{x})} \right)^{\frac{\gamma_8(\mathbf{x})-1}{\gamma_8(\mathbf{x})}} \right]} \right) \mathrm{d}\dot{m}_8(\mathbf{x}) \tag{2.30}$$

Equation 2.30 will be equated to Eqn. 2.25 to find the corresponding uniform flow for the same F_{Gi}. First, the solution becomes constrained from imposing the total temperature used in Eqn. 2.25 matches that of the mass-averaged enthalpy, $\left\langle c_{p8} T_{\text{tz},8} \right\rangle_{\text{M}}$, of the RDC exit flow. The mass-averaged total enthalpy is,

$$\left\langle c_{p,8} T_{\text{tz},8} \right\rangle_{\text{M}} = \frac{1}{\dot{m}_8} \iint_{A_8} c_{p,8}(\mathbf{x}) T_{\text{tz},8}(\mathbf{x}) \mathrm{d}\dot{m}_8(\mathbf{x}) \tag{2.31}$$

Similarly, the gas composition, represented by γ, is mass-averaged and preserved. The ideal amount of thrust produced by the corresponding "equivalent" uniform flow expanded isentropically to ambient conditions is given by,

$$F_{\text{Gi}} = \dot{m}_8 \sqrt{2\eta_n \left\langle c_{p,8} T_{\text{tz},8} \right\rangle_{\text{M}} \left[1 - \left(\frac{p_0}{\left\langle p_{\text{tz},8} \right\rangle_{\text{F}}} \right)^{\frac{\langle \gamma_8 \rangle_{\text{M}} - 1}{\langle \gamma_8 \rangle_{\text{M}}}} \right]} \tag{2.32}$$

where $\left\langle p_{\text{tz},8} \right\rangle_{\text{F}}$ denotes the force-averaged total pressure. It serves as the fictitious uniform total pressure that produces the same amount of ideal thrust as the non-uniform flow. Equation 2.32 should be interpreted as the definition of $\left\langle p_{\text{tz},8} \right\rangle_{\text{F}}$ as constrained by the given mass-averaged total enthalpy and γ.

Equating the thrust produced by the uniform flow (Eqn. 2.32) to the thrust produced by the non-uniform flow (Eqn. 2.30) results in the following expression for $\left\langle p_{\text{tz},8} \right\rangle_{\text{F}}$,

$$\frac{\left\langle p_{\text{tz},8} \right\rangle_{\text{F}}}{p_0} = \left[1 - \left(\frac{1}{\dot{m}_8} \iint_{A_8} \sqrt{\frac{c_{p,8}(\mathbf{x}) T_{\text{tz},8}(\mathbf{x})}{\left\langle c_{p,8} T_{\text{tz},8} \right\rangle_{\text{M}}} \left[1 - \left(\frac{p_0}{p_{\text{tz},8}(\mathbf{x})} \right)^{\frac{\gamma_8(\mathbf{x})-1}{\gamma_8(\mathbf{x})}} \right]} \mathrm{d}\dot{m}_8(\mathbf{x}) \right)^2 \right]^{\frac{\langle \gamma_8 \rangle_{\text{M}}}{1 - \langle \gamma_8 \rangle_{\text{M}}}} \tag{2.33}$$

2.4.2.2 Ideal EAP

While, in essence, the derivation of the thrust-averaged total pressure is similar to what is presented by Kaemming and Paxson to compute the ideal EAP [113], the actual derivation follows a different

path (see Appendix C for a detailed derivation of the ideal EAP in the nomenclature of this paper). To demonstrate the similarity, Eqn 2.33 is first recast in terms of a mass-averaged velocity.

$$\frac{\left\langle p_{\mathrm{tz},8}\right\rangle_{\mathrm{F}}}{p_0} = \left[1 - \frac{\left\langle u_{\mathrm{z},9\mathrm{i}}\right\rangle_{\mathrm{M}}^2}{2\left\langle c_{p,8}T_{\mathrm{tz},8}\right\rangle_{\mathrm{M}}}\right]^{\frac{\langle\gamma_8\rangle_{\mathrm{M}}}{1-\langle\gamma_8\rangle_{\mathrm{M}}}} \tag{2.34}$$

Velocity is an intensive property, suggesting that a mass-averaged velocity does not carry a thermodynamic interpretation. Nevertheless, the mass-averaged velocity becomes useful in the context of thrust.

$$F_{\mathrm{Gi}} = \iint_{A_8} u_{\mathrm{z},9\mathrm{i}}(\mathbf{x})\mathrm{d}\dot{m}_8(\mathbf{x}) = \dot{m}_8\left\langle u_{\mathrm{z},9\mathrm{i}}\right\rangle_{\mathrm{M}} \tag{2.35}$$

Since,

$$\left\langle u_{\mathrm{z},9\mathrm{i}}\right\rangle_{\mathrm{M}} = \frac{1}{\dot{m}_8}\iint_{A_8} u_{\mathrm{z},9\mathrm{i}}(\mathbf{x})\mathrm{d}\dot{m}_8(\mathbf{x}) \tag{2.36}$$

Thus, a mass-averaged velocity is mathematically sound and is equivalent to the specific thrust.

The energy equation in the form of total enthalpy enables further manipulation. By assumption, the mass-averaged total enthalpy is conserved from ⑧ to ⑨. Breaking the mass-averaged total enthalpy into the thermal and kinetic energy components gives,

$$\left\langle c_{p,8}T_{\mathrm{tz},8}\right\rangle_{\mathrm{M}} = \left\langle c_{\mathrm{p},8}T_{9\mathrm{i}}\right\rangle_{\mathrm{M}} + \frac{1}{2}\left\langle u_{\mathrm{z},9\mathrm{i}}^2\right\rangle_{\mathrm{M}} \tag{2.37}$$

$$= \left\langle c_{\mathrm{p},8}T_{9\mathrm{i}}\right\rangle_{\mathrm{M}} + \frac{1}{2}\left\langle u_{\mathrm{z},9\mathrm{i}}\right\rangle_{\mathrm{M}}^2 + \frac{1}{2}\left\langle (u'_{\mathrm{z},9\mathrm{i}})^2\right\rangle_{\mathrm{M}} \tag{2.38}$$

Appendix C provides the proof of Eqn. 2.38. Equation 2.38 decomposes the ideal exit velocity into a mean value (angle brackets) and variations from the mean value (denoted with a $'$). Solving Eqn. 2.38 for $\left\langle u_{\mathrm{z},9\mathrm{i}}\right\rangle_{\mathrm{M}}$, substituting the result into Eqn. 2.34, and re-arranging results in the following,

$$\frac{\left\langle p_{\mathrm{tz},8}\right\rangle_{\mathrm{F}}}{p_0} = \left(\frac{\left\langle c_{p,8}T_{\mathrm{tz},8}\right\rangle_{\mathrm{M}}}{\left\langle c_{p,8}T_{9\mathrm{i}}\right\rangle_{\mathrm{M}} + \frac{1}{2}\left\langle (u'_{\mathrm{z},9\mathrm{i}})^2\right\rangle_{\mathrm{M}}}\right)^{\frac{\langle\gamma_8\rangle_{\mathrm{M}}}{\langle\gamma_8\rangle_{\mathrm{M}^{-1}}}} \tag{2.39}$$

which is the same result for $\mathrm{EAP_i}$ as given by Kaemming and Paxson, with the denominator being equivalent to the EAP-related average static temperature ($\widetilde{T}_{9\mathrm{i}}$). Therefore, the sole difference between the formulations of ideal EAP and the thrust-averaged total pressure is that $c_{p,8}$ and γ_8 are not assumed to be constants.

2.4.3 Work Averaging

In some cases, preserving the potential work output of the flow if the non-uniform flow were to enter into a turbine is the quantity of interest. The naming convention for this discussion follows Section 2.3.1 where the end of the combustor and before the turbine is ④ and after the turbine is ⑤. Here, a process occurs between ④ and ⑤, unlike the assumption made in the previous analysis.

First, consider a uniform flow consisting of a perfect gas entering an isentropic turbine, which causes a change in total enthalpy across the turbine,

$$\dot{W} = \eta_t \dot{m} c_{p,4} (T_{\text{tz},4} - T_{\text{tz},5}) \tag{2.40}$$

Which, using isentropic relationships, can be written in terms of total pressure as:

$$\dot{W} = \eta_t \dot{m} c_{p,4} T_{\text{tz},4} \left[1 - \left(\frac{p_{\text{tz},5}}{p_{\text{tz},4}} \right)^{\frac{\gamma_4 - 1}{\gamma_4}} \right] \tag{2.41}$$

This equation is the common form for finding the turbine work since it is in terms of the turbine pressure ratio. The turbine efficiency factor η_t captures practical losses. The flow is, again, decomposed into infinitesimally small slices around the annulus with a small amount of mass flow through the area (see Eqns. 2.26 and 2.27). Each area's flow independently passes through an isentropic turbine to a uniform outlet *total* pressure of $p_{\text{tz},5}$ to extract work. There are enough stages that dampen out any non-uniformity in the flow by assumption [160, 161]. Utilizing the form of Eqn. 2.41, this is given by the following,

$$\mathrm{d}\dot{W}(\mathbf{x}) = \eta_t c_{p,4}(\mathbf{x}) T_{\text{tz},4}(\mathbf{x}) \left[1 - \left(\frac{p_{\text{tz},5}}{p_{\text{tz},4}(\mathbf{x})} \right)^{\frac{\gamma_4(\mathbf{x}) - 1}{\gamma_4(\mathbf{x})}} \right] \mathrm{d}\dot{m}_4(\mathbf{x}) \tag{2.42}$$

The flow across the different slices do not interact with one another in this framework. Repeating this process and integrating across all the slices gives the non-uniform flow's total work output capability (given a uniform outlet total pressure) as,

$$\dot{W} = \iint_{A_4} \eta_t c_{p,4}(\mathbf{x}) T_{\text{tz},4}(\mathbf{x}) \left[1 - \left(\frac{p_{\text{tz},5}}{p_{\text{tz},4}(\mathbf{x})} \right)^{\frac{\gamma_4(\mathbf{x}) - 1}{\gamma_4(\mathbf{x})}} \right] \mathrm{d}\dot{m}_4(\mathbf{x}) \tag{2.43}$$

The goal with averaging is to find the total pressure that a uniform flow would produce the same amount of work through a turbine with a uniform outlet total pressure of $p_{\text{tz},5}$. The work produced

by the corresponding "equivalent" uniform flow expanded isentropically to $p_{\text{tz},5}$ is given by,

$$\dot{W} = \eta_t \dot{m} \left\langle c_{p,4} T_{\text{tz},4} \right\rangle_{\text{M}} \left[1 - \left(\frac{p_{\text{tz},5}}{\left\langle p_{\text{tz},4} \right\rangle_{\text{W}}} \right)^{\frac{\langle \gamma_4 \rangle_{\text{M}} - 1}{\langle \gamma_4 \rangle_{\text{M}}}} \right] \tag{2.44}$$

where $\left\langle p_{\text{tz},4} \right\rangle_{\text{W}}$ indicates the work-averaged total pressure. Again, Eqn. 2.44 serves as a definition, and $\left\langle p_{\text{tz},4} \right\rangle_{\text{W}}$ is the uniform total pressure that produces the same amount of work as constrained by the given mass-averaged total enthalpy and γ.

The solution of the work-averaged total pressure ($\left\langle p_{\text{tz},4} \right\rangle_{\text{W}}$) comes from equating Eqns. 2.43 and 2.44. Appendix D gives algebraic simplification of equating Eqns. 2.43 and 2.44, with the final result being:

$$\left\langle p_{\text{tz},4} \right\rangle_{\text{W}} = \left(\frac{\eta_t p_{\text{tz},5}^{\frac{\langle \gamma_4 \rangle_{\text{M}} - 1}{\langle \gamma_4 \rangle_{\text{M}}}} \iint_{A_4} c_{p,4}(\mathbf{x}) T_{\text{tz},4}(\mathbf{x}) \mathrm{d}\dot{m}_4(\mathbf{x})}{\iint_{A_4} \eta_t c_{p,4}(\mathbf{x}) T_{\text{tz},4}(\mathbf{x}) \left(\frac{p_{\text{tz},5}}{p_{\text{tz},4}(\mathbf{x})} \right)^{\frac{\gamma_4(\mathbf{x})-1}{\gamma_4(\mathbf{x})}} \mathrm{d}\dot{m}_4(\mathbf{x})} \right)^{\frac{\langle \gamma_4 \rangle_{\text{M}}}{\langle \gamma_4 \rangle_{\text{M}} - 1}} \tag{2.45}$$

In the limit that γ_4 variations are negligible compared to the average value and assuming that $p_{\text{tz},5}$ is a constant value, the work-averaged total pressure becomes invariant to the arbitrary value of $p_{\text{tz},5}$.

$$\langle p_{\text{tz},4} \rangle_{\text{W}} \approx \left(\frac{\eta_t \iint_{A_4} c_{p,4}(\mathbf{x}) T_{\text{tz},4}(\mathbf{x}) \mathrm{d}\dot{m}_4(\mathbf{x})}{\iint_{A_4} \eta_t c_{p,4}(\mathbf{x}) T_{\text{tz},4}(\mathbf{x}) \left(\frac{1}{p_{\text{tz},4}(\mathbf{x})} \right)^{\frac{\gamma_4(\mathbf{x})-1}{\gamma_4(\mathbf{x})}} \mathrm{d}\dot{m}_4(\mathbf{x})} \right)^{\frac{\langle \gamma_4 \rangle_{\text{M}}}{\langle \gamma_4 \rangle_{\text{M}} - 1}} \tag{2.46}$$

This approximation simplifies the calculations; however, this work uses the full formulation in Eqn. 2.45.

If the turbine efficiency η_t is assumed to be the same for every $\mathbf{x}$ or one wishes to examine the ideal case ($\eta_t = 1$), it too can be eliminated; however, this would require designing the turbine around the non-uniform flow which poses practical challenges. Finally, Cumpsty and Horlock have shown that mass-averaged pressure becomes equivalent to work-averaged pressure in the limit that the variations in pressure are low [108].

2.4.4 Entropy Averaging

The thrust- and work-averaging techniques discussed thus far have assumed isentropic processes in their formulation. However, several studies have shown that the averaging procedures result in an artificial increase in entropy compared to the mass-averaged entropy [157, 158]. Simultaneously preserving the flow's entropy and total enthalpy is a different averaging technique, *entropy-averaging*. Entropy-averaging is a helpful metric since it is a highly idealized representation.

For a mixture of ideal gases, the integrated form of Gibbs relation gives the specific (per unit mass) entropy (s),

$$s(\mathbf{x}) = \frac{1}{\langle \mathcal{M} \rangle (\mathbf{x})} \sum_{i=1}^{N} \left\{ \chi_i \left[\hat{s}_i^o(T(\mathbf{x})) - \bar{R} \ln \left(\frac{p(\mathbf{x}) \chi_i(\mathbf{x})}{p_i^o} \right) \right] \right\} \tag{2.47}$$

where $\bar{R}$ is the universal gas constant and the mixture average molar mass $\langle \mathcal{M} \rangle$ is,

$$\langle \mathcal{M} \rangle (\mathbf{x}) = \sum_{i=1}^{N} \chi_i(\mathbf{x}) \mathcal{M}_i \tag{2.48}$$

The summation extends over the set of N different species present in the mixture, with each species having a molar mass of $\mathcal{M}_i$. The mole fraction of species i (χ_i) describes the mixture, which varies in space and time. The NASA polynomial parameterization gives the entropy using the reference molar (per unit mole) entropy ($\hat{s}^o$) for each species at a reference pressure (p^o) [162]. This work specifically evaluated entropy using Cantera based on the NASA polynomial fits [163].

The mass-averaging procedure applies to the specific entropy; thus, Eqn. 2.47 at ⑧ is mass-averaged, by again assuming the flow is isentropic between ④ and ⑧.

$$\langle s_8 \rangle_{\mathrm{M}} = \frac{1}{\dot{m}_8} \iint_{A_8} \frac{1}{\langle \mathcal{M} \rangle (\mathbf{x})} \sum_{i=1}^{N} \left\{ \chi_i \left[\hat{s}_i^o(T_8(\mathbf{x})) - \bar{R} \ln \left(\frac{p_8(\mathbf{x}) \chi_{8,i}(\mathbf{x})}{p_i^o} \right) \right] \right\} \mathrm{d}\dot{m}_8(\mathbf{x}) \tag{2.49}$$

Given a generic static state ⓠ and its corresponding total state ⓣⓠ, the entropy of the static state is equal to the entropy of the total state (i.e., $s_{\mathrm{q}} = s_{\mathrm{tq}}$). Thus, the total pressure and temperature uniquely define the entropy of a state for a given gas composition: $s_{\mathrm{q}} = \tilde{s}_{\mathrm{q}}(T_{\mathrm{tq}}, p_{\mathrm{tq}})$. The *entropy-averaged* total pressure ($\langle p_{\mathrm{tz},8} \rangle_{\mathrm{S}}$). Therefore, the mass-averaged total temperature (enthalpy), mass-averaged gas composition ($\langle \chi \rangle_{\mathrm{M}}$), and mass-averaged entropy define the *entropy-averaged* total pressure ($\langle p_{\mathrm{tz},8} \rangle_{\mathrm{S}}$) defined according to the following relation,

$$\langle s_8 \rangle_{\mathrm{M}} = \frac{1}{\langle \langle \mathcal{M} \rangle \rangle_{\mathrm{M}}} \sum_{i=1}^{N} \left\{ \langle \chi_i \rangle_{\mathrm{M}} \left[\hat{s}_i^o(\langle T_{\mathrm{tz},8} \rangle_{\mathrm{M}}) - \bar{R} \ln \left(\frac{\langle p_{\mathrm{tz},8} \rangle_{\mathrm{S}} \langle \chi_{8,i} \rangle_{\mathrm{M}}}{p_i^o} \right) \right] \right\} \tag{2.50}$$

where

$$\langle\langle \mathcal{M} \rangle\rangle_{\mathrm{M}} = \sum_{i=1}^{N} \langle \chi_i \rangle_{\mathrm{M}} \mathcal{M}_i \tag{2.51}$$

In practice, the total pressure is implicitly solved by equating Eqns. 2.49 and 2.50, and solving for $\left\langle p_{\mathrm{tz},8} \right\rangle_{\mathrm{S}}$. The term $\langle\langle \cdot \rangle\rangle_{\mathrm{M}}$, given by Eqn. 2.51, is computed from nested averaging procedures. First, the molar mass is averaged at each spatial point along the annulus exit based on the local composition ($\langle\langle \cdot \rangle\rangle$). Then, those averaged molar masses are mass-averaged over the entire annulus ($\langle \cdot \rangle_{\mathrm{M}}$).

The mass-averaging procedure given by Eqn 2.49 mathematically cannot be divided into the product of individually mass-averaged quantities like Eqn. 2.50. There are additional non-linear terms not represented in Eqn. 2.50 that appear because of the products of the various terms within the integrand of Eqn. 2.49. For instance, expressing the mass-averaged entropy as a function of purely mass-averaged quantities gives,

$$\langle s_8 \rangle_{\mathrm{M}} = \frac{1}{\langle\langle \mathcal{M} \rangle\rangle_{\mathrm{M}}} \sum_{i=1}^{N} \left\{ \langle \chi_i \rangle_{\mathrm{M}} \left[\hat{s}_i^o \left(\left\langle T_{\mathrm{tz},8} \right\rangle_{\mathrm{M}} \right) - \bar{R} \ln \left(\frac{\left\langle p_{\mathrm{tz},8} \right\rangle_{\mathrm{M}} \left\langle \chi_{8,i} \right\rangle_{\mathrm{M}}}{p_i^o} \right) \right] \right\} + \kappa \tag{2.52}$$

The only difference between Eqns. 2.50 and 2.52 is that the total pressure in Eqn. 2.52 is mass-averaged instead of entropy-averaged. The κ term captures the non-linear coupling terms and is necessary for Eqn. 2.52 to equal Eq. 2.49. Note how κ only emerges when trying to cast the mass-averaging integral into a reduced formulation with the target mass-averaged quantity (entropy) depending on other mass-averaged ones (pressure, temperature, and composition); thus, κ is the deviation caused by the specific formulation enforced, and its existence demonstrates that $\left\langle p_{\mathrm{tz},8} \right\rangle_{\mathrm{S}}$ is distinct from $\left\langle p_{\mathrm{tz},8} \right\rangle_{\mathrm{M}}$.

The mass-averaged entropy, total enthalpy (temperature), and gas composition are known and have physical interpretations, all being averages of extensive thermodynamic properties. Thus, the entropy-averaged total pressure ($\left\langle p_{\mathrm{tz},8} \right\rangle_{\mathrm{S}}$) is merely the total pressure that satisfies Eqn. 2.50 with the left-hand-side evaluated according to Eqn. 2.49. It remains a fictitious total pressure with no physical interpretation since it inherently encapsulates the deviations associated with the non-linear terms arising from the mass-averaging procedure in Eqn. 2.49 (or alternatively, κ in Eqn. 2.52). The resulting total pressure gives the same mass-averaged entropy for an equivalent uniform flow given the same mass-averaged total enthalpy (temperature) and gas composition. Likewise, the thrust- and work-averaged total pressures are mathematical constructs generated by having a uniform flow representation undergoing some physical process (i.e., flow expansion) while preserving some target properties (i.e., thrust or work) of the non-uniform flow. This work neglects the entropy production of such physical processes; however, the non-uniform would likely lead to

an increase in the mass-averaged entropy compared to the exit flow before the process.

The total temperature and pressures in Eqn 2.50 were defined solely with the axial velocity (i.e., with a subscript "z"), which introduces an error in the formulation of the entropy-averaged total pressure. Entropy is a fundamental thermodynamic quantity and is agnostic to flow direction, unlike the total temperature and pressure; however, determining entropy through total temperature and pressure introduces a velocity dependency on entropy. Specifically, any non-axial velocity would ultimately cause $\langle p_{tz,8} \rangle_S < \langle p_{t,8} \rangle_S$. Since total temperature is less sensitive to changes in velocity overall, it is assumed that $\langle T_{tz,8} \rangle_M \approx \langle T_{t,8} \rangle_M$. Thus, $\langle p_{tz,8} \rangle_S$ is an idealized total pressure for two reasons: the mixing/averaging process is assumed isentropic, and all the available total pressure is in the axial direction. From a thermodynamics view, this is the best-case scenario. Thus, a decrement from the entropy-averaged total pressure occurs as a mix of entropy production in mixing the non-uniform flow and losses caused by non-axial flow.

2.5 Demonstration using RDC Simulations

2.5.1 Description of RDC Simulations

The differences become more apparent when applying the different averaging procedures to the results of RDC numerical simulations. This work considered three simulations for the demonstration, and they were high-fidelity, three-dimensional DNS simulations of a hydrogen/air-operated RDC with radial air injection performed by Van Beck and Raman [17]. Sato et al. [8, 16], Bielawski et al. [164], and Van Beck and Raman [17] discuss the details of the simulated domain, numerical scheme, and chemistry model. Table 2.3 contains some of the critical features of the cases, including the air mass flow rate, equivalence ratio, and geometric areas relevant to this work. The three cases study a radial air injection with fuel injected through discrete portholes orthogonally near the air throat [16, 17]. This injection style is quite prominent in the RDC literature as it was one of the first published injection geometries [165]. Three discrete air mass flow rates are considered, with a unique flow rate for each case. The equivalence ratio for each simulation is 1 to be consistent with one another. The channel area ($A_{3,2}$) and exit area (A_8) are held constant across simulations. Importantly, there is no exit constriction/nozzle in this work for any of the cases; the combustor has a constant area channel that terminates in a bluff body ($A_{3.2} = A_8$).

2.5.2 Different Equivalent Total Pressures

The static pressure, temperature, gas composition, and axial velocity at the exit give the total pressure ($p_{tz,8}$) at every point around the annulus and in time. Figure 2.2 gives the distribution

Case	$\dot{m}$ [g/s]	ϕ	$A_{3.2}$ [cm^2]	A_8 [cm^2]
1	320	1.00	34.9	34.9
2	630	1.00	34.9	34.9
3	860	1.00	34.9	34.9

Table 2.3: Summary of the geometry and operating condition of the hydrogen/air numerical simulations used in this study. [16, 17]

of the $p_{tz,8}$ around the annulus for a single instance of time for Case 1, with the entire two-dimensional distribution being in Figure 2.2a. In contrast, Figure 2.2b highlights the variation at the three discrete radial locations: near the inner-body (red), at the mid-channel (black), and near the outer-body (blue). The other cases exhibit similar trends to those plotted in Figure 2.2. The non-uniformity caused by the two detonation waves and their associated oblique shocks is apparent; in this case, the total pressure increases by about 4.5. The total pressure decays rapidly in the circumferential direction; after about $\pi/2$ radians, the total pressure becomes asymptotic with a value of 1.3 atm. In this case, even the base pressure of 1.3 atm is larger than ambient conditions (1 atm). The variations in the radial direction in both these figures are much less significant than those in the circumferential direction since the channel width is sufficiently small [106, 107]. Even when radial stratification of fuel occurs, the pressure remains nearly constant in the radial direction, although the temperature may vary [166]. Due to minimal radial variations, the averaging integrals are reasonably approximated by only integrating in the circumferential direction at a given radial location. However, this work used the two-dimensional integrals instead of such an approximation.

The averaging procedures considered in this study, including both the experimental EAP (EAP_e) and ideal EAP (EAP_i), are then applied to the data. The spatial integrals are performed for individual time instances, generating an instantaneous spatial-average quantity. Then, the resulting values are averaged in time to produce the results presented in Table 2.4. Although the Mach numbers are known, EAP_e is computed with the unity Mach number assumption to match experiments. Additionally, to calculate $\langle p_{tz,8} \rangle_F$ it is assumed that $p_0 = 0.1$ atm while it is assumed that $p_{tz,5} = 1$ atm to calculate $\langle p_{tz,4} \rangle_W$. The results of Table 2.4 are the resulting average total pressures and show that the experimental EAP (EAP_e) is the lowest of these averages. Figure 2.3 further contextualizes the variations between the results of the different averaging procedures for the different cases by normalizing the results by the experimental EAP. The values in Figure 2.3 are the percent differences relative to the experimental EAP. The positive bars indicate that the total pressure from the experimental EAP is lower than the other averaging techniques. The assessment that EAP_e is closely related to the area-averaged pressure ($\langle p_{tz,8} \rangle_A$) is reinforced by the fact that $\langle p_{tz,8} \rangle_A$ is the closest to EAP_e. However, a few percent (2-6%) difference occurs due to the non-uniformity

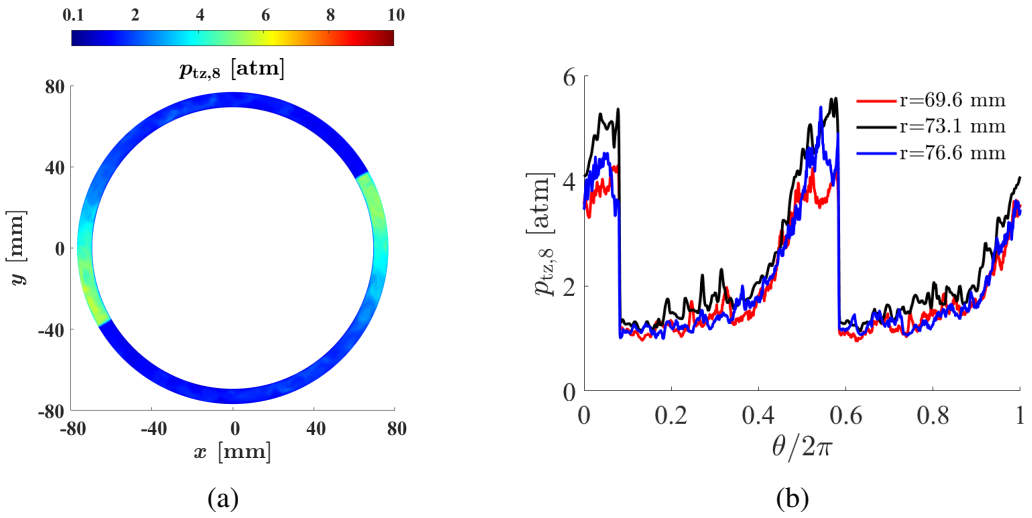

Figure 2.2: Variation of total pressure at the exit of RDC for a) full two-dimensional annulus and b) discrete radial locations. Plots are for a single instance in time.

Case	$\mathrm{EAP_e}$ [atm]	$\langle p_{tz,8}\rangle_A$ [atm]	$\langle M_{z,8}\rangle_A$	$\mathrm{EAP_i}$ [atm]	$\langle p_{tz,8}\rangle_F$ [atm]	$\langle p_{tz,4}\rangle_W$ [atm]	$\langle p_{tz,8}\rangle_S$ [atm]
1	1.41	1.49	0.60	1.64	1.63	1.69	1.95
2	2.35	2.40	0.94	2.58	2.50	2.70	3.02
3	3.30	3.35	0.97	3.47	3.38	3.60	4.04

Table 2.4: Summary of the different average total pressures across the simulated cases. Results assume: $M_{z,8} = 1$ for $\mathrm{EAP_e}$, $p_0 = 0.1$ atm for $\langle p_{tz,8}\rangle_F$, and $p_{tz,5} = 1$ atm for $\langle p_{tz,4}\rangle_W$.

coupling terms neglected in $\mathrm{EAP_e}$. The greater disagreement for Case 1 results from the area-averaged Mach number being ≈0.6, and $\mathrm{EAP_e}$ assumes a unity Mach number assumption [113].

It is apparent from Figure 2.3 that there are significant differences between $\mathrm{EAP_e}$ and the other averaging procedures given the simulation data considered here. For instance, the ideal EAP ($\mathrm{EAP_i}$) ranges from 5.1% to 16.5% larger than $\mathrm{EAP_e}$, with the upper limit of the discrepancy being more significant than what was reported by Kaemming and Paxson [113]. The more considerable discrepancy is a consequence of the subsonic Mach numbers in Case 1. The thrust-averaging ($\langle p_{tz,8}\rangle_F$) and the ideal EAP ($\mathrm{EAP_i}$) are typically within 1-3% of another due to the variations of $c_{p,8}$ and γ_8. Thus, the assumptions in $\mathrm{EAP_i}$ provide a valid approximation to the thrust-averaged value, although they inadvertently make $\mathrm{EAP_i}$ less conservative overall.

Finally, the entropy-averaging procedure results in the most significant discrepancy with $\mathrm{EAP_e}$, by being 22.3% to 38.2% larger. However, any meaningful process, whether thrust or work

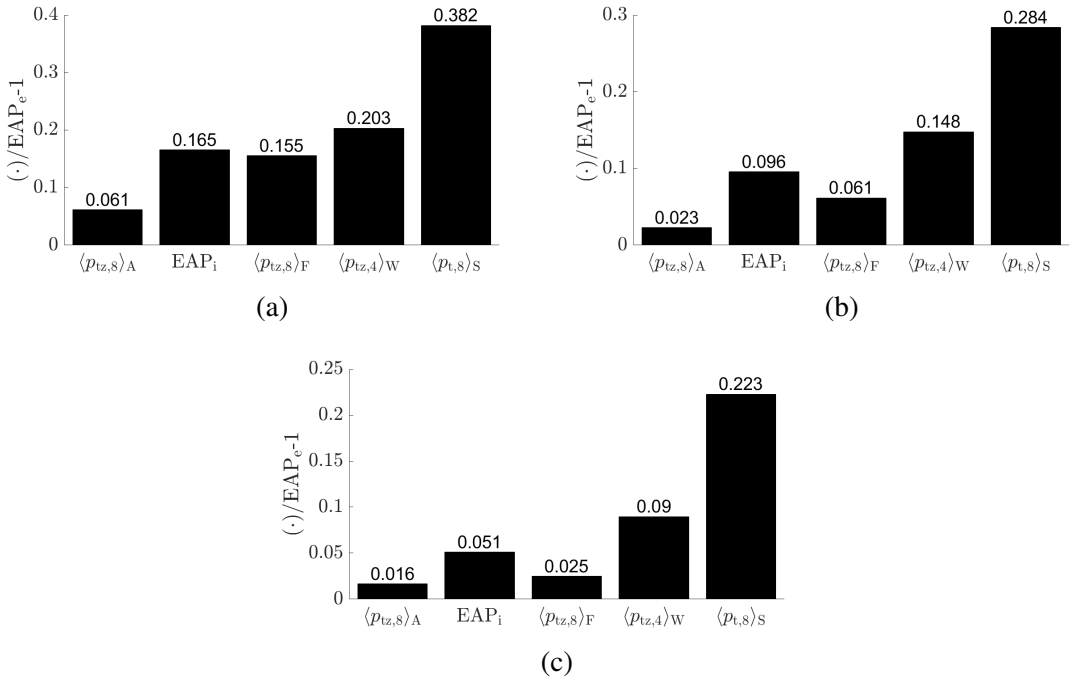

Figure 2.3: The different averaging techniques produce different measures of the "average" total pressure for a) Case 1, b) Case 2, and c) Case 3. Values relative to experimental EAP equivalent.

production, results in a lower total pressure. Thus, while thermodynamically sound, the idealistic entropy-averaged total pressure is practically unattainable. The reduction in total pressure relative to the entropy-averaged values is equivalent to a "mixing loss", or the increase in entropy, generated by homogenizing the non-uniform flow [157, 158]. The mixing loss creates an inescapable tension between thermodynamic processes within the RDC. The local gain at the detonation wave is less entropy production as the heat release occurs at a higher static pressure; however, a rotating detonation wave creates non-uniformities about the annulus, which leads to entropy generation. The balance between these competing concepts requires further investigation in the future.

Based on the results presented here, the definition of "pressure gain" across a RDC depends on the desired end application. In other words, the "pressure gain" for thrust-producing devices differs from the "pressure gain" for work-producing devices, even if the exit flow is identical. An interesting question arises from how these results would translate into turbojet/fan systems where a turbine is downstream of the combustor to power the compressor despite the primary goal being to produce thrust. Since the RDC exit flow first is utilized to extract work through the turbine, the resulting equivalent total pressure post-combustor and pre-turbine could be closer to the work-averaged value. The turbine can then either extract more work from the flow or, if the amount of extracted work remains constant, the total pressure at the outlet of the turbine could experience an increase as the presence of the turbine likely dampens out variations in total pressure [160, 161].

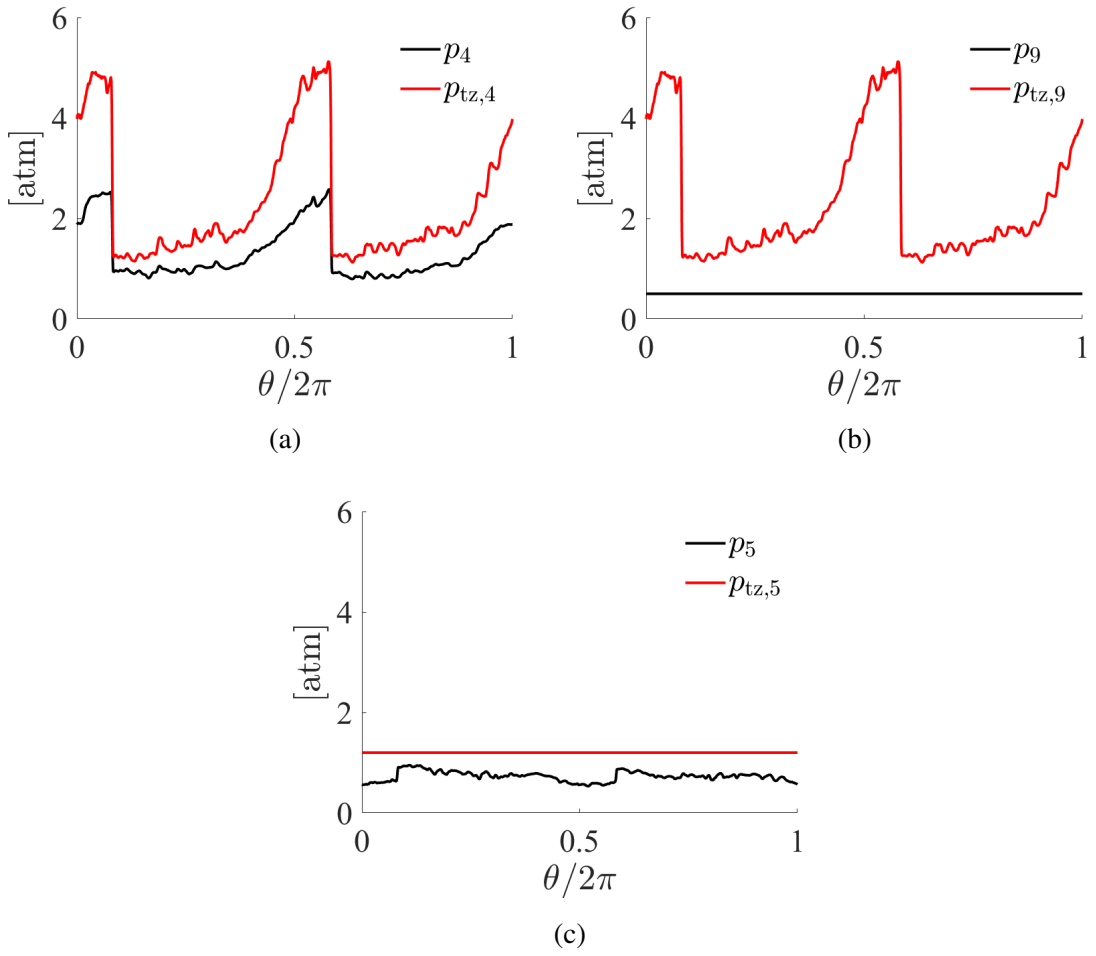

Figure 2.4: Static and total pressure at a) outlet of RDC, b) after thrust-averaging, and c) after work-averaging. Assumed outlet states in b) and c) are shown as flat lines.

Regardless, from a reduced order model of a propulsion device, the combustor would appear to perform better in a turbojet/fan than a rocket/ramjet despite identical processes occurring within the combustor. Overall, additional data from simulations are needed to verify these trends, specifically from simulations with geometries closer to the best-performing experimental geometries [13, 118].

2.5.3 Difference Between Thrust and Work-Averages

The difference between the EAP_i and $\langle p_{\text{tz},8} \rangle_\text{W}$ is significant as it contradicts the notion that EAP_i preserves the ability of the flow to produce thrust *and* work. The primary difference between the thrust- and work-averaged values is the assumed outlet state of the device. Visual representations of the different processes assumed in the averaging procedures are shown in Figure 2.4. Figure 2.4a is the circumferential profiles of static (black) and total (red) pressures at the RDC exit plane for Case

2 at an instance in time. This plane is the end of the combustor, ④. The thrust-averaging procedure assumes the flow passes through an idealized nozzle to a fictitious uniform static pressure (⑨). In this fictitious outlet state, the total pressure is not uniform nor equal to the static pressure (see Figure 2.4b). On the other hand, the work-average procedure assumes the flow passes through an idealized turbine to a fictitious uniform total pressure (⑤). In this fictitious outlet state, the static pressure is not uniform, nor is it assumed that it equals the static pressure (see Figure 2.4c). The velocity can be non-uniform after the nozzle or turbine for both thrust- and work-averaging procedures.

While the assumed outlet states differ, another explanation for the different results is that the thermodynamic processes of going through a nozzle or turbine differ. The purpose of the nozzle is to convert as much thermal energy in the flow into kinetic energy as possible since this maximizes the thrust (momentum transfer). The total energy in the flow remains unchanged. Thrust-averaging depends on the local thermal and kinetic energy ratio at each location around the annulus since the given ambient condition limits the conversion between the flow's thermal and kinetic energy. Meanwhile, a turbine is extracting work from the flow, which manifests as extracting thermal and kinetic energy from the flow. There is less dependence on the ratio of the energies since both types of energy get extracted, differentiating work-averaged from thrust-averaged.

The hypothetical applications of RDCs can further contextualize the differences in the resulting average total pressures. In power generation applications, the total pressure at the turbine outlet would be equivalent to the ambient static pressure; however, for propulsive jet engines, the flow would pass through a nozzle before reaching ambient static pressure. Even in the power generation application where $p_{t,5} = p_0$, removing the variation in velocity and reduction in total pressure causes the work-averaged pressure to be greater than the thrust-averaged pressure. Thus, while conventional wisdom states that the flow's ability to produce thrust and work are the same, this analysis indicates that this assumption is incorrect when the flow is non-uniform.

2.5.4 Dependence on Exit Conditions

An assumed outlet state of the device is required to calculate both thrust and work-averaged total pressures. Effectively, an unspoken, implicit assumption was made that stated that the results from the averaging are insensitive to the chosen outlet state. Pianko and Wazelt remarked that such averaging techniques are not intrinsic in that the formulation does not depend solely on the non-uniform flow by also being dependent on the final state [167]. However, they argued that the sensitivity of the total pressure averaging techniques to the downstream conditions, equivalent to the chosen outlet state in this work, is low for turbojets ($\leq 0.1\%$) [167]. The flow exiting RDCs typically has more significant spatial variance than turbojets, which may potentially influence the sensitivity; thus, this section evaluates the implicit assumption of the outlet state in greater detail.

For the sake of discussion, this section assumes that the results of the simulations remain unchanged despite the changes to the outlet condition. In other words, the flowfield at the exit plane remains the same regardless of the assumed downstream conditions. The assumed exit static pressure (p_0) used in thrust-averaging was varied from 0.001 atm to 1 atm to cover the range of static pressures for reasonable altitudes. If the p_0 value exceeds $p_{\mathrm{tz},8}(\mathbf{x})$ at any point around the annulus, the averaging results are disregarded because of the complex numbers. Likewise, the post-turbine total pressure ($p_{\mathrm{t},5}$) used in work-averaging was varied from 0.001 atm to 10 atm. Figures 2.5a and 2.5b give the results of this analysis for thrust-averaged and work-averaged pressures, respectively. The nominal values in Table 2.4, indicated with a superscript "*", normalize the averaged total pressures presented in both figures. In general, a value of p_0 optimizes $\left\langle p_{\mathrm{tz},8}\right\rangle_{\mathrm{F}}$, which is about 0.4 atm for the cases considered in this work. This "optimal" pressure likely varies depending on the geometry, chemistry, or other factors instead of being a universal truth. Once p_0 decreases below 0.05 atm, the resulting thrust-averaged total pressure drops significantly. Most commercial aircraft fly at an altitude with ambient pressures above this, so these variations are neglectable. However, high-altitude supersonic flights or rockets would see a meaningful change in the "pressure gain" compared to the sea-level conditions, despite no change in the mass-averaged entropy at the combustor exit and increasing thrust with decreasing exit pressures (assuming that the flow is not over-expanded). In this regard, "pressure gain" based on the thrust-averaged pressure is not intrinsic, and it does not uniquely portray the possible decrease in entropy production or the thrust production for a given exit flow. This observation is especially significant for rockets since the inlet conditions (driven by pumps) are independent of the ambient conditions, potentially producing the same combustor exit profile regardless of the ambient pressure. For instance, a recent effort in Japan observed that an RDC with a plug-shaped nozzle operating in space (p_0 = 0.1 Pa) had the same operating frequency of 20 kHz as a ground test with higher exit pressures (10 kPa) [168]. Therefore, it would be good practice to report the ambient pressure assumed for the calculation if a value of "pressure gain" based upon thrust-averaging procedures (like EAP) is reported from simulations.

The variations in work-averaged total pressures caused by the value of $p_{\mathrm{t},5}$ are overall less than thrust-averaged values. Even in the extreme of having the $p_{\mathrm{t},5}$ being 0.001 atm, the result is only at most 3% different than the initially assumed 1 atm. There is only a slight difference on the order of a 1% between the different cases. The work-averaged total pressure exhibits less sensitivity to its respective outlet condition than the thrust-averaged pressure. The reduced sensitivity is primarily due to the small variations in γ_4 around the annulus, allowing for $p_{\mathrm{t},5}$ to be effectively eliminated in the equation, as given by the approximation of Eqn. 2.46 (see Appendix D for further details). Another justification for these results can be made based on the breakdown of the thermal and kinetic energy of the flow. The work-averaging procedures assume an extraction of energy that is

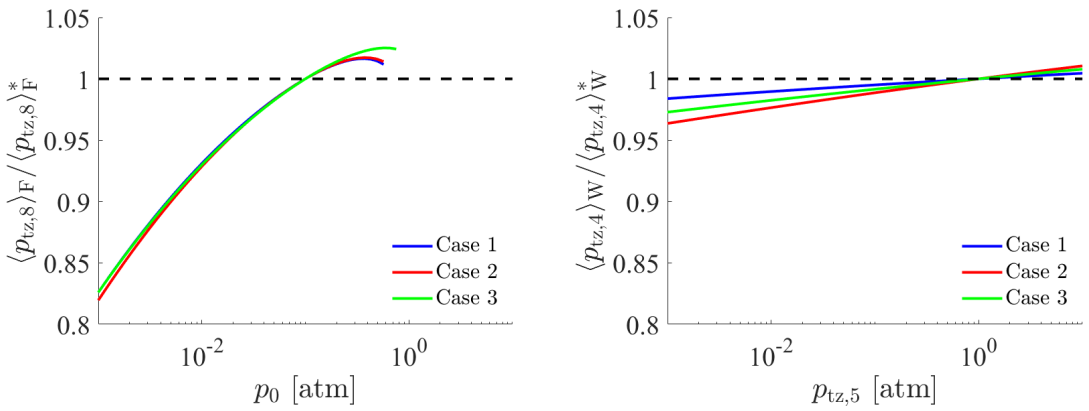

Figure 2.5: Changes in a) thrust-averaged total pressure and b) work-averaged total pressure with variable assumed exit conditions.

agnostic to the type of energy, and it only cares about the total energy/enthalpy. Therefore, for the work-averaged pressure to depend upon the assumed outlet condition, it would require the total enthalpy of the flow exiting the RDC to depend on downstream conditions, which is erroneous. Hence, $\langle p_t \rangle_W$ is insensitive to the downstream conditions. However, the transfer of thermal energy into kinetic energy does depend on downstream conditions; perfectly expanded nozzles are desirable since they maximize the efficiency of this transfer. Thus, the sensitivity of $\langle p_t \rangle_F$ on the downstream conditions.

Suppose a singular average total pressure to describe the performance of an RDC is desirable. In that case, preserving the flow's ability to produce work may be advantageous due to this greater insensitivity over a broader range of outlet conditions. Once again, casting these results in terms of entropy production, a lower total pressure would result in a larger average entropy than the mass-averaged value. It is then as if a thermodynamic penalty (entropy production) grows worse with decreasing ambient pressure for thrust applications. In contrast, work-producing applications are less prone to these losses despite the same RDC operation for the two applications.

2.6 Alternative Experimental Pressure Gain Methods

The results above demonstrate that the EAP_e is the smallest "average" total pressure and does not conserve any meaningful quantity of interest. However, the EAP method is currently the most prominent experimental method in the literature. Two additional methods of measuring the exit total pressure exist in the literature. The following section will examine both in detail to draw comparisons against EAP on a theoretical basis. Additionally, this section will demonstrate that

the various methods converge to the same result.

2.6.1 Area-Mach Relation Method

Brophy et al. [114, 115, 120] proposed that a combination of static pressure measurements in the detonation channel and the area-Mach relation is a suitable alternative to the EAP methodology. This method is colloquially known as the "NPS Method" because Brophy et al. is a research group from the Naval Postgraduate School (NPS). Instead of directly addressing the non-uniformity in the flow, a quasi-one-dimensional approximation is assumed in the NPS method. Specifically, the NPS method assumes single "average" values of Mach number at the exit plane, ⑧, and downstream of the detonation/combustion region but upstream of any area change, ④ from Figure 2.1. Note, ⑦ would be an equally appropriate description of this axial location since in the RDC experiments without a turbine, there is nothing to distinguish between ④ and ⑦; however, the notation of Brophy et al. utilized ④ and this notation is adopted here for the sake of consistency with their work [114].

The derivation and accompanying assumptions will now be detailed to evaluate the similarity and differences of the NPS method compared to the EAP method. Similar to the EAP methodology, the flow is assumed to be uniformly choked at the nozzle throat plane, $M_8 = 1$ such that ⑧ is equated to the sonic state (⊛). This assumption has the same limitations as EAP, where the choked assumption may not be valid at low mass flow rates or configurations without a nozzle. The NPS method also assumes that downstream of the detonation zone, the flow is approximately uniform in the circumferential direction. This assumption enables the area-Mach relation to be used to determine the average Mach number in the channel.

$$\left(\frac{A_4}{A_8}\right)^2 = \left(\frac{A_4}{A^*}\right)^2 \tag{2.53}$$

$$= \frac{1}{\widetilde{M}_4^2}\left[\frac{2}{\gamma_4+1}\left(1+\frac{\gamma_4-1}{2}\widetilde{M}_4^2\right)\right]^{(\gamma_4+1)/(\gamma_4-1)} \tag{2.54}$$

The $\widetilde{\ }$ above the Mach number denotes that the quantity is estimated, similar to the experimental EAP method in Section 2.4.1.2. The geometric areas of the nozzle throat and the detonation channel are readily known, allowing for this calculation. The γ_4 is assumed to be that of the combustion products and is again assumed to be a constant across the annulus. Using the definition of total pressure along with the estimated average Mach number and a measured static pressure at ④, a total pressure at ④, $\widetilde{p}_{t,4}$, can be found. Furthermore, the flow is assumed to be isentropic through the

remainder of the device, so the total pressure is effectively constant.

$$\widetilde{p}_{\mathrm{t},4} = p_4 \left(1 + \frac{\gamma_4 - 1}{2} \widetilde{M}_4^2\right)^{\gamma_4/(\gamma_4 - 1)} \tag{2.55}$$

$$\approx \widetilde{p}_{\mathrm{t},8} \tag{2.56}$$

To measure the p_4, initially, a single Capillary Tube Averaged Pressure (CTAP) measurement was employed [114, 115]. A CTAP is a long, small tube connected to a pressure transducer, and the tube dampens out the dynamic components of the flow which are prevalent in the highly turbulent and unsteady flow of a RDC [169, 120]. The fluidic dampening causes the pressure measurement to be more akin to a time-averaged static pressure than an instantaneous measurement. In a recent study, Codoni et al. expanded the NPS method by taking pressure measurements at several circumferential locations since they observed an asymmetry in the time-averaged pressure around the annulus at a fixed axial location [120]. Theoretically, the asymmetry would bias the results of the method when using only a single measurement. The cause of said asymmetry remains unknown, though it was determined to be fluidic and not an artifact of the instrumentation.

There are several issues regarding the theory of the NPS method outside the potential influence of circumferential variability in the time-averaged static pressure. Suppose the axial position of the pressure measurement is within the detonation zone, i.e., the axial region of space where the detonation wave(s) propagate. The static pressure increase across detonation will significantly skew the results since the assumed uniformity quickly falls apart. Hence, the NPS method requires measurements sufficiently downstream of the detonation zone. However, the location of the detonation zone for a given geometry or flow rate is, at this time, unknown a priori. Thus, there is ambiguity about whether the sensor is genuinely downstream of the detonation zone during the experimental design. Making the combustor longer would mitigate the ambiguity since Rankin et al. observed that the detonation zone is several centimeters long [100]; though, this may be undesirable if a more compact device is preferred. Even when the pressure measurements are "sufficiently" downstream of the detonation wave(s) in the RDCs, the flow rarely becomes truly uniform since the attached oblique shocks cause properties to still depend on the relative location of the detonation wave(s). Refer to the discussion in Section 1.5.4. If true, the assumptions imposed in this method would eliminate the need for the averaging procedures discussed in this chapter, which seems too reductive. This same argument also applies to the assumed uniformly sonic outlet Mach number, although the EAP method depends on a similar assumption.

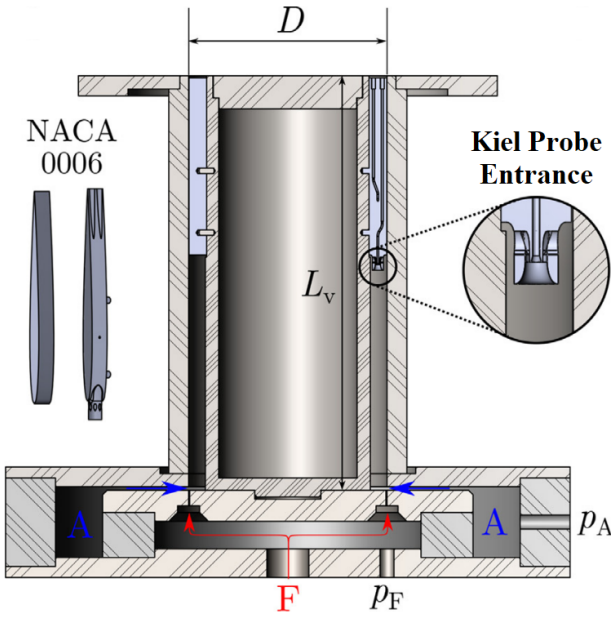

Figure 2.6: Kiel probes to measure the outlet total pressure. Figure reproduced from [13].

2.6.2 Direct Measurement Method

In contrast to EAP and the NPS method, Bach et al. directly measured the stagnation pressure at the outlet of the RDC with Kiel probes [13, 14]. A Kiel probe comprises a Pitot probe/tube encased in a specifically designed shroud that mitigates the flow directional, particularly the yaw, sensitivity of the Pitot tube [14]. The Pitot tube brings the flow to rest within the tube, and the subsequent stagnation/total pressure is measured. Bach et al. integrated the Kiel probes within nozzle guide vanes, with the entrance of the Kiel probe being at the leading edge of the nozzle guide vane. Thus, Bach et al. measured the total pressure before the area restriction, ④, as shown in Figure 2.6, reproduced from [13]. By measuring ④ like the NPS method, potential viscous and thermal losses would degrade the total pressure; the Kiel probe measurements may not capture these losses. One of the advantages of using the Kiel probes is that the number of necessary assumptions, particularly about the velocity and gas composition, is significantly reduced.

A high-speed pressure transducer can also be connected to the Kiel probe to provide greater time resolution of the total pressure measurements at discrete locations around the annulus. However, the measurements were only partially time-resolved since the Kiel probes employed by Bach et al. had a capillary tube of 100 mm between the entrance of the probe and the transducer [13]. This capillary tube offset introduces viscous dissipation and an acoustic transfer function between the leading edge and the transducer [14]. Even considering the lag imposed by the capillary tube, greater time resolution is achieved with the Kiel probes than with thrust and CTAP measurements, which typically have lower sampling rates. Since less fluidic averaging occurs within the Kiel

probe, the averaging (in this case, time-averaging) is done post-experiment in the data-processing step instead of during the experiment. The post-experiment averaging also contrasts with the thrust measurements needed for EAP as thrust is inherently an area-integrated quantity.

Overall, the Kiel probes introduced by Bach et al. hold significant promise as being the method to getting the outlet total pressure with potentially the least amount of bias or uncertainty, although they are not without their concerns [14] and are limited to several discrete locations about the annulus. However, the RDC community has not widely adopted the usage of Kiel probes in favor of integrated thrust stands, which gives the EAP since thrust is a valuable measurement.

2.6.3 Similarity of the Methods

Despite the varying levels of method assumptions and instrumentation, the three methods of estimating the total pressure at the outlet, Brophy et al. and Bach et al., have demonstrated that their respective methods give similar values to EAP. Brophy and Codoni measured the EAP in addition to performing the NPS method and found reasonable agreement, within ±10%, between the measurements [114, 120]. Likewise, in conjunction with the Kiel probe measurements, Bach et al. also measured the total pressure through the EAP method and found good agreement [13, 170]. The similarity of the methods extends beyond the comparisons made in the individual studies since when Bach et al. compiled all of the pressure gain measurements published in the literature into a single plot [14], reproduced in Figure 2.7, the measurements made through the NPS method (red dots) and the Kiel probes (gray triangles) capture the same trends as the measurements from the EAP method (the other colored dots) from studies by other groups [171, 165, 172, 116, 118]. In particular, all the different studies observed that the pressure gain grew less negative as the exit and inlet throat areas became closer. The experimental pressure gain measurements provided in this work, which will be discussed in Chapters 5-7 and use the EAP method, also agree with this trend. Overall, while the different methods employ different measurements and use different assumptions, it has been effectively proven that each method converges to the same value within experimental error.

The convergence of the methods is surprising, given the differences on the surfaces. For instance, both the EAP and NPS methods attempt to approximate the outlet total pressure while the Kiel probes measure it directly. Additionally, the EAP inherently contains more spatial information than both the NPS method and Kiel probes since EAP involves a thrust measurement instead of point measurements. Meanwhile, the Kiel probes have the potential for the greatest time resolution. At the time of writing, nobody in the literature has sought to understand why all the measurements give similar answers. This work asserts that the consistency between the different total pressure measurement techniques is a direct consequence of the periodic nature of the flowfield.

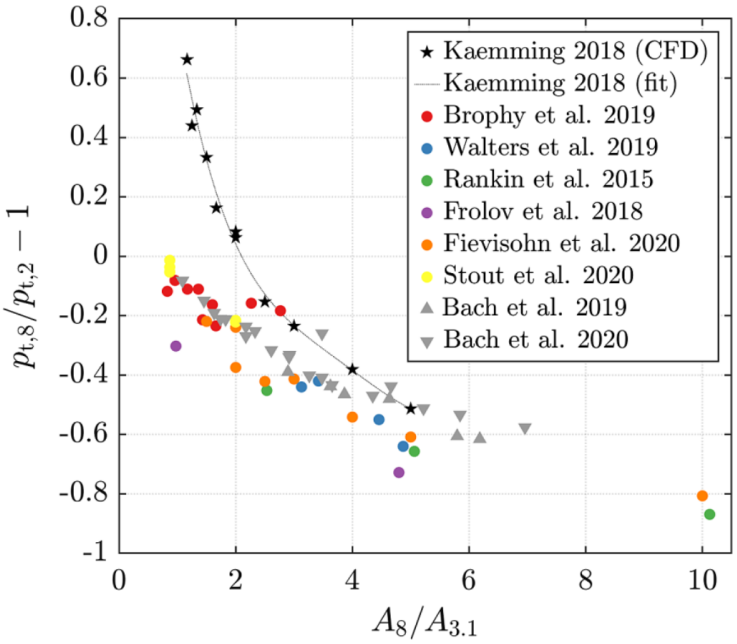

Figure 2.7: Comparison of published pressure gain (y-axis) measurements with respect to the ratio of outlet and inlet throat areas. Figure reproduced from [14].

In practice, both the measurements from the Kiel probes [14] and the results from the NPS method [120] are time-averaged to provide a singular value to report. Consider the case where both methods only use a single measurement at a single spatial location. The time-average of any thermodynamic quantity, Q, at a given circumferential, θ_i, and axial location z_i, is expressed as,

$$\left\langle Q|_{\theta_i,z_i}\right\rangle_t = \left(\int_{t_1}^{t_2} \mathrm{d}t\right)^{-1} \int_{t_1}^{t_2} f(t;\theta_i,z_i)\mathrm{d}t \tag{2.57}$$

The averaging procedure is over the interval given by $[t_1, t_2]$ where $t_2 > t_1$. For many RDC testing, the averaging window is between 0.1-1 seconds. This averaging window is significantly greater than the detonation period, so ensure averaging over thousands of cycles. Thus, it is most appropriate to consider the Kiel probe and NPS methods as time-averaged total pressures at specific spatial locations. Additionally, the CTAP measurements used for the NPS method are effectively time-averaged quantities [169] due to fluidic dampening, sensor response time, and low sample rate. Meanwhile, as established previously, $\mathrm{EAP_e}$ is effectively an area-averaged quantity, see Section 2.4.1.2; however, in practice, reported EAP or the associated PG values are steady-state values [114, 116, 13]. Thus, the instantaneous area-averaged values are subsequently time-averaged over a time window, similar to the methods. However, a time-averaged area-averaged quantity ($\mathrm{EAP_e}$) does not necessarily equate to a time-averaged point measurement (the other methods) for a generic flowfield, which seemingly contradicts the convergence observed in the literature.

The next step comes from considering that the flowfield in a RDC, while unsteady in the lab frame, is periodic in both spatial and time domains. Effectively, if the frame of reference moved with the detonation wave(s), the frame would become steady. Recall that performing area-averaging on axial planes implies circumferential integration. For an axial plane given by z_i and at time t_i, the area-average ($\left\langle Q|_{t_\mathrm{i},z_\mathrm{i}}\right\rangle_\mathrm{A}$) is:

$$\left\langle Q|_{t_\mathrm{i},z_\mathrm{i}}\right\rangle_\mathrm{A} = \left(\iint_A \mathrm{d}A\right)^{-1} \iint_A f(r,\theta;z_\mathrm{i},t_\mathrm{i})\mathrm{d}A \tag{2.58}$$

$$= \frac{1}{2\pi}\int_{\theta=0}^{\theta=2\pi} f(\theta;z_\mathrm{i},t_\mathrm{i})\mathrm{d}\theta \tag{2.59}$$

Suppose the wave periodically propagates at a constant speed in the θ direction. In that case, the area-averaged quantity, Q, at a specific instance in time is equivalent to a time-averaged quantity at a specific spatial location.

$$\left\langle Q|_{t_\mathrm{i},z_\mathrm{i}}\right\rangle_\mathrm{A} = \left\langle Q|_{\theta_\mathrm{i},z_\mathrm{i}}\right\rangle_\mathrm{t} \tag{2.60}$$

For brevity, this section omits the proof; however, Appendix E provides a rigorous demonstration of the above equality. In other words, an area-averaged quantity (e.g., $\mathrm{EAP_e}$) is equivalent to a time-averaged quantity (e.g., Kiel probes).

Thus, the difference between the area-averaged and time-averaged quantities is significantly mitigated by averaging all the measurements over a sufficiently long time window. Additionally, while in the above discussion, only single measurement points are considered for the NPS method and Kiel probes, in reality, several measurements at different locations are taken and then averaged together [120, 14]. Doing so effectively area-averages the time-averaged results, further reducing the differences compared to $\mathrm{EAP_e}$. Especially since reported $\mathrm{EAP_e}$ values are time-averaged versions of an area-averaged measurement. Thus, all the methods are consistent despite the differences in required measurements and assumptions due to the periodic nature of the RDC flowfield. With this in mind, determining the total pressure can follow any of the presented methods, and one can choose the methodology that requires the least complex set of measurements if that is desirable. However, this also means that these other experimental methods do not solve the issues that $\mathrm{EAP_e}$ has in under-predicting the other averaged procedures.

2.7 Discussion

From the onset, there are several concerns about the validity of using a global PG, specifically with EAP, as the primary performance metric for RDCs. First and foremost is the fact that EAP does not follow any conservation law after the averaging process by virtue of effectively being an

area-averaged quantity. Integrating experimental EAP measurements into a reduced order quasi-one-dimensional model to either infer loss parameters or predict future performances is subject to doubt. Furthermore, experimental investigators cannot claim that EAP they measure preserves the flow's ability to produce thrust or work as promised initially. The other research groups that use alternative methods to EAP are also constrained to area-averaged results. One could overlook the lack of conserving necessary quantities if EAP converged to the same result as the other averages, which conserve meaningful quantities; however, the results from the EAP are noticeably lower than the others. While EAP is known to be conservative based on the unity Mach number assumption [113], even when the assumption is valid (Cases 2 and 3), EAP is still overly conservative. The starkest contrast is between EAP and the entropy-averaged total pressure, which may be the most representative of the thermodynamic benefit since it considers the entropy of the exiting flow. Thus, the experimental EAP underpredicts the "truest" measure of the gain. Even if the experimental EAP better matched the thrust-averaged and work-averaged total pressures as initially claimed, the resulting total pressure is not intrinsic to the flow as it would depend on the outlet state. All this combines to suggest that the definition and implementation of experimental EAP does not withstand rigorous theoretical analysis, which leaves ambiguity and uncertainty in the EAP method and PG metric. However, there was no suitable experimental alternative at the time of writing, so this work still adopted them for usage in the experimental component of this work.

There may be concerns about how well the simulation results translate to experiments. Even high-fidelity simulations cannot simultaneously replicate the wave speed, thrust output, pressure profiles, etc., from experiments despite using the same geometry and testing conditions [173, 174, 175]. The flow non-uniformities around the annulus in experiments may be less than what simulations predict. Consider the experiments performed by Bach *et al.* where they captured a time-resolved total pressure measurement through Kiel probes at the exit of an RDC [14]. The sample time trace shows that the total pressure varies between 4 and 4.5 atm throughout the detonation cycles. The specific run had $\dot{m} = 500$ g/s, $\phi = 1.0$, the radial air injection, and an exit constriction resulting in $A_8/A_{3.2} = 0.67$. The most comparable case in this work would be Case 2; however, adding the nozzle likely dramatically influences the results. The simulation results shown in Figure 2.2a contrast the experimental in that the total pressure ratio across the oblique shock is 4-5 in the simulation and only 1.125 in the experiment. It is unknown if the more minor changes in total pressure are associated with the implementation of the nozzle, which homogenizes the exit flow by promoting a higher number of waves and higher channel/base pressure, or if some inherent difference between simulations and experiments causes the changes. Regardless, the smaller non-uniformities around the annulus lessen the difference between the different averaging techniques, which may add to the credibility of EAP and PG experimentally.

CHAPTER 3

Description of Experimental Setup

3.1 Overview

The discussion now turns away from the theoretical analysis discussed in the previous chapter to the experimental studies that explore the concept of pressure gain on a prototype RDC. This chapter details the general RDC geometry along with the geometric variations investigated throughout the remainder of this work. A description of the supporting infrastructure that enabled the experimental firing of the RDC can also be found in this chapter. Additionally, the instrumentation needed to characterize the RDC operation and the thrust takeout system required to get a pressure gain measurement will be detailed. Finally, this chapter will introduce the uncertainty analysis of the sensors that will ultimately propagate into the uncertainty of the pressure gain measurement.

3.2 RDC Geometries

The RDC design through the experiments in this work was the fixed inlet design presented previously instead of the variable inlet design investigated by Shepard [47, 50]. Nevertheless, the design was modular to allow for specific geometric parameters to be varied. Different injectors, exit constrictions, combustor lengths, and inner body diameter are some of the possible variations to the base design, and some previous work by Chacon and Shepard have previously explored some of these changes [176, 45, 58, 50]. However, this work focused on a few select changes to highlight the importance of such geometric parameters while fixing the other ones. In general, the inlet throat area ($A_{3.1}$), detonation channel area ($A_{3.2}$), and exit throat area (A_8) remained the same across all the studies presented in this work. In Chapter 5, no geometric changes are considered; meanwhile, Chapter 6 investigated changing the combustor length, and Chapter 7 modified the injector geometry. A summary of which geometric parameters were varied and fixed across the different chapters is presented in Table 3.1. A general description of the RDC, including the fixed

Study	Injector	$A_{3.1}$	$A_{3.2}$	A_8	L
Chapter 4 & 5	×	×	×	×	×
Chapter 6	×	×	×	×	✓
Chapter 7	✓	×	×	×	×

✓ indicates quantity was varied during the study.
× indicates quantity was kept constant during the study.

Table 3.1: A summary of which geometric properties varied during the different studies outlined in the following chapters.

parameters, is given later in a dedicated section. Dedicated sections will also detail the geometric variations highlighted in Chapters 6 and 7, which both change a specific geometric parameter.

3.2.1 General Description of the RDC

The RDC tested here is cylindrical, with an annular gap between the inner and outer bodies that form the detonation channel. Within the detonation channel, the outer diameter of the annulus, d_o, was 154 mm (6.065 in), while the inner diameter of the annulus, d_i, was 138.7 mm (5.46 in). The diameter combination resulted in an annular gap of 7.62 mm (0.30 in) during the constant area portion of the channel, between (3.2) and (7). The dimensions are consistent with many other annular RDCs tested in the literature [44, 177, 178]. An area reduction occurs through a converging nozzle before the gases are exhausted from the RDC. The area is reduced by smoothly extending the inner body diameter through a smooth contour over the last 11.9 mm (0.469 in) of the detonation channel. The nozzle terminates with an inner diameter of 14.66 cm (5.77 in), such that the ratio of the outlet area (A_8) to the detonation channel area ($A_{3.2}$) was 0.5. The nozzle does not have a diverging portion; thereby, it is truncated and terminated at the minimum area/throat ((8)). The truncated nozzle produces a well-defined throat at the exit. It also removes the nozzle expansion efficiency on the thrust measurement, which is advantageous as it better isolates the performance of the RDC from the nozzle design [113].

3.2.2 Injection Geometries

Most of the tests conducted for this work focused on a single injection geometry, the axial air inlet. Chapters 4, 5, and 6 focus solely on this geometry. A modified version of the axial air inlet is employed in Chapter 7 to investigate the effects of a worse injector diodicity; see Table 3.1. As such, a description of both injection geometries follows, and Figure 3.1 visualizes both geometries.

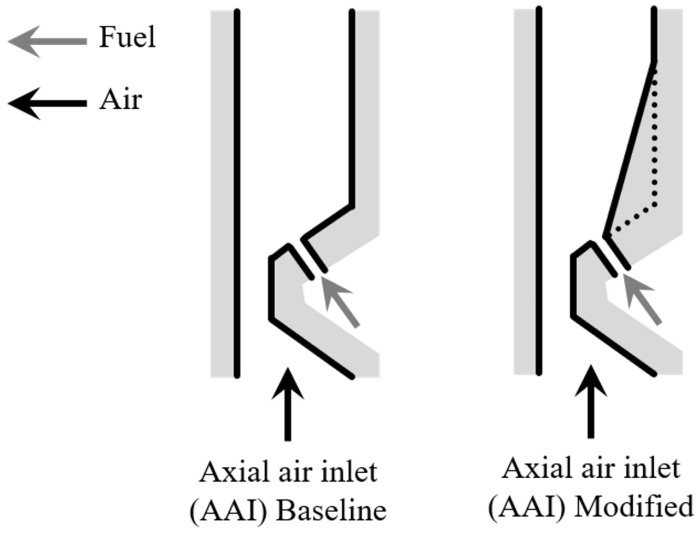

Figure 3.1: Air inlets considered in this work. Left) Baseline geometry used throughout this work and right) modified inlet to study inlet diodicity.

3.2.2.1 Axial Air Inlet

The Axial Air Inlet (AAI) has been the subject of several previous studies from the University of Michigan [45, 58]. The defining characteristic of the AAI is the axial air injection through a constricted annular gap. The AAI was constructed by smoothly extending the inner diameter through a contour while maintaining the same outer diameter as the detonation channel. The inner diameter increased until the annular gap at the throat was 1.59 mm (0.063 in). The air injector throat area ($A_{3.1}$) is 7.67 cm^2 (1.19 in^2). This throat area resulted in an area ratio between the air inlet throat and detonation channel of 0.215 (i.e., $A_{3.1}/A_{3.2} = 0.215$). The inverse of this ratio was 4.65. The throat area was constant for about 4.88 mm (0.192 in) before the inner diameter diverged and the area expanded. The area expansion was symmetrical with the upstream area convergence. Unlike the air stream, fuel was injected discretely through 120 circular injectors with a diameter of 0.889 mm (0.035 in) evenly spaced around the circumference. The fuel injectors were located downstream of the air inlet throat on the rear-facing surface, and the injection angle was 30° relative to the central axial axis. Therefore, the fuel injection is a jet-in cross-flow; however, the cross-flow is undergoing an expansion from the area reduction.

3.2.2.2 Modified Axial Air Inlet

Everything upstream of the fuel injectors in the Modified Axial Air Inlet (AAI-M) was identical to the AAI. Thus, the geometry of the air inlet throat and the fuel injectors remain the same between the two designs. However, instead of injecting air over a symmetric shoulder and having a rapid

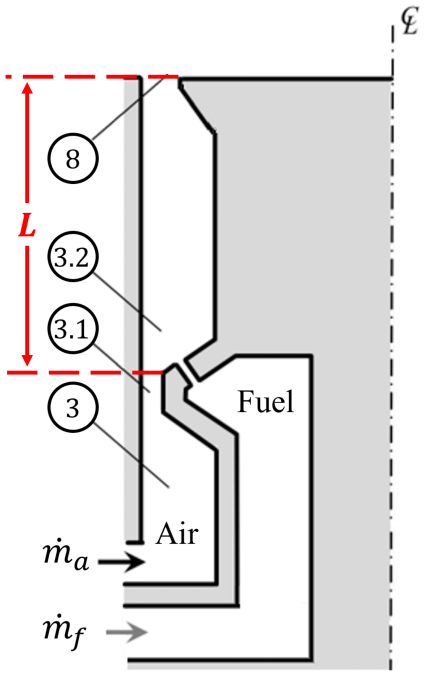

Figure 3.2: Combustor length defined from inlet throat (end of constant area portion) to exit throat.

downstream expansion, a streamlining of the downstream flow path slowed the rapid expansion of the mixture; see the right-hand side of Figure 3.1. This streamlining was achieved by linearly reducing the inner diameter of the annulus to the nominal inner diameter of 139 mm (5.46 in) at an angle of 12.5°. The divergence begins immediately downstream of the fuel injectors. Chacon theorized that a toroidal re-circulation region anchors at the shoulder in the standard inlet, which traps hot products and provides activation energy to the fresh mixture before the arrival of the detonation wave [58]. The inlet modification mitigated the re-circulation region, which may change the operation of the RDC. The modified design also lowered the pressure drop across the inlet in the reverse (upstream) direction compared to the un-modified design, thereby lowering the diodicity of the air inlet. In theory, this should promote additional backflow to occur during operation.

3.2.3 Combustor Length

In Chapter 6, the length of the RDC combustor (refer back to Table 3.1) was the geometric parameter that was varied. Here, the combustor length, L, was defined from the end of the inlet throat (end of constant area portion) to the exit throat, as shown in Figure 3.2. The end of the inlet throat is fluidically the smallest area due to viscous forces acting along the walls during the constant area portion, making it the true throat. As described previously, the nozzle's throat was also the exit plane of the RDC. The study presented in Chapter 6 considered four different combustor lengths:

Configuration	L [mm]	d_i [mm]	d_o [mm]	$A_8/A_{3.2}$	$A_{3.2}/A_{3.1}$	$L/\pi d_\mathrm{m}$
A	71	139	154	0.50	4.65	0.154
B	102	139	154	0.50	4.65	0.222
C	118	139	154	0.50	4.65	0.256
D	137	139	154	0.50	4.65	0.298

Table 3.2: Relevant geometric parameters of tested RDC configurations. Variables (in order are): L, combustor length; d_i, inner diameter of annulus; d_o, outer diameter of annulus; $A_8/A_{3.2}$, ratio between exit throat and annulus areas; $A_{3.2}/A_{3.1}$, ratio between annulus and air inlet throat areas; $d_\mathrm{m} = 1/2\,(d_\mathrm{i} + d_\mathrm{o})$, mean annulus diameter

71, 102, 118, and 137 mm. These are labeled as configurations A, B, C, and D in Table 3.2, which summarises the essential geometric parameters utilized. The nominal combustor length (L_0) from previous studies was 102 mm [45]; subsequently, configuration B is the standard detonation channel geometry used in the other chapters. In addition to the aforementioned geometric parameters, the length normalized by the mean annulus circumference, $\pi d_m = \pi(d_\mathrm{i} + d_\mathrm{o})/2$, is given to draw comparisons to the work of Bluemner et al. [133] The different lengths corresponded to -30%, +16%, and +34% variations from L_0. Adding spacers to the inner- and outer-bodies lengthened the channel while maintaining a constant plenum length. Outer-body spacers were necessary to maintain a static pressure measurement at the exit plane. This measurement estimates p_8 (with the state definition presented in Figure 2.1). Chapter 5 will be used to evaluate the average static Mach number. A new inner-body piece allowed for a shorter length when used with the standard outer-body. The length was, again, such that the exit plane had an associated pressure measurement. Since the length of the nozzle remained the same, effectively, the change in the combustor length only affected the length of the constant area portion of the detonation channel.

3.3 General System Description

With a description of the RDC geometry established, this section focuses on the infrastructure surrounding the RDC and the control sequence utilized during experimentation.

3.3.1 Control System and Data Acquisition

An in-house National Instruments (NI) LabVIEW control program handled control of the entire experiment. The control program executed an automated timing sequence that constituted a test firing of the RDC. The internal clock for the timing sequence operated at 200 Hz. Within the timing sequence, various solenoid ball valves actuate to control the flow of the gaseous reactants

to the RDC system. Additionally, BNC breakout boxes outputted TTL signals (5 V) within the timing sequence to act as triggers for spark plugs, data acquisition systems (DAQs), cameras, etc., as needed. Digital I/O signals, in the form of TTL signals, were generated using seven BNC-2090 breakout boxes, while a custom relay box controlled the power to the solenoids. Connected to the BNC breakout boxes were two NI PCI-6259, one NI PCIe-6353, and one NI PCI-6133 multi-function I/O card(s). Each card had two associated breakout boxes except for the NI PCI-6133 card, which only had one connected breakout box. Although the program is automated while executing the experiment, all the timing information of the discrete events was user-provided before testing.

The steady-state air and fuel flow rates are additional user inputs. The program took the input mass flow rates and orifice sizes, computed the necessary upstream pressure, and then converted that necessary pressure into a voltage to be applied to the pressure regulator using experimental calibrations. The following section provides a detailed description of the gas delivery system. The controller can start at one flow rate before switching to another in a single piece-wise step. Although the controller makes an instantaneous switch in requested flow rates, the fluids take longer to respond, resulting in a transient change in the flow rates of about one second. This capability was vital to certain test conditions while measuring thrust, as will be discussed in the following chapters.

The control program additionally served as one of the DAQs. Specifically, the two NI PCI-6259 and one NI PCIe-6353 cards acted as a low-speed DAQ with a sample rate equivalent to the refresh rate of the timing sequence, 200 Hz. Up to 48 sensors were connected and measured simultaneously with the six BNC breakout boxes. The DAQ measured the voltage of each sensor in a differential mode relative to the ground and logged for the entire duration of the timing sequence. Running in parallel to the central control program was a program that sampled at a significantly greater speed than the primary program. This high-speed DAQ program controlled the NI PCI-6133 data card, and the typical sampling rate was 0.5 MHz, although this varied depending on the experiment. An internal clock independent of the main control program enabled the higher sampling rate. The NI PCI-6133 data card connected to a single BNC-2090 breakout box, and again, the DAQ recorded the differential voltage relative to the ground. In total, up to eight high-speed measurements were taken simultaneously. Due to the finite memory onboard the NI PCI-6133, a TTL pulse from the main program at a user-specified time triggered the high-speed DAQ program to begin data collection. Typically, this data collection time encompassed the fuel-on portion of the test with one second of margin before and after the introduction of fuel.

3.3.2 Gas Delivery Systems

3.3.2.1 Air Delivery

High-pressure air entered the room from an external high-pressure tank to deliver air to the system. The high-pressure air flowed through a reducing dome pressure regulator, Groove WH 408-K5 Powereactor Dome Regulator. An air-loaded regulator, Tescom 44-1566, externally controlled the dome regulator by setting the downstream pressure. Likewise, a Tescom ER3000 pressure controller operated the air-loaded regulator. Connected to the inlet of the air-loaded regulator was a type K gas cylinder containing N_2 gas to provide the upstream pressure. Shop air, approximately 110 psi, was connected to the Tescom ER3000. The dome regulator was required since its C_v enabled the high flow rates, up to 1 kg/s, needed for testing, unlike the Tescom 44-1566. The LabVIEW controller operated the Tescom ER3000 to set the Tescom 44-1566 outlet pressure, and the dome regulator's outlet pressure matched that pressure. A precision choked orifice metered the flow; therefore, the pressure upstream of the choked orifice (downstream of the dome regulator) controlled the mass flow rate of air.

The mass flow through a choked orifice ($\dot{m}_\mathrm{o}$) is given by,

$$\dot{m}_\mathrm{o} = C_\mathrm{d} A_\mathrm{o} p_{\mathrm{t,o}} \sqrt{\frac{\gamma}{R T_{\mathrm{t,o}}} \left(\frac{2}{\gamma+1}\right)^{\frac{\gamma+1}{\gamma-1}}} \tag{3.1}$$

where $p_{\mathrm{t,o}}$ and $T_{\mathrm{t,o}}$ are the total pressure and temperature upstream of the orifice, C_d is the discharge coefficient of the orifice, and A_o is the orifice area. Pressure transducers and thermocouples were upstream of the choked orifice. Flow upstream of the orifice is assumed to be sufficiently slow that the measured static pressure and temperatures are equivalent to the total quantities. The choked orifice on the airline had a diameter of 13.97 mm (0.550 in) and a C_d of 0.99 as given by the manufacturer. Downstream of the choked orifices, electro-pneumatic ball valves controlled when air entered the system. A relay box controlled by the LabVIEW program actuated the ball valves (solenoids). After the ball valves, the airline transitions from a fixed pipe to one or more flexible hose that connects to the RDC. For the fixed inlet geometry, this process took place in a manifold with six flexible hoses connecting to the RDC in the radial direction. The air injection ports were equally spaced about the circumference and were 45.2 mm (1.78 in) downstream of the mid-plane of the inlet throat. It was confirmed that the pressurization of the six flexible hoses did not contribute to the load-cell measurement and, thus, did not impact the thrust measurements.

3.3.2.2 Fuel Delivery

A similar setup controlled the gaseous fuel delivery to the RDC, except there were five independently controlled fuel lines. Each fuel line could have a different type of fuel and flow rate of said fuel. Instead of an external high-pressure volume, the fuel originated from a type K gas cylinder. Since the fuel flow rates are lower than the air, the lower C_v values of the air-loaded pressure regulator, Tescom 44-1566, were sufficient to provide the necessary flow rate without needing the larger dome regulator. Once again, Tescom ER5000 pressure controllers were connected to the regulators to get the required pressure upstream of the choked orifices for the desired flow rates, and shop air was again connected to the Tescom ER5000 controllers. A choked orifice metered each fuel line, and it was possible to change the orifice size depending on the mass flow requirements. The choked orifices ranged from 1.321 mm (0.052 in) to 3.175 mm (0.125 in) in diameter. The C_d for each discrete fuel orifice was experimentally validated, with most being approximately 0.87.

There were two primary reasons that the orifice size would need to be swapped depending on the gas and/or flow rate. First, the orifices must remain choked for metering purposes and to isolate from downstream perturbations. If the downstream pressure in the fuel line becomes too large, the orifice may unchoke for a given flow rate, indicating the orifice area was too large. The other reason is to protect the Tescom 44-1566 pressure regulators. Given the outlet pressure threshold of 600 psi for the Tescom, the system's maximum allowable outlet pressure was 500 psi for a margin of safety. If the desired flow rate for a given orifice would result in a required upstream orifice pressure greater than 500 psi, that orifice can be deemed too small. The LabVIEW program performed background calculations to ensure the system would not exceed the pressure threshold. Therefore, the orifice size selection satisfied the choking constraint while simultaneously protecting the system.

Downstream of the choked orifices, electro-pneumatic ball valves were used on each fuel line to control when fuel entered the system. After being independently metered and passed through the ball valves, the five fuel lines fed into an in-line static mixing chamber to mix the streams into a single fuel stream. Mixing different fuel streams enabled testing various mixtures of single-component gases, and the chamber produced the mixtures in real time. Even though pure H_2 was the sole fuel tested in this work, the fuel still passed through the mixing chamber. After the mixing chamber, one or more flexible feed hoses bring the fuel mixture to the RDC. Six hoses injected fuel radially through elbows into the fixed inlet RDC geometry. Again, the pressurization of the flexible hoses exerted a negligible amount of force on the load cell.

3.3.3 Coupled Exhaust and Afterburner

A consequence of testing the RDC within an enclosed space is the need for an exhaust system directly connected to the RDC. Figure 3.3 is a picture of the exhaust system. The gases exhausted

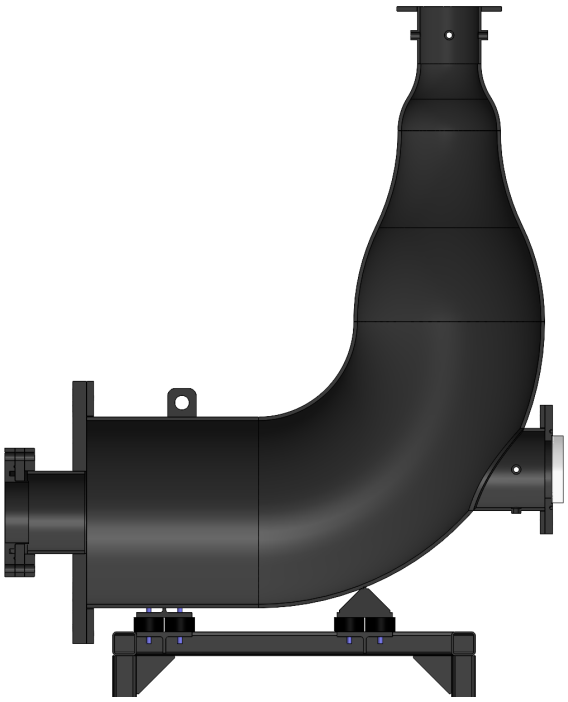

Figure 3.3: Coupled exhaust vessel and afterburner. The RDC is not shown but would be to the left of the image.

from the RDC entered a large vessel that was 51 cm (20 in) in diameter and approximately 2 m (78 in) long. The vessel included an elbow which diverted the horizontal flow exiting the RDC to become vertical. A 10 cm (4 in) pipe connected to the top of the vessel, and the pipe ran for approximately 20 m before exhausting to the atmosphere outside the building. A pressure transducer and thermocouple probe were instrumented at the beginning of the 10 cm pipe to monitor the properties of the exit flow.

Despite the size of the exhaust, the entire system experiences back-pressurization during the ignition sequence of the RDC. Shepard theorized that back-pressurization occurs due to a fluidic impedance that arises when the high-velocity and high-temperature post-combustion products interact with the slower-moving and cold gases before ignition [179]. The fluidic impedance effectively chokes the flow in the reduced pipe at the top of the exhaust, increasing the pressure upstream of the reduction (impacting the exhaust and RDC). The back-pressurization persisted up to 0.5 s before the pressure in the system dropped and reached a quasi-steady state value. Due to the elevated pressures, a large pressure force acted upon the RDC, which potentially could have saturated or damaged the load cell; Chapter 5 discusses this. However, a previous work concluded that this back-pressurization had minimal impact on the operating characteristics of the RDC [179].

During testing, fuel and oxidizer flow is established before ignition of the RDC since the mixture must precede the externally provided activation energy. A pre-detonator initiated ignition, and the

following section describes the pre-detonator in greater detail. However, the flow before ignition can lead to an accumulation of the reactive mixture in the coupled exhaust system. If the mixture accumulates too much, an explosion within the exhaust vessel is possible once ignition occurs. This process is referred to as a hard start and is considered a safety concern. Four axially oriented pilot flames were downstream of the RDC to minimize the accumulation of fresh reactants. This series of pilot flames is referred to collectively as the afterburner, which can be seen by the two flanges on the left-hand side of Figure 3.3. The afterburner consists of a stoichiometric mixture of H_2/air and an air mass flow rate of approximately 15 g/s. Any un-burnt reactants ignite after passing through the afterburner. Ignition of the afterburner occurred before the introduction of fuel into the RDC, and the afterburner flames persisted throughout the entire time fuel was within the RDC. Thus, the afterburner consumed the un-combusted reactants, leaving the RDC. In other words, since the combustion efficiency of the RDC remains unknown, the afterburner ensures that all fuel is reacted before entering the exhaust vessel, thereby mitigating the explosion risk.

3.3.4 Pre-Detonator

Initially, the sole ignition source of the RDC was a flashback from the downstream afterburner previously described. As the flame propagated upstream into the RDC, thermo-acoustic instabilities promoted the growth of the detonation waves from the deflagration that the afterburner initiated. However, this proved inconsistent with an integrated nozzle, which made flashback more challenging. A custom pre-detonator provided a more reliable ignition source. A pre-detonator is akin to a detonation tube or a pulse detonation engine since single-shot detonation waves are created and injected into the RDC detonation channel. The fuel and oxidizer mixture, H_2/O_2, were introduced simultaneously into a small chamber through automotive fuel injectors. Both injectors were Black-Ops Honda F22C injectors with 36 lb/hr for the H_2 and 150 lb/hr for the O_2, respectively. The DAQ sent TTL pulses to a dedicated control box, which then fired the injectors once for each TTL pulse. The injectors were fired at 20 Hz for about 50 ms to fill the initial chamber. After the injection of the reactants, a time delay of 50 ms occurred to prevent the spark plug from firing while the injectors were open. After the time delay, the spark plug was fired at 100 Hz using an ignition coil, JEGS 555-40162, and TTL pulses for another 50 ms. Overall, the control program repeated the entire firing process at about 6 Hz. This work performed an iterative study of varying the injector open time, spark plug delay, and the feed pressures of the fuel/oxidizers until consistent and repeatable detonation waves occurred. The exact flow rate of either reactant is unknown, although based upon a previous study [180], the mixture is believed to be approximately stoichiometric.

After ignition by the spark plug, the subsequent flame traveled through a 1/2 in tube towards the RDC. A Schelkin spiral within the tube aided the DTD transition. After about 12.7 cm (5 in)

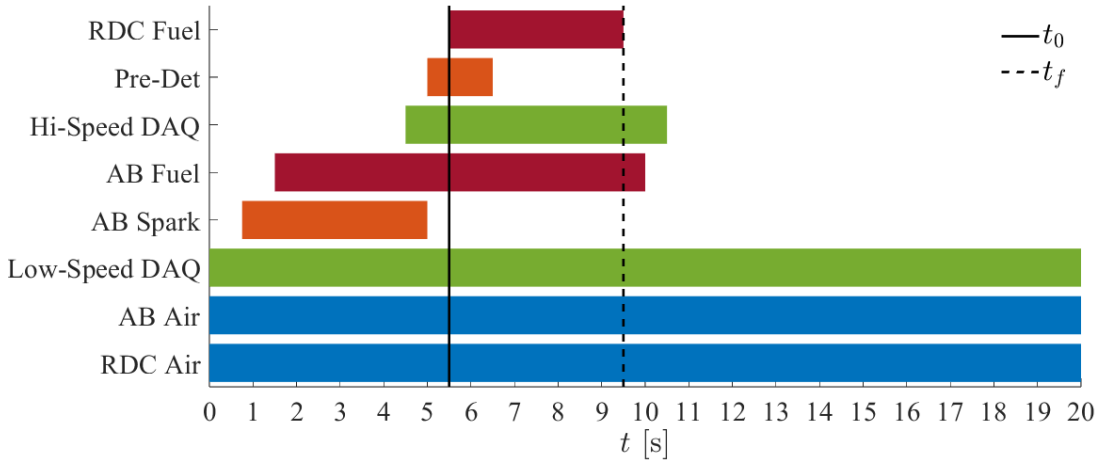

Figure 3.4: Automated timing sequence for a four-second duration RDC test. Start and end times are user inputs in the LabVIEW control program.

of 1/2 in tube, the area was reduced to a 1/4 in tube directly connected to the detonation channel of the RDC through the outer wall. The 1/4 in tube was about 1.2 m (48 in) long to assist in the DTD. The detonation was injected radially into the channel to avoid a directional preference in the RDC. Based on observation from the high-speed camera, the detonation bifurcates after injection into the annulus. The two detonation waves propagated in both directions around the annulus, beginning to ignite the pre-existing mixture. The fuel and air were typically flowing before the initial pre-detonator shot. Eventually, the two detonation waves interacted with one another, and, following this, a highly transient and dynamic ignition period occurred that is not well understood and is beyond the scope of this current work. If the ignition was successful after the transient period, the newly formed detonation wave(s) continuously propagated about the annuls. This process did not always occur with the first shot of the pre-detonator; therefore, the pre-detonator fired at 6 Hz for the first second of the test. If a detonation wave in the RDC establishes before the last shot of the pre-detonator, subsequent shots do not significantly disturb the detonation wave(s). However, this work does not explore this extensively.

3.3.5 Testing Sequence

While previous sections contained brief, interspersed descriptions of the testing sequence, this section provides a comprehensive overview of a general testing sequence. Figure 3.4 provides a graphical representation of a typical timing sequence for a sample four-second test duration. The exact timing sequence was subject to adjustments depending on the exact requirements for a given experiment. The test duration is defined based on the fuel-on time, which ranges from two to

five seconds throughout this work. In Figure 3.4, the flow of oxidizer and fuel are blue and red, respectively. Meanwhile, ignition events are orange, and the data collection is green. Both the RDC and afterburner (AB) air flowed the entire test duration, including after RDC fuel ceased. The additional airflow ensured the hot products were properly exhausted to limit the system's heating. The AB spark plug and pre-detonator started firing before introducing the RDC fuel to mitigate the possibility of fuel accumulation before ignition. In the case of the pre-detonator, it continued to fire at 6 Hz for one second into the fuel-on portion of the run. The afterburner remained lit 0.5 s after fuel shut-off to accommodate the lag between the ball valve closing and the last fuel injection into the RDC. The start of the RDC portion is denoted by t_0 while the end of the RDC fuel is indicated by t_f. Surrounding the RDC fuel-on portion was the high-speed data acquisition, which started one second before t_0 and ended one second after t_f to capture the whole transient nature of the system.

3.4 Measurements

Various measurements were taken within the RDC during the course of this work, with different studies requiring different instrumentation. The measurements presented here are those directly related to the analysis presented later instead of a comprehensive list of all measurements taken.

3.4.1 Channel and Plenum Pressure Measurements

Various pressure transducers were used throughout testing to characterize the RDC flowfield in the plenums and channel. The response time of an individual pressure transducer determines whether the measurement is categorized as low-speed or high-speed. One such low-speed transducer, a TE U5244-000005-200PA, was placed at the base of the air plenum, which was nominally 62.8 mm (2.47 in) upstream of the inlet mid-plane. To avoid being influenced by one of the six jets of air from the discrete injection into the plenum, this azimuthal location of this measurement bisected the arc connecting adjacent jets. In other words, there was a 30° angular separation between this measurement and the adjacent air injection ports. A TE U5244-000005-200PA was also placed at the base of the fuel plenum to provide a similar measure of the static pressure in the fuel plenum. Fuel enters the plenum through six discrete streams like the air; thus, the fuel plenum measurement also bisected the arc connecting adjacent jets to avoid the expansion associated with jets.

Additionally, along the outer wall were flush-mounted CTAP measurements that spanned axially from the air plenum to the exit plane of the combustor, all at the same azimuthal location. A CTAP is a long, small tube connected to a pressure transducer, and the tube dampens out the dynamic components of the flow, which are prevalent in the highly turbulent and unsteady flow of a RDC

[169, 120]. Here, the CTAPs were 1.59 mm (1/16 in) steel tubes with an inner diameter of 1 mm (0.040 in), and they were approximately 1 m (39 in) long. TE U5244-000005-200PA transducers measured the pressure at the end of the tube. In total, this work used 17 CTAPs along the outer wall. The low sampling rate of all these specific pressure transducers, 200 Hz, was significantly less than the detonation frequency, which was on the order of several kHz. As such, the under-sampling resulted in the measurements being effectively time-averaged static pressure measurements.

This work also utilized several high-speed pressure measurements to resolve the dynamics of the system and measure the pressure across the detonation wave(s). Flush-mounted to the outer wall, about 40.5 mm (1.60 in) upstream of the end of the air throat, in the air plenum was a Kulite XTL-HA-123G-190-17BARA. This high-speed measurement was in the same circumferential position as its low-speed counterpart; thus, the air injection streams do not significantly impact the measurement. Flush-mounted to the top of the fuel plenum was a Kulite XTEL-190L-250A, which was directly opposite of the low-speed pressure measurement at the base of the fuel plenum. Flush-mounted along the outer wall of the detonation channel were several water-cooled Kulite EWCTV-13-312-500A. These could be placed at four discrete axial positions in series (at the same azimuthal location). The exact axial positions depend on the combination of spacers utilized. Still, the nominal axial positions are 8.79 mm (0.346 in) upstream, 10.3 mm (0.404 in) downstream, 30.6 mm (1.20 in) downstream, and 50.9 mm (2.00 in) downstream of the end of the air inlet throat. In particular, the 12.7 mm axial position is effectively where the constant area portion of the detonation channel begins for AAI, which is likely the axial location of the base of the detonation wave(s). The high sampling frequency, 0.5 MHz, can partially resolve the pressure rise across the detonation wave. However, the sensor may not fully resolve the discontinuous (infinite response) pressure front due to the finite physical response time of the sensors.

3.4.2 Aft High-Speed Video

For most tests in this work, a high-speed camera recorded a chemiluminescence video of the annulus from the aft, which allowed for post-processing identification and tracking of the waves in the RDC. Optical access is provided through the connected exhaust system by a 178 mm (7.00 in) diameter fused quartz window with a thickness of 31.8 mm (1.25 in). The viewing aperture of the window was 159 mm (6.25 in) in diameter. The window was about 1.5 m (60 in) downstream from the end of the combustor in the elbow portion of the exhaust; see Figure 3.3. The central axis of the window was not coaxial, with the central axis of the RDC being about 11cm (4.5 in) higher than the RDC. Thus, the videos were taken at a slight angle, on the order of a few degrees, to have an unobstructed view of the entire annulus.

Two models of high-speed CMOS cameras were used across all the different experiments. A

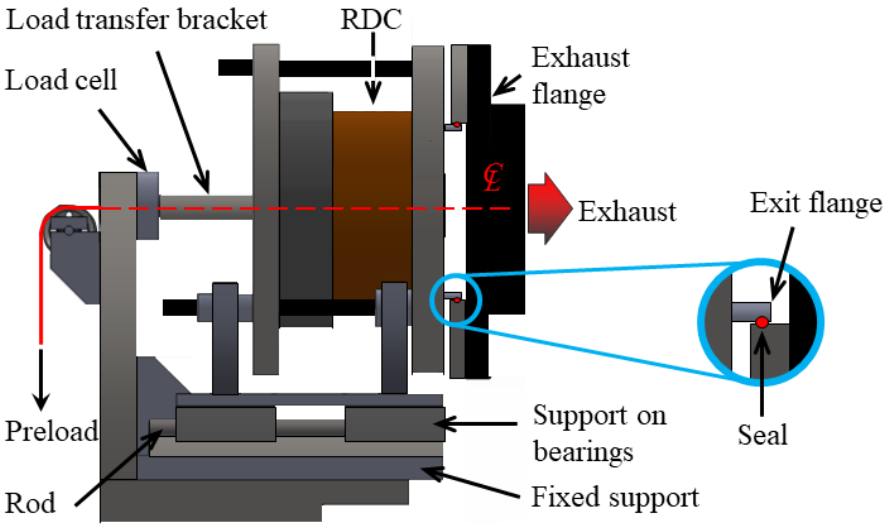

Figure 3.5: A schematic diagram of the assembled thrust stand integrated with a round RDC. Air/fuel feed lines and accessories are not shown for clarity. The radial seal for the exit flange is highlighted in the blue circle.

Phantom TMX5010 typically recorded the video with a resolution of 768x640 pixels covering the entire annulus, an exposure time of 10 μs, and a frame rate of 60k fps. The light was collected with a 105mm f/2.8 macro lens, with the focal length being within the detonation channel, just upstream of the exit plane. No filtering of the collected light occurred before being recorded. Given the nature of the mostly H_2/air combustion studied throughout this work and the spectral range of the camera, most of the detected light can be attributed to OH* chemiluminescence near 300 nm. The camera would have also measured the broadband visible light produced in a H_2/air flame. In several experiments, a Phantom v711 was utilized instead of the TMX5010. Videos taken with the v711 had a resolution of 288x280 pixels covering the entire annulus, an exposure time of 7 μs, and a frame rate of 55k fps. The v711 used the same lens, and the light was, again, not filtered. The onboard memory of the v711 was less than the TMX5010; thus, only about 1.4 s worth of video could be saved, unlike the TMX5010, which could save over five seconds worth of video at the described settings. The v711 recorded video during the last second of fuel-on time, while the TMX5010 recorded the entire duration of fuel-on times (up to five seconds). Both cameras began recording after receiving a TTL pulse from the DAQ, with the timing controlled by the LabVIEW program.

3.4.3 Thrust Measurement System

A diagram of the RDC on the thrust stand is shown in Figure 3.5. The RDC was mounted on a frame that sits and translates freely on a rail system. The point of deflection on the arrangement is co-linear to the combustor's axis and centered on the load cell axis. The load cell (EFN30-1KN-C20005) is a pancake type that measures tension and compression forces. The full scale is 1000 N, and the accuracy is 0.1% of the full scale, although, as will be seen in a later section, the uncertainty of the measured thrust is worse than this. In our setup, positive thrust production results in a compressive force acting upon the load cell. A pre-load is applied to the load cell through a pulley, causing the load cell to experience tension (the opposite direction of thrust). A 9.01 kg (19.9) mass hung from the pulley, which applies a force of 177 N (39.7 lbf). The voltage output of the load cell was recorded at 200 Hz by the existing data acquisition system.

While most reported RDCs on thrust stands exhaust to the ambient atmosphere, the facility at Michigan requires the RDC to be directly connected to a dedicated exhaust system, as indicated by the red arrow in the schematic. For safety concerns, the RDC must seal against the exhaust flange. The RDC originally sealed against the exhaust flange with a fiber-glass rope seal with silicon gasket material. However, not only was the instrumentation of the flange past this seal challenging but the RDC would de-mate during operation. This exhausted products to the room and increased the area over which pressure could exert a force upon the RDC. Thus, this work implemented a radial seal to seal the exhaust properly. Figure 3.5 in the highlighted circle highlights a schematic of the radial seal. On the RDC side, an extruded bore sits within the concentric downstream piece that is attached and seals to the exhaust flange. A graphite packing seal creates the interfaces between the exhaust piece and the bore connected to the RDC (red circle). Initially, a high-temperature o-ring was used instead of graphite, but the o-ring would temporarily "stick" on the bore during operation, causing erroneous thrust measurements. Graphite, in comparison, significantly reduces the friction between the two pieces. The radial seal did not significantly alter the gross thrust measurement, based upon comparisons between the theoretical gross thrust based on one-dimensional analysis and the results of non-reacting tests. However, the potential force contributions of the radial seal could not be readily quantified during a detonative operation where the elevated temperature may cause more seizing; however, since the friction would impede motion, the force is in the opposite direction of what the load cell would measure. Therefore, the reported values of the corrected thrust are conservative.

The base pressure acting upon surfaces at the exit plane is needed to convert the measured resultant force acting upon the load cell into the gross thrust (see Section 4.1). These surfaces are the face of the truncated nozzle on the center body and the exit flange used to seal the exhaust flange. Adding holes in the nozzle's bluff face and exit flange enabled flush-mounted CTAPs to be added. Thus, both surfaces were instrumented with many CTAPs to measure static pressure

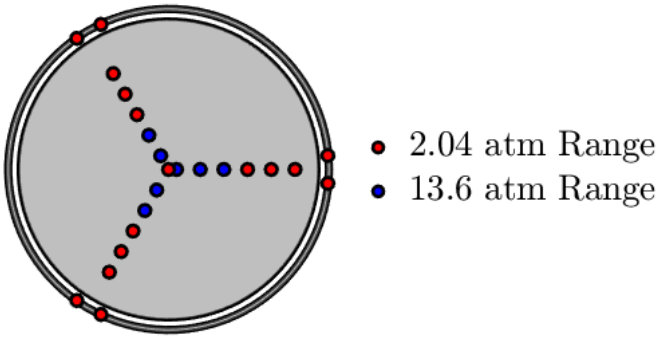

Figure 3.6: Diagram of instrumentation of center body (inner gray circle) and exit flange (outer gray ring) for base drag corrections. Red circles and blue circles denote pressure transducers with a range of 2.04 atm and 13.6 atm respectively.

distribution and subsequent base drag along the exit flange and center body. The CTAPs exited the RDC through the inner body. The locations of the CTAP placements along both surfaces are visualized in Figure 3.6 as red and blue circles. The gray areas represent the surface areas that the base drag acts upon, that being 169 cm^2 (26.2 in^2) and 11.5 cm^2 (1.79 in^2) for the center body and exit flange, respectively. The exit flange was explicitly designed to reduce the effective area as much as possible.

The center body contained 17 CTAPs, each at a different radial position (including the center) and three potential circumferential locations. The outer radial position, 6.16 cm (2.43 in), was determined based on machining considerations. Between the center of the nozzle and the aforementioned outermost radial location, the remaining pressure measurements were discretized along the radial direction to be equally spaced. The positions were then cyclically assigned to the circumferential legs as the radial location increased. Since pressure distribution along the truncated nozzle was unknown a priori, this process enabled the measurements to resolve potential radial and circumferential variations. Similar work has been done by Brophy et al. previously [114]. However, the present study utilized more measurements with a wider range of circumferential locations than the study from Brophy et al.

Similarly, the exit flange had six CTAPs along the protruded bore; see Figure 3.5. There were three pairs, each being at a different circumferential location. The measurement pairs were for redundancy. All six CTAPs had the same radial position due to size constraints, as the lip of the bore had a width of 2.35 mm (0.093 in), which is only slightly larger than the CTAP tubes. Instead of running the tube through the bore, which contained a 90° bend, passages were 3D printed into the bore that the CTAPs could externally connect to. A summary of the radial and circumferential

location of all the CTAPs is tabulated in Appendix F.

This work used two different pressure transducer models for the CTAPs along the nozzle: one with a range of 0-2.04 atm (TE U5244-000005-030PA) and one with a range of 0-13.6 atm (TE U5244-000005-200PA), due to a limited number of the 2.04 atm models. Brophy et al. previously reported nearly atmospheric pressure measurements along a truncated nozzle of a similar rig [114]; thus, the smaller range of the 2.04 atm sensors was sufficient to measure the theorized base pressures. In general, the 2.04 atm transducers had overall greater accuracy than the 13.6 atm as the noise typically scales with the full scale. Thus, in subsequent plots, these sensors will have larger error bars. In Figure 3.6, red circles are for the 2.04 atm transducers, while the blue circles are for the 13.6 atm transducers. All six CTAPs along the exit flange used the 2.04 atm transducers, while ten selective CTAPs along the center body employed the 2.04 atm transducers. Other than the center, which had a 2.04 atm transducer, the sensor positions with the smallest radial locations had the 13.6 atm transducers since those radial locations corresponded to the smallest effective areas. Appendix F provides a table of the transducer for each location for reference.

3.5 Sensor Calibration and Uncertainty

One of the primary contributions to the RDC literature from this work is a detailed uncertainty analysis of the pressure gain metric, given in Chapter 5. The uncertainty in individual measurements/sensors was required to perform such an uncertainty analysis. This section supplies the details of this process.

3.5.1 Thrust System Uncertainty

A linear calibration is used for all experimental measurements to convert the output voltage to the unit of measure. The load cell was calibrated statically by applying loads of known weight and recording the output voltage of the load cell (1000 samples at each load weight). This calibration process was repeated over ten times to provide a range of linear calibrations for the load cell. The pressure sensors on the RDC were calibrated *in-situ* by conducting static calibration by manually pressurizing the combustor over a range of pressure values (from atmospheric pressure to 2.75 atm) and acquiring 1000 pressure samples at each discrete pressure. The linear calibration was computed from the discrete points using the least-squares method, and the calibration parameters (slope m and intercept b) for some of the critical measurements are shown in Table 3.3. The load cell output is labeled as F_{L}, while the pressures measured on the nozzle and exit flange are p_{cb} and p_{fl}, respectively. Table 3.3 only reports a single pressure transducer for p_{cb} and p_{fl}; however, these values are representative of the other transducers. The pre-load applied to the load cell is the cause

Quantity	m [V^{-1}]	b [–]	δm [V^{-1}]	δb, [–]	δV [V]
F_L	217 N	-197 N	1.56 N	4.90 N	6.12×10^{-2}
p_{cb} (2.04 atm)	0.515 atm	-0.507 atm	5.49×10^{-4} atm	2.19×10^{-3} atm	4.06×10^{-3}
p_{cb} (13.6 atm)	3.44 atm	-3.44 atm	3.22×10^{-3} atm	4.65×10^{-3} atm	5.61×10^{-4}
p_{fl}	0.514 atm	-0.507 atm	5.40×10^{-4} atm	2.16×10^{-3} atm	5.08×10^{-3}
p_3	3.42 atm	-3.41 atm	6.39×10^{-3} atm	9.21×10^{-3} atm	1.15×10^{-2}
p_8	3.42 atm	-3.39 atm	7.75×10^{-3} atm	1.11×10^{-2} atm	1.39×10^{-2}

Table 3.3: Linear calibration and calibration uncertainties of key measurements used in this work.

of the negative intercept, indicating that the pre-load extends the range of measurable compressive loads (thrust).

The sources of uncertainty in the measurements come from the uncertainty in the linear fit parameters (for slope m and intercept b: δm and δb, respectively), as well as uncertainty in the measured voltage (δV) from the DAQs and electrical noise. For a linear calibration constructed from a number N of samples of a measured voltage V, with a slope m and an intercept b, the total uncertainty is:

$$\delta y^2 = \left(\frac{\partial y}{\partial m}\delta m\right)^2 + \left(\frac{\partial y}{\partial V}\delta V\right)^2 + \left(\frac{\partial y}{\partial b}\delta b\right)^2 \tag{3.2}$$

which can be simplified to:

$$\delta y^2 = (V\delta m)^2 + (m\delta V)^2 + (\delta b)^2 \tag{3.3}$$

This work assumes that the measurements follow a normal distribution centered on the "true" value to determine the uncertainty in the linear calibration parameters. The best estimate for standard deviation (σ) in the measured y, computed from the linear calibration, can be shown to be [181]:

$$\sigma_y = \sqrt{\frac{1}{N-2}\sum_{i=1}^{N}(y_i - mV_i - b)^2} \tag{3.4}$$

The above equation is effectively a measure of the variation of the y estimated from the linear calibration ($m_i + b$) and the measured y (y_i). Thus, this uncertainty only applies when independent measures of x and y are made (i.e., during the calibration process). Only the x (which has the units of volts) is recorded during the experiment, necessitating using Eqn. 3.3 to find the uncertainty.

Lest-squares fitting of the calibration data provides the slope and intercept of the linear calibrations. Thus, the following equations give for the uncertainties in the parameters based on Eqn. 3.4

and the least-squares fitting equations [181]:

$$\sigma_b = \sigma_y \sqrt{\frac{\sum_{i=1}^{N}(V_i^2)}{\Delta}} \tag{3.5}$$

$$\sigma_m = \sigma_y \sqrt{\frac{N}{\Delta}} \tag{3.6}$$

where Δ is:

$$\Delta = N \sum_{i=1}^{N}(V_i^2) - \left(\sum_{i=1}^{N} V_i\right)^2 \tag{3.7}$$

The uncertainties above are derived assuming a standard deviation from a normal distribution of errors, which only allows one to have a 68% confidence interval. However, this work considers 95% confidence intervals (a z-score of 1.96). Thus,

$$\delta m = 1.96\sigma_m \tag{3.8}$$

Table 3.3 also shows the uncertainties in linear calibration parameters for the load cell and pressure transducers. Similarly, the uncertainties of all individual pressure transducers used along the nozzle and exit flange are visualized in Figures 3.7a and 3.7b, respectively. The applied voltage, 1.5 V, is representative of voltages during testing. The 13.6 atm pressure transducers resulted in larger uncertainties at lower radial locations than the 2.04 atm transducers (see Figure 3.6). In general, the transducers with a range of 2.04 atm have overall lower uncertainty (about 0.002 atm compared to 0.005 atm) in the measurements due to the reduced full-scale. Some 13.6 atm sensors had uncertainties comparable to those with the 2.04 atm range, suggesting variability between sensors. Chapter 5 discusses that placing the sensors with larger uncertainties at lower radial locations mitigates their contribution to the computed drag acting on the nozzle. Both sets of sensors had a combined uncertainty that is less than 0.2% of the full scale.

3.5.2 Flow Rate Uncertainty

This work studies several parametric studies of different combinations of air mass flow rate, $\dot{m}_\mathrm{a}$ and equivalence ratio, ϕ, for H_2/air operation. However, instead of reporting the air mass flow rate, air mass flux defined relative to the throat area of the air inlet ($A_{3.1}$) is reported.

$$\dot{m}''_\mathrm{a} = \dot{m}_\mathrm{a}/A_{3.1} \tag{3.9}$$

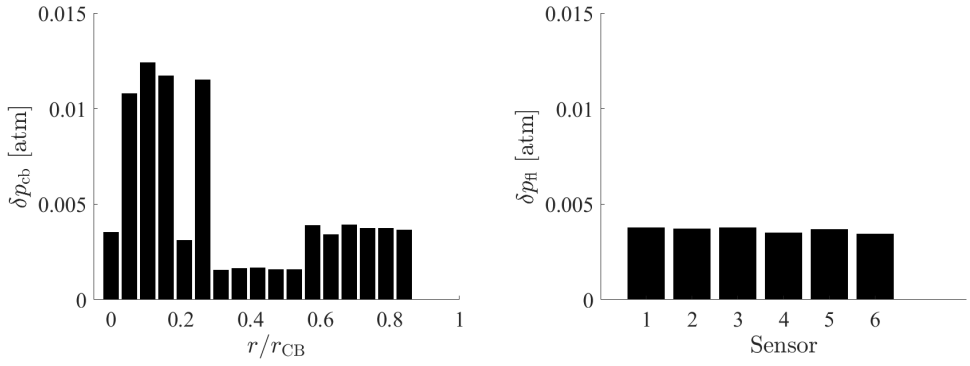

Figure 3.7: Uncertainty in pressure measurements on the a) center body (truncated nozzle) and b) exit flange.

This work reports mass flux in favor of mass flow rate because Chacon et al. observed that sustained detonation wave propagation scales better with mass flux than mass flow rate [176]. Mass flux also better captures the changes in specific properties as the air inlet is made more open (increasing the area) [47].

The random uncertainty in the mass flux and equivalence ratio comes from the uncertainty in the mass flow rates of air and fuel caused by the pressure and temperature measurements according to,

$$(\delta\dot{m}_{\mathrm{o}})^2 = \left(\frac{\partial\dot{m}_{\mathrm{o}}}{\partial p_{\mathrm{t,o}}}\delta p_{\mathrm{t,o}}\right)^2 + \left(\frac{\partial\dot{m}_{\mathrm{o}}}{\partial T_{\mathrm{t,o}}}\delta T_{\mathrm{t,o}}\right)^2 \tag{3.10}$$

$$= \left(\frac{\dot{m}_{\mathrm{o}}}{p_{\mathrm{t,o}}}\delta p_{\mathrm{t,o}}\right)^2 + \left(\frac{-\dot{m}_{\mathrm{o}}}{2T_{\mathrm{t,o}}}\delta T_{\mathrm{t,o}}\right)^2 \tag{3.11}$$

The above equation arises from the partial derivatives of Eqn. 3.1. These uncertainties then propagate into the air mass flux and equivalence ratio. The pressure transducer and thermocouple upstream of the orifices could not be calibrated like the measurements on the engine. Instead, this work arbitrarily assumes that $\delta p_{\mathrm{t,o}}$ is 1 psi (which is 0.2% of the full scale) and $\delta T_{\mathrm{t,o}}$ is 5 K (comparable to the electrical noise observed). This results in the error bars on the mass flux ranging from ±1-4% of the nominal flux values, with the lower fluxes having the larger relative uncertainty. Similarly, the equivalence ratio has error bars ranging from ±2-4% of the nominal equivalence ratio values, with the lower fluxes having the larger relative uncertainty.

Several sources of systematic error exist for the air mass flux and equivalence ratio. For the air mass flux, there is a systematic error potentially caused by the orifice area (A_{o}), the orifice discharge coefficient (C_{d}), and the area of the air inlet throat ($A_{3.1}$). Likewise, the area and discharge

coefficient of the choked orifices on the air and fuel delivery systems impact the equivalence ratio. This work neglected the uncertainty in discharge coefficients. While the manufacturers give the machining tolerances for the diameters of the orifices, the exact dimensions remain unknown. This study assumes that the diameter follows a uniform distribution given by the machining tolerances to account for the unknown dimension. The machining tolerances used to generate the distributions are $\pm 12.7\mu$m ($\pm$0.0005in) on the choked orifice diameter, $\pm$ 0.127mm ($\pm$0.005in) on the air inlet outer diameter, and $\pm$0.051mm ($\pm$0.002in) on the air inlet inner diameter. A uniform distribution requires the least amount of prior knowledge and will maximize the uncertainty (information entropy) [182], making it ideal for this purpose. A Monte-Carlo simulation [183] of 100,000 samples randomly sampled the uniform distributions and calculated the corresponding areas for the sampled diameters. Doing so generates the Probability Density Function (PDF) of the areas according to the assumed uniform distributions. A Monte-Carlo simulation is beneficial for the case where two independent distributions are combined into a single distribution, as in the case of finding the air inlet area, making it simpler and faster than analytically deriving the possible errors. The systematic uncertainty is calculated based on a 95% confidence interval from the mean of the resultant PDF. For the choked orifice, the systematic uncertainty in the area leads to an uncertainty of about $\pm$0.1% the nominal, measured flow rate. For the air inlet, the possible range of areas is $\pm$4.5% the nominal area value; this directly translates to a potential $\pm$4.5% systematic change in the reported mass fluxes which is larger than the random uncertainty for the air mass flux. The importance of the systematic uncertainties will diminish with larger air inlet throat areas by having more open throats or increasing the overall scale of the RDC. Finally, a similar process is used throughout this work to evaluate the systematic uncertainty caused by machining tolerances.

CHAPTER 4

Improving Base-Drag Corrections for Rotating Detonation Combustor Gross Thrust Measurements

4.1 Introduction

As discussed in Section 2.4.1.2, the gross thrust output is necessary to determine the EAP. The gross thrust is the combination of the axial momentum of mass leaving the combustor at the exit state and the sum of the pressure forces acting upon the cross-sectional area of the annulus at the exit plane (state ⑧):

$$F_{\mathrm{G}} = (\dot{m}_{\mathrm{f}} + \dot{m}_{\mathrm{a}})u_{8,z} + (p_8 - p_\infty)A_8 \tag{4.1}$$

Any momentum in the radial or circumferential direction does not produce usable thrust and thus does not contribute to F_{G}. Such momentum is effectively a loss mechanism, although this work does not evaluate its impact.

However, the reactive force measured by the load cell (F_{L}) differs from the gross thrust produced by the RDC (F_{G}) due to additional pressure forces acting upon the RDC. The CV analysis presented in Figure 4.1 is employed to correct for the other contributions to the measured thrust. The combustor is symmetric about the centerline axis. The CV is the dashed red line, and the axis of symmetry of the combustor is shown on the right by the black dash-dot line. The different forces (pressure and momentum flux) acting upon the surfaces of the control volume that contribute to the axial momentum balance are displayed. At the same time, the black arrow indicates the resultant force (F_{L}). The system injects air and fuel radially; thus, there is no incoming axial momentum. Ambient pressure acts upon the exposed bottom of the combustor. This ambient pressure (p_∞) is assumed to be constant during the test duration. On the outflow portion of the device, there is the momentum flux of the hot products and pressure forces around the annulus (F_{G}), as well as the base drag generated by the pressure acting on the end face of the center body (p_{cb}) and on the outermost

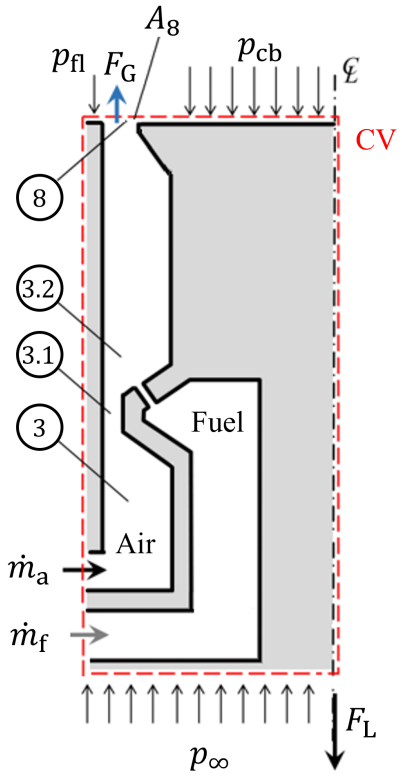

Figure 4.1: Definition of control volume and conditions at boundaries used to determine the thrust produced by the combustor. The truncated converging nozzle is shown.

flange (p_{fl}). The overall axial momentum balance on the CV is then:

$$F_L = F_G + \iint_{A_{cb}} \Delta p_{cb} dA + \iint_{A_{fl}} \Delta p_{fl} dA \tag{4.2}$$

The pressure force terms are expressed with gauge pressures, i.e., relative to the ambient value ($\Delta p = p - p_\infty$) to account for the ambient pressure acting on the exposed bottom surface of the combustor. Re-arranging to solve for the gross thrust results in:

$$F_G = F_L - \iint_{A_{cb}} \Delta p_{cb} dA - \iint_{A_{fl}} \Delta p_{fl} dA \tag{4.3}$$

$$= F_L - D_{cb} - D_{fl} \tag{4.4}$$

The application of Eqn. 4.3 to the instantaneous measurements of the different quantities generates an estimate of the instantaneous gross thrust ($F_G(t)$).

The need to measure the base drag is evident from Eqn. 4.3; thus, before discussing the RDC gross thrust and subsequent total pressure measurements, a detailed discussion of the base drag

acting upon bluff surfaces is necessary. This chapter quantifies and analyzes the base drag, while Chapter 5 focuses on the gross thrust and pressure gain measurements. The following discussion is an effort to increase the accuracy of the base drag measurements, specifically those acting upon the truncated nozzle. This study used seventeen pressure measurements, CTAPs, along the truncated nozzle to provide a well-resolved radial and circumferential pressure distribution, a first for RDC literature. The measurements indicate that the typical axisymmetric assumption is invalid, and the error from not performing a two-dimensional integration is estimated. Due to physical limitations, one typically cannot have a pressure measurement near the edge of the truncated nozzle, and this work explores how to address this shortcoming when using the standard Newton-Cotes integration methods. Finally, the high fidelity in the radial distribution enabled an experimental comparison between the Newton-Cotes and Gauss-Kronrod integration techniques proposed by Fievisohn et al. [129]. The combination of these analyses and accounting for the uncertainty in the individual pressure sensors provides a detailed uncertainty analysis of the base drag correction. Based on the observations made in this study and the detailed uncertainty analysis results, this study offers recommendations to improve future base drag measurements that are critical when dealing with truncated nozzles for RDC gross thrust measurements. Specifically, the recommendations maximize the accuracy and precision of the base drag measurements with the constraint of using as few measurements as possible since such measurements are costly and take up space in the experiment.

4.2 Geometry and Tested Operating Conditions

The data collected for this experiment was on the AAI injector with the 50% converging nozzle. The nominal combustor length of 102 mm corresponds to Configuration B in Tab. 3.2. Section 3.2 gives more details about the geometry and configurations. This geometry combination is the baseline against which future chapters with different geometry changes compare.

This study employed a parametric study of different values for the air mass flux, $\dot{m}''_a$, and equivalence ratio, ϕ, with hydrogen/air operation. Figure 4.2 shows the conditions tested for this work. As mentioned, the successful detonative operation scales better with air mass flux evaluated at the inlet throat conditions than with the flow rate [176]. Thus, the air mass flux is the ratio of the independently controlled, prescribed air mass flow rate and the geometric air inlet throat ($\dot{m}''_a = \dot{m}_a / A_{3.1}$). Each case considered in this work had sustained detonative operation. The number of detonation waves, or multiplicity (N_D), is indicated in Figure 4.2 by the marker shapes. One ($N_D = 1$) and two co-rotating ($N_D = 2$) wave operations are denoted with circles and triangles, respectively. While two co-rotating waves occurred in most test cases, several tests at low mass fluxes and equivalence ratios exhibited only one wave, highlighted in Figure 4.2 with the gray

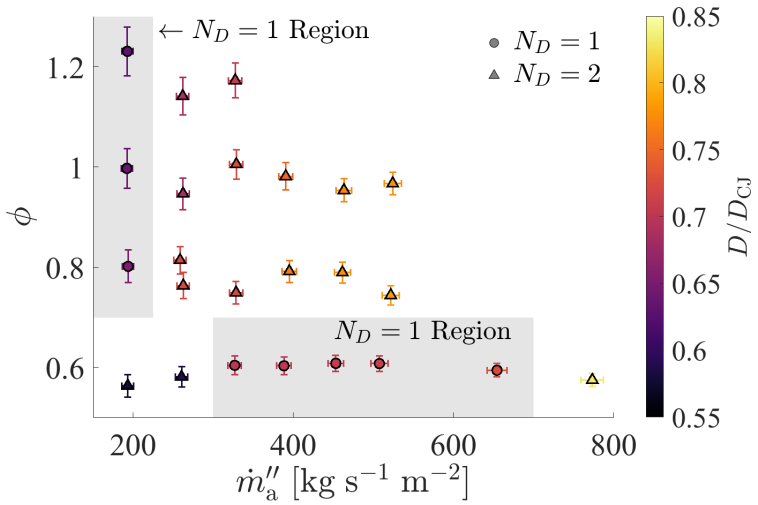

Figure 4.2: Summary of test conditions tested in this study. The number of detonation waves and their normalized wave speed are given by marker shape and coloration, respectively.

boxes. Figure 4.2 also gives the detonation wave speed (D) normalized by the ideal CJ velocity (D_{CJ}) as the color of the markers. This work will give detonation velocities in favor of frequencies such that the results are independent of the specific geometry and chemistry. Many of the tests had normalized velocities that were 70-80% of D_{CJ}, with the primary exceptions being the tests with mass fluxes of 193 and 260 kg s^{-1} m^{-2} and $\phi = 0.6$. The normalized wave speeds during these tests were approximately 57%, comparable to acoustic speed in the hot combustion products. These two nearly-acoustic detonation waves contrast the surrounding conditions.

Through the parametric study, the pressure and the gas velocities at the exit of the RDC annulus can be varied. Since the downstream ambient pressure remains the same, this will generate different expansion processes for the different test points, creating varying base drag amounts. The magnitude of the pressures measured at each sensor location will inevitably differ from case to case, and the spatial distribution acting on the surface of the pressure field may also change with the different flow conditions. Additionally, the parametric study examined the evolution of performance measurements and the relative uncertainties in those measurements, as will be seen in Chapter 5.

4.3 Sample Pressure Measurements

To provide contextualization of the base drag calculations that are presented later in this work, some representative measured pressure distributions (i.e., $p(r, \theta)$) along the center-body are provided in Figure 4.3. The test conditions for the shown cases were: $\dot{m}''_a = 330$ kg s^{-1} m^{-2} and $\phi = 0.55$,

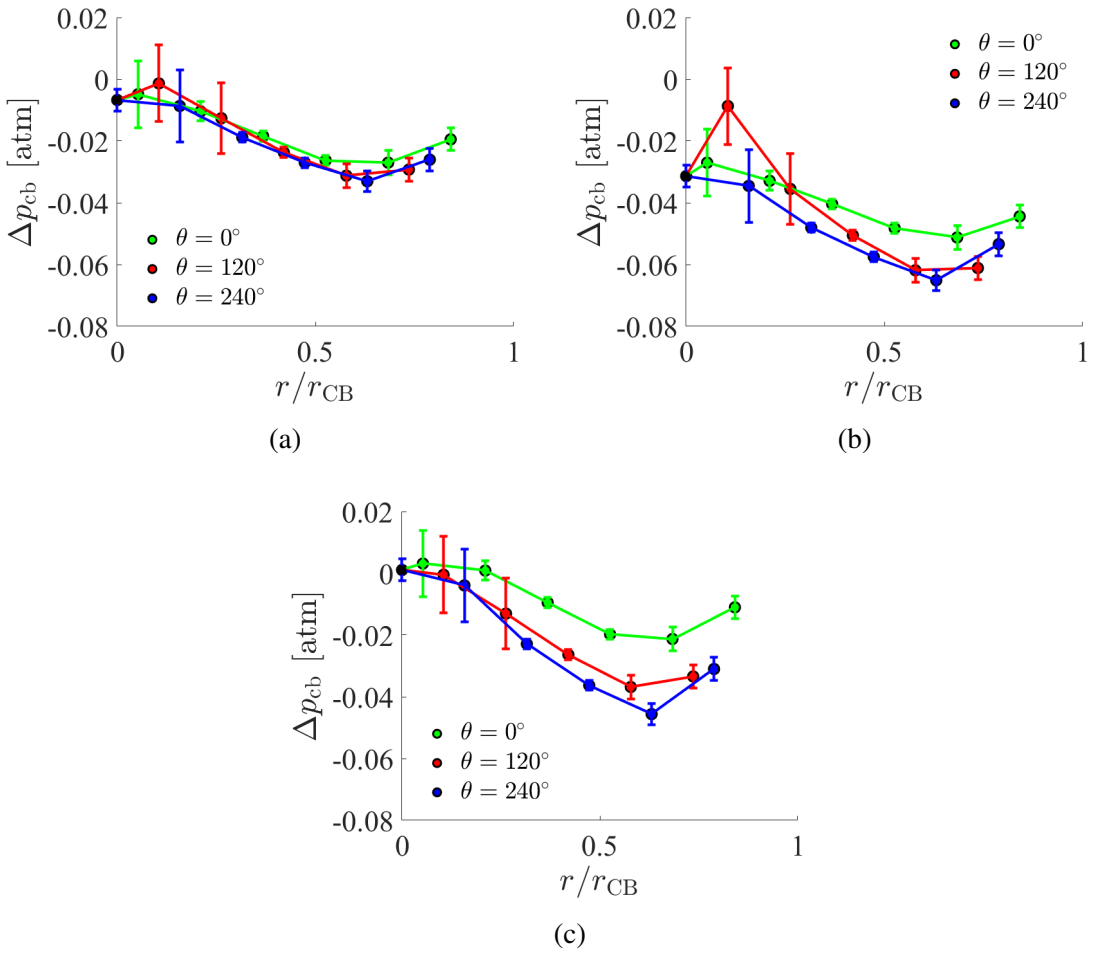

Figure 4.3: Pressure at different radial and circumferential locations for a) $\dot{m}''_{\mathrm{a}} = 330$ kg s^{-1} m^{-2} and $\phi = 0.55$ b) $\dot{m}''_{\mathrm{a}} = 329$ kg s^{-1} m^{-2} and $\phi = 1.01$ c) $\dot{m}''_{\mathrm{a}} = 507$ kg s^{-1} m^{-2} and $\phi = 0.61$. An asymmetry is observable in most cases.

$\dot{m}''_{\mathrm{a}} = 329$ kg s^{-1} m^{-2} and $\phi = 1.01$, and $\dot{m}''_{\mathrm{a}} = 507$ kg s^{-1} m^{-2} and $\phi = 0.61$ for Figures 4.3a, 4.3b, and 4.3c respectively. The pressures in Figure 4.3 are average pressures relative to ambient conditions during the last 0.5s of fuel-on operation (Δp). The symbol color gives the sensor's circumferential location (θ), while the central point ($r = 0$) is a black dot, indicating it does not belong to any circumferential locations. The x-axis gives the radial locations, normalized by the radius of the edge of the truncated nozzle attached to the center body (r_{CB}), which is 7.33 cm (2.89 in). The lines connecting the data points are to guide the reader. Focusing on the radial variations, a qualitative general shape is observable for the different circumferential locations. Starting from the center, a small increase in pressure occurs until about 1cm ($0.14r_{\mathrm{CB}}$) away from the center. Afterward, the pressure decreases below the central pressure, reaching its lowest point at about 5cm ($0.68r_{\mathrm{CB}}$) from the center. Finally, the pressure increases towards the elevated pressures seen

at the exit of the annulus. The pressure at the exit of the annulus is always greater than or equal to ambient conditions, which may explain why the measured gauge pressure increases significantly as r approaches r_{CB}. Overall, this profile resembles a cubic polynomial in relation to r and is similar to previous computational work [122].

While the radial shapes are similar for all the results presented in Figure 4.3, the circumferential distribution varies. Specifically, Figure 4.3a appears to be axis-symmetric in that the radial distributions of the different colors seem to overlap mostly, while Figures 4.3b and 4.3c do not share in this symmetry. For instance, the radial profiles at $\theta = 0°$ (green line) and $\theta = 240°$ have no overlap after the measurement point at 1.16 cm ($0.16r_{\mathrm{CB}}$). The spread (i.e., minimal overlap) in the three profiles greater than the error bars suggests an asymmetry of the pressure field. The error bars convey the individual sensor's random uncertainty as calculated from the sensor calibrations. A small subset of conditions tested had the axis-symmetric pressure field similar to Figure 4.3a. The cause for the asymmetry is unknown, although minor imperfections in the geometry, i.e., non-concentric annulus, differences in fuel injectors, etc., might be the cause. The lack of axial symmetry is especially important with respect to base drag calculations since, typically, the pressure is integrated only in the radial direction by assuming an axis-symmetric profile [115]. Section 4.4.3 will discuss the impact of this assumption in further detail later.

4.4 Numerical Integration for the Base Drag

The base drag acting upon the center-body (D_{cb}) or the exit flange (D_{fl}) is the integration of the pressure distribution over the area of either the nozzle or the flange. For instance, consider D_{cb},

$$D_{\mathrm{cb}} = \iint_{A_{\mathrm{cb}}} \Delta p_{\mathrm{cb}}(r,\theta)\mathrm{d}A \tag{4.5}$$

$$= \int_0^{2\pi} \int_{R_{\mathrm{cb},1}}^{R_{\mathrm{cb},2}} r\Delta p_{\mathrm{cb}}(r,\theta)\mathrm{d}r\mathrm{d}\theta \tag{4.6}$$

where $p_{\mathrm{cb}}(r,\theta)$ is unknown a priori and Δp_{cb} is the gauge pressure ($\Delta p_{\mathrm{cb}} = p_{\mathrm{cb}} - p_\infty$). Discrete pressure measurements can be made at n locations and numerically integrated to approximate the integral in the following manner,

$$\iint_A \Delta p_{\mathrm{cb}}(r,\theta)\mathrm{d}A \approx \sum_{i=1}^{n} w_i \Delta p_{\mathrm{cb}}(r_i,\theta_i) \tag{4.7}$$

In the above equation, w_i are the weights assigned to the i-th pressure measurement at location (r_i,θ_i). Thus, the individual pressure measurements are the nodes of the numerical integration.

Imposing an axisymmetric assumption (i.e., $p \neq f(\theta)$), a further simplification is possible,

$$D_{\text{cb}} \approx 2\pi \sum_{i=1}^{n} w_i \Delta p_{\text{cb}}(r_i) \tag{4.8}$$

As demonstrated in the previous section, the axisymmetric assumption is invalid for some conditions tested. Due to this, this study will evaluate the base drag with and without the symmetric simplification to examine the impact of the assumption later in Section 4.4.3. Furthermore, the determination of the weights is method dependent (i.e., Newton-Cotes, Gaussian quadrature, etc.) and will also be discussed in Sections 4.4.1 and 4.4.2. While this process applies to both base drags, the focus here will be on the center body since the effective area is nearly 15 times larger than the exit flange by design. Thus, the pressure field will likely vary more along the center body, magnifying the impact of each pressure measurement and the numerical integration.

4.4.1 Newton-Cotes Method

This work initially chose the locations of the pressure measurements for the base drag corrections without a specific numerical integration scheme in mind. A Newton-Cotes integration method is most suitable since the measurements are at pre-described locations (nodes). Typically, in literature, to find the base drag from CTAP measurements, a midpoint rule (1 point scheme) is utilized where the effective area (weight) of the pressure measurement (node) is multiplied by the pressure and then summed over [115]. The effective areas are concentric circles that bisect the radial distance between the nodes. Formally, the weights from this midpoint rule are,

$$w_i = \begin{cases} 2\pi \left(\frac{r_{i+1}}{2}\right)^2 & i = 1 \\ 2\pi \left[\left(\frac{r_i + r_{i+1}}{2}\right)^2 - \left(\frac{r_i + r_{i-1}}{2}\right)^2\right] & i = 2, ..., n-1 \\ 2\pi \left[r_{\text{CB}}^2 - \left(\frac{r_i + r_{i-1}}{2}\right)^2\right] & i = n \end{cases} \tag{4.9}$$

The normalized weights of the nodes are shown in Figure 4.4 to illustrate the relative importance of the individual measurements in the midpoint rule, with a value of 1 on the x-axis being the edge of the nozzle. A normalized weight is the effective area divided by the total area of the truncated nozzle. In other words, the normalized weight is the individual weight divided by the summation of the weights. The largest integration weights are near the edge due to the r term in the integrand of Eq. 4.6. While there is a linear increase in weights with r, the last data point is much higher than the others by having a normalized weight of 0.33. In other words, 1/3 of the base drag calculation comes from a single pressure measurement, which requires further evaluation.

One of the most problematic aspects of measuring base drag on a truncated nozzle and/or cap

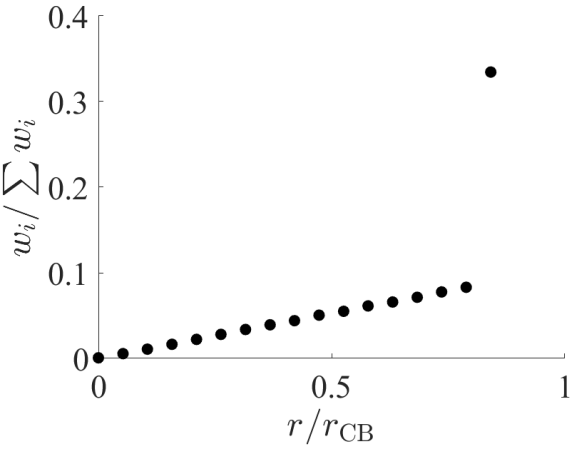

Figure 4.4: Normalized weights of nodes used for midpoint rule. The last effective area extends to the edge of the center body.

is getting a measurement at the outermost edge of the nozzle. Due to physical constraints, this measurement is impractical, which ultimately causes a significantly larger weighting on the last node. Furthermore, since the pressure at the edge is unknown, an assumption is necessary to close the integral. Consider the radial pressure distribution shown in Figure 4.5, the same data presented in Figure 4.3a. For simplicity, this specific test condition, $\dot{m}''_{\mathrm{a}} = 330$ kg s^{-1} m^{-2} and $\phi = 0.55$, was chosen for the axisymmetric pressure field. This study considers two scenarios to bound the range of solutions. First, the pressure at the edge is the same as the measurement at the outermost position (red triangle). Physical intuition leads to the belief that the pressure would not drop moving towards the edge, making this the lower bound of possible pressures. This scenario is equivalent to applying the 0.33 weight seen in Figure 4.4 to the outermost measurement point. The second scenario estimates the pressure by extrapolating the measured pressure distribution (blue triangle). This extrapolation is performed by applying a cubic fit to the data and computing the pressure at r_{CB} from that fit. This study chose a cubic fit since it resulted in near-unity R^2 values. The pressure at the exit plane of the annulus is greater than the pressure acting on the truncated nozzle; thus, the pressure close to the edge should increase. While this second scenario does not provide a true upper bound, it is the best estimation with the current instrumentation. The red triangle would increase the overall gross thrust compared to the blue triangle since a (more) negative gauge pressure acting upon the cap results in a positive increase in gross thrust. Thus, the extrapolated pressure provides a more conservative measure of thrust.

With an assumed edge pressure, the pressure is effectively "known" at 18 radial locations along the truncated nozzle, including the endpoints of integration, the center, and the edge. Again, for the sake of discussion, an axisymmetric assumption is applied for now, i.e., pressure is only a function of r. While the midpoint rule remains valid, a higher accuracy method is preferred since the

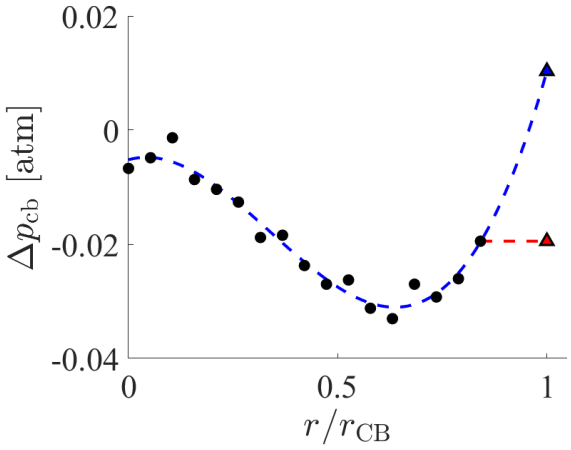

Figure 4.5: Nozzle edge pressure is either equivalent to the last measurement (red triangle) or from extrapolated cubic fit (blue triangle) of measurements (black circles). Case where $\dot{m}''_{\mathrm{a}} = 330$ kg s^{-1} m^{-2} and $\phi = 0.55$.

midpoint rule is only first-order accurate. However, implementing the 18-point method may result in instability in the numerical integration (i.e., Runge's phenomenon); thus, a composite method of the lower order is necessary. Therefore, to compute the base drag, a composite trapezoidal rule (two-point scheme), which is of order two accurate, is employed to integrate the pressure. Note that the spacing between the outermost CTAP and the edge pressure differs from the spacing between the remainder of the points, which is why this work does not use the more accurate Simpson's rule.

The results of the base drag calculation during the steady portion of the runs are shown in Figure 4.6a for all conditions considered in this work. The subscript "N" on D_{cb} indicates a Newton-Cotes method. The circles denote the base drag computed when the edge pressure is assumed to be equivalent to the outermost CTAP (see the red triangle in Figure 4.5). Meanwhile, the triangles are for the base drag with the extrapolated pressure (see the blue triangle in Figure 4.5). The color of the markers gives the equivalence ratio in this and the following figures. Since this work tested the equivalence ratio discretely at 0.2 increments, the interpretation of the color bar is as follows: black for ϕ =0.6, red for ϕ =0.8, green for ϕ =1.0, and blue for ϕ =1.2. The negative base drag causes an increase in gross thrust since the vacuum pulled on the truncated nozzle face would act on the engine in the opposite direction of the measured gross thrust. As anticipated, the base drag on the nozzle grows more positive with the extrapolated pressure compared to the constant edge pressure. Figure 4.6b highlights this difference between scenarios ($\Delta D_{\mathrm{cb,N}}$) by showing the change in gross thrust from using the extrapolated pressure over applying the last CTAP measurement over the area up to the edge.

$$\Delta D_{\mathrm{cb,N}} = D_{\mathrm{cb,N}}(\text{constant } p) - D_{\mathrm{cb,N}}(\text{extrap. } p) \tag{4.10}$$

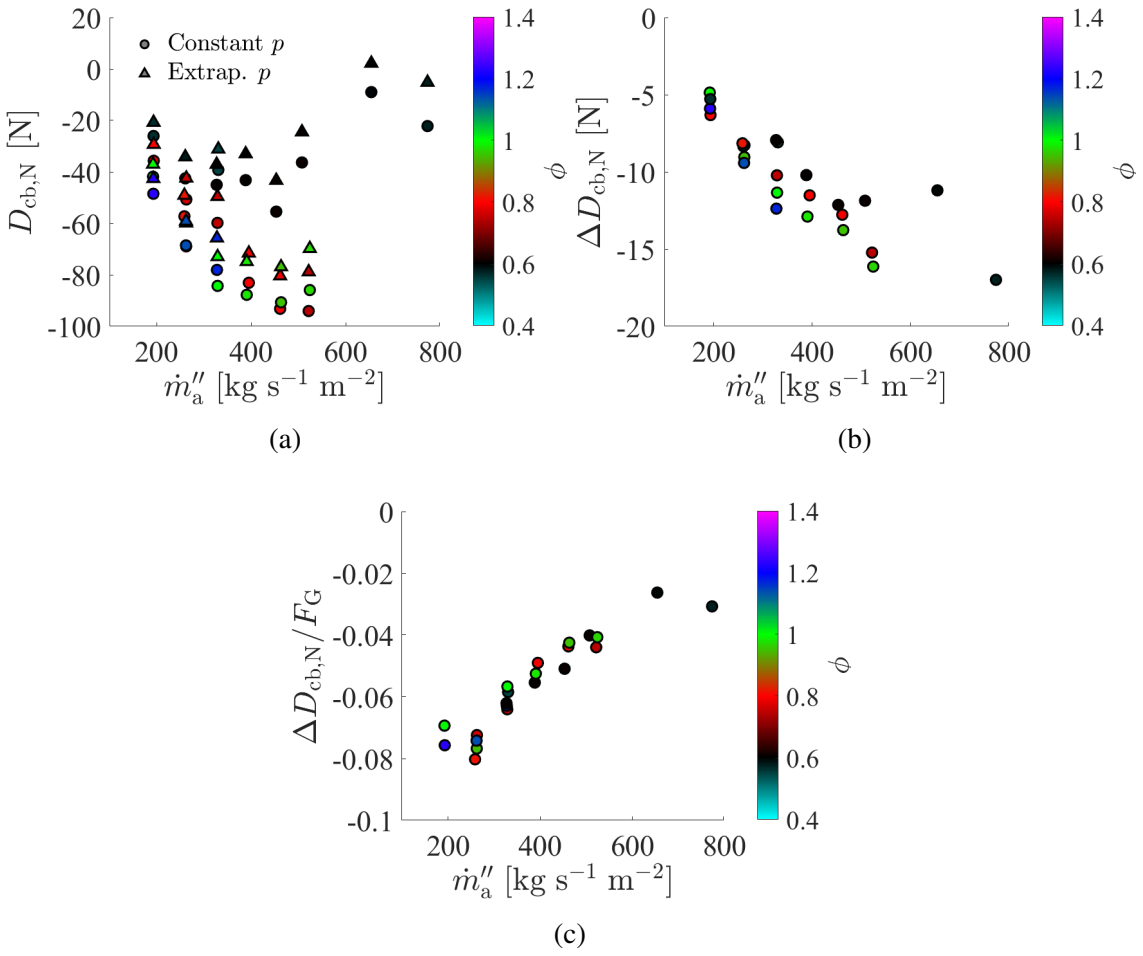

Figure 4.6: Computing the base drag with an edge pressure that is either a) constant or extrapolated gives b) different values that are c) contextualized against gross thrust.

Although the difference between the two scenarios grows with increasing flux, both capture the same overall trends. For now, this work takes the difference to be a measure of the uncertainty in the base drag solely from the edge pressure. Effectively, the uncertainty in the edge pressure is equivalent to the difference between the extrapolated pressure and outermost CTAP measurement. Figure 4.6c shows the importance of this relative to the gross thrust, where Section 5.2 in the following chapter reports the gross thrust measurements. The gross thrust values are preemptively used here to highlight the relative impact of this uncertainty. The impact of edge pressure is more important at the lowest flux, and the relative importance steadily decreases with increasing mass flux to about 3% of the gross thrust value, depending upon the equivalence ratio. Nevertheless, this is still non-negligible, highlighting the importance of edge pressure. Thus, to improve the numerical integration, either a CTAP measurements closer to the edge to limit extrapolation or a numerical integration method that does not utilize the edge pressure is needed.

4.4.2 Gauss-Kronrod Method

A Gauss-Kronrod quadrature scheme is an alternative means of numerical integration to lower the numerical error [116]. Unlike the Netwon-Cotes method used previously, which assigns weights to given locations, one solves the pressure measurements' location and weights before instrumentation in a Gauss-Kronrod scheme. The locations and weights come from systems of equations that enable the exact integration of polynomials of order $2n-1$, where n is the number of measurement points. The Kronrod extension allows for a higher order scheme ($3n+1$) by adding $n+1$ additional points to the pre-existing Gaussian scheme, where n is the number of points in the original Gaussian quadrature. While helpful in minimizing the number of pressure measurements necessary, the scheme requires assuming a polynomial shape, which can lead to errors without prior knowledge. Fievisohn et al. previously assumed the pressure distribution was a monic-polynomial [116]. Furthermore, unlike a fine discretization of the Newton-Cotes, the method cannot find the "true" functional form. In this section, this study compares a simulated Gauss-Kronrod scheme to the results of the Newton-Cotes integration.

Fievisohn et al. describe the process for determining the nodes and the weights, which is repeated here for clarity. A Gaussian scheme starts by finding a polynomial orthogonal to the weight function ($w(r)$) with n roots, where n is the number of desired points. Mathematical this is,

$$\int_a^b r^k w(r)\mathcal{P}_n(r)\mathrm{d}r = 0 \qquad \text{for } k = 0, 1, ..., n-1 \tag{4.11}$$

where $\mathcal{P}_n$ is a monic polynomial of degree n.

$$\mathcal{P}_n(r) = r^n + c_1 r^{n-1} + ... + c_{n-1} r^0 \tag{4.12}$$

Since this study applies the Gaussian scheme to Eqn, 4.6, the weight function within the integral in Eqn. 4.11 is the radial position ($w(r) = r$). Likewise, the integration bounds are the inner and outer radii ($a = R_1$ and $b = R_2$ respectively) as determined by the geometry. Thus, Eqn. 4.11 can be rewritten as,

$$\int_{R_1}^{R_2} r^{k+1}\mathcal{P}_n(r)\mathrm{d}r = 0 \qquad \text{for } k = 0, 1, ..., n-1 \tag{4.13}$$

The coefficients in the monic polynomial, i.e., $c_1, c_2, ..., c_{n-1}$ are determined by expanding Eqn. 4.13 and solving the resulting system of equations. Solving the system of equations finds the polynomial orthogonal to the weight function. The nodes of the Gaussian quadrature, r_i, are then the roots of the monic polynomial. Note that a Gaussian scheme will not have the nodes at either the integral bounds, making it an open scheme. Being an open scheme also alleviates one of the problems of the Newton-Cotes method, where the pressure at the edge can be a significant source

of uncertainty.

Once the nodes are determined, the weights of the Gaussian nodes, w_i, are needed. These are found by solving the following system of equations:

$$\int_{R_1}^{R_2} r^{k+1} dr = \sum_{i=1}^{n} w_i r_i^k \qquad \text{for } k = 0, 1, ..., n-1 \tag{4.14}$$

The resulting nodes (r_i) and weights (w_i) can then be used in Eqn. 4.8 to find the base drag.

$$D_{\text{cb,G}} \approx 2\pi \sum_{i=1}^{n} w_i \Delta p(r_i) \tag{4.15}$$

The sub-script "G" is appended to denote the Gaussian integration.

As stated previously, one can add a Kronrod extension to the Gaussian scheme by adding $n+1$ points and reusing the original nodes from the Gaussian scheme for a total of $2n+1$ nodes. The Kronrod extension enables a higher-order scheme of $3n-1$. Another benefit of this approach is that the difference between the higher and lower-order methods approximates the error associated with the numerical integration (ϵ).

$$\epsilon = |D_{\text{cb,K}} - D_{\text{cb,G}}| \tag{4.16}$$

where $D_{\text{cb,K}}$ is the base drag from the Gauss-Kronrod scheme and $D_{\text{cb,G}}$ is the base drag from the Gaussian scheme. While less accurate than a Gaussian scheme with $2n+1$ points, the error approximation is necessary for the error propagation for the thrust and subsequent PG measurements.

The process of determining the nodes of the Guass-Kronrod scheme is similar to the Gauss scheme.

$$\int_{R_1}^{R_2} r^{k+1} \mathcal{P}_n(r) \mathcal{P}^*_{n+1}(r) \mathrm{d}r = 0 \qquad \text{for } k = 0, 1, ..., n \tag{4.17}$$

where $\mathcal{P}_n(r)$ is the same monic polynomial solved for in Eqn. 4.13 and $\mathcal{P}^*_{n+1}(r)$ is the monic polynomial of order $n+1$ for the Kronrod extension. Since the original polynomial from Eqn. 4.13 is utilized the Gaussian nodes (x_i) are preserved. The additional nodes are the roots of $\mathcal{P}^*_{n+1}(r)$, and when combined with the x_i nodes from the Gaussian form $2n+1$ set of nodes denoted by x_j.

After solving the node locations for the Gauss-Kronrod scheme, the weights, w_j, come from the following system of equations,

$$\int_{R_1}^{R_2} r^{k+1} dr = \sum_{j=1}^{2n+1} w_j x_j^k \qquad \text{for } k = 0, 1, ..., n \tag{4.18}$$

r [cm]	r/r_{CB}	w_i [cm^2]	w_j [cm^2]
0.869	0.119	-	1.207
2.602	0.355	9.771	5.126
4.581	0.625	-	8.614
6.192	0.845	17.078	7.970
7.112	0.971	-	3.932

Table 4.1: Nodes and weights of Gauss-Kronrod scheme with $n = 2$ and $r_{CB} = 7.33$ cm.

During this study, the author created a Matlab function that performs the calculations for the nodes and weights using symbolic math for an arbitrary n, R_1, R_2. The Matlab function generated a Gauss-Kronrod scheme with the lower order method being of order 3 (2 points) and the higher order method being of order 7 (additional 3 points), similar to what was done by Fievisohn et al. [116]. The inner radius was 0, and the outer radius was $r_{CB} = 7.33$ cm. Table 4.1 lists the nodes and weights. While the x_i nodes are a subset of the x_j nodes, their associated weights w_i in the Gaussian are different than the weights (w_j) found in Eqn. 4.18. The differences are shown in Table 4.1. Note that the sum of the weights in either scheme is equivalent to the total area of the truncated nozzle (A_{cb}).

$$A_{cb} = 2\pi \sum_{i=1}^{n} w_i \tag{4.19}$$

$$= 2\pi \sum_{j=1}^{2n+1} w_j \tag{4.20}$$

The author did not initially consider a Gauss-Kronrod scheme during the experimental design since the distribution was unknown a priori; thus, pressure measurements at the nodes of the Gauss-Kronrod scheme are not directly available. This study assumed that the pressure distribution measured by the 17 CTAPs is reflective of reality such that interpolations/extrapolations accurately estimate the pressures at the nodes ($p(r_j)$) listed in Table 4.1. Again, for now, the axisymmetric assumption is imposed in this analysis for simplicity. The last node at 7.112 cm for the Kronrod extension is at a larger radial direction than the last CTAP measurement. The pressure at the last node came from an extrapolation of the cubic fit of the pressure distribution along the nozzle, similar to Section 4.4.1. While this will generate some error, this error will be less impactful overall than the Newton-Cotes method since the weight on the last node is smaller than the points where the measurements exist.

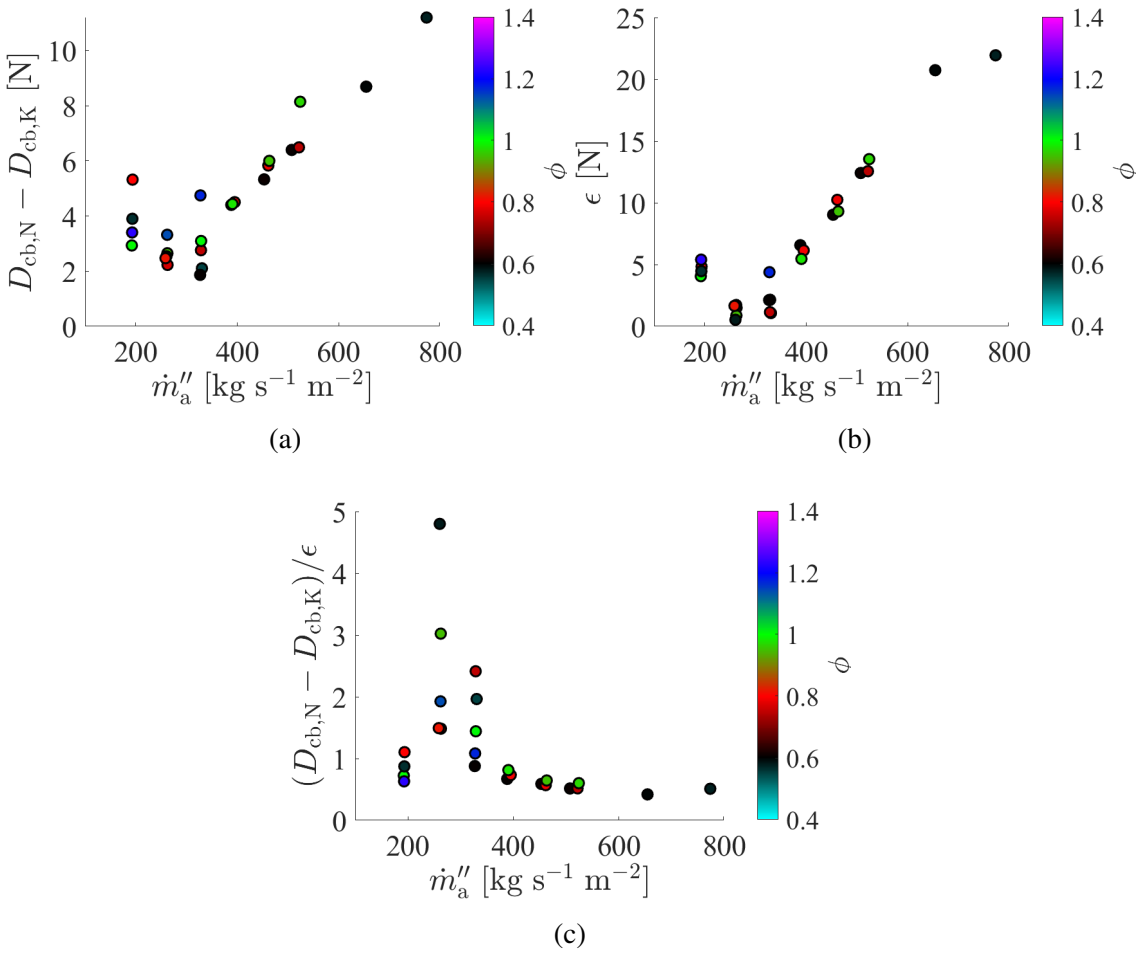

Figure 4.7: a) Comparing the trapezoidal rule and Gauss scheme, where the b) numerical integration error in the Gauss-Kronrod scheme c) typically captures the differences between the two.

The base drag found from the Gauss-Kronrod scheme is,

$$D_{\mathrm{cb,K}} \approx 2\pi \sum_{j=1}^{2n+1} w_j \Delta p_j \tag{4.21}$$

Figure 4.7a makes the comparison between the base drag with extrapolated pressure computed through the composite trapezoidal rule Newton-Cotes method ($D_{\mathrm{cb,N}}$) and the base drag from the simulated Gauss scheme ($D_{\mathrm{cb,G}}$). A positive sign here indicates that the base drag from the Gauss-Kronrod scheme is more negative, which would raise the computed gross thrust. The two schemes agree most closely at about 190 kg s^{-1} m^{-2} and diverge from one another with increasing flux. The increasingly negative difference in base drag suggests that the Gauss-Kronrod integration would result in a more conservative (lower) gross thrust.

The estimated numerical error in the Gauss-Kronrod scheme, shown in Figure 4.7b, increases with increasing mass flux. The exception is around 300 kg s^{-1} m^{-2}, where the error is inextricably the smallest, though this may result from the cubic fit matching the data the best at that flux. Meanwhile, Figure 4.7c displays the difference in measured base drag as computed using the Newton-Cotes and Gauss-Kronrod schemes (i.e., Figure 4.7a) normalized by the estimated error from the Gauss-Kronrod method (i.e., Figure 4.8). This comparison demonstrates that, for the most part, the estimated numerical error (ϵ) includes the potential differences between the two integration methods. Thus, one can interpret the differences between numerical integrations as the result of the inherent uncertainty of the numerical integration. However, for air mass fluxes around 300 kg s^{-1} m^{-2}, this is not true since the estimated error in the Gauss-Kronrod scheme is close to zero at those fluxes (see Figure 4.8). As such, the difference between the two integration techniques becomes much more significant than the error. Overall, these results indicate the Gauss-Kronrod scheme is accurate compared to the composite trapezoidal rule scheme despite using only five data points instead of 18 data points and assuming a functional form of the pressure distribution a priori. The agreement likely occurs because the measured pressure distribution is modeled well (with high R^2 values) by a cubic fit, i.e., the monic polynomial used in the Gauss scheme. However, different geometries may have a pressure distribution that a cubic fit can not well model.

Further contextualization of the significance of the numerical error comes by comparing it to the gross thrust, Section 5.2. This comparison is made in Figure 4.8. The numerical integration error is always tiny compared to the gross thrust, being below 5% even at the lowest fluxes. There appears to be an asymptote where the numerical error becomes a nearly constant 1.75% irrespective of the mass flux once the mass flux exceeds 350 kg s^{-1} m^{-2}. If true, this result is ideal as it mitigates the uncertainty from a previously unresolved source.

Further reduction in numerical error occurs if the number of points for the Gauss quadrature increases from $n = 2$. For instance, if $n = 3$ (increasing the total number of nodes from 5 to 7) the error is reduced by almost 50%. In implementing a higher-order virtual Gauss-Kronrod scheme, additional points of necessary extrapolation arose; thus, while the numerical integration may decrease, the additional extrapolations will influence/constrain the error estimates. Furthermore, since the calculations presented here use interpolations of pre-existing data, there will likely be a convergence of the Gauss-Kronrod and trapezoidal rule schemes. In other words, the Gauss-Kronrod would eventually become fit to the data collected, which limits the possible analysis in this study. Overall, Gauss-Kronrod appears helpful in computing the base drag with fewer sensors. However, suppose the experiment aims to characterize the pressure distribution on the truncated nozzle face. In that case, having more sensors may still be preferable, as was done here.

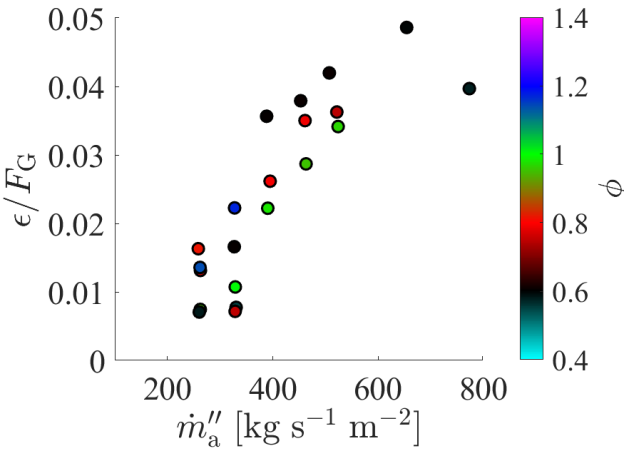

Figure 4.8: Simulated Gauss-Kronrod error compared to gross thrust.

4.4.3 Axisymmetric Evaluation

Until this point, this study imposed the axisymmetric assumption when computing the base drag on the truncated nozzle for simplicity. Now, this study will utilize a two-dimensional numerical integral to evaluate the impact of the asymmetry. The two-dimensional numerical integration is given by,

$$D_{\text{cb,2D}} \approx \frac{1}{n_j} \sum_{j=1}^{n_j} \sum_{i=1}^{n_i} w_{ij} p(r_i, \theta_j) \tag{4.22}$$

$$\approx \frac{1}{n_j} \sum_{j=1}^{n_j} \sum_{i=1}^{n_i} w_{ij} \Delta p \left(r_i \cos\left(\frac{2\pi j}{n_j}\right), r_i \sin\left(\frac{2\pi j}{n_j}\right)\right) \tag{4.23}$$

where n_j is the number of circumferential locations (in this case, three) and n_{ij} is the number of radial locations for a given circumferential location. Equation 4.22 is presented this way since one of the legs has one more measurement than the other. The weight, w_{ij}, is a matrix since the i-th node on the j-th leg has a different radial location than the other legs.

This study used a composite trapezoidal rule to integrate in the circumferential direction. The trapezoidal rule has a higher convergence rate, approximately $1/N^4$, for smooth periodic functions compared to the standard convergence rate, $1/N^2$. A simple, albeit incomplete, explanation is that specific terms in expanded trapezoidal rule cancel out from the derivatives at the two endpoints of the integration being equivalent [184]. Using cylindrical coordinates, the pressure variations in the circumferential direction are periodic and smooth at the bounds $\theta = 0$ and $\theta = 2\pi$. Thus, the trapezoidal rule provides increased accuracy to the integral in the circumferential direction with a limited amount of data points.

Again, the pressure on each leg is extrapolated to the edge to perform a closed numerical integration in the radial direction. While the extrapolation inevitably introduces errors, all the pressure distributions indicate that the edge pressure should be greater than the outermost CTAPs. Thus, if the pressures were assumed constant up to the edge from the outer CTAP, one would accrue an equal amount of unquantifiable errors. Figure 4.9a compares the base drag for the asymmetrical pressure field ($D_{\mathrm{cb,2D}}$) is compared against the one for the symmetrical pressure field with extrapolated pressure ($D_{\mathrm{cb,N}}$). This difference is interpretable as the change in gross thrust caused by two-dimensional numerical integration with positive values corresponding to an increase in gross thrust. The data is scattered around no difference (0) with increasing equivalence ratio, causing the difference to decrease (become more negative). It appears that for higher fluxes, the difference grows worse as the base drag computed with the two-dimensional integration becomes more negative (having a larger magnitude) than in the axisymmetric case. However, this difference cannot be used as a measure of asymmetry since it is possible to have zero difference despite being very asymmetrical. Figure 4.9b shows the relative scale between the difference in base drag compared to the total gross thrust. The impact of the axisymmetric assumption can be seen most at the lower fluxes, where the difference can result in up to a 6% change in the gross thrust. The absolute value of the relative change grows smaller with increasing mass flux for a given equivalence ratio until about 500 kg s^{-1} m^{-2}, where the absolute value grows further away from 0. Most of the data falls within the ±4% of the gross thrust, indicating that the assumption introduces an uncertainty of the same order as the uncertainty from the edge pressure for the Newton-Cotes scheme or the integration error for the Gauss-Kronrod scheme. The reported gross thrust, Section 5.2, values were calculated using the base drag from the two-dimensional numerical integration presented in this section.

The overall changes in gross thrust from the typical axisymmetric midpoint method ($F_{\mathrm{G,old}}$) to the two-dimensional numerical integration (F_{G}) are in Figure 4.10a. Meanwhile, the relative changes in the gross thrust are in Figure 4.10b. The shift to the trapezoidal rule instead of the midpoint rule, extrapolating to find a better estimate of the edge pressure and not assuming axisymmetric pressure, reduced the overall thrust, which implies a more conservative estimate of the performance as a decrease in measured thrust would result in a reduction of estimated pressure gain. The changes to numerical integration cause up to a 12% change in the gross thrust at the low flux cases. While the relative change does decrease with increasing flux, this study has nevertheless improved the thrust measurement since the two-dimensional numerical integration has fewer overall assumptions and increased accuracy compared to the previous method of finding base drag. Overall, this study highlights that proper numerical integration is necessary for the base drag to get accurate pressure gain measurements, especially since the PG may only be several percent greater than current deflagrative combustors.

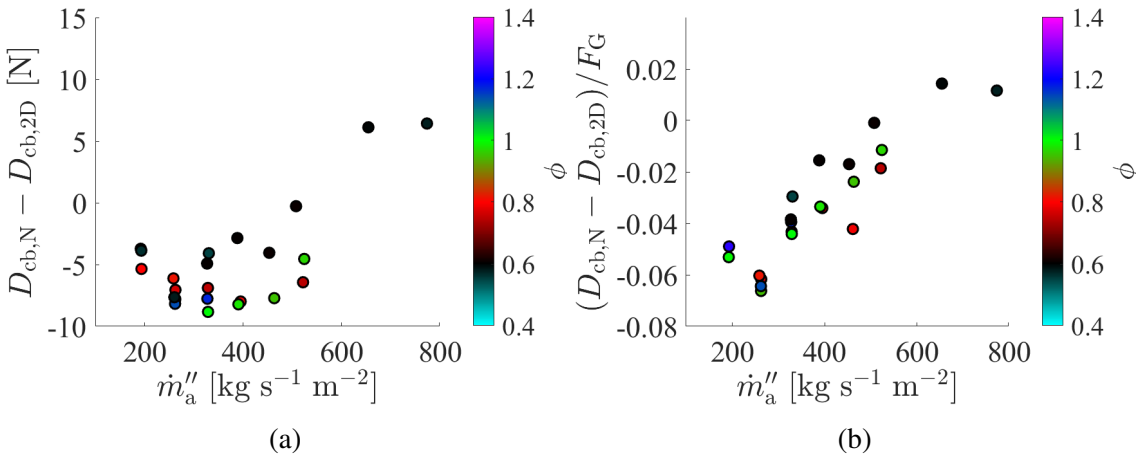

(a) (b)

Figure 4.9: The base drags with ($D_{\mathrm{cb,N}}$) and without ($D_{\mathrm{cb,2D}}$) axisymmetric assumption are a) different which is b) contextualized against the gross thrust.

4.5 Exit Flange Aside

While the focus here has been the numerical integration of the base drag acting upon the truncated nozzle, a similar analysis also applies to the base drag acting upon the flange. However, due to the design of the flange, the area that pressure could react on for the flange is 11.54cm^2 (1.79in^2), which is significantly smaller than the 168.70cm^2 (26.15in^2) for the truncated nozzle. The flange is only slightly wider than the 1/16 in the tube used for the CTAP measurement, mitigating any possible radial variation and removing the need for numerical integration in the radial direction, which was by design. Thus, this work computed the base drag by applying a composite trapezoidal rule to integrate along the circumferential direction across the six measurements. As stated, the trapezoidal rule converges more rapidly (less needed points) for periodic functions than non-periodic ones. Although this work took six measurements along the flange, there were effectively only three circumferential locations due to pairs of measurements being close to each other, as was discussed in Section 3.4.3.

4.6 Discussion

Thrust measurements are notoriously noisy and challenging to implement correctly in an experimental setting, even before considering characterizing the base drag. Wanting to isolate the gross thrust from a load cell measurement with said base drag measurements further adds to the complexity of the method. As established in this section, the truncated nozzle originates from the effort to isolate the performance of the RDC from the performance of the nozzle expansion process. Mea-

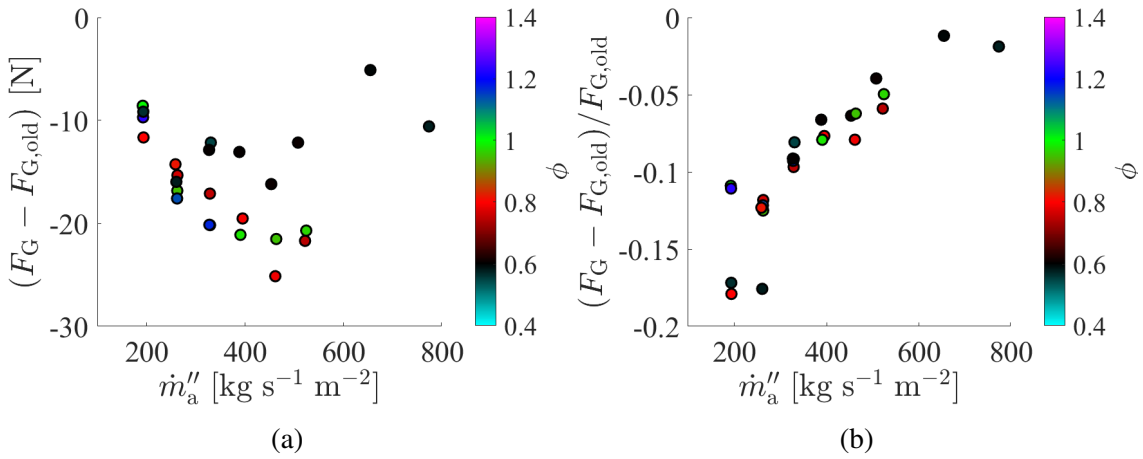

Figure 4.10: By utilizing two-dimensional integration a) the gross thrust decreases compared to previously using the midpoint rule ($F_{G,old}$), which is shown b) relative to the gross thrust.

suring said base drag is non-trivial, with the best experimental practice measuring the pressure at discrete locations along flat surfaces. This chapter showed that the choice of sensors, measurement locations, and numerical integration technique introduces significant uncertainty to the desired gross thrust measurement. That considerable uncertainty in gross thrust also does not include other sources, such as the load cell. Therefore, before even considering a thrust measurement or using the EAP method, concerns about the precision of the experimental procedure are introduced. Such precision concerns come even though this study utilized nearly twice as many pressure measurements as other studies [114, 116] and used a composite numerical integration method. Therefore, it is reasonable to expect such uncertainties to exist in other rigs and the experimental results found in the literature.

One of the objectives of this study was to understand how to make accurate and precise base drag measurements with as few data points as possible. As with any numerical integration, the number of data points will impact the results through the convergence rate, especially when the underlying shape is unknown a priori since interpolation occurs between the discrete data points. There is an inherent trade-off between the accuracy of the integration and the number of measurement points. As such, based on the results of the present study, the following recommendations are given for future studies to strike a balance between the two competing constraints intentionally:

- One should compute the base drag using a composite, two-dimensional numerical integral. Therefore, pressure measurements must have different discrete radial and circumferential locations.

- Pressure needs to be measured at a minimum of three discrete circumferential locations

evenly distributed in the circumferential direction to capture any asymmetry in the pressure distribution. The convergence rate of the trapezoidal rule in numerically integrating a periodic function is $1/N^4$; thus, three points give an error of 1.2%, although the error further reduces with a greater number of points.

- A radially-weight Gauss-Kronrod scheme is ideal for the radial integration. Based upon the approximate cubic radial pressure distribution observed in this work, a Gaussian scheme of order three (two points) with a Kronrod extension of order seven (additional three points) for five radial locations would be suitable. While the Kronrod extension does not drastically improve the accuracy of the numerical integration, it provides an invaluable estimation of the uncertainty associated with the integration.

- A Newton-Cotes integration along the radial direction instead of the recommended Gauss-Kronrod remains valid; however, the edge pressure is paramount to the numerical integration. A pressure measurement at the edge is required, or the necessary assumptions lead to significant uncertainties. The Kronrod extension typically inherently solves the edge pressure issue by having the outermost radial node be effectively at the edge of the nozzle.

- In general, low-noise pressure transducers reduce the overall base drag uncertainty. The worst pressure differential measured was about 0.08 atm (1.17 psi), which is relatively small compared to the ambient exhaust pressure. Since most pressure transducers have uncertainty/noise that scales with their full-scale value, minimizing the range of the pressure transducers while still spanning the range of expected values can provide additional uncertainty mitigation.

If one follows the above recommendations, the combined uncertainty from the pressure measurements and numerical integration should be on the order of a few percent of the final gross thrust measurement. The exact values provided in the above recommendations should serve as a lower bound and are recommended to minimize the number of needed measurements while maximizing the information gained. Improved accuracy and reduced uncertainty will require more costly instrumentation and take up space within the experiment. In general, most of the reduction in uncertainty from previous experiments will come from resolving the asymmetry and being less dependent on the edge pressure measurement to bound the Newton-Cotes integration.

CHAPTER 5

Evaluation of Uncertainties of Pressure Gain Measurements

5.1 Introduction

With the base drag analysis performed in the previous chapter in mind, now the gross thrust and pressure gain measurements are evaluated for the same test conditions and geometry (refer back to Section 4.2). Ultimately, the detailed analysis of the base drag found in the previous chapter informs the detailed uncertain analysis of the PG metric as measured by the EAP method. This chapter further explores the possible sources of uncertainty (both random and systematic) and demonstrates their relative impact on pressure gain measurements through the EAP methodology. The ultimate goal is to evaluate if the EAP methodology can be sufficiently precise for measuring a definitive pressure gain and how to minimize the known sources of uncertainty. This chapter presents a detailed uncertainty propagation through the EAP method, starting from the linear calibrations of sensors used in the experiment and propagating through to the final pressure gain measurement. The errors introduced through the force corrections needed to compute gross thrust highlight some uncertainty sources in EAP. In addition, the work will discuss the (significant) systematic uncertainty introduced by the exit choked flow assumption to evaluate how robust the EAP methodology is experimentally. The exit Mach number is estimated by directly measuring the static pressure at the exit plane. Without the Mach number assumption, the pressure gain measurement is corrected (improving accuracy), and the overall uncertainty is reduced (improving precision). This chapter also introduces a method that uses direct time-averaged measurements to estimate pressure gain that does not invoke the EAP methodology. Overall, the work presented in this chapter is to inform future testing such that the overall precision and accuracy of the pressure gain measurement increases.

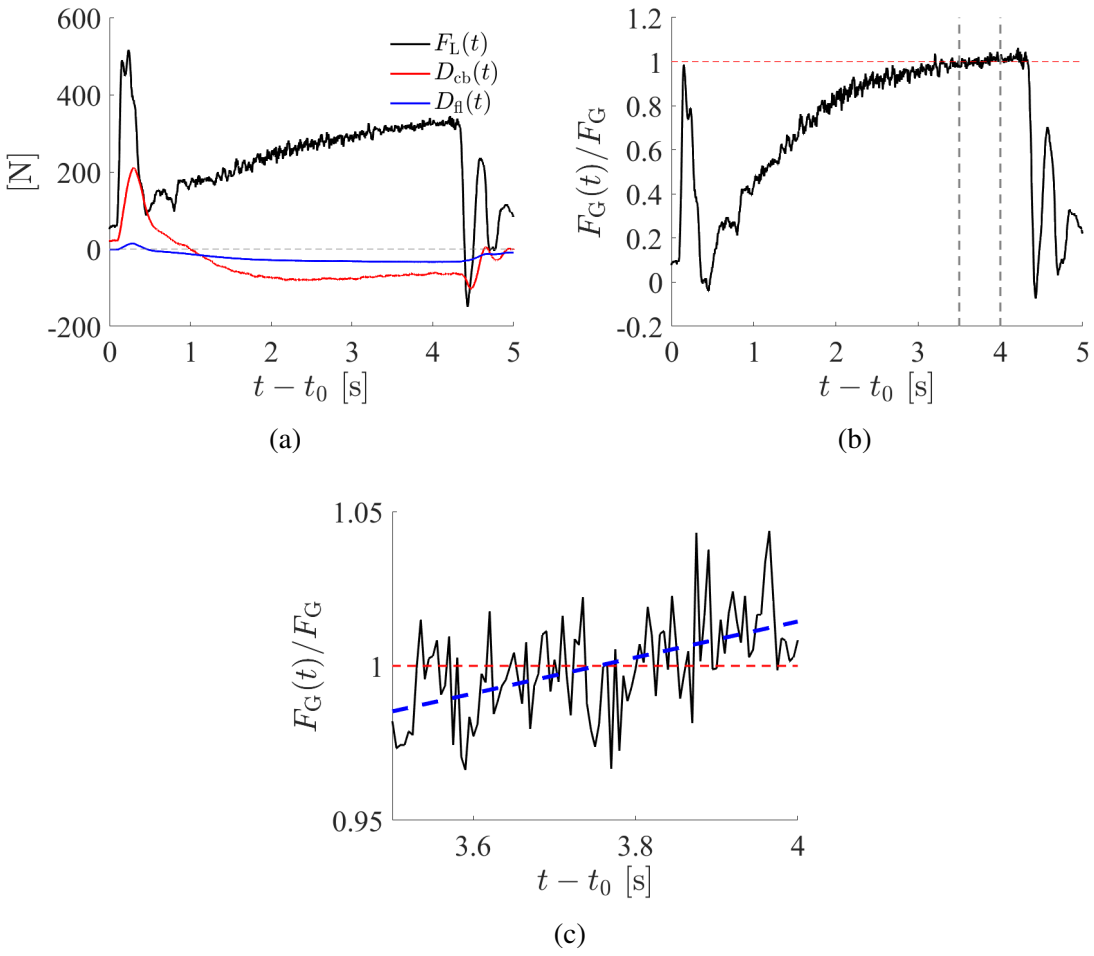

Figure 5.1: a) Time history of load cell measurement (resultant force) and base drag forces. b) Variation of the gross thrust relative to the quasi-steady state value. c) Average over the last 0.5 seconds of the run to produce a quasi-steady value; the time variation over this region in time is comparable to the noise. The operating condition is $\dot{m}''_a$ = 524 kg s^{-1} m^{-2} and ϕ = 0.97.

5.2 Thrust Measurements and Analysis

5.2.1 Quasi-Steady Measurements

This work distinguishes time-varying quantities by adding (t) next to the variable name, like the example of the time history of the reactant force from the load cell and the base drag forces in Figure 5.1a. This example comes from when the air mass flux was 524 kg s^{-1} m^{-2} and an equivalence ratio of 0.97 with ignition at 388 kg s^{-1} m^{-2} and 0.60 to protect the load cell. The mid-run increase in air mass flux was one of the largest ramps performed, and the temporal variations of the forces are similar for other conditions that require mid-run ramping of flow rates. The traces in Figure 5.1a are raw (i.e., unfiltered) measurements. Time is relative to the fuel solenoids opening (t_0),

with this run lasting four seconds total. The significant spike in all the forces at the beginning (the first 0.5 seconds after t_0) of the run is attributed to the initial ignition process as the entire system momentarily pressurizes due to being coupled to an exhaust chamber [47]. A similar exhaust chamber effect occurred at the end of the run (greater than 4 seconds after t_0) with the cyclic loading and unloading of the combustor after the detonation wave dies. A fluidic oscillation occurs from being coupled to an exhaust chamber, which is observed in other unsteady measurements, such as the CTAP pressure measurements throughout the combustor, some of which can be seen in Figure 5.1a in the center body base drag force.

The change in test condition mid-run resulted in the transient behavior in all the forces that began to level off after 3 to 3.5 seconds into the run. Steady operation (i.e., constant number of waves and nearly constant wave speeds) occurs before the forces level off, typically around 2 to 2.5 seconds. A quasi-steady value of gross thrust occurred during the last 0.5 seconds of the run. The measurement is classified as quasi-steady since there may still be a slight increase (on the order of a few percent) in the gross thrust over this averaging window for some runs, on top of the inherent noise. To better visualize the temporal variations of measured or computed quantities, Figure 5.1b normalizes the time history of gross thrust ($F_G(t)$) by the quasi-steady state value (F_G). The dashed gray vertical lines denote the averaging window. The ramping of both fuel and air mass flow rates caused the gross thrust to increase by a factor of four from the initial condition. Around 3 seconds into the run, the time derivative of the gross thrust relative begins to decrease as the profile starts to flatten out. The averaging window is shown in Figure 5.1c for a closer examination of the steadiness. The noise introduces rapid increases/decreases of about 3.5% of the steady value (about 14.6 N). One could argue that a gradual increase is still occurring over this window, as evidenced by the dashed blue line, a linear data fit over the window. However, the change over the 0.5 seconds of this linear fit is 12.1 N, which is less than the uncertainty. The same is true for the other conditions.

The author postulates that if the gradual increase in thrust reflects reality, it would be due to the thermal transients of the combustor, such as heating and expansion, though this is unverified. Another possible explanation is the lag in time between the observed increase in mass flow rate at the upstream metering location and the increased mass flow entering into the RDC. The metered mass flow rate asymptotically reaches its nominal value within a fraction of a percent about 2 seconds after ignition while the load-cell measurement continually increases. Likewise, the base drag would increase if additional mass entered the system, but it too varied by less than a percent. Thus, while possible, the mass flow rate explanation is unlikely. Nevertheless, this work takes the quasi-steady state value as the accurate representation of the thrust output, and the experimental noise/uncertainty encapsulates the unsteady increase.

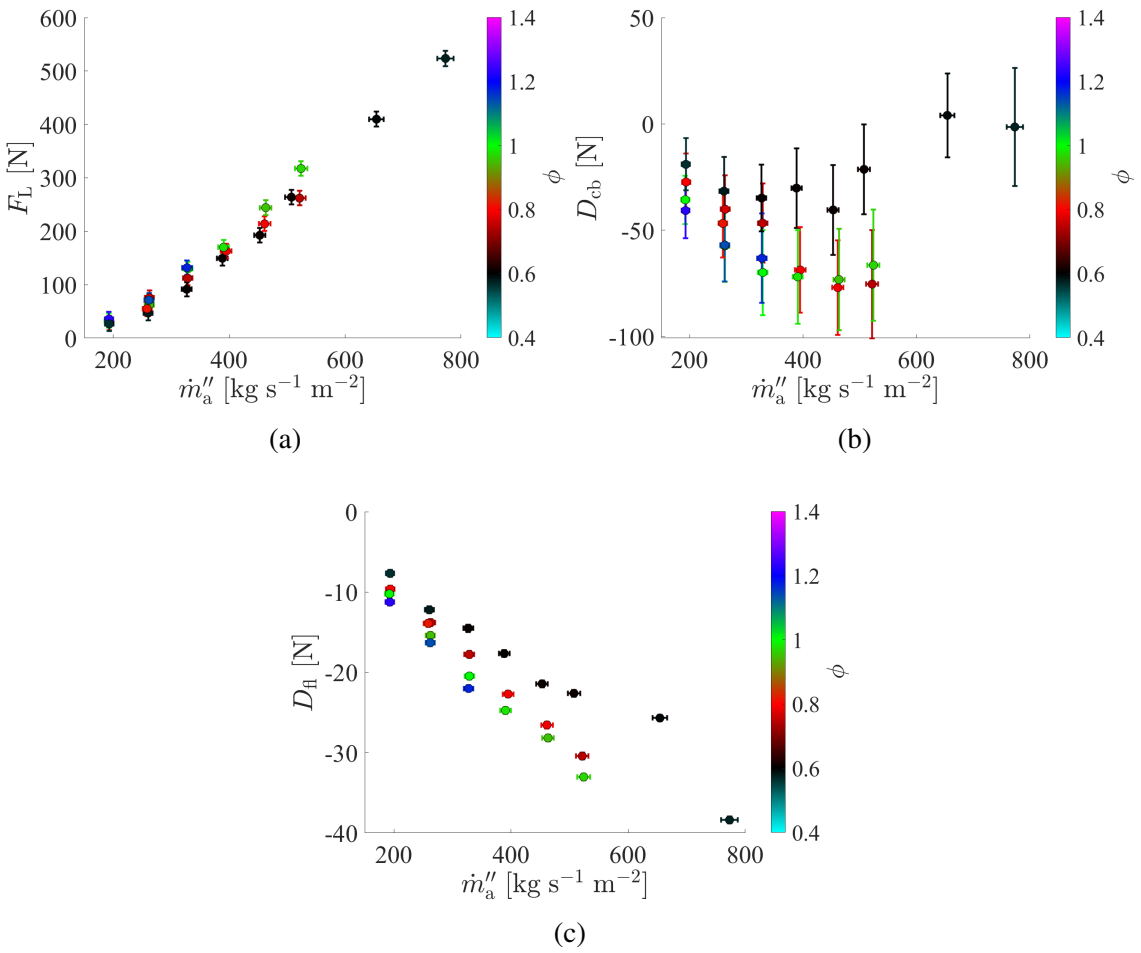

Figure 5.2: a) The resultant force increases more rapidly than drag forces. b) center body drag has a non-monotonic relationship with mass flux. c) Flange drag comparable to center body drag despite smaller area.

5.2.2 Different Contributions to Gross Thrust

To determine the sense of scale between the three force contributions to the gross thrust, each component in Eqn. 4.3 is examined. Figure 5.2 shows the different contributions from the load cell measurement, Figure 5.2a, the base drag acting on the center body, Figure 5.2b, and the base drag acting on the flange, Figure 5.2c. Each value is a time-average over the last 0.5 seconds of fuel-on operation. According to Eqn. 4.3, the negative base drag values would increase the gross thrust relative to the resultant force. An increase in the force magnitude with an increasing equivalence ratio is observable for all three forces since a higher equivalence ratio means more chemical potential energy in the system. Looking at Figure 5.2a, it is immediately apparent that the resultant force grows much more rapidly with increasing flux than either of the base drag

corrections. While at the lowest fluxes, all the forces are comparable (being about 10-20 N), the resultant force grows to be nearly a factor of five times greater than the sum of the base drags at the highest fluxes. Overall, the order of importance to the gross thrust in descending order is resultant force, center body drag, and flange drag.

Focusing now on the base drag on the center body in Figure 5.2b, a non-monotonic relationship with mass flux is observable. Until 500 kg s^{-1} m^{-2}, the drag increases in magnitude (grows more negatives) as the flux increases. However, for the $\phi = 0.6$ conditions tested at fluxes above 500 kg s^{-1} m^{-2}, a decrease in the magnitude (grows more positive) occurs. After 600 kg s^{-1} m^{-2}, the drag is only several Newtons, indicating an order of magnitude change in the force. The change in the pressure distribution acting upon the center body likely occurs with a change in the overall wave dynamics within the combustor. This study could not confirm this, although Fievisohn et al. previously observed that a change in the number of waves significantly alters the center body drag [129].

Despite the small area on the modified flange piece, the flange drag contributes a comparable amount of force as the center body drag (compare Figure 5.2c to Figure 5.2b). The comparable force results from the greater vacuum pulled on the flange than the center body. In general, the flange base drag is about one-half the magnitude of the center body drag, except for at the highest fluxes tested. At those high fluxes, the flange drag remains monotonically increasing in magnitude with flux, unlike the center body drag, which exhibited a decrease in the force magnitude. The flange area is further downstream than the combustor's exit plane, likely causing the lack of change. The flow field generated from the expansion of the flow around the nozzle edge would have a more substantial radial component than the flow past the flange since the flow would recover in the axial direction as it moves downstream. Additionally, the vertical error bars in Figure 5.2c are negligible compared to Figure 5.2b, which the next section will discuss further.

Finally, the gross thrust is the summation of the different contributions. Figure 5.3 shows the variation of the average thrust measured across all the operating conditions tested in this study. The measured thrust increases monotonically with mass flux (flow rate owing to the constant inlet area) and equivalence ratio. As expected, since the resultant force was significantly greater than the base drags, the nearly linear relationship with air mass flux is preserved in the gross thrust.

5.3 Thrust Uncertainty Analysis

This study developed a detailed uncertainty analysis of the thrust equation (Eqn. 4.3) to evaluate thrust measurement uncertainties. For this uncertainty analysis, the standard approach for the propagation of uncertainties for uncorrelated uncertainties, where the sensitivity of the final thrust measurement to each measurement component, is utilized. The individual measurement uncertain-

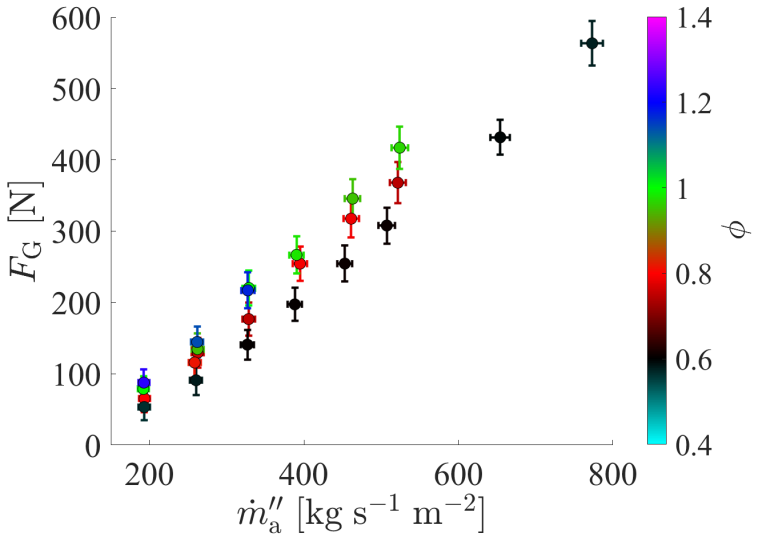

Figure 5.3: Gross thrust values for tested conditions; increases linearly with mass flux, and increases with increasing equivalence ratio.

ties combine in quadrature because of the underlying Gaussian distributions. Here, δy denotes the uncertainty in a value y. Thus, the gross thrust uncertainty δF_G for independent measurements is:

$$\delta F_G^2 = \left(\frac{\partial F_G}{\partial F_L}\delta F_L\right)^2 + \left(\frac{\partial F_G}{\partial D_{cb}}\delta D_{cb}\right)^2 + \left(\frac{\partial F_G}{\partial D_{fl}}\delta D_{fl}\right)^2 \tag{5.1}$$

$$= \delta F_L^2 + \delta D_{cb}^2 + \delta D_{fl}^2 \tag{5.2}$$

Thus, the error bars for the thrust come from analyzing the uncertainty in the gross thrust and the base drag calculations on both the flange and center body. All the variables in Eqn. 5.2 are time-varying; thus, the average over the steady portion will be taken, similar to the thrust.

5.3.1 Resultant Force Uncertainty

As Section 3.5.1 discussed, performing many load cell calibrations gives the uncertainty in the resultant force measurement. This study set the uncertainty caused by the intercept (δb) to zero since this study also tared each test's resultant force before airflow in post-processing. The slope of the load cell calibration is treated as a constant throughout the run, although hysteresis in the system may cause it to change slightly after the ignition spike. The hysteresis introduces an unknown uncertainty. For now, the uncertainty in the resultant force measurement combines the uncertainties in slope and measured voltages, and Figure 5.4a gives the analysis results. The uncertainty is, at maximum, 1.4% of the sensor's full scale (1000 N), although the uncertainty continues to grow

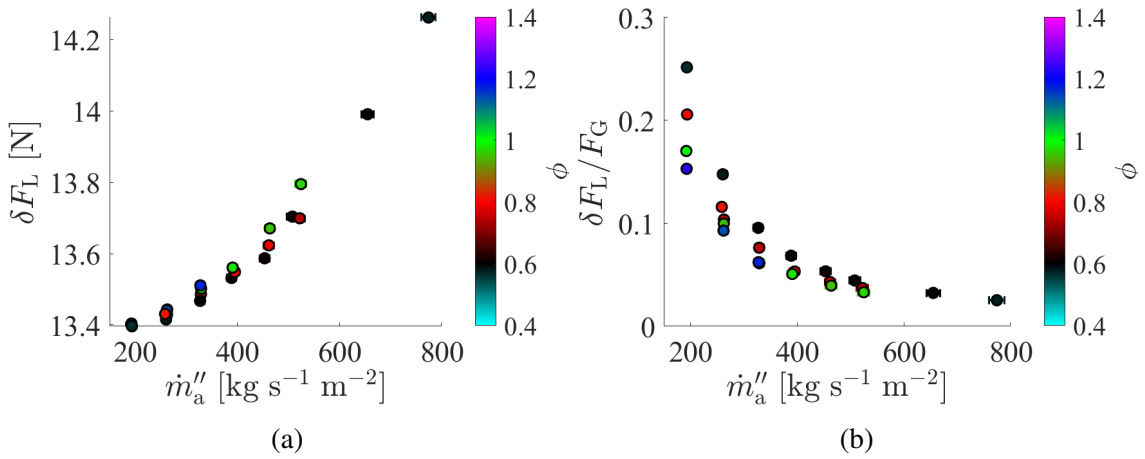

Figure 5.4: a) The total uncertainty of resultant force (F_L) for tested conditions; the maximum is about 1.4% of the full scale of the load cell. b) The total uncertainty in F_L relative to gross thrust for tested conditions; largest values at low mass fluxes.

with increasing gross thrust (increasing flux). This uncertainty decreases relative to the gross thrust with increasing mass flux and/or equivalence ratio; see Figure 5.4b. At the highest flux tested, the resultant force introduces 1.2% uncertainty to the measured gross thrust; however, at the lowest flux tested, the uncertainty reaches over 10% the measured gross thrust, which is a significant source of uncertainty.

5.3.2 Base Drag Uncertainty

The uncertainty in the base drag stems from the numerical integration, the actual pressure measurements, and machining tolerances. For instance, consider the base drag along the center body,

$$D_{cb} \approx \frac{1}{n_j} \sum_{j=1}^{n_j} \sum_{i=1}^{n_i} w_{ij} \Delta p \left(r_i, \theta_j\right) \tag{5.3}$$

The components of the uncertainty are,

$$\delta D_{cb}^2 = \epsilon^2 + \left(\frac{\partial D_{cb}}{\partial p(r_i, \theta_j)} \delta p(r_i, \theta_j) \right)^2 \tag{5.4}$$

where ϵ is the error associated with the numerical integration, which only approximates the surface integral. As established in the previous chapter, this work used a composite Newton-Cotes method when computing the base drag on any surface. The Newton-Cotes cannot experimentally determine the numerical integration error since the functional form of the pressure distribution is unknown

a priori, and the function's derivatives are needed to find the error. The numerical error based upon a fitted function would also depend on the fitted distribution's quality. Using a simulated Gauss-Kronrod scheme, it was shown in Figure 4.8 that ϵ was several percent of F_G). However, this work did not directly measure pressure at the node locations for the Gauss-Kronrod scheme; thus, Figure 4.8 only serves as an approximation for demonstrative purposes. Therefore, the numerical integration error ϵ is neglected here until future studies implement the Gauss-Kronrod scheme. The base drag uncertainty and subsequent uncertainties would increase by including ϵ.

5.3.2.1 Center Body

A two-dimensional numerical integral using the trapezoidal rule in the radial and circumferential directions integrates the random uncertainty in the pressure measurements. The uncertainty in the overall thrust measurement is reduced by selectively placing the sensors with lower uncertainty at nodes with the most significant weight (radial position) for numerical integration. One can do this process before testing to improve the thrust measurements. However, Section 4.4.1 demonstrated the need for an assumed edge pressure in the center body drag calculation, introducing significant uncertainties. To further differentiate the impact of the edge pressure, this work breaks the uncertainty into two components: the known sensors uncertainty and the edge pressure uncertainty. The integral of the uncertainties in the pressure measurements (assuming that the edge pressure has no uncertainty) results in approximately 4.96 N of uncertainty. This result has no significant variability across the different conditions. The uncertainty introduced by the unknown edge pressure is the difference in base drag when computed with an extrapolated pressure and with a constant pressure from the outermost radial CTAP, Section 4.4.1. Again, this uncertainty is intentionally large to highlight the importance of an edge pressure measurement and guarantee that the "true" value is within the confidence interval around the extrapolated edge pressure.

The combined uncertainties, Figure 5.5a, reveal that while the sensors' uncertainties contribute a non-negligible amount, most of the uncertainty is due to the lack of an edge pressure measurement. In an absolute sense, the uncertainty does increase with mass flux and equivalence ratio. However, the gross thrust rises more rapidly with mass flux, resulting in a relative decrease in uncertainty, Figure 5.5b. This relative uncertainty ranges from 23% of F_G at the lowest flux to 4.9% of F_G at the highest mass flux tested. Furthermore, the base drag on the center body introduces more uncertainty than the load cell (which is typically much noisier than pressure transducers) solely due to the unknown edge pressure. A pressure measurement closer to the edge here would drastically reduce the uncertainty in the base drag (down to 4.96 N). Thus, either including a pressure measurement at the edge of the cap (which can be challenging from a practical standpoint) or utilizing a numerical integration scheme that is less dependent upon the edge pressure (i.e., Gauss-Kronrod quadrature) will significantly reduce the base-drag uncertainty. Such a reduction

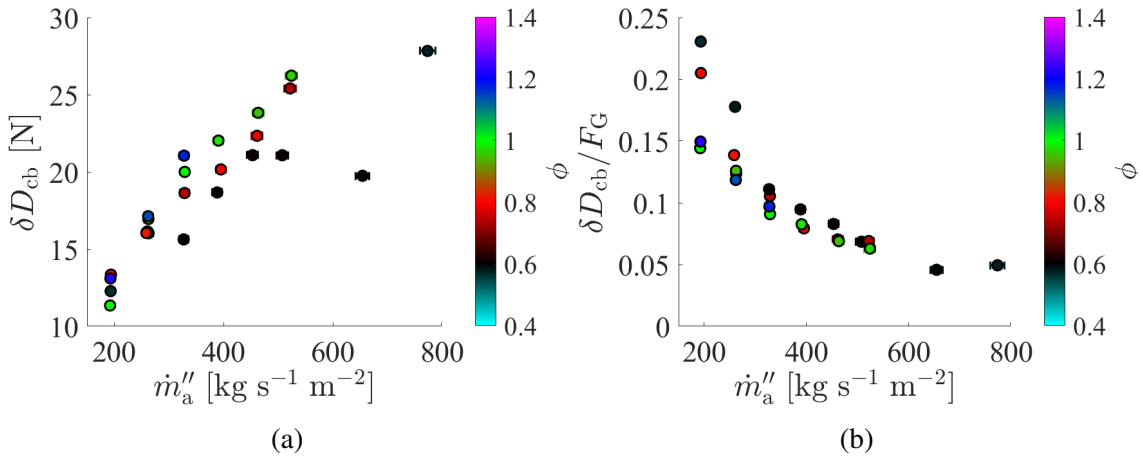

Figure 5.5: The a) total and b) relative uncertainty in base drag along the center body (D_{cb}) due to pressure sensors and unknown edge pressure for tested conditions.

would substantially improve the measure of gross thrust and subsequently the PG.

The integration of the base drag depends on the sensors' physical positioning along the bluff body nozzle and the outer diameter of the nozzle. A Monte-Carlo sampling assessed the potential systematic impact of imprecise machining. The sensor's radial (r_i) and circumferential (θ_j) positions, along with the nozzle outer diameter, are all treated as following uniform distribution defined by the respective machining tolerances. This study independently and randomly sampled the uniform distributions before integrating each combination according to Eqn. 5.3 with the measured pressure profile. After 10,000 times, the Mone-Carlo gives the distribution of base drag values subject to changes in measurement locations. Here, the systematic uncertainty in the base drag is the maximum deviation from the mean value. Overall, this source of uncertainty is on the order of 0.1% of the nominal thrust value; thus, this systematic error is negligible compared to other uncertainties.

5.3.2.2 Flange

A similar integration of the pressure uncertainties is possible for the flange base drag. According to Section 4.5, a trapezoidal rule integrates in the circumferential direction for the flange. The combination of low noise sensors and a smaller flange area results in an uncertainty of approximately 0.43 N, with negligible variation across various conditions. The variability from this value is less than or equal to 1%. This uncertainty is a few orders of magnitude smaller than the gross thrust, which is about 0.1% of the gross thrust. Compared to the resultant force uncertainty in Figure 5.4a, this contribution is negligible and can be neglected.

With the reduced area comes a more significant relative uncertainty caused by the machining

tolerances. In this circumstance, the machining tolerances lead to a possible ±5.4% variation of the flange area from its nominal value. This ±5.4% variation directly results in a systematic error in the base drag on the flange (Figure 5.2c) of ±5.4%. However, this only results in an uncertainty of a few Newtons since the flange force is the most minor thrust component by design. While greater than the random uncertainty from the pressure sensors, this component is still on the order of 0.1% of the gross thrust. Previously, the random and systematic uncertainty was much more considerable with the face-seal configuration due to the larger areas. The larger areas also could not be well defined based on the placement of the seal. Furthermore, more systematic uncertainty arose when the face seal would de-mate during operation. Thus, the negligible random and systematic uncertainties from the flange correction due to a well-defined smaller area on the radial seal marks an improvement in the thrust measurement. Thus, the author recommends a radial seal configuration like the one presented here to other researchers who want to take thrust measurements while still confined to a coupled exhaust system.

5.3.3 Combined Thrust Uncertainty

The uncertainty in the gross thrust measurements, Figure 5.6a, comes from summing the estimated uncertainties for the individual components of the thrust in quadrature. Since the individual uncertainties increased in an absolute sense with increasing mass flux and equivalence ratio, so does the combined uncertainty. However, the uncertainty never becomes less than 10 N, which can reach up to 25% of the gross thrust measurements at the lowest fluxes (Figure 5.6b). The uncertainty never becomes negligible, although it does decrease to about 3.5% of F_G at the highest fluxes tested. Since the sensitivity to the uncertainty falls with higher fluxes, more precise gross thrust measurements can be made by not testing near the lower limit of operability in terms of flux. However, as seen during the later discussion in the PG discussion, it is still advisable to test at the lower fluxes despite the considerable uncertainty.

Returning to the discussion of Figure 5.3, the error bars at lower mass fluxes encapsulate most of the change in thrust caused by increasing equivalence ratio, obfuscating any dependence on the equivalence ratio at those conditions. Since the uncertainty does not scale as fast as the gross thrust (Figure 5.6b), at higher mass flux values, the variation of the measured thrust with equivalence ratio is larger than the error bars. Thus, the thrust measurement system can properly capture the variation of thrust associated with equivalence ratio changes for sufficiently large mass fluxes but not at the lowest fluxes. The run-to-run variability of similar conditions (see 260 kg s^{-1} m^{-2} at $\phi = 0.8$ and 330 kg s^{-1} m^{-2} at $\phi = 0.6$) is captured by the error bars, indicating that the measurements are repeatable.

The two primary contributors to the considerable thrust uncertainty are the load cell and the edge

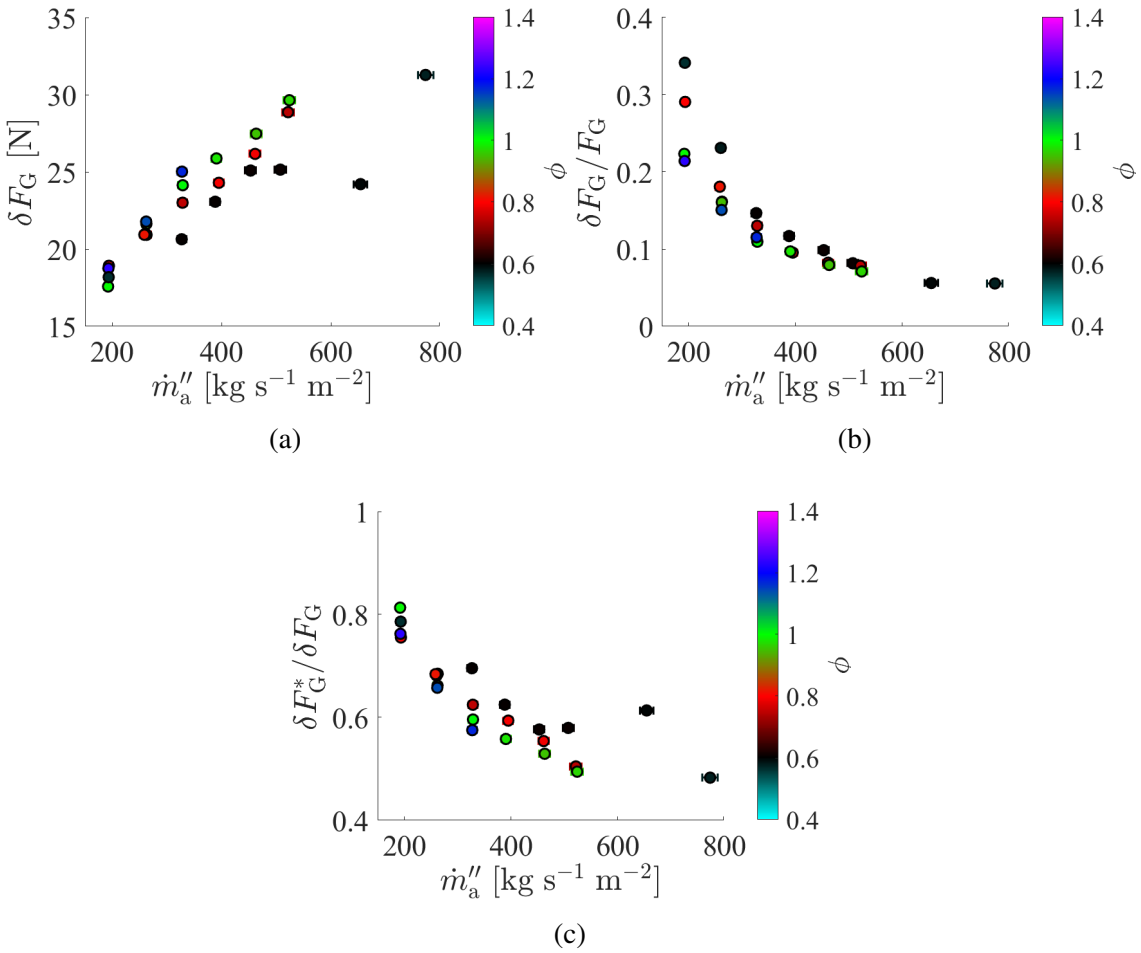

Figure 5.6: The a) total and b) relative uncertainty in gross thrust for tested conditions. The relative uncertainty decreases with increasing flux, going from over 30% down to 5%. c) Relative uncertainty in thrust if the edge pressure is measured instead of estimated.

pressure extrapolation, with the edge pressure ultimately providing more uncertainty by design. As a thought experiment, this study introduces a separate thrust uncertainty (denoted with a superscript *) as the uncertainty combination, assuming that the edge pressure uncertainty is similar to that of a pressure transducer. In other words, if one repeated the tests with a sensor much closer to the edge of the center body, δF^*_G would be the resulting uncertainty. As seen in Figure 5.6c, eliminating the imposed large uncertainty in the edge pressure with an actual measurement would reduce the uncertainty in the gross thrust by up to 50% at the highest fluxes. In such a case, the load cell limits the uncertainty floor, especially at the lower fluxes, with a small contribution from the remaining pressure uncertainties on the nozzle. Such a thought experiment highlights another way to improve the measurement technique to provide a more precise (and likely more accurate) thrust value. Even if physical constraints make such instrumentation challenging, the penalty in uncertainty accrued

by not having such instrumentation is too great to ignore completely.

5.4 Pressure Gain Measurements and Analysis

5.4.1 Exit Gas Composition

A gas composition is needed to compute the EAP as detailed in Section 2.4.1.2. This work assumes an exit gas composition since it did not evaluate the composition experimentally. Specifically, the ratio of specific heats at the exit (γ_8) would depend on the equivalence ratio (ϕ), combustion efficiency (η_c), and exit temperature (T_8). In this study, the RDC was operated with H_2/air, so the combustion efficiency is approximately:

$$\eta_c = \frac{\chi^r_{H_2}}{\chi^r_{H_2} + \chi^u_{H_2}} \tag{5.5}$$

Where $\chi^r_{H_2}$ is the mass fraction of H_2 that undergoes reaction/combustion while $\chi^u_{H_2}$ is the mass fraction of H_2 that does not undergo any reactions before the exit. This section makes no distinction between combustion that occurs through detonation or deflagration. Furthermore, this study does not consider incomplete reactions within the RDC. A non-unity η_c results in an effective ϕ lower than that of the global ϕ with additional unreacted fuel in the system that can have some impact on the thermodynamic properties of the bulk flow. Lower combustion efficiencies likely arise from non-optimized designs that have poor mixing.

The exit temperature T_8 would differ from the temperature produced by the chemical reactions as the flow is expanded towards the exit, making it some function dependent on the combination ϕ, η_c, geometry, amount of combustion in detonation vs deflagrative modes, etc. While the exit temperature would vary depending on the circumferential location, this section uses an area-average temperature as the thrust produced is an integrated quantity across the circumferential direction. Note that due to the expected elevated of $T_8 \geq 800$K, γ_8 is a function of T_8 as vibrational modes of the molecules are activated.

Varying both η_c and T_8 results in the contour plot of γ_8 shown in Figure 5.7a, when $\phi = 1$. The range of temperatures and combustion efficiencies capture the expected values from experiments, with the temperature range being specifically chosen based on thermocouple measurements taken at the exit plane. The lower range of combustion efficiencies is likely unrealistic in actual RDCs, but it provides a sense of the possible changes. As the η_c increases while T_8 is held constant, the γ_8 decreases. Similarly, as T_8 increases while η_c is constant, the γ_8 decreases. An increase in the number of reactions (i.e., increase in η_c) should also increase T_8, both of which would further reduce γ_8. Overall, the value of γ_8 deviates by ±4% from the average value of approximately 1.3,

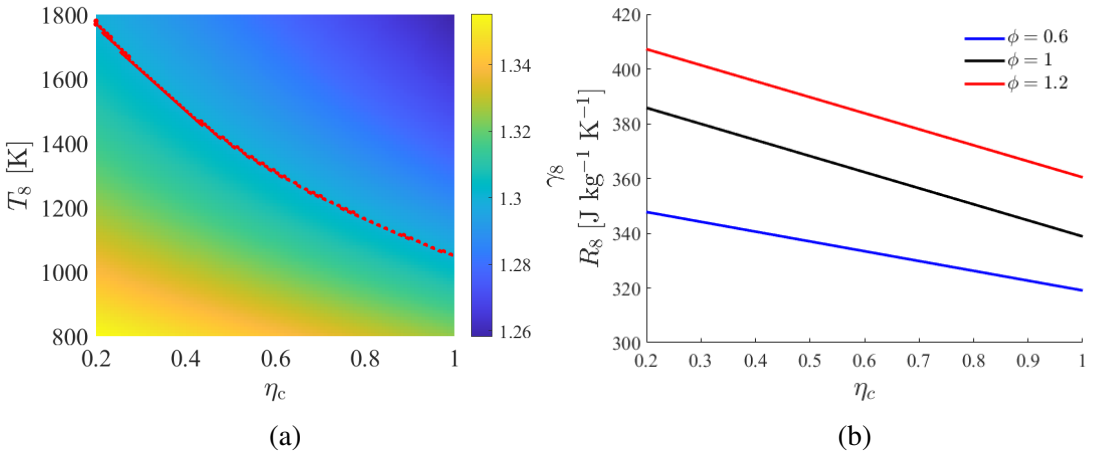

(a) (b)

Figure 5.7: a) Change in ratio of specific heats (γ_8) over expected range of η_c and T_8 for $\phi = 1$; variation of γ_8 within ±4% of 1.3 (red dotted curve). b) Gas constant (R_8) decreases with both ϕ and η_c; variation of R_8 due to η_c is ±6% of mean value.

the red-dotted curve in Figure 5.7a. There will be a slight dependence on the equivalence ratio to the average γ_8, although the variance always stays within the ±4%. This variance is a source of systematic uncertainty. Whenever a γ_8 is necessary for calculations, this work used the mean based on the γ_8 distribution for the specific equivalence ratio and the range of values for the combustion efficiency and exit temperature, Figure 5.7a.

The same process also determines the gas constant at the exit (R_8) whenever needed. Unlike γ_8, the gas constant is not a function of temperature. The gas constant will only depend on the equivalence ratio and combustion efficiency. Figure 5.7b provides some examples of the variability in the gas constant due to combustion efficiency for three equivalence ratios spanning the range tested in this work. A decrease in combustion efficiency is equivalent to a reduction in the effective equivalence ratio, hence the negative relationship. Once again, for a specific run, the mean of the gas constant across the range of combustion efficiencies for the measured experimental equivalence ratio provides an estimate for the gas constant for that specific run. The variability caused by the combustion efficiency is about ±6% of the mean value, a possible systematic error. The systematic uncertainties of the R_8 and γ_8 values could be removed by experimental evaluation, although they would then become a source of random uncertainty.

5.4.2 EAP and Pressure Gain Calculations

This work quantified the PG realized by the combustor from the thrust measurements by applying the concept of EAP introduced by Kaemming and Paxson [113]; see Section 2.4.1.2. The equivalent static pressure based on a simple thrust balance equation that would generate the measured gross

thrust is:

$$\widetilde{p}_8 = \frac{F_G + p_\infty A_8}{A_8 \left(1 + \gamma_8 M_{8,z}^2\right)} \tag{5.6}$$

Which is a simple re-arrangement of Eqn. 2.10. Typically, a unity axial Mach number (i.e., choked exit flow) is assumed, simplifying the above equation.

$$\widetilde{p}_8 = \frac{F_G + p_\infty A_8}{A_8 \left(1 + \gamma_8\right)} \tag{5.7}$$

The corresponding total pressure (referred to as EAP), still assuming the unity exit Mach number, is then:

$$\text{EAP} = \widetilde{p}_{tz,8} = \widetilde{p}_8 \left(\frac{\gamma_8 + 1}{2}\right)^{\frac{\gamma_8}{\gamma_8 - 1}} \tag{5.8}$$

Recall that a subscript 8 denotes the exit plane conditions, a subscript "z" denotes the axial direction, and $\widetilde{(\,)}$ denotes quantities computed from the EAP methodology. This chapter dropped the subscript "e" previously used in Eqn. 2.11 to indicate this is an experimental measure for brevity. The ambient pressure (p_∞) is measured before each test. Taking the static pressure in the air plenum as an estimate of the total pressure of the reactants entering the combustor due to low speeds in the plenum ($p_3 \approx p_{t,3}$), the change in stagnation pressure between the entrance and exit to the combustor (Eqn. 5.8) defines the PG:

$$\text{PG} = \frac{\text{EAP}}{p_3} - 1 \tag{5.9}$$

The steady-state value of PG is again defined by averaging the last 0.5 seconds of the fuel-on portion. The resulting variation of PG with mass flow rate and equivalence ratio is then shown in Figure 5.8. The PG is the highest for fuel-rich cases and decreases with the equivalence ratio, suggesting better mixing processes that allow more heat to support the detonation. The slight decrease in PG with increasing mass flux for a given equivalence ratio is likely from a more significant total pressure drop across the injector with increasing flux. These results indicate that positive PG will likely occur at low mass fluxes to minimize the penalty incurred by the injector design. However, the most significant uncertainties in the gross thrust (see Figure 5.6b) occur at these lowest fluxes, posing a natural tension between precise thrust measurements and possible higher PG values. Additionally, the large error bars (described in the following section) encompass all the variations in the data, suggesting that PG may currently be too imprecise to resolve the observable trends.

To compare their measurements to the literature, Bach et al. [14] compiled the previously existing experimental and computational results of PG, reproduced in Figure 2.7. Thus, Figure

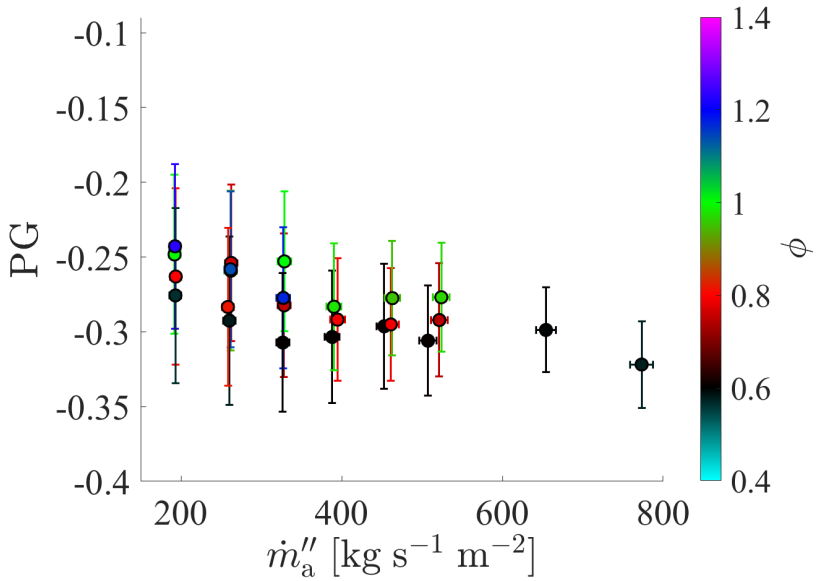

Figure 5.8: Pressure gain measurements for tested conditions; large error bars span all variations in the data.

2.7 enables comparisons between this study's PG and the values in the literature. In this study the $A_8/A_{3.2} = 0.5$ and $A_{3.1}/A_{3.2} = 0.21$ resulting in a geometric ratio of $A_8/A_{3.1} = 2.38$. Based on the compiled literature, one would expect a PG around -0.25. The results in this chapter agree with this since the PG ranged from -0.243 to -0.322. This agreement also exists despite the different injection geometry utilized here. Although this work did not focus on achieving better performance, increasing the inlet throat area (becoming more open) and lessening the total pressure drop across the injector would improve overall performance.

5.4.3 Pressure Gain Uncertainty

5.4.3.1 Random Uncertainty

The uncertainty in the estimated PG was analyzed using the same approach for the thrust measurements. Thus, this study breaks up the uncertainty of PG into the independent uncertainties of the different terms contributing to its computation and combined in quadrature:

$$\delta \mathrm{PG}^2 = \left(\frac{\partial \mathrm{PG}}{\partial F_\mathrm{G}}\delta F_\mathrm{G}\right)^2 + \left(\frac{\partial \mathrm{PG}}{\partial p_\infty}\delta p_\infty\right)^2 + \left(\frac{\partial \mathrm{PG}}{\partial p_3}\delta p_3\right)^2 \tag{5.10}$$

Appendix G gives the partial derivatives needed for Eqn. 5.10.

For now, this study assumes that the partial derivative of $M_{8,\mathrm{z}}$ with respect to anything is zero

for the time being. Meanwhile, the random uncertainties in the gross thrust, ambient pressure, and plenum pressures are available. Shown in Figures 5.9a and 5.9b are the uncertainties in the PG from the gross thrust and plenum pressure, respectively. The contribution from the ambient pressure is negligible compared to the other terms. Both uncertainties decrease with increasing flux, indicating that the sensitivity reduces with larger thrust values. The uncertainty from gross thrust is over five times that from the plenum pressure, which is, on average, only ±0.01 PG). Due to combining through quadrature, the gross thrust contributes over 93% to the combined uncertainty, Figure 5.9c, making it much more significant than the plenum pressure. Even if one cut the gross thrust uncertainty in half by removing the large uncertainty from the edge pressure (see Figure 5.6c), the gross thrust would still contribute over 80%. Thus, while the plenum pressure is not negligible in the uncertainty in PG, the thrust uncertainty would have to be reduced by nearly two orders of magnitude before it becomes the most significant source of uncertainty. Such a reduction in uncertainty would require replacing the load cell and measuring the edge pressure.

As mentioned earlier, the error bars representing this random uncertainty in Figure 5.8 are sufficiently large to obfuscate trends in equivalence ratio at a given air mass flux. The general magnitude of error bars is likely significant enough to complicate future comparisons between different injection schemes if the geometric ratios are the same. Furthermore, comparing the PG uncertainty to the PG itself shows that this uncertainty is quite significant, relatively speaking (Figure 5.9d). This impact is ±23% of the measured PG at the lowest fluxes. Even at the highest fluxes after the uncertainty decreases, there is a ±9% uncertainty in the PG value, mainly due to the substantial uncertainties in the thrust measurement.

The EAP uses a bluff body nozzle to separate the nozzle's performance (i.e., the expansion process of the nozzle) from the combustor since there is no expansion after the contraction. Because of this, a base drag measurement on the bluff body nozzle is necessary for gross thrust corrections. The previous chapter demonstrated that precise gross thrust measurements are challenging because of this base drag without proper instrumentation at the edge of the bluff body nozzle (or without making some assumption about the pressure profile). This issue can be circumvented by testing at high gross thrust conditions as the relative uncertainty decreases, but the lower thrust cases (i.e., lower fluxes) seem to have better PG. Regardless, the uncertainty makes definitive claims of positive performance even more challenging despite the conservative nature of EAP. For instance, at the largest flux tested (with the lowest uncertainty), even a PG of positive 0.03 would not have indicated definitive gain since the 95% confidence interval would still span into negative values. Overall, there is a limit to the precision of the experimental EAP methodology that requires a rigorous experimental design to mitigate.

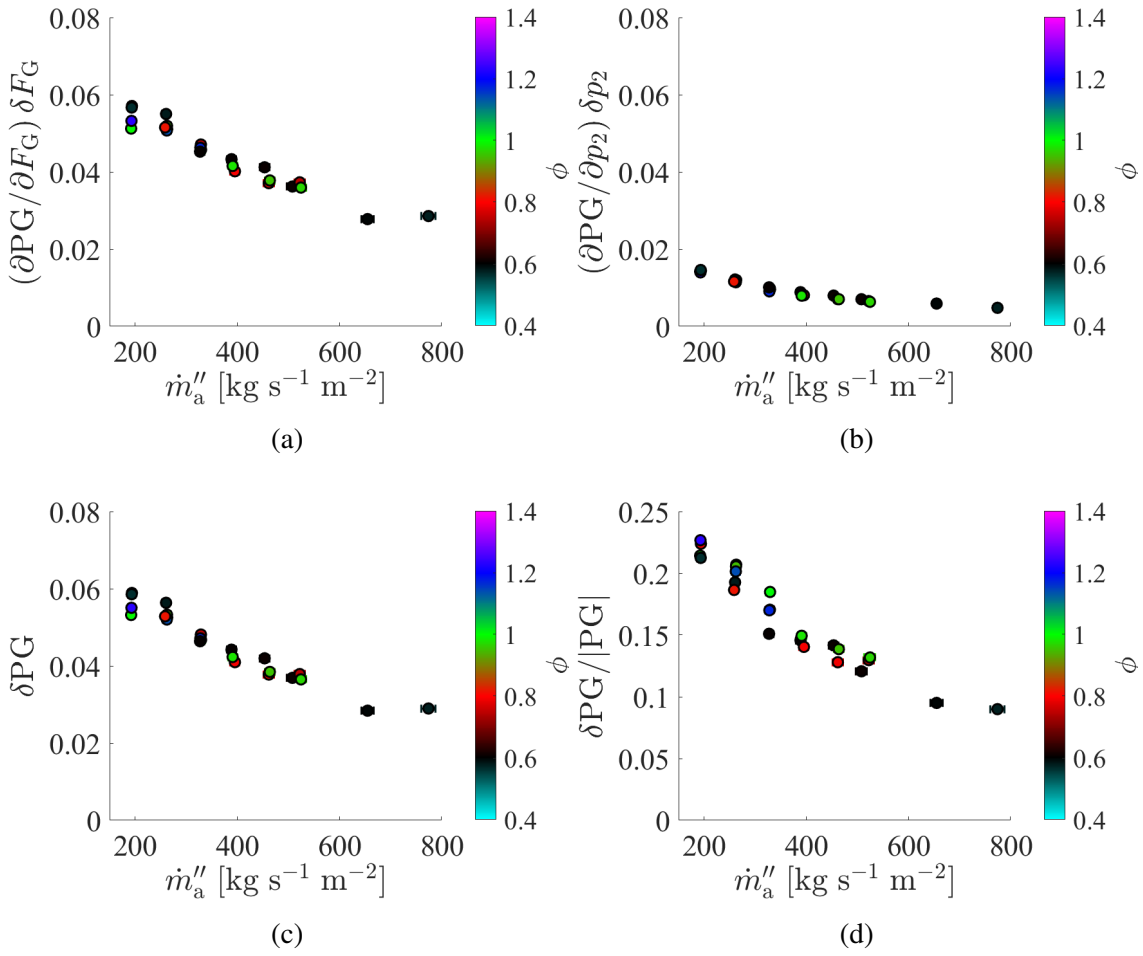

Figure 5.9: Pressure gain uncertainty introduced by a) gross thrust and b) plenum pressure measurements. The c) total and d) relative uncertainty in PG for tested conditions; higher fluxes exhibit less uncertainty.

5.4.3.2 Systematic Uncertainty

There are three identifiable sources of systematic uncertainty in the pressure gain calculation: the exit gas composition (γ_8), the exit area (A_8), and the exit Mach number ($M_{8,z}$):

$$\delta PG_{sys} = \pm\frac{\partial PG}{\partial A_8}\delta A_8 \pm \frac{\partial PG}{\partial \gamma_8}\delta\gamma_8 \pm \frac{\partial PG}{\partial M_{8,z}}\delta M_{8,z} \tag{5.11}$$

Again, Appendix G gives the above partial derivatives.

Recall that Section 5.4 previously calculated the uncertainty in γ_8 by varying the expected combustion efficiency and exit temperatures. Once propagated through the PG calculation, it is observable that a change in γ_8 would change the measured PG value in this work by at most 0.002

for the lowest mass flux tested, which is less than 1% of the PG value. This sensitivity decreases even further with increasing thrust. Fievisohn et al. performed a similar analysis considering the impacts of the change in γ_8 over a range of η_c values. They also found less than 1% variation in EAP due to the uncertainty in γ_8 and equilibrium chemistry [129]. Thus, if one measured the exit composition, it would not significantly impact the accuracy of the EAP methodology and subsequently PG.

A Monte-Carlo approach gives the uncertainty associated with machining tolerances in the exit area. The physical dimensions are assumed to follow a uniform distribution given by the machining tolerances, with the Monte-Carlo sampling revealing that the uncertainty in A_8 is ±2.7%. The computed change in PG from this uncertainty is in Figure 5.10a. Unlike most uncertainties considered thus far, the relative sensitivity of the area scales with increasing gross thrust; therefore, as the gross thrust grows with the increasing flux, so does the possible systematic uncertainty from the exit area.

This systematic uncertainty further increases the target PG to demonstrate definitive gain. For instance, consider the highest flux tested with the possible systematic uncertainty of ±0.018, which is 5.4% of the nominal PG value. Even though the random uncertainty is the smallest for this case, if everything else stays the same, a positive value of 0.05 is required to overcome the combination of the systematic and random uncertainties to demonstrate definitive gain. Overall, one can not neglect this systematic error when assessing the performance of RDCs through the EAP methodology. Thankfully, this uncertainty is controllable either by precisely measuring the area or by scaling the RDC such that the tolerances on A_8 are sufficiently small (0.1% of A_8). However, scaling the RDC may have competing effects since the gross thrust may also increase, raising sensitivity to the exit area.

The last uncertainty to evaluate is the unity Mach number at the exit plane ($M_{8,z} = 1$) assumption necessary for the EAP methodology. This assumption is likely invalid for geometries without a constriction or at low flow rates, even if the geometry does have a constriction. Subsequently, this would introduce systematic errors in calculating PG. Kaemming and Paxson analyzed the change in EAP with variation in exit Mach number when they introduced the concept of EAP [113]. They found that the variation in EAP over the range of expected $M_{8,z}$ in RDCs was about +5.4% of the EAP found with the $M_{8,z} = 1$ assumption. The choked flow assumption is conservative since it minimizes EAP while holding all other quantities constant. Using an estimated uncertainty of 5.4% in EAP, the following expression describes the impact of the assumption on $M_{8,z}$:

$$\frac{\partial \mathrm{PG}}{\partial M_{8,z}} \delta M_{8,z} = \frac{\partial \mathrm{PG}}{\partial \mathrm{EAP}} \frac{\partial \mathrm{EAP}}{\partial M_{8,z}} \delta M_{8,z} \approx \frac{1}{p_3} (\epsilon_M \mathrm{EAP}) = \epsilon_M (\mathrm{PG} + 1) \tag{5.12}$$

Where, according to the above discussion, $\epsilon_M = 0.054$. The actual sensitivity coefficient (i.e., the

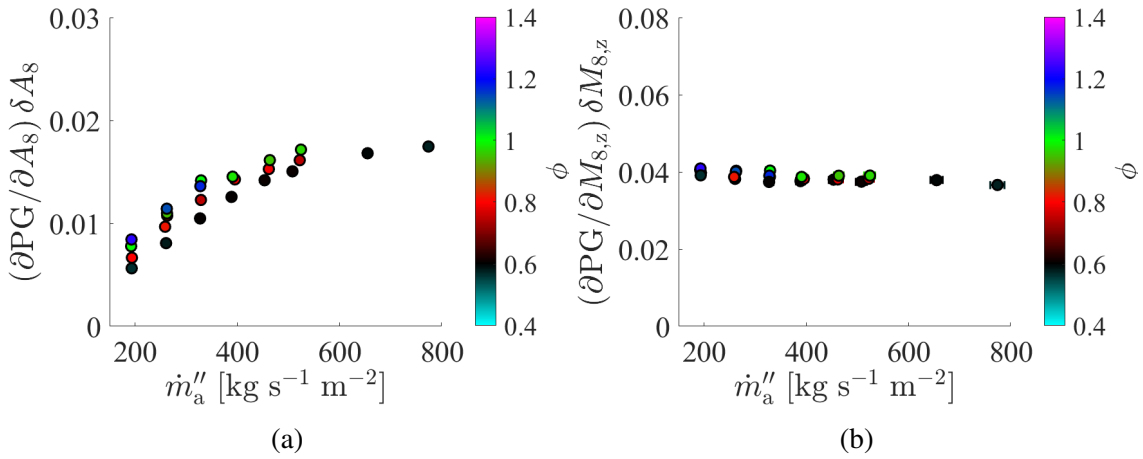

Figure 5.10: Systematic uncertainty in pressure gain introduced by a) exit area uncertainty and b) choked Mach number assumption. Exit area can increase or decrease PG while Mach number can only increase PG.

partial derivative with respect to the Mach number) is in Appendix G; however, for now, $\delta M_{8,\mathrm{z}}$ is unknown, and Eqn. 5.12 estimates the error. Due to the sonic exit flow assumption inherent to the current implementation of EAP, the systematic uncertainty will worsen once the desirable PG$\geq$ 0 is measured experimentally. Figure 5.10b provides the estimated systematic error in the PG based on the Mach number. Since the largest (least negative) PG occurred at the lowest fluxes, the largest uncertainty occurs at those fluxes, although there is no significant variation across the operating conditions. The non-unity Mach numbers can only cause the PG to grow more positive (EAP is a conservative metric); thus, Figure 5.10b should be interpreted as how much the PG could increase if a non-unity Mach number within the expected range occurred. Thus, a non-unity Mach number would be beneficial in reaching better performance (higher PG), here representing a potential relative increase of PG by 13-16%.

5.5 Some Considerations on Exit Mach Number Assumption

5.5.1 Exit Mach Number Estimation

Assuming choked flow at the exit ($M_{8,\mathrm{z}} = 1$) affects the estimated PG in a systematic and significant way and can distort conclusions on achieving a positive gain. At the lower mass fluxes, even with a nozzle constriction, it is unlikely that the combustor exit is, on average, over the cycle, choked due to the low incoming flow speeds. This section introduces an analysis that experimentally estimates the Mach number at the exit of the combustor ($M_{8,\mathrm{z}}$) from available measurements under a set of

assumptions. The estimated Mach number assesses if the assumptions used to define the EAP are valid and evaluates the systematic impact of non-unity $M_{8,z}$.

The experimental setup in this work contained a flush-mounted static pressure measurement at the exit plane of the combustor (i.e., the nozzle throat, ⑧). Since a CTAP took this measurement, this exit pressure is effectively time-averaged. This pressure measurement at this location is referred to as p_8 by analogy with the computed $\widetilde{p}_8$. A direct comparison between this measurement and $\widetilde{p}_8$ is in Figure 5.11a. Since all the data points fall above the 1:1 dashed gray line, the measured p_8 always exceeds that computed from the thrust balance in Eqn. 5.7. For this to be true, the axial Mach number must be less than unity from Eqn. 5.7. Additionally, some $\widetilde{p}_8$ values are below atmospheric. These equivalent pressures are not physically possible due to exhausting into an exhaust chamber at standard pressure, further indicative of sub-sonic Mach numbers at those conditions.

The error bars for p_8 are from the experimental calibration of the pressure sensor. The error bars are not observable in Figure 5.11a since they are approximately ±0.004 atm, smaller than the data point marker itself. Meanwhile, the error bars for $\widetilde{p}_8$ are given by:

$$\delta\widetilde{p}_8^2 = \left(\frac{\partial\widetilde{p}_8}{\partial F_\mathrm{G}}\delta F_\mathrm{G}\right)^2 + \left(\frac{\partial\widetilde{p}_8}{\partial p_\infty}\delta p_\infty\right)^2 \tag{5.13}$$

$$= \left(\frac{\delta F_\mathrm{G}}{A_8\left(1+\gamma_8 M_{8,\mathrm{z}}^2\right)}\right)^2 + \left(\frac{\delta p_\infty}{1+\gamma_8 M_{8,\mathrm{z}}^2}\right)^2 \tag{5.14}$$

In the above relationship, the uncertainty contributed by the ambient pressure is negligible (by several orders of magnitude) compared to that from the thrust. The uncertainty in $\widetilde{p}_8$ increases with mass flux going from 0.04 atm to 0.08 atm. The uncertainty in $\widetilde{p}_8$ also increases with increasing equivalence ratio.

The following relationship gives the systematic uncertainty sources:

$$\delta\widetilde{p}_{8,\mathrm{sys}} = \pm\frac{\partial\widetilde{p}_8}{\partial A_8}\delta A_8 \pm \frac{\partial\widetilde{p}_8}{\partial\gamma_8}\delta\gamma_8 \pm \frac{\partial\widetilde{p}_8}{\partial M_{8,\mathrm{z}}}\delta M_{8,\mathrm{z}} \tag{5.15}$$

$$= \pm\frac{F_\mathrm{G}}{A_8^2(1+\gamma_8 M_{8,\mathrm{z}}^2)}\delta A_8 \pm \frac{\widetilde{p}_8 M_{8,\mathrm{z}}^2}{1+\gamma_8 M_{8,\mathrm{z}}^2}\delta\gamma_8 \pm \frac{2\widetilde{p}_8\gamma_8 M_{8,\mathrm{z}}}{1+\gamma_8 M_{8,\mathrm{z}}^2}\delta M_{8,\mathrm{z}} \tag{5.16}$$

For now, this analysis neglects the uncertainty introduced by the Mach number and assumes that the exit is choked to reflect the EAP methodology. The relative uncertainties introduced by A_8 and γ_8 in Figure 5.11b are represented with triangles and squares, respectively. Importantly, Figure 5.11b allows for comparisons against the random thrust uncertainty (circles). Unlike the random uncertainty, the relative systematic uncertainty increases with increasing gross thrust, ranging from

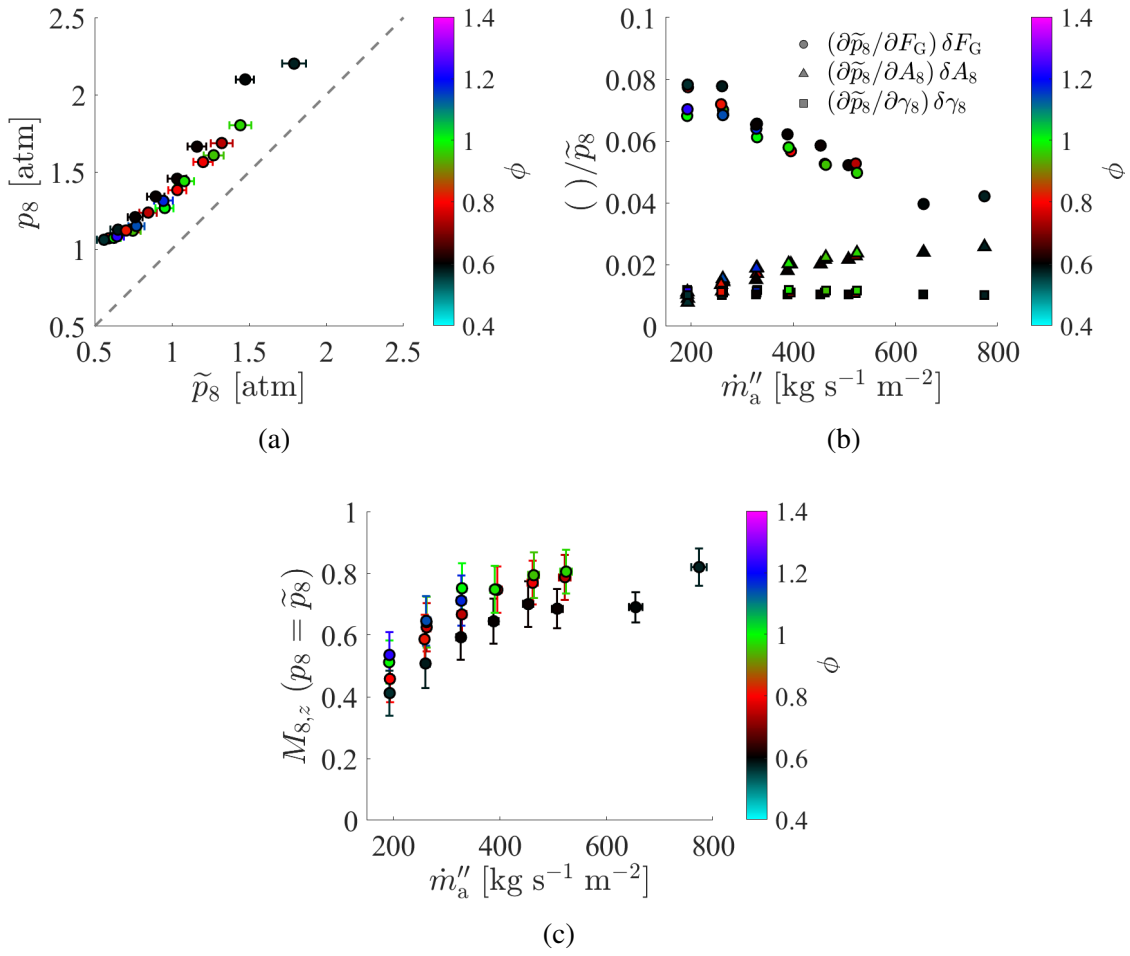

Figure 5.11: a) Comparison between measured static pressure (p_8) and the estimated static pressure ($\widetilde{p}_8$) from the thrust balance equation. Discrepancy implies subsonic Mach numbers. b) Relative uncertainty in $\widetilde{p}_8$ across tested conditions. c) Cycle-averaged exit Mach number computed by matching p_8 and $\widetilde{p}_8$. All Mach numbers are subsonic.

0.8% to 2.5% for A_8 and 0.7% to 1% for γ_8. The thrust uncertainty is still overall more significant for all the conditions tested. Still, it is possible that at higher mass fluxes, the systematic uncertainty may grow larger than the random uncertainty.

Even if one considers the maximum expected systematic error from A_8 and γ_8 with the random uncertainty, the estimated static pressure never matches the experimentally measured version. Thus, the discrepancy between these pressures must reflect a systematic error in the choked Mach number assumption. Therefore, the difference can estimate the cycle-averaged axial Mach number at the exit. An estimated exit Mach number comes from re-arranging Eqn. 5.7 and imposing that the

measured pressure and the pressure from the thrust balance match ($p_8 = \widetilde{p_8}$),

$$M_{8,z}^2 = \frac{1}{\gamma_8}\left(\frac{F_G + p_\infty A_8}{p_8 A_8} - 1\right) \tag{5.17}$$

Solving this equation results in a Mach number (averaged over the steady portion) that ranges between 0.4 and 0.8 across the mass fluxes tested, Figure 5.11c. These results contrast the unity Mach number assumption in the EAP methodology. The subsonic cycle-averaged Mach numbers occur despite the presence of an area contraction. Up until 450 kg s^{-1} m^{-2}, the Mach number increases with mass flux; however, it reaches an asymptotic value of 0.8 after this flux, indicating that a fully choked exit is not likely by this metric. An equivalence ratio dependence is observable such that higher equivalence ratios result in greater axial Mach numbers, although the cause is unknown.

The error bars for the random uncertainty, Figure 5.11c, were generated according to:

$$\delta M_{8,z}^2 = \left(\frac{\partial M_{8,z}}{\partial F_G}\delta F_G\right)^2 + \left(\frac{\partial M_{8,z}}{\partial p_\infty}\delta p_\infty\right)^2 + \left(\frac{\partial M_{8,z}}{\partial p_8}\delta p_8\right)^2 \tag{5.18}$$

$$= \left(\frac{1}{\gamma_8 p_8 A_8}\delta F_G\right)^2 + \left(\frac{1}{\gamma_8 p_8}\delta p_\infty\right)^2 + \left(-\frac{(M_{8,z} + 1/\gamma_8)}{p_8}\delta p_8\right)^2 \tag{5.19}$$

Once again, the uncertainty due to the pressure terms is negligible compared to the thrust uncertainty. The error bars range from ±0.05 at the highest flux to ±0.08 at the lowest flux, with a slight negative dependence on mass flux.

The remaining systematic uncertainty comes from:

$$\left(\partial M_{8,z}\right)_{sys} = \pm\frac{\partial M_{8,z}}{\partial \gamma_8}\delta\gamma_8 \pm \frac{\partial M_{8,z}}{\partial A_8}\delta A_8 \tag{5.20}$$

The sensitivities to γ_8 and A_8 increase with increasing gross thrust (mass flux). At the lowest flux conditions, the possible systematic uncertainties from γ_8 and A_8 are ±0.007, an order of magnitude less than the random uncertainty. However, at the largest flux case, the uncertainty from γ_8 becomes ± 0.017 while the uncertainty from A_8 increases to ±0.037, comparable to the random uncertainty. However, even at the largest mass fluxes tested, the combination of error bars and maximum expected systematic uncertainty are still below a unity Mach number, indicating that, by this metric, a unity Mach number occurs.

Since $\widetilde{p_8}$ originates from the basic thrust equation, it may be a fictitious pressure instead of a cycle-averaged pressure, unlike the measurement. In that case, the calculated Mach number would not reflect reality, and this work has not directly evaluated this. Alternatively, this work proposes a second method to assess the exit Mach number by imposing mass continuity through

the system. Using the measured static pressure, an assumed gas composition, and a measure of the cycle-averaged temperature, the exit Mach number can be estimated as:

$$M_{8,\mathrm{z}} = \frac{\dot{m}_{\mathrm{T}}\sqrt{R_8 T_8}}{p_8 A_8 \sqrt{\gamma_8}} \tag{5.21}$$

where $\dot{m}_{\mathrm{T}}$ is the sum of the air and fuel mass flow rates.

This study included a type-B thermocouple flush mounted at the nozzle throat, similar to the static pressure measurement, to estimate the exit gas temperature. The measurement accuracy is subject to the thermocouple leads not being in the flow, wall heating, etc. However, this study assumes that the measurement provides a reasonable temperature estimation, albeit with imposed uncertainties of a few hundred Kelvin (arbitrarily chosen to be 400 K for the uncertainty analysis). Figure 5.12a shows the steady-state temperatures across the different operating conditions. An apparent increase in the measured temperature due to increasing mass flux and equivalence ratio is observable across most conditions. There is a jump in temperature between 190 kg s^{-1} m^{-2} and 260 kg s^{-1} m^{-2}, likely caused by an increase from one to two waves. The error bars are arbitrarily large; thus, they do not necessarily reflect the uncertainty of the measurement, but they were selected to demonstrate the sensitivity to this quantity. Overall the measured temperatures are comparable to the cycle-averaged exit conditions seen in computational work [102] and experimental work that used CARS thermometry [185].

The computed steady-state values of $M_{8,\mathrm{z}}$ using the temperature measurement are in Figure 5.12b. Similar to the previous analysis, the results indicate that for all mass fluxes tested, $M_{8,\mathrm{z}}$ is subsonic and seems to be approaching an asymptomatic value of about 0.8 after 450 kg s^{-1} m^{-2}, depending on the equivalence ratio. These results seem to agree with the results presented in Figure 5.11c, but a discussion on the sources of uncertainty is necessary before the direct comparisons. The propagation of the random uncertainties in calculating the Mach number in this way is as follows:

$$\delta M_{8,\mathrm{z}}^2 = \left(\frac{\partial M_{8,\mathrm{z}}}{\partial \dot{m}_{\mathrm{T}}}\delta\dot{m}_{\mathrm{T}}\right)^2 + \left(\frac{\partial M_{8,\mathrm{z}}}{\partial T_8}\delta T_8\right)^2 + \left(\frac{\partial M_{8,\mathrm{z}}}{\partial p_8}\delta p_8\right)^2 \tag{5.22}$$

$$= M_{8,\mathrm{z}}^2\left[\left(\frac{\delta\dot{m}_{\mathrm{T}}}{\dot{m}_{\mathrm{T}}}\right)^2 + \left(\frac{\delta T_8}{2T_8}\right)^2 + \left(\frac{\delta p_8}{p_8}\right)^2\right] \tag{5.23}$$

The δT range (400 K) is comparable, albeit slightly greater, than the spread in data observed by Athmanathan et al., where they experimentally measured the exit temperature [185]. Unsurprisingly, the considerable uncertainty in temperature causes it to be the primary source of uncertainty in $M_{8,\mathrm{z}}$, contributing over 95% in quadrature. The error bars are ±0.1 at the low fluxes but grow to ±0.15 at the higher fluxes, which are greater than the uncertainties in the other method for computing

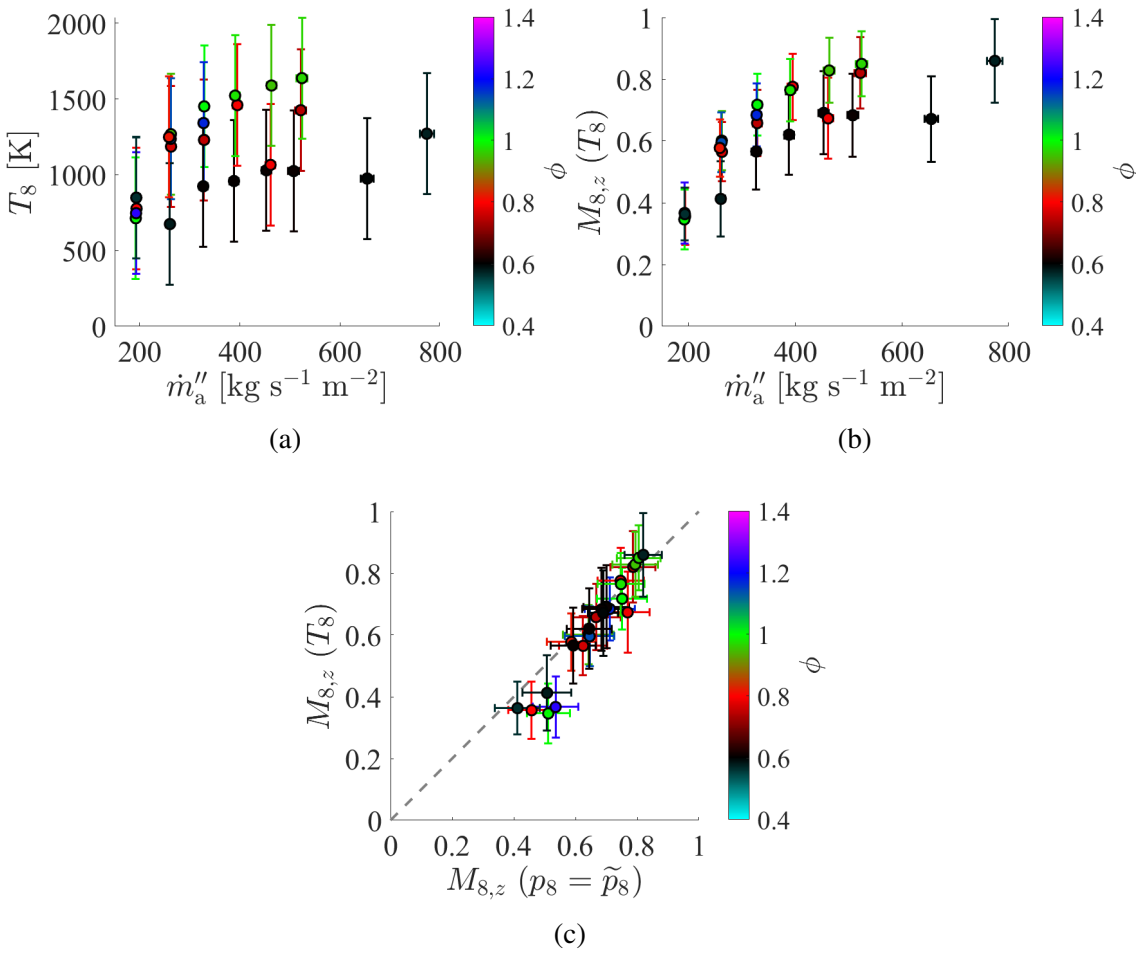

Figure 5.12: a) Cycle-averaged exit temperature across tested conditions. b) Cycle-averaged exit Mach number across all operating conditions is subsonic. c) Comparison between different methods for estimating exit Mach number.

Mach number. The selection of the considerable uncertainty on the temperature measurement was intentional, and more precise temperature measurement through laser diagnostics or a better understanding of how well a thermocouple can capture the average temperature of the flow will vastly improve this analysis.

Unlike the initial method for computing the Mach number, Eqn. 5.17, the gas constant (R_8) acts as another source of systematic uncertainty:

$$(\delta M_{8,z})_{sys} = \pm\frac{\partial M_{8,z}}{\partial R_8}\delta R_8 \pm \frac{\partial M_{8,z}}{\partial A_8}\delta A_8 \pm \frac{\partial M_{8,z}}{\partial \gamma_8}\delta\gamma_8 \tag{5.24}$$

$$= M_{8,z}\left[\pm\frac{\delta R_8}{2R_8} \pm \frac{\delta A_8}{A_8} \pm \frac{\delta\gamma_8}{2\gamma_8}\right] \tag{5.25}$$

Section 5.4.1 previously estimated the uncertainty in R_8 by varying the combustion efficiency over a wide range of possible values. The uncertainty was approximately $0.06R_8$ with slight variations depending on the equivalence ratio. The uncertainties in A_8 and γ_8 are $0.027A_8$ and $0.04\gamma_8$ respectively. These systematic uncertainties could increase/decrease the Mach number by nearly 10% of the nominal value. Thus, the systematic uncertainty is on the same scale as the random uncertainty.

Qualitatively, the trends with both mass flux and equivalence ratio match the trends first observable by matching the static pressure to the equivalent static pressure, Figure 5.11c. In the direct comparison between the Mach numbers from the two methods, Figure 5.12c., nearly all the data clusters are around the 1:1 dashed, gray line, which shows that the Mach numbers are almost identical between the two methods. Even for the data points further off the line (at the lower Mach numbers), the combination of the vertical and horizontal error bars still captures the 1:1 line in the spread. This result is perhaps unsurprising since both methods depend on the measured p_8, and this comparison only cross-validates instead of demonstrating accuracy to the actual Mach number.

However, a thrust measurement is not utilized in computing the Mach number from imposing mass continuity (Eqn. 5.21). Thus, a PG measurement can be performed with static pressure and temperature (thermocouple) measurements at the exit plane instead of measuring thrust with a thrust stand and performing base drag corrections. Essentially, the cycle-averaged pressure measurement is analogous to the equivalent pressure from the thrust balance equation ($p_8 = \widetilde{p}_8$). While the NPS method [120] also does not require a thrust measurement, using area-Mach relations is necessary. Additionally, measurements in the detonation channel can be influenced by where the detonation wave resides; measuring at the axial location where the detonation wave is would result in higher static pressure. Measuring at the throat avoids the complexity of the axially varying pressure profile, another advantage of this method.

5.5.2 Impact of Non-Choked Exit Conditions

A non-unity $M_{8,\mathrm{z}}$ can be readily introduced in the definition of EAP by using the isentropic flow relationship to find EAP from $\widetilde{p}_8$ including the estimated $M_{8,\mathrm{z}}$ values. The resulting form that includes a non-unity $M_{8,\mathrm{z}}$ is:

$$\mathrm{EAP}(M_{8,\mathrm{z}}) = \widetilde{p}_8 \left(1 + \frac{\gamma_8 - 1}{2} M_{8,\mathrm{z}}^2\right)^{\frac{\gamma_8}{\gamma_8 - 1}} \tag{5.26}$$

$$= \left(\frac{F_\mathrm{G}}{A_8} + p_\infty\right) \frac{\left(1 + \frac{\gamma_8 - 1}{2} M_{8,\mathrm{z}}^2\right)^{\frac{\gamma_8}{\gamma_8 - 1}}}{\left(1 + \gamma M_{8,\mathrm{z}}^2\right)} \tag{5.27}$$

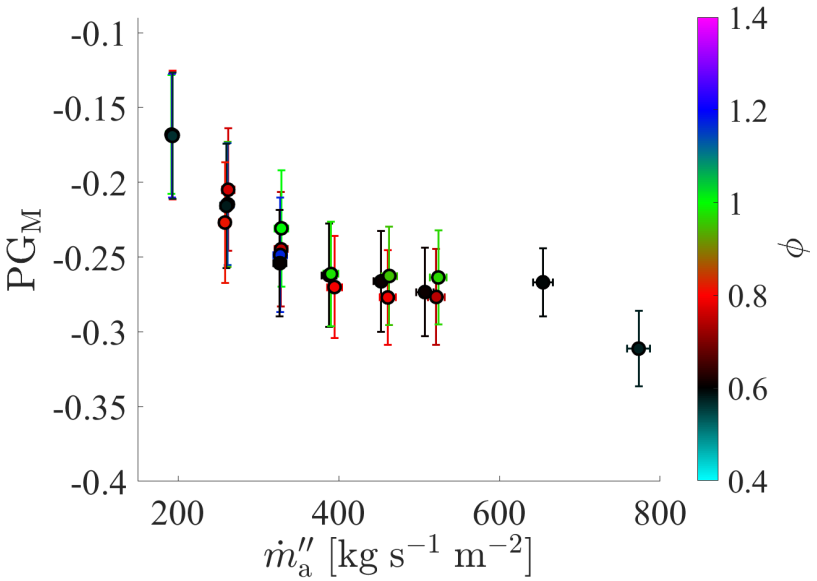

Figure 5.13: Modified PG with estimated exit Mach number correction for tested conditions. The best performance of RDC at lowest tested mass fluxes.

From which a modified PG (PG_M) that includes a non-unity $M_{8,z}$ is:

$$PG_M = \frac{EAP(M_{8,z})}{p_3} - 1 \tag{5.28}$$

5.17 This analysis used the Mach number from Eqn. 5.17, although Eq. 5.21 is equally applicable. The modified PG, Figure 5.13, has a more pronounced trend with mass flux rate compared to the traditional PG, Figure 5.8. The decreasing relationship with mass flux directly results from the increasing exit Mach number and pressure drop across the injector with increasing flux. These results further support the hypothesis that the best performance occurs by minimizing the pressure drop across the injector with low mass fluxes. The case with the least negative PG_M value, which occurs at the lowest Mach number (lowest mass flux), is now -0.174 compared to the previous -0.251. While still not demonstrating positive gain here, an increase in PG by about 0.08 for designs that demonstrate $-0.1 \leq PG \leq 0$ could be sufficient to show either positive or neutral PG.

For a more thorough comparison between the two PGs, consider Figure 5.14a. The dashed, gray line is the 1:1 line, and the color bar marks the exit Mach number estimated for that operating condition (Figure 5.11c). As anticipated, the modified PG with a subsonic $M_{8,z}$ is always above the 1:1 line by having larger (less negative) PG values. When $M_{8,z}$ reaches about 0.8 (light orange data points), there is little difference between the modified and original values of the PG. Importantly, the difference between the two computed PGs at the lowest Mach numbers is greater than the 95% confidence intervals (error bars). A further comparison, Figure 5.14b, shows the percent difference

between the two forms of PG as a function of mass flux and equivalence ratio (color-bar). At higher fluxes (where the Mach number asymptotes to 0.8), there is only a 5% error without the Mach number correction, consistent with the approximated 5.4% uncertainty in EAP highlighted in Eqn. 5.12. However, the error can grow as large as 38% at lower mass fluxes. Assuming the assumptions for the estimated Mach number presented here hold, this means that the EAP methodology significantly under-predicts the performance of the combustor at the low mass fluxes but is fairly accurate at fluxes greater than 450 kg s^{-1} m^{-2}.

The error bars for the modified PG are from the following equation:

$$\delta \mathrm{PG}_{\mathrm{M}}^2 = \left(\frac{\partial \mathrm{PG}_{\mathrm{M}}}{\partial F_{\mathrm{G}}}\delta F_{\mathrm{G}}\right)^2 + \left(\frac{\partial \mathrm{PG}_{\mathrm{M}}}{\partial p_{\infty}}\delta p_{\infty}\right)^2 + \left(\frac{\partial \mathrm{PG}_{\mathrm{M}}}{\partial p_3}\delta p_3\right)^2 + \left(\frac{\partial \mathrm{PG}_{\mathrm{M}}}{\partial p_8}\delta p_8\right)^2 \tag{5.29}$$

This equation is similar to Eqn. 5.10 with the added term that includes the contribution of the measured exit pressure since the Mach number depends on it. Another important distinction is how $\partial \mathrm{PG}_{\mathrm{M}}/\partial M_{8,\mathrm{z}}$ is treated. Instead of being a separate uncertainty term, its impact on the PG is in the partial derivatives of PG (through the product rule). The partial derivatives are not shown here but can be found in full in Appendix G.

As expected from the results of the PG computed using the choked assumption, the gross thrust is the driving force of the uncertainty. Compared to the uncertainty from the pressure terms, the gross thrust contributes over 90% of the error in quadrature, with the plenum pressure providing the remaining uncertainty. The ambient pressure uncertainty was negligible, similar to the results shown in Figures 5.9a and 5.9b. Figure 5.14c compares the uncertainty (a stand-in for precision) for computing the PG with and without the unity Mach number assumption. Similar to Figure 5.14a, the dashed, gray line is the 1:1 line, and the color bar marks the exit Mach number estimated for that operating condition (Figure 5.11c). Generally, the data points fall below the 1:1 line, indicating improved precision and lower uncertainty for the modified PG. This improved precision results from the sensitivity coefficients (i.e., partial derivatives) of the individual measurements in Eqn. 5.10 decreasing with $M_{8,\mathrm{z}}$; see Appendix G. The two uncertainties converge more as the Mach number grows closer to unity.

The data points shown in Figure 5.14c are technically slightly misleading since the range of Mach numbers considered in δ PG was between 0.8 and 1.2 based upon the results from Kaemming and Paxson [113]. The Mach numbers presented in this work (Figures 5.11c and 5.12b) can fall below the 0.8 bound. With this information, the uncertainty due to the un-evaluated Mach number would grow, causing δ PG to grow. In turn, this would cause the data points in Figure 5.14c to potentially fall even further below the 1:1 line, further indicating an increase in precision. Finally, the possible systematic uncertainty from the exit area remains in the modified PG, although the sensitivity to area variations decreases slightly with a subsonic Mach number, further increasing

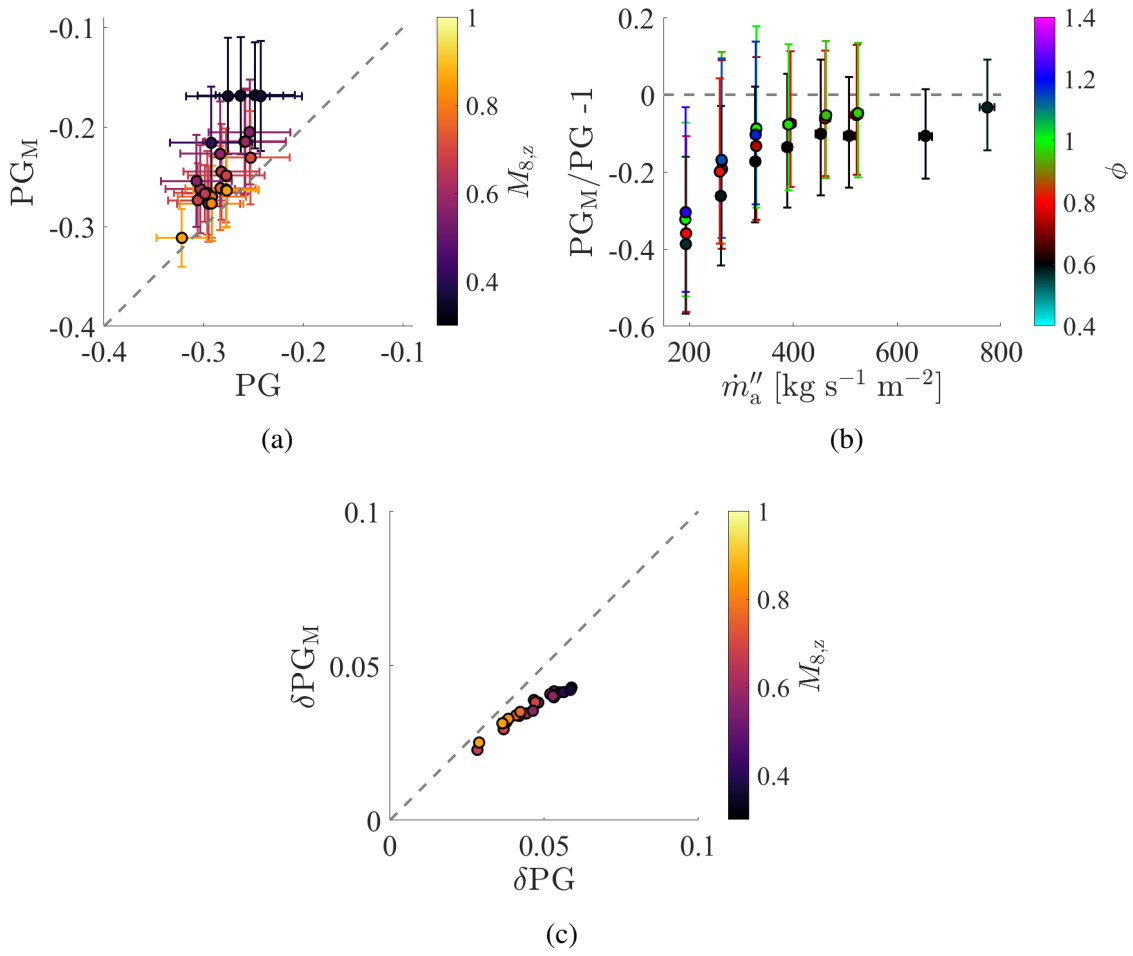

Figure 5.14: a) Comparison between modified pressure gain with Mach number correction (PG_M) and pressure gain with the choked assumption (PG). Subsonic flow causes PG_M to be larger when the exit Mach number is below 0.8. b) Ratio of PG_M and PG across test conditions. c) Uncertainty comparison of PG_M and PG with choked assumption.

the precision of the measurement.

5.6 Discussion

This work presents a methodology to identify and quantify the systematic and random uncertainty of the thrust measurement produced by an RDC to estimate the EAP in an experimental setup. Some sources of uncertainty can be reduced through design, although some uncertainty sources are inevitable (e.g., individual measurements). For instance, consider the base drag acting upon the exit flange. Even in testing rigs that are open to the atmosphere, some base drag would exist due to flow re-circulation caused by the flow leaving the annulus. These flange areas can be quite large such

that even slight differences in pressure result in large forces and/or force uncertainties. The size also causes proper instrumentation to be impractical; thus, the drag is either neglected or only has a few measurement points. This study demonstrated that this area can be minimized and instrumented for a rig exhausting into a closed chamber, thereby improving the gross thrust measurement. Another step to improve the measurement is to either have a proper edge measurement on the truncated nozzle or switch integration schemes to a Gauss-Kronrod scheme to eliminate the strong dependence on the edge pressure. Other steps to improve gross thrust include removing the sources of systematic error caused by machining tolerances by measuring the inner and outer diameter at the exit plane via a metrology lab. Thus, although the error bars for gross thrust and subsequently PG are larger currently, future experimental designs can take advantage of the results of this work to improve precision, which will be vital for net positive gain demonstration. As is, the current EAP has limited precision and accuracy, which hinders the goal of showing definitive pressure gain across RDCs.

The PG in this work follows the conventional definition by comparing the total pressure at the outlet to the total pressure of the oxidizer plenum. However, the merits of this definition have been questioned in recent work since it does not account for the fuel plenum pressure [112, 50]. Plaehn et al. and Shepard independently argued that not accounting for the fuel plenum pressure prevents an accurate representation of the total energy available to the system and does not account for the additional thrust that could be provided by merely raising the fuel plenum pressure [112, 50]. Using the results from a RDC operated with gaseous oxygen and a natural gas-operated RDC, Plaehn et al. showed that by neglecting the fuel pressure, an overestimation of the PG is made [112]. In particular, the relative difference was about 15-20%, comparable to this work's uncertainties. Likewise, Shepard suggested that the fuel plenum pressure is often significantly greater than the oxidizer plenum; thus, if the PG is defined to include the fuel pressure, it would be less than the already negative PG values [50]. While this would seemingly be a systematic error in PG, it is more appropriate to distinguish the two measures of PG. This study found the uncertainty in the total pressure at the outlet (the EAP) as it is being measured indirectly in experiments through assumptions. Choosing what the total pressure is referenced against, while it can effectively change the result, is then not inherently a source of measurement uncertainty in the EAP method.

The subsonic cycle-average exit Mach numbers require further discussion. First, consider the air inlet of the RDC. Intuitively, the flow chokes in the throat of the inlet from high flow rates and small areas. However, an area-averaged Mach number computed using a static pressure measurement in the plenum is below one, suggesting the inlet is not choked [186]. This result comes from neglecting the unsteadiness induced by the detonation wave. After the passage of the detonation wave, a portion of the annulus becomes unchoked from the elevated pressure. The injector then recovers until the local flow is choked again at circumferential locations far from the detonation wave. The unchoked portion is typically thought of as the result of fluidic "blockage" [47, 139].

Thus, the average Mach number across the annulus would have to be less than one for any amount of blockage, recovering back to the steady-state result [186]. It is theorized a similar unsteadiness effect at the exit plane prevents the entire exit annulus from being choked, thereby resulting in subsonic area-averaged Mach numbers. While the detonation wave likely does not extend to the exit plane, the attached downstream propagating oblique shock wave could cause local subsonic flow, thereby introducing asymmetry.

Both methods presented here for finding the Mach number demonstrate a below unity area-average Mach number; however, they both relied upon a single static pressure measurement. A CTAP measurement is more akin to a time-average across many detonation cycles, which is assumed to match the area-average across the annulus; see Section 2.6 and Appendix A. The usage of a CTAP measurement in determining the total pressure at the exit is reminiscent of the colloquially termed "NPS Method" developed by Codoni and Brophy [114, 120], which uses CTAP measurements in the channel and area-Mach relations to compute $\widetilde{p}_{t,8}$; see Section 2.6. However, Codoni et al. have found that an asymmetrical static pressure profile can exist around the annulus even in the CTAP measurements [120]. Overall, more CTAPs and/or additional diagnostics at the exit plane in the future will be crucial to further characterize the performance of RDCs through additional insight into the "average" exit state. While the EAP remains a conservative metric by assuming a unity Mach number, it is left up to the reader to decide whether they wish to evaluate the performance of the Mach-corrected EAP presented here in addition to the conservative form of EAP. The conservative (traditional) EAP should still be reported in future work to better compare against previous literature, and subsequent chapters in this work will do this.

CHAPTER 6

Pressure Gain Invariant to Changes to Detonations Caused by Combustor Length

6.1 Introduction

With the method of measuring PG and quantifying the uncertainty in said PG established in the previous chapters, the remaining two chapters interrogate certain parts of the RDC flowfield with targeted geometric changes to observe whether there are measurable changes to performances associated with those changes. This chapter focuses on addressing two primary questions. First, do the details of the operational mode or wave dynamics matter with regard to performance as measured by the PG? In the literature, the expected PG is distilled down to the area ratio of the inlet throat to the outlet throat and the incoming mass flux [170]. However, this approach obfuscates the various operational modes and physics occurring within the combustor by disregarding the specifics of the detonation wave(s). The disconnect between global performance (PG) and details about the operational mode has seen minimal exploration [187, 136], despite much of early RDC research focusing on the "quality" of the detonation wave in regards to the CJ condition [10, 11, 43]. Additionally, in work by Walters et al., [119], a non-detonative case effectively achieved the same PG as a detonative case, which is concerning. This chapter investigates this gap by focusing on creating changes in the detonation wave dynamics through combustor length changes without changing the inlet and outlet areas.

Experimentally, several groups demonstrated that the thrust and specific impulse of RDCs with rocket injectors do not significantly change with length alterations [136, 137, 138]. Therefore, the second question of this chapter is: does the performance insensitivity as measured by specific impulse with respect to combustor length extend to performance as measured by PG? While thrust and specific impulse are helpful performance metrics, they neglect the increase in plenum pressure needed to drive the bulk flow in RDCs [139]. For instance, a combustor with a smaller plenum pressure and the same specific impulse performs better than another combustor requiring a higher plenum pressure to achieve the same specific impulse.

Configuration	L [mm]	d_i [mm]	d_o [mm]	$A_8/A_{3.2}$	$A_{3.2}/A_{3.1}$	$L/\pi d_\mathrm{m}$
A	71	139	154	0.50	4.65	0.154
B	102	139	154	0.50	4.65	0.222
C	118	139	154	0.50	4.65	0.256
D	137	139	154	0.50	4.65	0.298

Table 6.1: Relevant geometric parameters of tested RDC configurations. Variables (in order are): L, combustor length; d_i, inner diameter of annulus; d_o, outer diameter of annulus; $A_8/A_{3.2}$, ratio between exit throat and annulus areas; $A_{3.2}/A_{3.1}$, ratio between annulus and air inlet throat areas; $d_\mathrm{m} = 1/2\,(d_\mathrm{i} + d_\mathrm{o})$, mean annulus diameter

This study addressed both questions by systematically varying the length and testing the RDC across a parametric study of air and H_2 flow rates for each discrete length. The differences in operational mode and wave dynamics were categorized and characterized for each combustor length. Here, wave dynamics refers to the collection of the wave number (multiplicity), speed, and strength. High-speed pressure transducers and an aft high-speed chemiluminescence video evaluated such metrics within the RDCs. This work identifies two operational modes that do not conform to the standard notions of stable operation, and statistical approaches are applied to characterize them properly. Meanwhile, the approach detailed in the previous chapters quantified each configuration's performance (thrust and PG). Therefore, the performance of the RDC as measured by EAP and PG were directly compared to both the length changes and the changes in the detonation wave(s) and their associated operational modes.

6.2 Geometry and Tested Operational Conditions

As mentioned in Section 3.2.3, this study considered four different combustor lengths while the inlet and outlet geometries remained constant. The combustor lengths (L), defined from the end of the inlet throat (end of constant area portion) to the exit throat, were 71, 102, 118, and 137 mm. These are labeled configurations A, B, C, and D in Table 3.2, reproduced here as Table 6.1 for convenience. Throughout this chapter, the different lengths will be referred to by the configuration name for brevity. In addition to the aforementioned geometric parameters, the length normalized by the mean annulus circumference, $\pi d_m = \pi(d_\mathrm{i} + d_\mathrm{o})/2$, is given to draw comparisons to a similar work by Bluemner et al. [133].

This study considered a parametric study of a discrete combination of air mass fluxes, from 150 kg s^{-1} m^{-2} to 650 kg s^{-1} m^{-2}, and equivalence ratios, 0.6 to 1.2, of H_2/air operation. Visual representations of the test matrices, Figure 6.1, contain additional details that the following sections will discuss further. Overall, all tests exhibited sustained rotating detonative operation. Unlike

other work in literature [133], no longitudinal pulsing was observed despite the relatively small $L/\pi d_{\mathrm{m}}$. The lack of pulsations could result from different injection geometry or higher mass fluxes. As discussed in previous chapters, the testing duration was 4 seconds to achieve a quasi-steady thrust measurement and perform mass flow rate ramping. Both the air and mass flow rates reached a steady state value with about 1-2 seconds remaining during the run.

6.3 Classification of Wave Mode with Respect to Length

This section will address the changes to the detonation wave system induced by varied combustor lengths before discussing the results from the performance measurements. In doing so, the changes or lack thereof in the performance metrics can be contextualized with respect to the detonation wave(s) instead of in isolation to the changes to the wave(s). This section focuses on identifying and classifying the various operational modes observed in this study, whereas the following section (Section 6.4) provides quantitative statistical measurements of the wave properties, like speed and pressure ratio. After the classification and characterization of wave modes, Section 6.5 will present the performance measurements.

The classification of the operational mode of a RDC identifies whether the pressure waves or combustion occur in a rotating, pulsed [133], or deflagrative manner. Often, the operational mode also defines a sub-classification of a rotating mode based on the distinct features of the wave system, whether that be the number of waves (multiplicity), the relative propagation direction of multi-wave systems, a measure of the temporal steadiness of the mode, number of secondary waves [45], etc. Since every test from this study exhibited sustained rotating detonation waves, the focus here is on the later description of the operational mode. This study observed five distinct operational modes of rotating detonation wave(s). These were as follows:

1. **Mode 1:** Single wave (1W)
2. **Mode 2:** Two co-rotating, *indistinguishable* waves (2WI)
3. **Mode 3:** Two co-rotating, *distinguishable* waves (2WD)
4. **Mode 4:** Multiple waves that follow a transient super cycle (TSC)
5. **Mode 5:** Chaotic operation of multiple waves (CH)

The first two operational modes are commonly observed throughout the literature and do not require much additional description [43]. Instead, the description of 2WI is provided primarily to juxtapose the latter operational modes. To the authors' knowledge, 2WD and TSC have not been described

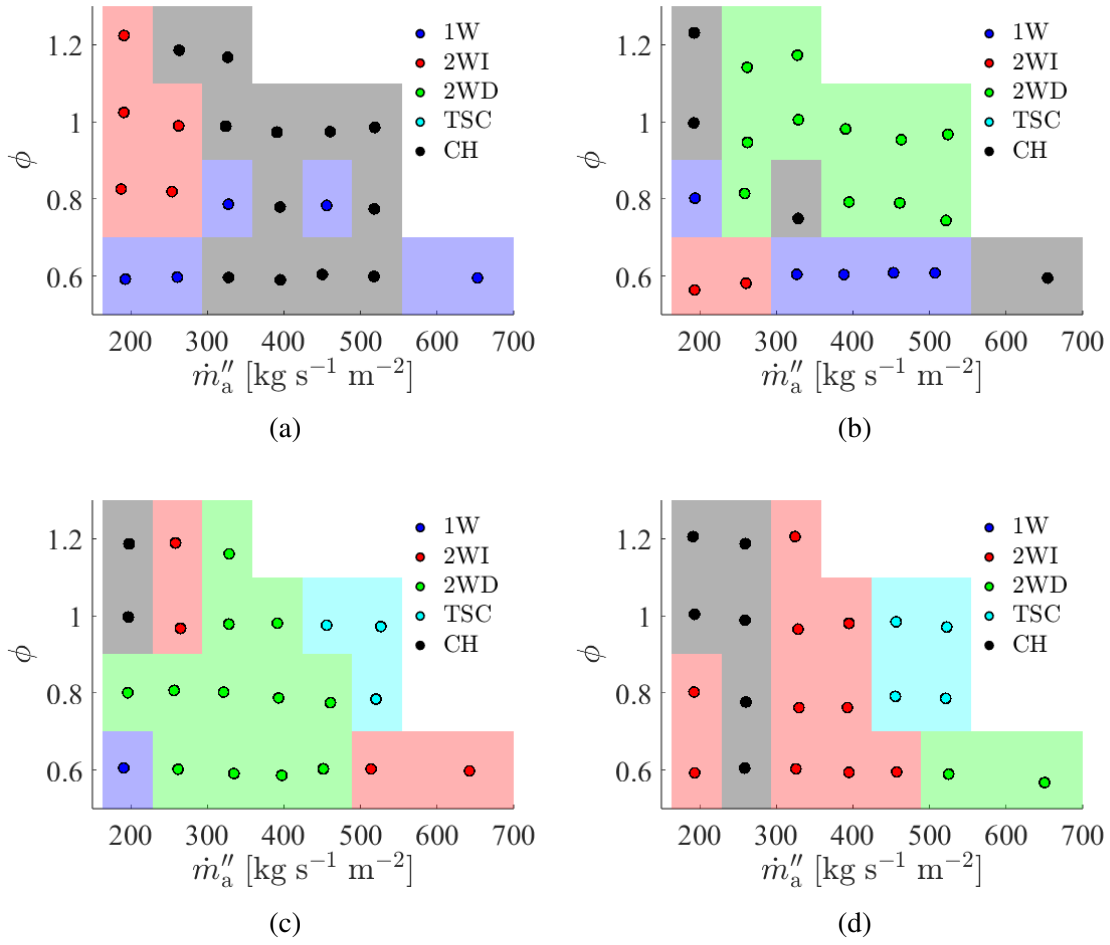

Figure 6.1: Map of operational modes for Configurations. a) A, b) B, c) C, and d) D.

before this work. For conciseness, this study does not consider further sub-classifications based on the number of secondary waves [45] or the detonation wave(s) speed.

This section will discuss additional details later; however, the maps between test conditions and the operational mode for each tested configuration, Figure 6.1, provide needed initial contextualization. Figures 6.1a, 6.1b, 6.1c, and 6.1d are for configurations A, B, C, and D respectively. The color of the individual markers denotes the classified operational mode. Likewise, the shaded regions match the colors of the markers, added to highlight the regions at which a particular operational mode was common. Discerning the trends between the different configurations is challenging; however, some general observations are possible. First, the number of waves typically increases with length, as evidenced by SW (blue) effectively not existing in configurations C and D. Second, configuration A, the shortest combustor, had more CH (black) operation than the other configurations, with it being its most common operation mode. Third, either 2WI (red) or CH replace the

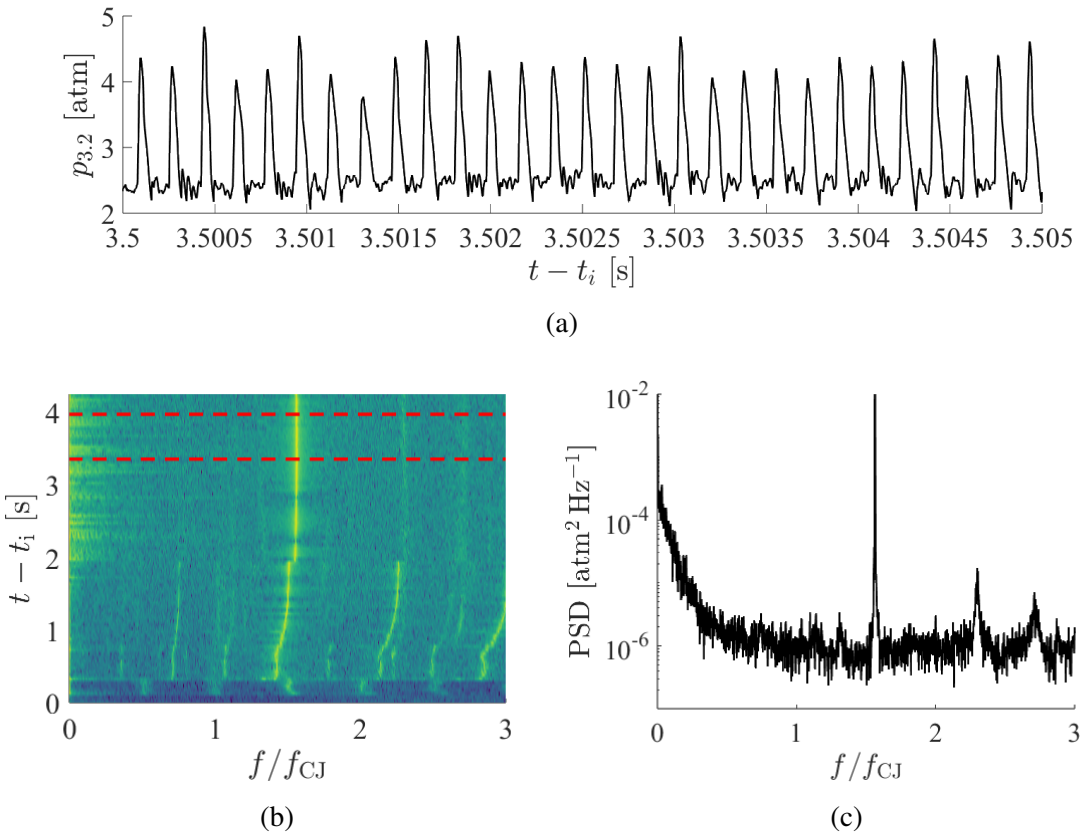

Figure 6.2: The channel pressure a) trace, b) time-varying spectrum, and c) time-averaged spectrum of a 2WI operation. Data from $\dot{m}''_a = 513$ kg s^{-1} m^{-2} with $\phi = 0.6$ in Configuration C.

2WD (green) operation that was prominent in configurations B and C. Finally, TSC (cyan) was only observed in the longest configurations, C and D, and only at large mass fluxes and equivalence ratios greater than 0.8.

6.3.1 Two Indistinguishable Co-Rotating Waves (2WI)

Operation with multiple co-rotating detonation waves is common in the literature [43]. This study also observed such an operation, where a pair of co-rotating waves propagated about the annulus. A sample high-speed channel pressure measurement, Figure 6.2a, is from a test of configuration C where the mass flux was 513 kg s^{-1} m^{-2} and the equivalence ratio was 0.6. Time is relative to when fuel introduction, t_i. The sharp rise from the detonation waves is evident and repeatable. Notably, the two detonation waves are *indistinguishable* (2WI) from one another as the peak pressures remain effectively constant, although there is a stochastic variability. The regularity of the peaks is further demonstrated by the time-varying spectral content as shown in Figure 6.2c. The frequencies are relative to the CJ frequency (f_{CJ}), which comes from the ideal CJ velocity. Again,

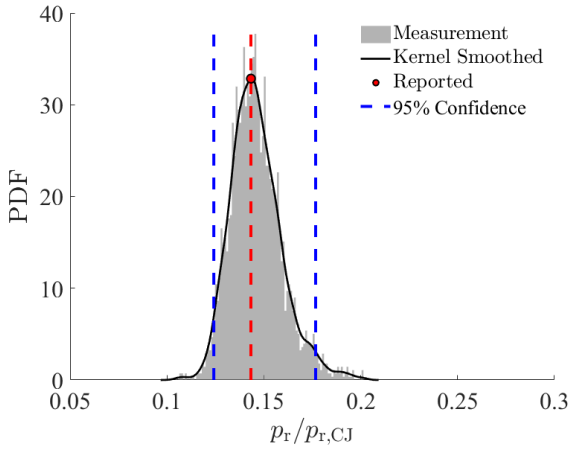

Figure 6.3: Probability density function of cycle-to-cycle pressure ratio across detonation waves for 2WI.

this work conducts all ideal detonation wave calculations (wave speed or pressure ratio) using NASA Chemical Equilibrium with Applications (CEA) at the prescribed global equivalence ratio [23]. The flow rates were increased during this test to achieve the nominal conditions (refer back to Sec. 6.2), which caused the increase in frequency before $t - t_i = 2$ s. Once the flow rates became steady, the frequency became steady, and the RDC reached a statistically stationary operation. The dashed red lines indicate the portion of the run over which the time-averaged spectrum in Figure 6.2c was generated. The prominent peak at $1.56 f_{CJ}$ corresponds to two waves that individually propagated at $0.78 f_{CJ}$. Since the waves are indistinguishable, there is no spectral peak at $0.78 f_{CJ}$, which contrasts the 2WD as will be discussed in the following section. This 2WD mode is the operational mode that the others will be compared against since it is commonly observable in the literature.

Individual detonation waves in Figure 6.2a were identified by their peak pressures to generate a statistical measure of the detonation wave properties. The ratio between these peak pressures and estimated base pressures gives the pressure ratio across the detonation wave(s). The estimated base pressure was computed by interpolating between the pressure troughs, or local minima, in the detonation cycle before and after the detonation wave peak pressure [188]. This procedure is repeated for each detonation wave during the steady portion of the test for approximately 3,000 discrete measurements of the peak pressure, base pressure, and pressure ratio, generating empirical PDFs. Figure 6.3 gives a PDF of the pressure ratio (p_r), normalized by the idealized CJ conditions ($p_{r,CJ}$), for the 2WI case considered thus far. In general, the PDF for 2WI is close to being normally distributed, consisting of a single mode with a slight skew to the right. The dashed red line and point give the peak of the estimated PDF generated by smoothing the data using a kernel. The kernel estimates the distribution of the empirical data without making assumptions about the

functional form of the underlying distribution. The smoothing function and bandwidth of the kernel parameterize it. The choice in bandwidth dictates the level of smoothing; here, the built-in Matlab algorithm automatically determined the bandwidth was automatically determined using the algorithm in Matlab, although the algorithm is best suited for normal distributions. Finally, the 95% confidence interval, found from the empirical cumulative distribution, is marked with the dashed blue lines. By utilizing this statistical approach, the most probable value of the pressure ratio, which may differ from the mean, can be characterized along with the variance and skew of the distribution.

6.3.2 Two Distinguishable Co-Rotating Waves (2WD)

In contrast to the previously described two-wave behavior, this study also observed a co-rotating, two-wave operation where the waves were distinguishable. To the author's knowledge, this is the first reporting of such an operational mode. As such, what follows is a rigorous demonstration of the existence of distinguishable waves. The analysis will focus on interpreting high-speed point measurements while only using high-speed video to confirm the conclusions reached from the in-depth analysis of the point measurements. This study concentrates intentionally on pressure measurements as other experiments may not have such videos, allowing for the transference of the process detailed here to other experiments to identify similar operational modes.

Figure 6.4a shows a sample high-speed channel pressure measurement for this type of operational mode, which is for when $\dot{m}''_{\mathrm{a}} = 451$ kg s^{-1} m^{-2} and $\phi = 0.6$. A general trend is evident where a stronger detonation wave with a peak pressure of about 3.5 atm precedes a weaker detonation wave of about 3 atm. Generally, every second detonation wave appears weaker than the preceding wave, highlighted with red arrows. The PDF of the cycle-to-cycle measurements of the pressure ratio across each detonation wave is bi-modal, see Figure 6.5, supporting the observation of two distinct pressure ratios. This bi-modal distribution is representative of every case that exhibited this behavior, although the distance between the PDF peaks varied depending on the operational conditions. The width of the distribution, as measured by the dashed blue lines, is greater than Figure 6.3 on account of being bi-modal. The variability in the two distinct pressure ratios appears to be individually normally distributed. At the end of the test, the time-varying spectral content, Figure 6.4b, highlights that the operation is statistically stationary, which may cause the normal distributions. The strongest observable peak, $1.50 f_{\mathrm{CJ}}$, in the time-averaged spectrum, Figure 6.4c suggests that two co-rotating detonation waves existed in the RDC, like the 2WI mode. However, additional spectral peaks at $0.75 f_{\mathrm{CJ}}$ and $2.25 f_{\mathrm{CJ}}$ exist, which were not present in the 2WI case. These peaks are precisely 0.5 and 1.5 multiples of the primary frequency. The aft high-speed video identified two co-rotating waves, confirming that two co-rotating detonation waves traveled

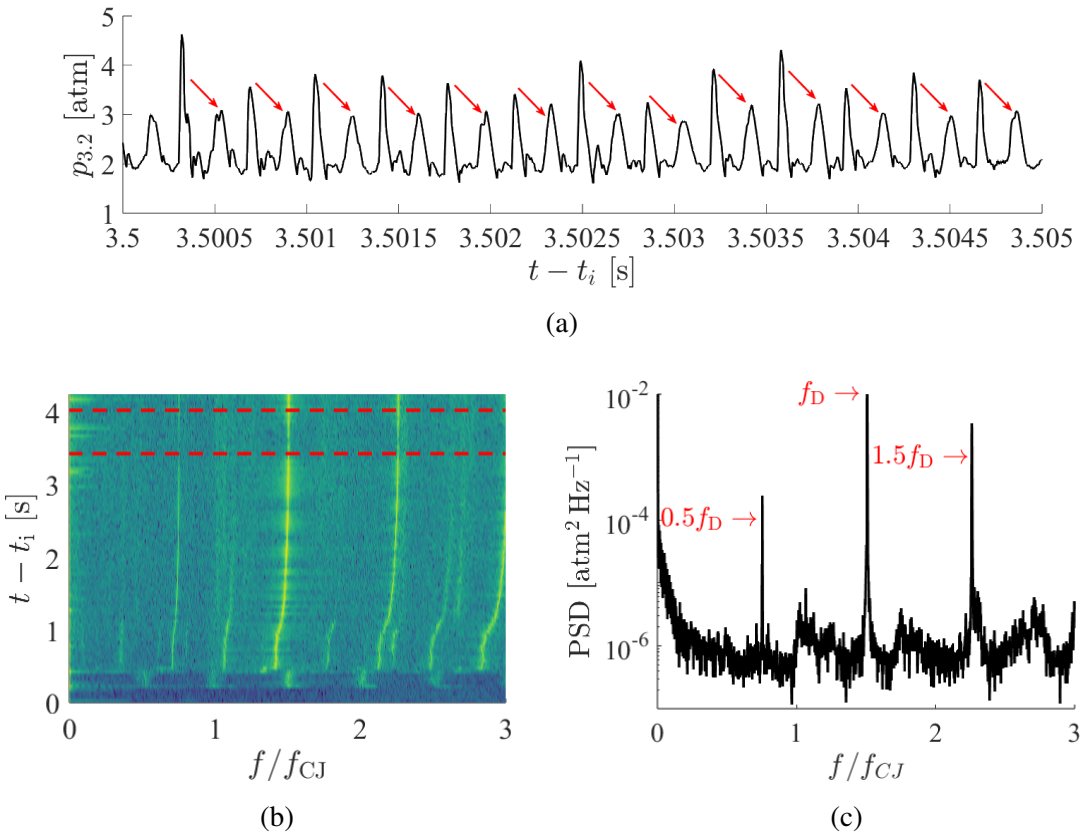

Figure 6.4: The channel pressure a) trace, b) time-varying spectrum, and c) time-averaged spectrum of a 2WD operation. Data from $\dot{m}''_a = 451$ kg s^{-1} m^{-2} with $\phi = 0.6$ in Configuration C.

at $0.75 f_{CJ}$, leading to the prominent peak at $1.50 f_{CJ}$. The alternating behavior would result in the additional frequencies as the larger pressure ratio wave passed the sensor at a frequency of $0.75 f_{CJ}$. Meanwhile, the sensor observed a pressure spike caused by the passage of a wave at a frequency of $1.50 f_{CJ}$ since there were two waves.

The cause of the alternating pressure rise requires further examination. Chacon et al. previously observed that secondary wave(s) can non-linearly interact with the detonation wave, resulting in larger, alternating pressure spikes [45]; thus, secondary wave(s) may seem like a plausible explanation for this phenomenon. There are several requirements for secondary wave(s) to be the cause given the spectrum in Figure 6.4c. First, the secondary wave(s) would have to be the same speed as the primary detonation wave(s) since differences in speed would appear as a distinct frequency peak [45] in the spectrum, which is not the case. Second, the point of interaction between the secondary and primary detonation wave(s) must be at the sensor location for the non-linear interaction to be measured. Since the wave(s) must all be traveling at the same speed, there cannot be a phase shift between the waves; otherwise, the interaction point would not be at the sensor

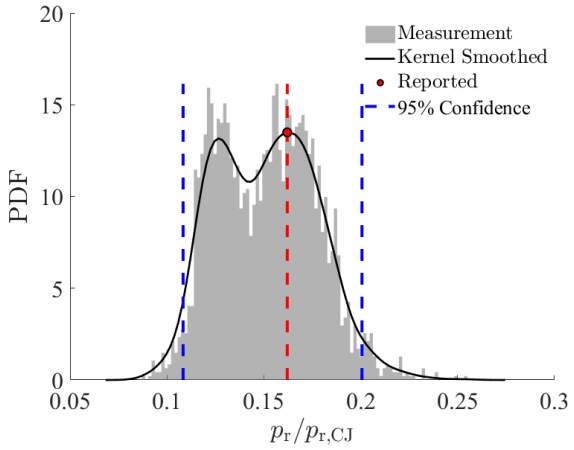

Figure 6.5: Probability density function of cycle-to-cycle pressure ratio across detonation waves for 2WD.

location. Finally, the number of secondary waves would have to be odd. Since there cannot be a phase shift, an even number of secondary waves would result in a secondary wave always passing the sensor simultaneously with one of the detonation waves. All three criteria must be true for secondary waves to be responsible for the observed phenomenon. While possible, it was deemed highly improbable to be true in reality, thereby disproving secondary waves as the cause. Furthermore, the additional spatial information gained from the aft video confirmed that secondary waves were not present in the test. An alternative theory would be that the second "detonation wave" was instead a reflected oblique shock off the nozzle that rotates with the detonation wave. However, unless the reflected shock caused auto-ignition of the mixture, this theory does not appropriately explain the chemiluminescence associated with the second wave as detected by the video.

Thus, the spectrum must then be the result of two detonation waves that are continuously traveling at the same speed but with different individual pressure ratios, making the waves in the wave pair inhomogeneous or *distinguishable* co-rotating detonations (2WD). The distinction between 2WD and 2WI is made based on the distinguishability of the waves since the multiplicity is the same and the speeds are comparable. Theoretically, 2WD would likely perform worse than 2WI since a significant portion of the heat releases occurs in the weaker wave with a lower pressure ratio. This lower pressure ratio would produce more entropy than the larger pressure ratio; thus, if both waves had the larger pressure ratio (2WI), they would generate less entropy than in 2WI with the lower observable peak pressures.

In the simplified one-dimensional ZND model, a unique relationship exists between wave speed and pressure ratio for a given global mixture, which would prohibit 2WD. However, loss mechanisms such as parasitic deflagration or mixture leakage cause the global mixture to no longer solely determine the relationship between pressure ratio and wave speed [10, 105]. Continually

propagating detonation waves in RDCs likely exist due to balancing complex physics on multiple scales. There are both local chemistry and shock dynamics at the wavefront. At the same time, there is dissipation and feedback to the air and fuel injectors that ultimately create a suitable flowfield in front of the detonation. Therefore, the two detonation wavefronts may experience a different combination of these multi-scale phenomena. For instance, a reflected oblique shock from the nozzle may interrupt the injector response, creating a local region of higher or lower equivalence ratio, which then, in turn, experiences varying amounts of secondary combustion. The result is that the waves achieve the same wave speed, albeit with different strengths in terms of pressure. Since the wave speeds are identical, one cannot overtake the other, allowing stable propagation.

6.3.3 Transient Super-Cycle (TSC) in Wave Dynamics

The previously discussed operational modes are effectively statistically stationary in that the number and direction of the waves do not change significantly in time. However, under some test conditions, a phenomenon arose where the number, direction, and speed of the waves varied rapidly but periodically over several detonation cycles. This phenomenon occurred solely at the highest fluxes (greater than 450 kg s^{-1} m^{-2}) and equivalence ratios (greater than 0.8) for configurations C and D; see Figs. 6.1c and 6.1d.

The channel pressure measurement, Figure 6.6a, more closely resembles that of 2WI than 2WD since there is no obvious pattern on the small scale shown. The case shown in Figure 6.6a was for configuration D operarting with an air mass flux of 522 kg s^{-1} m^{-2} and $\phi = 0.97$. However, the spectral content, whether that be time-varying in Figure 6.6b or time-averaged 6.6c, shows both more and broader spectral peaks than the previous modes. A few of the prominent (not harmonic) spectral peaks are 1.35, 1.70, 2.11, and 2.51 f_{CJ}, which each likely corresponded to a unique wave system within the RDC. These tones persisted over the entire time window shown with the dashed red lines, as shown in Figure 6.6b. The nearly constant frequencies give the impression that all the waves existed simultaneously, although it may be an artifact of the time windows of 5 ms used to generate Figure 6.6b. The broadness of the spectral peaks suggests that the wave speeds of the individual wave systems were changing. Finally, while it typically is preferential to identify a primary wave system, in general, the spectral strengths of the tones are comparable, making such distinctions challenging.

This study utilized the method of Circuit Wave Analysis (CWA) to gain additional insight into the phenomenon's behavior. The method of CWA reduces the high-speed videos of the detonation wave propagation in the annulus into the properties of each wave system present in the RDC [45]. Specifically, it detects the multiplicity, strength, direction, and speed of wave systems in the annulus. The method of CWA was applied to every 71 frames of the 50,000 fps chemiluminescence video,

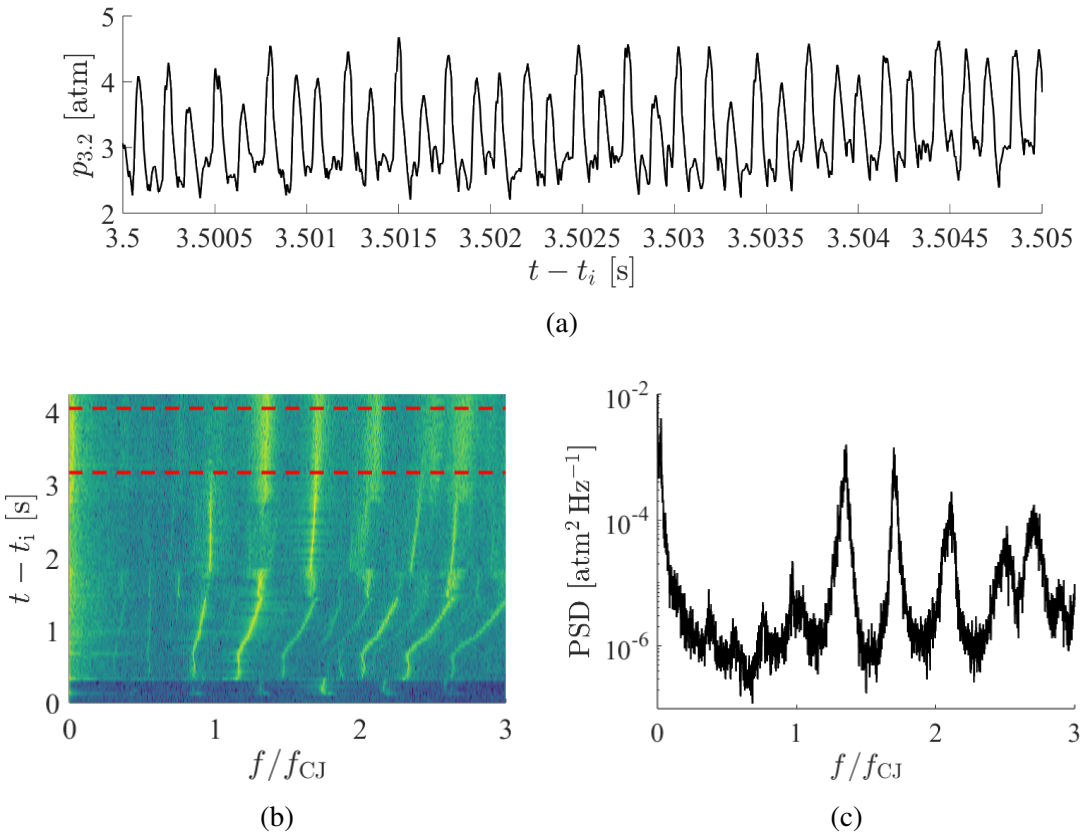

Figure 6.6: The channel pressure a) trace, b) time-varying spectrum, and c) time-averaged spectrum of a TSC operation. Data from $\dot{m}''_a = 522$ kg s^{-1} m^{-2} with $\phi = 0.98$ in Configuration D.

resulting in a temporal resolution of 1.42 ms. This temporal resolution is greater than the temporal resolution of the time-varying spectrum (e.g., Figure 6.6b). Figure 6.7a shows a sample of the time variation of the wave systems, with the definition of a wave system being a combination of a unique multiplicity and direction. The y-axis gives the normalized velocity of the individual waves (v) within the wave system. Each symbol corresponds to the predominant wave system within the RDC at that time, and the symbol's color indicates the wave system's multiplicity (N). The predominant wave system refers to the one with the greatest spectral strength, i.e., the strongest or most coherent wave system propagating during the time window and in that direction. Other wave systems may have existed during the time window, but this analysis neglects said waves. Note that the multiplicity here (N) is distinct from the multiplicity of the detonation wave (N_D) since this analysis makes no direct distinction between the primary and secondary waves. Finally, CWA considers the positive and negative (clockwise and counter-clockwise) directions of rotation independently, with the velocity's sign denoting the direction. An example interpretation of Figure 6.7a is as follows: for given $t - t_i$, N=2 (red) for positive v and N=4 (green) for negative v

corresponds to two-wave operation in the positive direction and four-wave operation in the negative direction at that $t - t_i$.

A cyclical pattern is discoverable with careful inspection of Figure 6.7a. During the following discussion, the reader is encouraged to reference the generic visualization of the cyclic process, Figure 6.7b. Essentially, Figure 6.7b is the same as Figure 6.7a with the boxes replacing the markers and additional annotations. The cyclical pattern is as follows. First, a pair of co-rotating waves propagated in the positive direction. At the same time, five co-rotating waves propagated in the opposite (negative) direction at nearly acoustic speeds. After about five rotational cycles of the wave pair, one of the counter-propagating waves was consumed or died out, while the remaining four waves sped up marginally. A rotational cycle refers to the time (τ_D) it took one of the individual waves in the wave pair to complete a lap around the annulus. One of the four counter-propagating waves ceased to exist after another approximate $10\tau_D$, and the three remaining counter-propagating waves accelerated again. Meanwhile, the co-rotating wave pair in the positive direction persisted but gradually decelerated as the counter-propagating waves accelerated. Hence, the negative slant to the red boxes in Figure 6.7a. Faster counter-propagating waves likely consume more reactants, reducing the wave pair's speed, which aligns with previous observations of counter-propagating waves [45]. After another approximate $10\tau_D$, the system underwent another rapid transition characterized by a direction change of two co-rotating waves and the multiplicity of the counter-propagating waves increasing back to five. This transition could be either the three waves transitioning to two waves and out-competing the initial wave pair or the wave pair switched directions. All the modal transitions occurred within one or two rotational cycles, which is a transition much faster than the temporal resolution achieved with CWA. Therefore, the transition mechanisms remain a mystery. Regardless of the exact mechanism, at the end of this super-cycle, the system has returned to having a co-rotating wave pair and wave system with five co-rotating waves that rotate in the opposite direction as the wave pair. The process is then repeated cyclically following a super-cycle pattern and time-scale (τ_S) several times the wave pair's rotational time. For that reason, this study will hereafter refer to this behavior as *transient super-cycle transient* operation (TSC).

This study then tracked the fundamental wave properties (N and v) relative to the position within the super-cycle. First, the super-cycle period τ_S is defined to be the elapsed time between two directional shifts (indicated by the dashed black lines in Figure 6.7b). The period was defined in this manner to study if there was a directional preference or if the system was insensitive to direction. There was some amount of variability to τ_S, as is reflected in the PDF presented in Figure 6.8 for the specific case of Figure 6.7b. The distribution was close to normal except for several periods that skewed the distribution to the right. The peak of the PDF is the representative super-cycle period, $\bar{\tau}_S = 18.5$ ms. Afterward, an algorithm parsed through each super-cycle, and

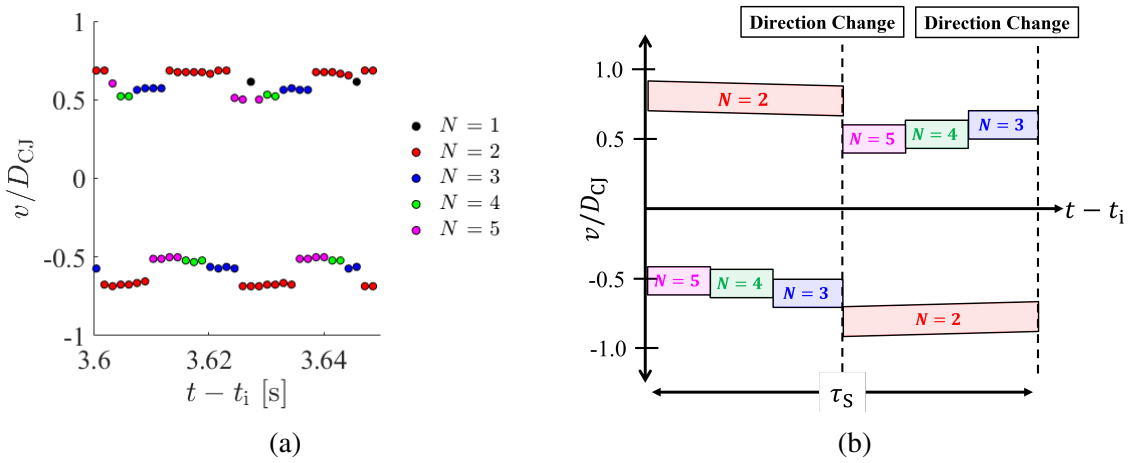

Figure 6.7: a) The time variation of multiplicity (N), speed (v), and direction of the wave systems mid-run. b) Simplified representation of the super-cycle. Data from $\dot{m}''_a = 522$ kg s^{-1} m^{-2} with $\phi = 0.98$ in Configuration D.

the multiplicity and speed of individual waves in the systems were re-sampled and binned into 25 points along the super-cycle phase. The algorithm binned both directions of rotation (positive and negative) independently to resolve the discontinuities of the directional switches better. The algorithm ran for all the super-cycles within the time indicated by the dashed red lines in Figure 6.6b, or about 50 super-periods.

At each phase within the super-cycle, a PDF exists for either the multiplicity or wave speed. Plotting each of the PDFs simultaneously results in bi-variate histograms as shown in Figure 6.9. Figures 6.9a and 6.9c give the wave multiplicity while Figs. 6.9b and 6.9d give the wave speeds. The subscripts on the variables indicate the positive and negative directions. The dashed red lines guide the reader and plot the trajectory of the PDF peaks in the phase space. Both directions had the same behavior, except for a 180° phase difference between the positive and negative directions. The co-rotating wave pair existed for half of the super-period in both directions, indicating no directional preference. Overall, the pattern originally identified in Figure 6.7b is confirmed, but additional details are now accessible. For instance, the higher multiplicities (4 and 5) were more prone to cycle-to-cycle variable than the wave pair, as demonstrated by the color diffusivity at $t/\bar{\tau}_S < 0.2$ in Figure 6.9a. There was little difference in the individual wave speeds of four and five-wave systems, and both were near acoustic speeds, hinting that there were only small differences between the wave systems. In contrast, the step changes in speed going from four to three or three to two were much more significant; see Figure 6.9b. The three-wave operation, $0.2 \leq t/\bar{\tau}_S < 0.5$ in Figure 6.9b, had the most stable wave speed of all the systems. Meanwhile, the wave pair speed decreased with each subsequent decrease in the number of waves in the opposite direction in a nearly piecewise

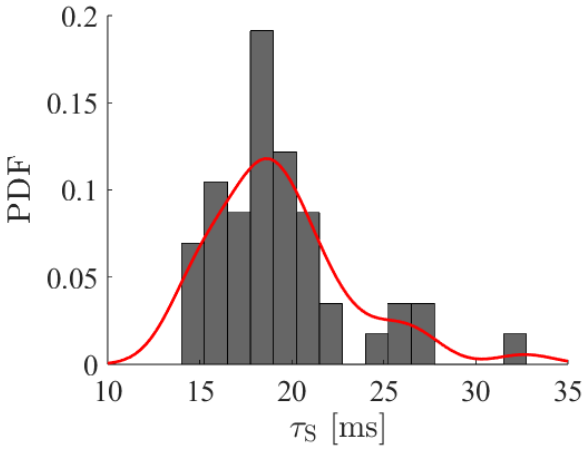

Figure 6.8: Probability density function of super-cycle period.

fashion. However, there was a slight upturn in speed right before the direction switch. The cause is unknown, although that last point had significant wave speed variability, likely reflecting the transient process of the direction change.

As previously mentioned, only the longest combustors and highest fluxes exhibited TSC. Both increasing air mass flow rate/flux and lengthening the combustor have been seen to promote additional detonation waves. Following these trends, it is reasonable to expect that if three co-rotating detonation wave operations were to exist with the given geometry, they would have occurred in the region of TSC operation. To that effect, before the onset of the phenomenon in Figure 6.6b), the test exhibited a stable three-wave operation during the transient portion of the run. The three-wave operation is the tone at $1.65 f_{CJ}$ ranging from 2 to 2.75 seconds into the run. The high-speed video confirmed the three waves. During this portion of the run, the air and fuel rates increased towards the nominal flow rates. The speed of the three-wave system gradually increased until the phenomenon began when the flow rates became nearly steady. While this three-wave operation did not last the entire run, its existence supports the hypothesis that TSC occurred in the same region where the RDC would have undergone a modal transition to a higher multiplicity. The existence of TSC may also suggest that the given geometry may not support steady three-wave operation. While the switch from steady to unsteady operation is not well understood, it is intriguing that the steady three-wave operation occurred when the plenum pressures increased to accommodate the increasing flow rates. Perhaps different boundary conditions in the plenum, inlets, and/or injectors result in a more stable system. Regardless, if a similar operation is observed in a different configuration, altering the combustor length (e.g., shortening the length) could result in a more steady operation like the other modes. Eliminating the TSC may be advantageous as it creates time-varying exit conditions, which may be undesirable for actual applications.

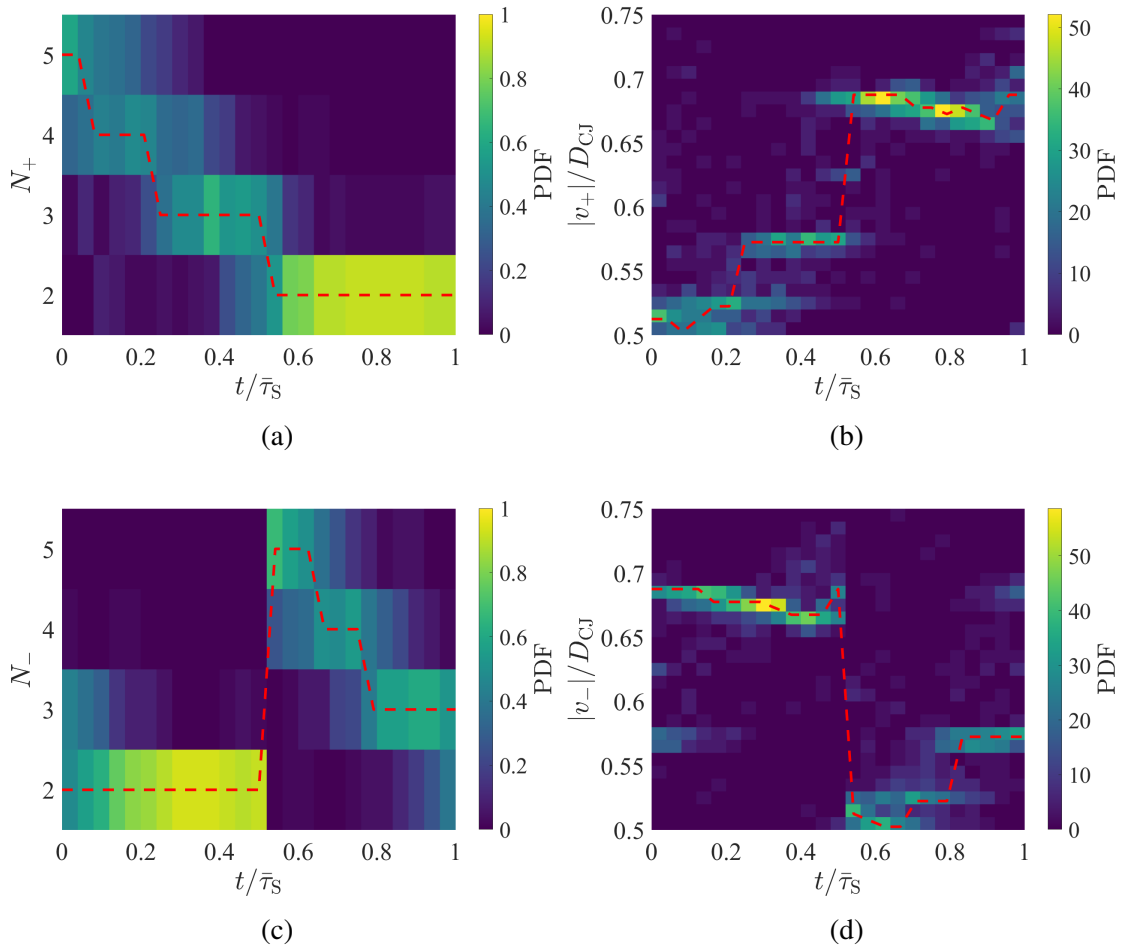

Figure 6.9: Distributions along the super-cycle phase of multiplicity (a and c) and normalized velocity (b and d) in the positive (a and b) and negative (c and d) directions.

6.3.4 Chaotic Operation (CH)

Each operational mode described so far either has one dominant stable wave system or the variations in the waves follow a discernible pattern, allowing for easy classification. However, not every test condition exhibited an operation that could neatly fall into the pre-determined operational mode classifications, and this study will hereafter refer to this as *chaotic* operation (CH). The system may still have followed a pattern like TSC, but if such a pattern existed, it was too complex to distill in a manner equivalent to previously described classifications. In general, such CH operation consists of multiple competing wave systems that come in and out of existence.

The channel pressure, time-varying spectral content, and time-averaged spectrum for a sample CH case, Figure 6.10, are presented to compare the other operational modes. This sample case is from configuration B operarting with $\dot{m}''_a = 193$ kg s^{-1} m^{-2} and $\phi = 1.23$. The time-resolved

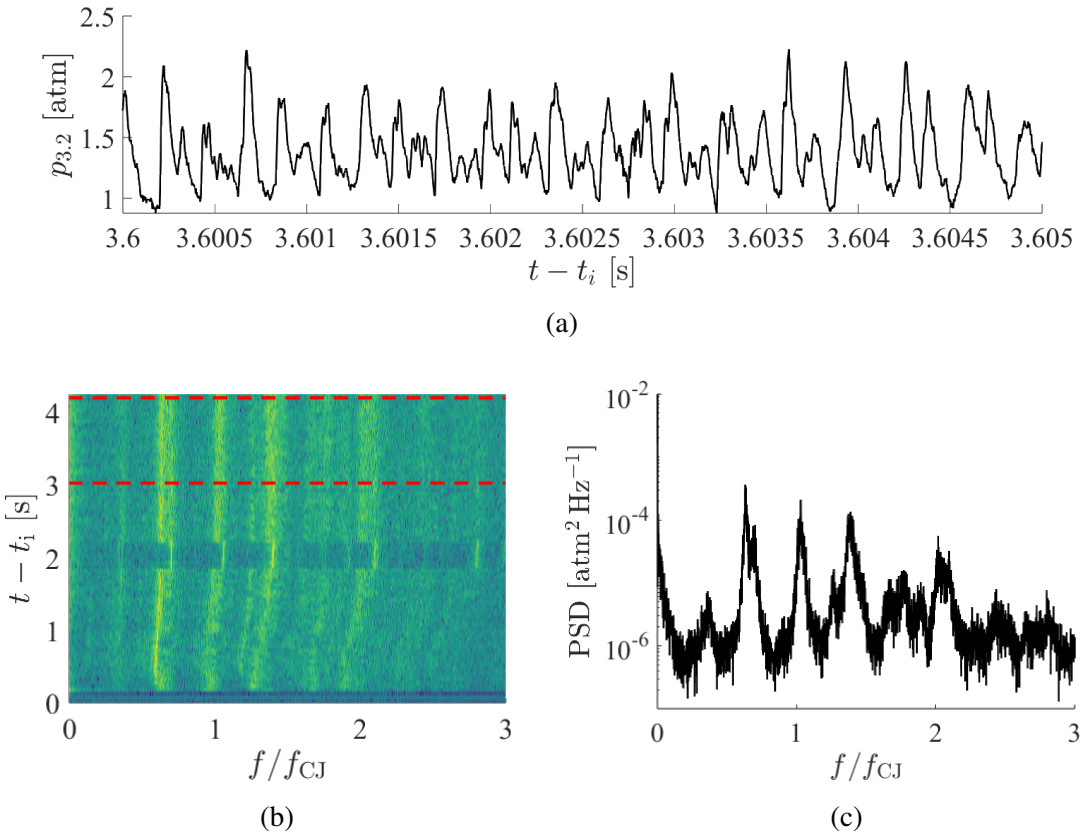

Figure 6.10: The channel pressure a) trace, b) time-varying spectrum, and c) time-averaged spectrum of a CH operation. Data from $\dot{m}''_a = 193$ kg s^{-1} m^{-2} with $\phi = 1.23$ in Configuration B.

pressure, Figure 6.10a, somewhat resembles 2WD in that stronger pressure spikes are followed by weaker pressure spikes, although the pattern is not repeatable. The spacing between the different pressure rises is also more irregular than the other modes, reflected in the spectral content in Figure 6.10c. Similar to the TSC operation but dissimilar to either the 2WD or 2WI operation, there were multiple prominent spectral peaks, with each of the peaks being broad. These peaks persisted in a quasi-steady manner as shown in Figure 6.10b, although there was a brief time around $t - t_t = 2$ where the operation stabilized momentarily. The broadness of the spectral peaks indicates that waves accelerated and decelerated around distinct wave speeds, which suggests that multiple wave systems arose during the test, with each system having a unique speed to identify it, like the TSC.

Due to the initial similarities to TSC, this study also applied the method of CWA to high-speed video taken from this case as well, Figure 6.11. Several distinct wave systems are identifiable. In increasing speed order, these were: a two-wave ($N = 2$) system with $v = 0.52D_{CJ}$, a three-wave ($N = 3$) system with $v = 0.59D_{CJ}$, a one-wave ($N = 1$) with $v = 0.62D_{CJ}$, and a two-wave ($N = 2$) system with $v = 0.68D_{CJ}$. All of these match the tones from Figure 6.10c, indicating

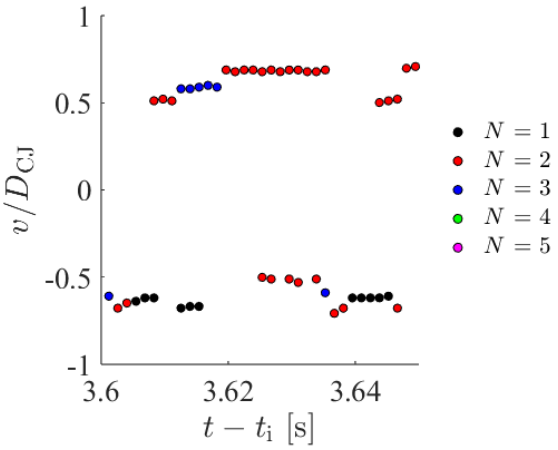

Figure 6.11: The time variation of multiplicity (N), speed (v), and direction of the wave systems mid-run. Data from $\dot{m}''_{\mathrm{a}} = 193$ kg s^{-1} m^{-2} with $\phi = 1.23$ in Configuration B.

that they appeared frequently throughout the test duration. The system transitioned between these different wave systems along with the direction of the wave systems; however, unlike the TSC operation, the wave system changes followed no discernible pattern This sample CH operation is further differentiated from TSC since there were times when counter-rotating waves did not exist, see the lack of markers in Figure 6.11 in the negative direction around $t - t_{\mathrm{i}} = 3.62$. While similar underlying processes may have occurred in this sample CH operation and the TSC operation, the differences were sufficiently significant enough to warrant distinction.

The specific details about the number of wave systems and the speed and multiplicity of the wave systems, Figure 6.11, do not reflect every CH operation. These details varied between the different CH operations, but the transient nature of the operational modes remained consistent. Thus, this study defines the CH operation as a lack of cohesion and quasi-steady transient operation. The ultimate purpose of discussing such an operation is to highlight that the operational mode of the RDC may not always follow simple classifications since the underlying physics couples in a complex manner that can result in transient global features. The question remains whether or not the CH operation, which seems undesirable, impacts performance significantly, which Section 6.5 will discuss.

6.4 Change in Wave Properties Induced by Length

Whereas the previous section focused on classifying and describing the different operational modes, this section looks at quantifying changes to the wave properties. Specifically, the wave speed and the pressure ratio are discussed as global metrics of the non-ideality of the waves so that this study

can compare the measured performance metrics to metrics describing the detonation wave(s). In general, the discussion in this section focuses on the changes, or lack thereof, in wave speed or pressure ratio with respect to length. Different operational modes may influence the detonation wave properties; however, additional changes within the system can also affect the detonation wave properties. Therefore, there is less emphasis on the specific operational modes in favor of a more global viewpoint. For these comparisons, singular values of the measured properties are given based upon the peak of the empirical PDFs.

6.4.1 Speed of Individual Waves

The wave speed (D) of the primary detonation wave(s) is a metric often used to characterize the waves. The wave speed was determined using CWA [45] and cross-validated with the time-averaged spectrum. The primary detonation wave(s) are distinguishable from the secondary waves due to the greater spectral strength. The cross-validation of CWA was necessary due to the combination of the exit constriction partially blocking the view of the annulus and observed combustion occurring statically around the annulus. Normalizing the wave speeds by the ideal CJ detonation wave speed (D_{CJ}) enables better comparisons between the wave speed of the individual wave(s) across different equivalent ratios. The normalized individual wave speeds in Figs. 6.12a, 6.12b, and 6.12c correspond to air mass fluxes of 327, 393, and 520 kg s^{-1} m^{-2}, respectively. The qualitative trends at these mass fluxes are representative of the remainder of the tests. Many subsequent plots which track changes in some quantity across the combustor length follow a similar format as Figure 6.12. The marker color indicates the equivalence ratio, excluding $\phi = 1.2$, as this was not tested for every air mass flux, while the marker shape indicates the operational modes described previously. The different equivalence ratios have a horizontal offset to minimize the overlap of the error bars, which denote the 95% confidence interval of the empirical PDF. The dashed lines connecting the points are given solely to guide the reader and have no physical interpretation.

As noted previously, the combustor with the shortest length, configuration A, had predominantly one wave (circle) or chaotic (star) operation. Both operation modes exhibited the most significant variability in wave speed, i.e., the largest error bars. Generally, even when a single dominant wave exists (1W), one-wave operation is not as steady as two-wave operation in these configurations. Both 2WI (upward-pointing triangle) and 2WD (square) had minuscule error bars, making them unobservable. Meanwhile, the wave speed of TSC (downward-pointing triangles) operation marked in Figure 6.12 is for the two-wave operation that was most frequently the most prominent wave system; however, the highly skewed error bars for TSC are a result of the other wave systems with greater multiplicity that occurred throughout the test.

A general trend is observable across configurations B-D (L >100 mm) in which the normalized

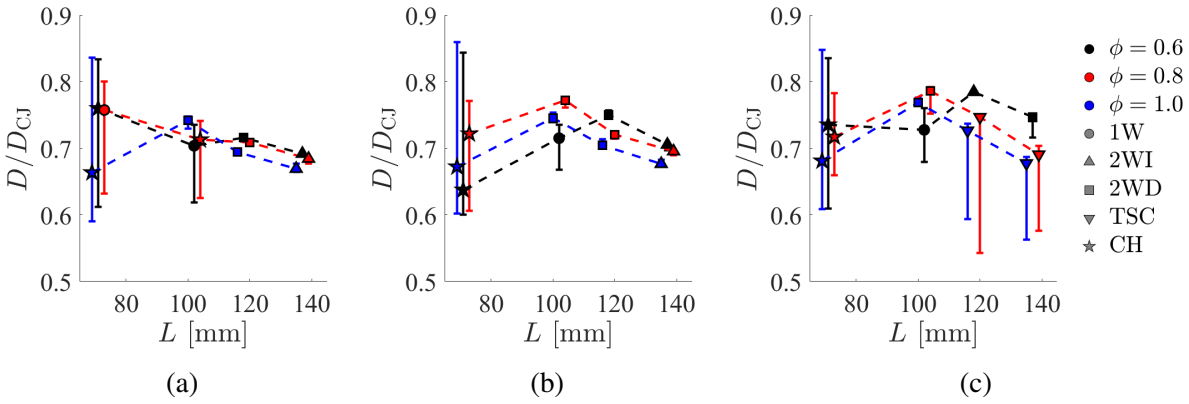

Figure 6.12: Normalized speed of individual detonation wave(s) for a) $\dot{m}''_a$ = 327 kg s^{-1} m^{-2} b) $\dot{m}''_a$ = 393 kg s^{-1} m^{-2} and c) $\dot{m}''_a$ = 520 kg s^{-1} m^{-2}.

speed of individual waves decreases nearly with increasing combustor length if 1W and CH operational modes are neglected. Thus, as length increases, the waves become slower as long as the detonation wave multiplicity remains the same. The cause of this trend is unknown, although there may be a link to the eigenfrequencies of circumferential acoustic modes of an annular chamber, which are inversely proportional to the axial length of the chamber [189]. Meanwhile, trends in the 1W and CH operational modes are more challenging to decipher due to the spread; however, when ϕ = 0.6 (black markers), an increase in wave speed can be observed going from 1W in configuration B to 2W in configuration C in each of the mass fluxes in Figure 6.12.

The author theorizes that the wave speed decreases with combustor length for a fixed multiplicity until a threshold length or criterion. This length may correspond to when the wave(s) slow to a speed where the injectors recover well before the detonation wave arises, thereby creating a larger fill region. This larger fill region can then promote and sustain an additional detonation wave. Although a second co-propagating detonation wave would change the injector recovery, the system can re-balance to support the extra wave. After switching to a higher multiplicity, the individual wave speed rises significantly closer to the ideal CJ value. The wave speed jump increase may be caused by a reduction of deflagration before the detonation (parasitic combustion), as the resident time of fresh reactants in the channel before detonation wave arrival decreases, and the shortened time scale between detonation waves would mitigate the amount of auto-ignition or flame propagation that could occur. Previous studies have noted that parasitic combustion is detrimental to detonation wave speed [60, 11, 105]. Nevertheless, since the testing in this work never yielded a sustained three-wave operation, the generality of the increase in wave speed after an increase in multiplicity caused by length cannot be confirmed.

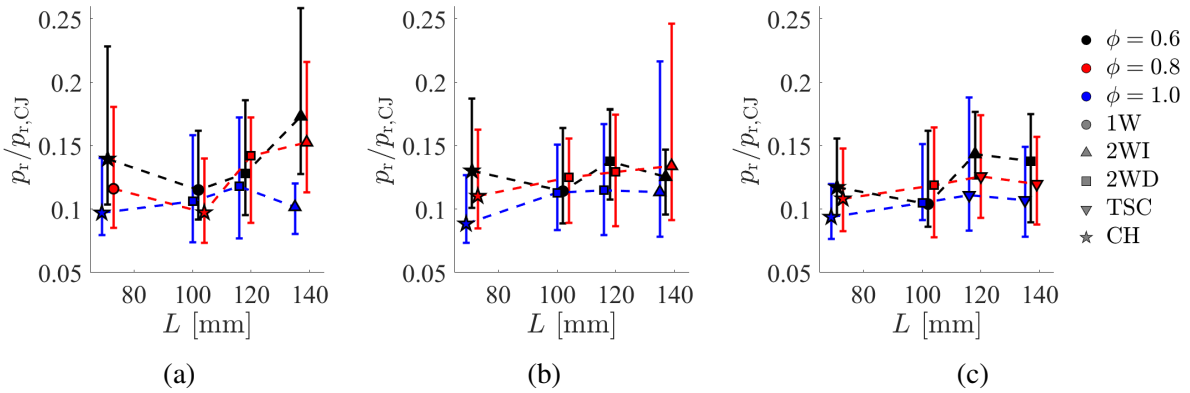

Figure 6.13: Normalized pressure ratio of individual detonation waves for a) $\dot{m}''_a$ = 327 kg s^{-1} m^{-2} b) $\dot{m}''_a$ = 393 kg s^{-1} m^{-2} and c) $\dot{m}''_a$ = 520 kg s^{-1} m^{-2}.

6.4.2 Pressure Ratio across Waves

As discussed previously, cycle-to-cycle variability exists within the pressure measurements, whether from changes to the detonation wave(s), merely an artifact of the limited temporal response of the sensor, or a consequence of thermal drift in the sensor. The variability results in empirical PDFs of the pressure ratio; see Figs. 6.5 and 6.3 for examples. Thus, this work takes the most probable values of the empirical PDFs when reporting a pressure ratio for a test. Additionally, this work reports the larger pressure ratio in the case of a bi-modal distribution, Figure 6.3. The pressure ratios for the same cases considered in Figure 6.12 are given in Figure 6.13. Like the wave speed, the pressure ratio is normalized by the corresponding CJ condition ($p_{r,CJ}$). Many of the PDFs were right-skewed, such that the upper error bar is larger than the lower error bar in Figure 6.13. This skew could be the result of several factors. One was thermal drift or heating of the sensor, which artificially lowered the measured signal, reducing the base pressure and increasing the ratio. Another explanation is the non-linear interaction between the primary detonation wave(s) and secondary waves, which would locally create even higher pressure regions [45]. Regardless of the cause, the spread in pressure ratios is comparable among all the different operational conditions, including the bi-modal distributions of 2WD.

The waves are relatively weak since the pressure ratios are low for all the tests, being about 10-15% of the CJ pressure ratios. There was a marginal increase in the pressure ratio with increasing length, although the error bars encompass such changes. The minute changes in pressure ratio contrast the more observable changes in wave speed discussed previously. The divorce between changes in wave speed and pressure ratio is likely a result of loss mechanisms, which cause the relationship between the speed and pressure of the detonations to no longer be unique. Regardless, the low-pressure ratios are likely not ideal for performance in terms of entropy production.

6.5 Minimal Performance Changes from Length

6.5.1 Gross Thrust

The attention can return to quantifying the performance of the RDC now that the previous sections have established some characteristics about the operation and detonation wave(s). The first performance metric considered is the gross thrust (F_G) produced by the RDC, with Chapters 4 and 5 detailing the necessary experimental procedure. Figure 6.14 presents the variations in measured gross thrust as length changes three discrete air mass fluxes. These mass fluxes are the same as those in Figure 6.12 which are 327 kg s^{-1} m^{-2}, 393 kg s^{-1} m^{-2} and 520 kg s^{-1} m^{-2} for Figs. 6.14a, 6.14b, and 6.14c respectively. The gross thrust increases nearly linearly with air mass flux, reflected in the change in the scale of the y-axes in Figure 6.14. The gross thrust increases with the equivalence ratio, i.e., the marker color. Both of these trends are reminiscent of the results from Section 5.2.

A non-monotonic relationship existed between gross thrust and length, although the scale in Figure 6.14 makes this difficult to discern. To better visualize the relationship, the change in gross thrust relative to the shortest length ($F_{G,A}$) is presented in Figure 6.15. Depending on the operational condition, the gross thrust could either decrease or increase with a step change in length, hence the non-monotonic relationship. Overall, configuration C had the greatest gross thrust of the configurations by being 5-12% larger than $F_{G,A}$. However, the measurement uncertainty again encapsulates the variations for a fixed equivalence ratio. The overlapping uncertainty grows worse with smaller thrust values, which occur at the lower. Additionally, the changes in operational mode (symbol markers) also do not cause significant changes to the gross thrust. Therefore, it is inconclusive if there are changes in gross thrust production with respect to length changes or the operational mode changes induced by length.

6.5.2 Fluidic Blockage

Thrust alone is, however, insufficient to make a complete comparison between the different configurations as it does not consider the impact of the mode of operation on the plenum pressure driving the flow ($p_{t,2}$), and thus the resulting gross thrust. The impact of the mode of operation is here quantified in terms of an effective fluidic blockage fraction (B_m). The blockage fraction is defined based on the ratio of the tested mass flux through the combustor to the mass flux of a "cold" or non-reacting flow (no fuel injection) test at the same plenum pressure ($\dot{m}''_{C|P}$) [139, 50],

$$B_m = 1 - \frac{\dot{m}''_a}{\dot{m}''_{C|P}} \tag{6.1}$$

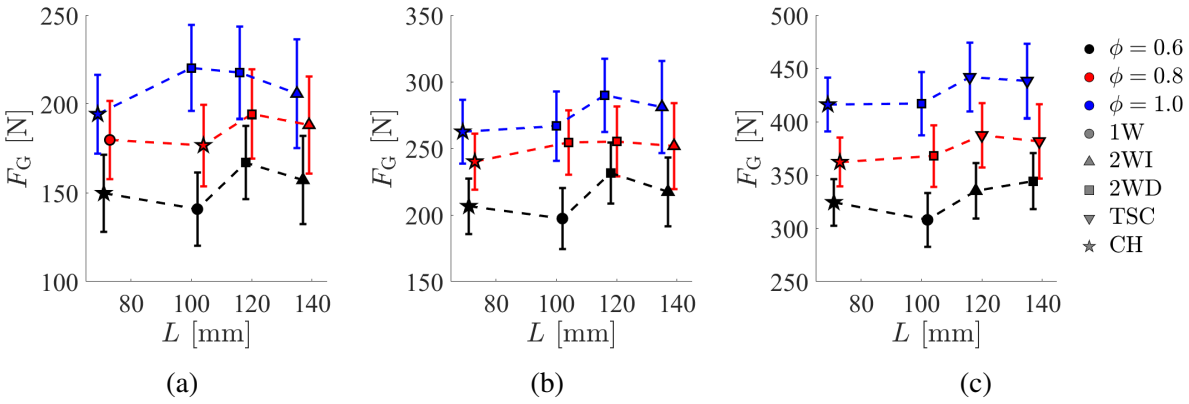

Figure 6.14: Gross thrust output for a) $\dot{m}''_a$ = 327 kg s^{-1} m^{-2} b) $\dot{m}''_a$ = 393 kg s^{-1} m^{-2} and c) $\dot{m}''_a$ = 520 kg s^{-1} m^{-2}.

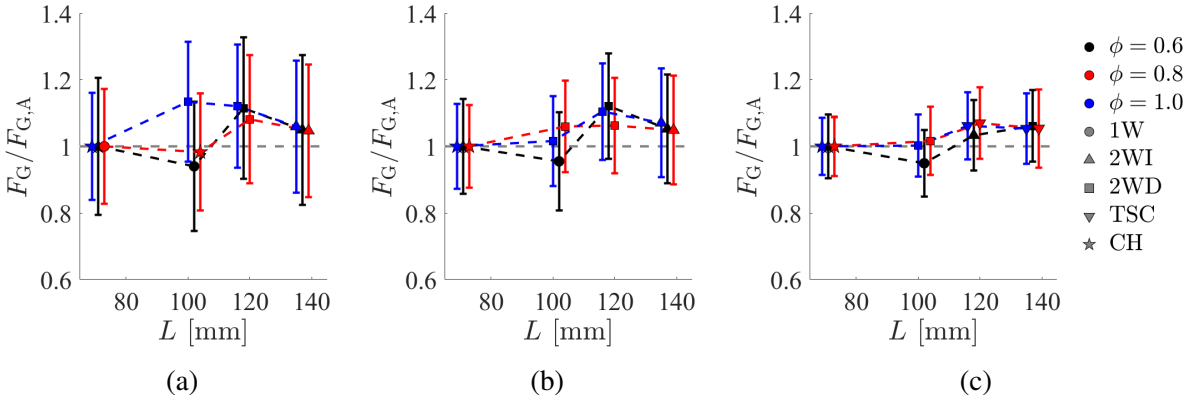

Figure 6.15: Change in gross thrust output relative to Configuration A ($F_{G,A}$) for a) $\dot{m}''_a$ = 327 kg s^{-1} m^{-2} b) $\dot{m}''_a$ = 393 kg s^{-1} m^{-2} and c) $\dot{m}''_a$ = 520 kg s^{-1} m^{-2}.

This quantity is equivalent to the fraction of the inlet area reduced by the fluidic blockage induced by the pressure rise across the detonation wave. The geometry of the air inlet controls the cold-flow characteristics (e.g., pressure drop, discharge coefficient, etc.). Thus, the cold-flow plenum pressure to drive a given mass flow through the combustor did not change with length. The additional viscous losses from the extra channel length are assumed to be negligible. Thus, a higher value of B_m (more blockage) for a given mass flux indicates that detonative operation causes the air plenum pressure to increase more for that configuration.

Figure 6.16 shows the blockage fraction of the air inlet for the same mass fluxes as the previous figures. Typically, the blockage fraction decreases with increasing mass flux for a given equivalence ratio. Additionally, the blockage fraction generally increased with increasing combustor length. An increase in the number or severity of higher static pressure regions (waves) within the combustor

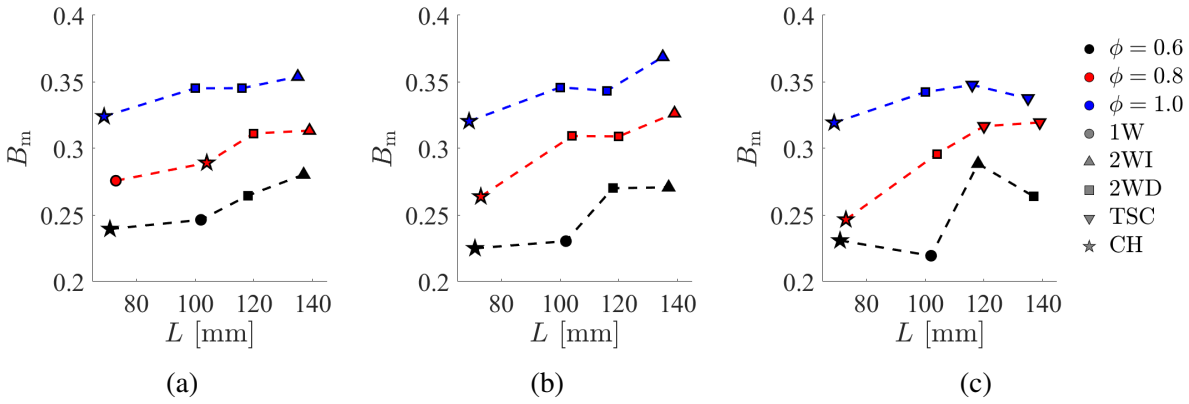

Figure 6.16: The fluidic blockage fraction for a) $\dot{m}''_a$ = 327 kg s^{-1} m^{-2} b) $\dot{m}''_a$ = 393 kg s^{-1} m^{-2} and c) $\dot{m}''_a$ = 520 kg s^{-1} m^{-2} across tested configurations.

may have caused this increase in blockage; however, the exact cause is unknown as no relationship between the detonation wave(s) and blockage exists at this time. Regardless, while there is a minor benefit of thrust production (ignoring uncertainty), the additional thrust comes at the cost of an increased air inlet flow blockage and, thus, plenum pressure.

6.5.3 Pressure Gain

One advantage of measuring performance through PG is that it is a more comprehensive metric than gross thrust because it includes both the thrust production and the plenum pressure penalty (increase) associated with inlet blockage. This study also utilized the EAP methodology according to the approach outlined in the previous chapters. Figure 6.17 shows a subset of the PG measurements for the different combustor lengths considered in the study at the same mass fluxes as previous figures. The Mach number correction introduced in Section 5.5 is not used here to allow better comparisons between these results and other values found in the literature. Overall, this study's range of measured PG varies from -0.21 to -0.32. These values align with literature results based on $A_8/A_{3.1}$ = 2.30, Figure 2.7 [14]. Regardless of combustor length, the best PG occurred at the lowest mass flux for a given equivalence ratio, Figure 6.17a. The static pressure drop across the air inlet from turbulence increases with increasing mass flux, causing the general trend of worse (more negative) PG with increasing mass flux, as was noted in the previous chapter.

Only slight variation existed between the PG for the same conditions across the different lengths. The absolute change in PG across the lengths for a given equivalence ratio is approximately 1-2%. These slight variations are well within the experimental uncertainty of the PG. Thus, the minor increase in thrust is balanced by the rise in plenum pressure, resulting in minimal changes to PG. Therefore, the PG metric appears insensitive to combustor length and the changes in operational

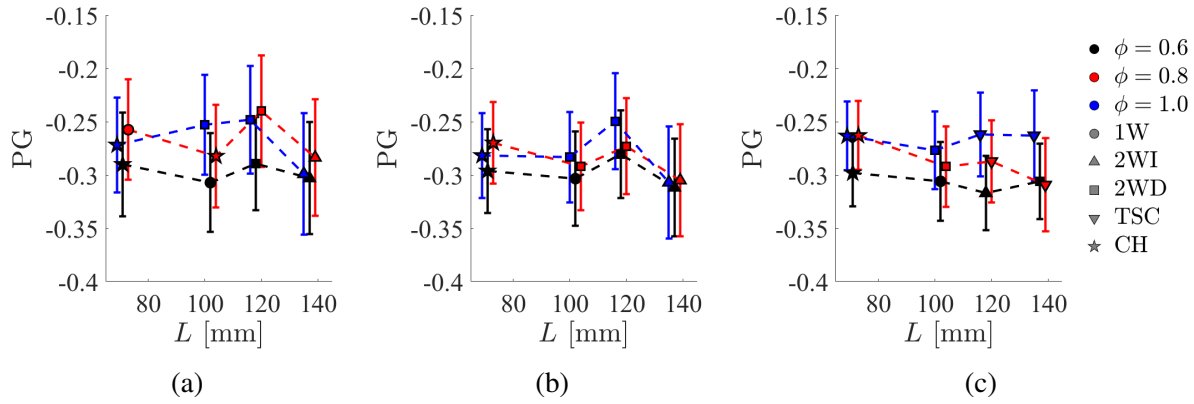

Figure 6.17: The pressure gain for a) $\dot{m}''_a = 327$ kg s^{-1} m^{-2} b) $\dot{m}''_a = 393$ kg s^{-1} m^{-2} and c) $\dot{m}''_a = 520$ kg s^{-1} m^{-2}.

mode induced by the length. Previous studies saw a similar insensitivity with specific impulse [136, 138, 137], although, as mentioned previously PG has the advantage of incorporating the changes in the upstream conditions.

6.5.4 Relating Pressure Gain to Wave Dynamics

The negligible difference in PG occurred despite the significant changes in the wave dynamics. Consider Figure 6.18, which compares the PG measured with the normalized speed of the detonation wave(s), first presented in Figure 6.12. Figures 6.18a, 6.18b, and 6.18c are for a fixed equivalence ratio of 0.6, 0.8, and 1.0 respectively. Unlike previous figures, the marker color in Figure 6.18 indicates the RDC configuration instead of the equivalence ratio. The results from all mass fluxes are shown in Figure 6.18, including those not discussed in Figure 6.12. A detonation wave is said to be more "ideal" if its speed is closer to the CJ value. While not a direct and comprehensive measure of the "quality" of the detonation wave, it is nevertheless typically accepted as a proxy. A CJ detonation should have a larger thermodynamic gain than less-ideal waves since the heat release occurs in a high-pressure region. If this were true, one would expect the PG to be maximized (least negative) near a normalized wave speed of one. The results of this study do not support this. Instead, the PG is effectively constant across the measured wave speeds, especially considering the significant uncertainties in the measurements. Suppose the normalized wave speed is an adequate comparison metric for the detonation. In that case, these results lead to the conclusion that PG is invariant (or at the least insensitive) to the changes in the detonation wave(s) within the combustor. However, these results may also indicate that the normalized wave speed is a poor measurement of the "quality" of the wave. The latter is more optimistic, but the former is equally plausible.

From these results, the ratio between the inlet and exit throats appears to be the principal

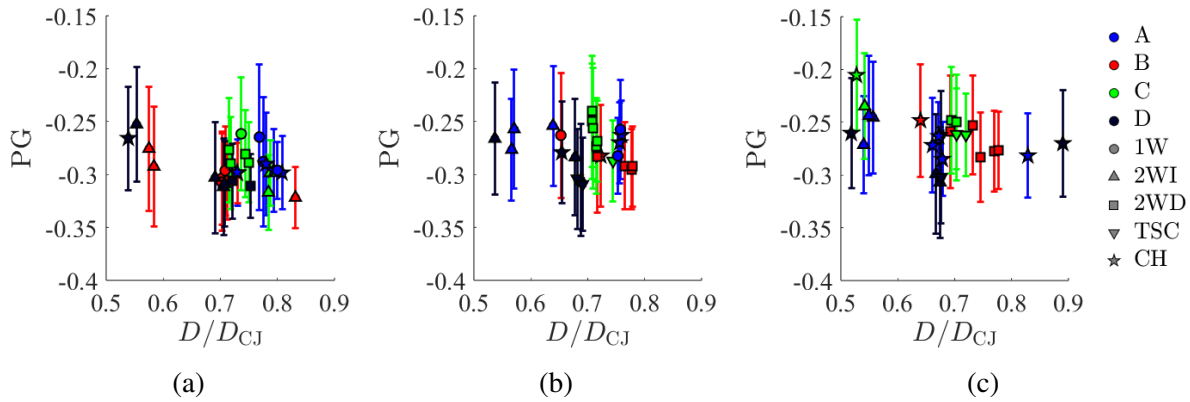

Figure 6.18: A comparison between changes in the individual wave speed and measured pressure gain for a) ϕ =0.6, b) ϕ = 0.8 and c) ϕ =1.0.

geometric quantity determining PG [13], while combustor length does impact PG meaningfully. Several explanations are plausible, although there are currently no means of verification. First, there could be a re-balancing of loss mechanisms within the system on local scales such that the global performance metrics remain the same. A hypothetical example is that a stronger detonation wave (as measured by a more ideal wave speed instead of a greater pressure ratio) results in a more significant local gain at the detonation wave front, but the expansion process from that local state to the ambient exit has increased losses when compared to the expansion from a weaker detonation. Likewise, the expansion may become more isentropic as the wave slows and grows weaker. Similarly, stronger waves may cause worse blockage and thus accrue greater losses at the inlet. The different wave systems would also likely have different heat release distributions (i.e., secondary combustion [10, 11]) that could also combine to achieve net zero change.

Another possible explanation for the performance insensitivity is that the gain across this study's detonation wave(s) is small compared to other losses, such as the inlet pressure drop. The air inlet geometry and amount of back-pressurization remained the same in this work. Thus, the pressure loss is effectively constant across the different configurations for the same global flow rates. This pressure drop could dictate the PG instead of what happens at the detonation wave. The reader is encouraged to refer back to Figure 6.13, which highlights the overall low-pressure ratios observed in this study. Suppose one theorizes that the local thermodynamic gain at the wave scales with this pressure ratio, irrespective of the wave speed, it would be logical to conclude that the weak waves observed in this work have a sufficiently small local gain that losses across the inlet dwarf the local gains. Additionally, suppose changes by the detonation are indeed small. In that case, the EAP methodology may not currently have enough precision to account for small-scale effects occurring within the device. An increased understanding of the interplay between loss mechanisms

and the detonation wave is needed to understand the decoupling from changes in the detonation wave (which, in this case, is caused by length variations) and changes in performance.

6.6 Discussion

Ultimately, the operational mode, wave speed, and other details of detonation waves had a negligible impact on the RDC performance as measured by PG for the fixed geometry and outlet conditions tested here. However, it may be possible that the quantification of performance in terms of PG evaluated according to the concept of EAP is incomplete. The evaluation of the averaging techniques presented in Chapter 2 would support this notion but is insufficient in concluding whether this is true. Furthermore, the overall significant uncertainties explored in the previous chapters may prevent adequately measuring the relatively small changes in global performance from the local changes at the detonation wave. Finally, at this time, it cannot be concluded if the insensitivity is due to a redistribution of competing effects (such as secondary combustion, back-flow, etc.) or if the air inlet/fuel injector losses dominate the overall losses of the system. Either way, it is mildly concerning that the "gain" of a RDC is irrespective of the titular rotating detonation wave(s). Regardless, one may exploit other practical benefits if the performance is insensitive to the characteristics and dynamics of the detonation wave(s).

First, the observed invariance would allow for compact designs in which the combustor length is as short as possible while maintaining rotating detonation(s). While the length cannot be too short to avoid pulsing detonations [133], and there might be minimum length requirements to sustain rotating detonations [30], compactness of the combustor could allow for alternative integration approaches specific to a different application or introduce additional volume and weight savings [136]. So long as rotating detonations occur, this shortening of the combustor occurs without sacrificing performance. All of this assumes that there is no decrease in combustion efficiency from the shortening of the combustor, which would require future evaluation.

A second benefit is the ability to "tune" (i.e., change) the detonation frequency or change the operating mode without sacrificing performance. There are geometric relations that result in stable multi-detonation wave operation that one could tailor to the required exit conditions (e.g., degree of homogeneity, exit flow speeds at the exit, etc.). Even though the 2WD, TSC, or CH operation seen here did not significantly affect performance, the time variations and/or additional non-uniformities are likely undesirable from a system integration standpoint. Changing the length would lessen the integration challenges by stabilizing the detonation wave. Likewise, if the upstream conditions are of more importance, one could lessen the combustor length to minimize blockage (plenum pressure increase) caused by the detonation. Either way, this could be beneficial in integrating an RDC into a closed system while maintaining the same level of performance.

CHAPTER 7

Impact of Detonation-Induced Blockage on the Pressure Gain

7.1 Introduction

Although the previous chapter observed that PG is insensitive to changes in the detonation wave if the inlet and outlet areas are held constant, there is still interest in exploring if significant changes in PG can occur outside of changing the mass flux or inlet/outlet areas [14] to assess how open the design space for RDCs are. Whereas the previous chapter focused solely on changing the combustor length, additional geometric parameters can be varied while still fixing the inlet area, outlet area, and fuel injection scheme. Examples of such geometric parameters are the annular gap (i.e., inner and/or outer diameters) and specific details, such as the shape of the inlet or outlet. For instance, recent studies by Brophy et al. varied the annular width for various combinations of area ratios, and they observed seemingly significant changes to the measured PG through the NPS method [121, 48]. However, in such studies, the physical area of the inlet was allowed to vary since Brophy et al. focused on maintaining a specific ratio between the inlet and channel areas. By maintaining a fixed center line diameter, the channel area grew with increasing channel width, which also increased the inlet area. Therefore, the changes in the PG observed in such studies cannot be attributed solely to the channel width, as the change in the inlet area may have also influenced the results. Thus, changing the annular gap introduces increased complexity in both hardware and comparisons to other devices as it no longer follows the trend identified by Bach et al. [14]. Such complexities are avoided in this study by instead focusing on the inlet by modifying its flow path while maintaining the same geometric inlet area.

This work changed the inlet instead of the outlet geometry due to the recent interest in the impact of backflow on the resulting PG. Backflow is gases with the locally higher total pressure/energy expanding in the direction opposite to bulk flow producing thrust. It is then theorized that the work that the fluid must exert to halt the backflow and correct the axial direction serves as a loss and may produce entropy if the process is not isentropic. Computationally, this hypothesis was

tested in a two-dimensional simulation [148] and a reduced-order thermodynamic model [154]. For instance, the work by Paxson and Miki illustrated that if 15% of the products flowed back into the inlet, the PG decreased 50% relative to the idealized PG where no backflow was present [148]. Such studies have then focused on the injector *diodicity*, or the ratio of the forward and backward pressure drops or fluidic areas. A perfectly diodic injector would prevent backflow entirely, which, based on the computational results, would be ideal for PG. However, it has also been theorized that as the inlet areas increase to increase PG [14], the backflow also increases. As such, several experimental studies have begun investigating injectors with increased diodicity [155, 55, 145, 156]. Several research groups designed the higher diodicity injectors around the concept of a Tesla valve [190, 191] to accommodate the passive injection used in RDCs. Barnouin et al. attempted to experimentally demonstrate better performance (PG) with a higher diodicity injector, but the results were somewhat inconclusive [156], thereby leaving a lack of an experimental demonstration of the theorized impact of the backflow on PG.

This chapter seeks to address that gap in the experimental literature. Whereas some contemporary works have tested injectors with a higher diodicity [145, 156], this work takes the alternative approach by intentionally modifying the inlet to have a worse diodicity. The worse diodicity results from an alteration of the flow path downstream of the inlet throat, reducing the pressure drop in the backward direction. The PG measured from the modified inlet is then compared to the baseline inlet. In doing so, this study will attempt to answer whether the experimental PG is sensitive to changes in the flow at the inlet or if the losses will re-balance, similar to the previous chapter's observation. Essentially, before trying to "optimize" the injectors as done in other studies, this study first establishes whether one can reasonably expect to measure a difference in PG given the same inlet, channel, and outlet areas. Even considering the considerable uncertainties, this study observed a significant decrease in PG for the modified inlet. The changes in PG are then compared to measures of the coupling between the detonation channel and the plenum. Such measures include the strength of the upstream propagating oblique shocks and the overall fluidic blockage. Therefore, this study is the first to experimentally demonstrate the impact of injector diodicity on PG by illustrating the increased amounts of backflow/coupling are detrimental to PG.

7.2 Geometry and Tested Operating Conditions

As discussed in Section 3.2.2, two inlet configurations are considered for this portion of the work. The visual of the two geometries is repeated here in Figure 7.1 for convenience. The first inlet is the baseline AAI from all the previous experimental chapters. The second inlet is a modified version of the baseline, AAI-M. The streamlined downstream flow path mitigates possible re-circulation regions and lowers the pressure drop in the reverse (backflow) direction. In other words, the

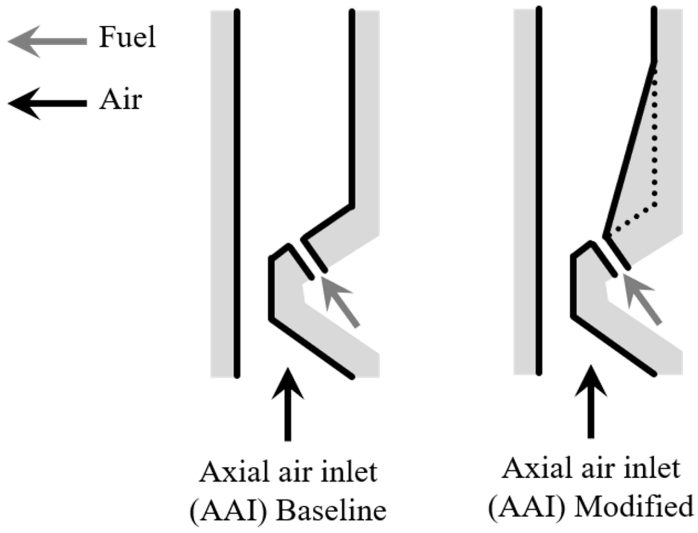

Figure 7.1: Air inlets considered in this work. Left) Baseline geometry used throughout this work and right) modified inlet to study inlet diodicity.

AAI-M has a worse diodicity than the baseline. Outside of the inlet changing, all other geometric parameters remained the same. The modification of the inlet did not alter the inlet throat area, and the same 50% reducing nozzle was employed. The length of the combustor was 119 mm, the same as Configuration C from the previous chapter.

Since this study will compare the modified inlet to the standard inlet, the test conditions tested in Chapter 6 were repeated for AAI-M. The parametric study consisted of the same discrete combination of air mass fluxes, from 150 kg s^{-1} m^{-2} to 650 kg s^{-1} m^{-2}, and equivalence ratios, 0.6 to 1.2, of H_2/air operation. Again, all tests exhibited sustained rotating detonative operation, and the testing duration was 4 seconds to accomplish a quasi-steady measurement of thrust and perform mass flow rate ramping, as discussed in previous chapters. Both the air and mass flow rates reached a steady state value with about 1-2 seconds remaining during the run.

7.3 Change in Wave Mode from Modified Inlet

This section covers fewer details of the operating mode as operation with AAI-M did not result in any new operational modes. Section 6.3 previously identified and classified the operational modes in great detail. The operation map for AAI from Section 6.3 (Configuration C), Figure 7.2a, and the operation mode for the new AAI-M configuration, Figure 7.2b recap the exhibited operational modes across all tests. Recall that the five distinct operational modes of rotating detonation wave(s) are as follows:

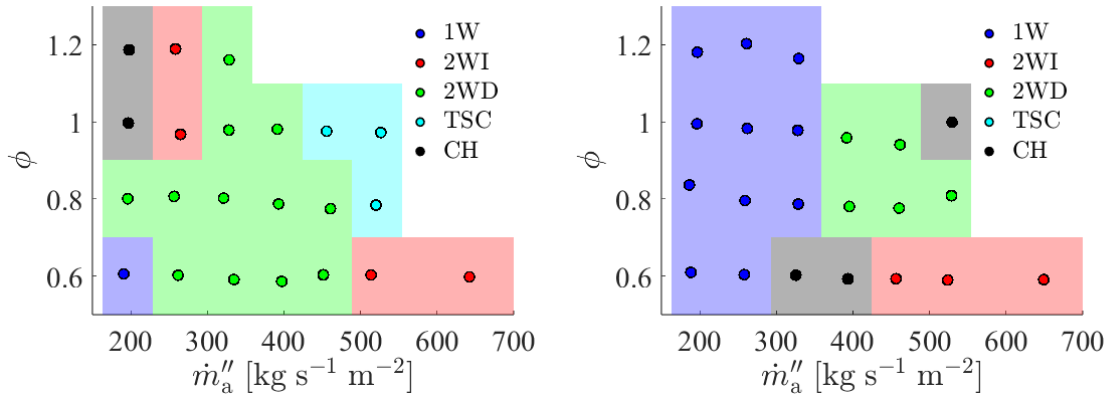

Figure 7.2: Map of operational modes for a) AAI and b) AAI-M for the same combustor length, inlet area, and outlet areas.

1. **Mode 1:** Single wave (1W)
2. **Mode 2:** Two co-rotating, *indistinguishable* waves (2WI)
3. **Mode 3:** Two co-rotating, *distinguishable* waves (2WD)
4. **Mode 4:** Multiple waves that follow a transient super-cycle (TSC)
5. **Mode 5:** Chaotic operation of multiple waves (CH)

Figure 7.2 highlights that the modified inlet significantly impacted the operating mode at lower mass fluxes. Whereas, 1W operation was rare for the baseline configuration, only appearing once when $\dot{m}''_a = 190$ kg s^{-1} m^{-2} and $\phi = 0.6$, many tests of AAI-M resulted in 1W operation. Specifically, effectively, all tests with $\dot{m}''_a \leq 330$ kg s^{-1} m^{-2} resulted in 1W regardless of the equivalence ratio. The reduction in multiplicity may result from the injector recovery as influenced by the inlet modification. The CH operation at 325 and 393 kg s^{-1} m^{-2} and $\phi = 0.6$ appear to be a transient state between 1W and 2WI as the system rapidly transitions between the two modes. The rapid transitions did not repeat periodically, differentiating this CH operation from TSC. The remaining tests, $\dot{m}''_a \geq 393$ kg s^{-1} m^{-2}, resulted in similar operating modes between the two inlets with regions of both 2WI and 2WD operation. Finally, no test with AAI-M resulted in TSC operation.

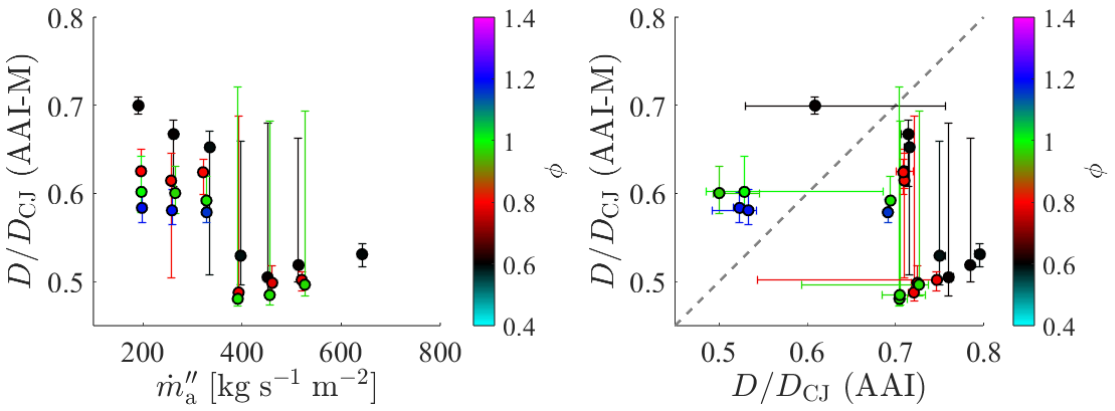

(a) (b)

Figure 7.3: a) Evolution of wave speed across the operating map. b) Direct comparison of wave speed between inlets.

7.4 Change in Wave Properties from Modified Inlet

As expected with any other geometric change, the properties of detonation wave(s) changed due to the inlet modification. This study again considers the detonation wave speed and pressure ratio as global metrics of the non-ideality of the detonation waves. Similar to the previous chapter, the focus is on these metrics independent of the operating mode, even though the operating mode affects the speed and pressure ratios. For these comparisons, singular values of the measured properties are given based upon the peak of the computed empirical PDFs, and error bars indicate 95% of the data points. In the case of the pressure ratio, a more detailed investigation into the distribution of base and peak pressures is necessary. The previous chapter did not utilize the same thorough investigations since the four lengths would cause such analysis to scale exponentially.

7.4.1 Speed of Individual Waves

Before comparing the wave speeds (D) between the inlets, Figure 7.3a presents measured wave speeds for AAI-M. As was done in the previous chapter (Section 6.4), wave speed was measured using CWA [45] and cross-validated with the time-averaged Power Spectral Density (PSD) of high-speed pressure measurements. To better compare the wave speed of the individual wave(s), this work normalizes the speed by the ideal CJ detonation wave speed (D_{CJ}). When 1W operation occurred, the detonation wave propagated at speeds between 60%-70% D_{CJ}, with leaner equivalence ratios resulting in larger normalized wave speeds. The non-normalized wave speeds (about 1160 m/s) did not change between the equivalence ratios; therefore, the decrease in normalized wave speed with increasing equivalence ratio is indicative that the added potential heat release from the

higher equivalence ratios did not directly support the detonation wave. Additional evidence for this comes from the high-speed video in which the increase in equivalence ratio correlated with a visible increase in the amount of combustion occurring downstream of the RDC. After $\dot{m}''_a$ increased to 390 kg s^{-1} m^{-2} and the multiplicity rose from one to two waves, a step-change in wave speed was observed. A decrease in wave speed with an increase in multiplicity has been commonly observed in the RDC literature [192, 187]. In this case, the wave speed dropped to nearly 50% D_{CJ}, almost acoustic speeds in the post-combustion gases. These low speeds persisted throughout all the tests that exhibited two waves.

Figure 7.3b directly compares the wave speed for each test with AAI-M to the corresponding test with AAI. A handful of the 1W operating modes observed with AAI-M had a larger wave speed than the corresponding wave(s) with AAI since some near acoustic speeds also occurred with AAI. However, most data points generally fall below the 1:1 line, which is unsurprising considering the acoustic speeds observed in AAI-M when more than one wave was present. Still, some of the 1W operating modes were also slower than the corresponding tests with AAI. Therefore, while not universally true, it is concluded that the flow path modification generally resulted in slower detonation wave(s). The current study could not determine the cause of the slower waves since the determination is beyond the scope of this work. Nevertheless, this observation is consistent with previous testing of the AAI-M without the nozzle [58].

7.4.2 Pressure Ratio across Detonation Waves

7.4.2.1 Direct Comparisons

A high-speed channel measurement measured the pressure ratio across the detonation wave(s) ($p_{r,3.2}$) to assess the ideality of the detonation wave(s). This study took the channel measurement at the same distance from the fuel injectors and inlet throat for both inlets; however, the cross-sectional area at the measurement point differed between AAI and AAI-M. Specifically, the measurement location for the AAI-M was at an axial location where the area diverged from the modification; thus, the cross-sectional area at the measurement location was approximately $0.73A_{3.2}$ for AAI-M and $A_{3.2}$ for AAI. The change in cross-sectional area may then change the resulting pressure measurements. Figure 7.4a gives the normalized (by the ideal CJ value, $p_{r,CJ}$) pressure ratios for AAI-M across all operating conditions. Based solely on the markers, the normalized pressure ratio decreased with increasing equivalence ratio; the measured pressure ratios did not increase as rapidly with equivalence ratio as the ideal CJ values. However, the large error bars cause the differences caused by changes in mass flux and equivalence ratio to be less statistically significant.

Like Figure 7.3b did for wave speeds, Figure 7.4b directly compares the pressure ratios between the inlets for similar test conditions. Recall from the last chapter that some of the tests in AAI

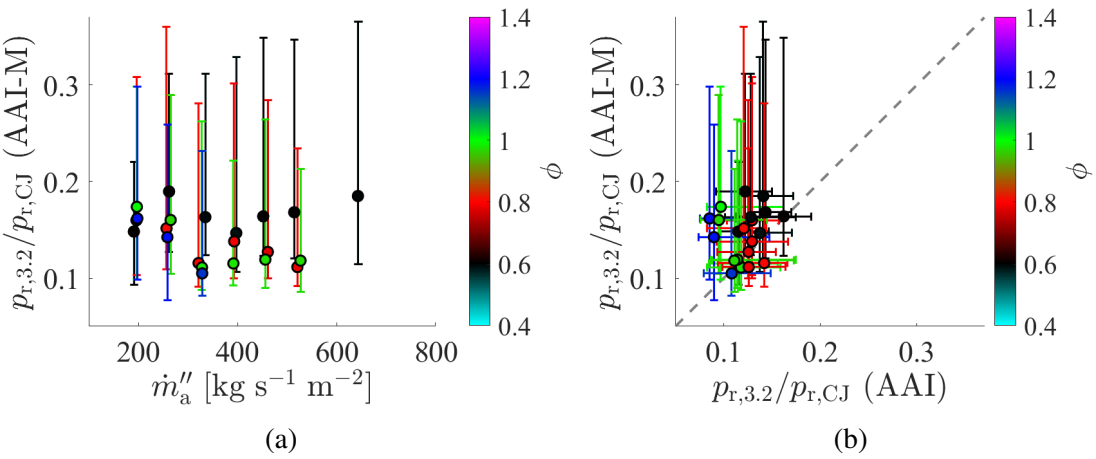

Figure 7.4: a) Evolution of detonation pressure ratio across the operating map. b) Direct comparison of pressure ratio in the channel between inlets.

resulted in distinguishable co-rotating waves (2WD), which had bimodal pressure ratio distribution (Section 6.3.2). This study took the larger peak as the most probable value for those tests. Two main observations are made from Figure 7.4b. First, many of the markers are above the dashed gray, 1:1 line, which on first pass would lead to the conclusion that the pressure ratios were larger. Greater pressure ratios would be consistent with the previous testing of AAI-M without a nozzle [58]. Such conclusions neglect the error bars which span across the dashed 1:1 line. The second main observation is that the error bars are much more significant in the y-direction than in the x-direction. In other words, the distribution of measured pressure ratios for AAI-M is much broader and skewed to the right. A more detailed analysis of the PDFs of the pressure ratios is warranted to understand these observations better.

7.4.2.2 Statistics of Individual Tests

The pressure ratio across the detonation wave(s) consists of two parts, the peak pressure (p^+) and base pressure (p^-), that are each independently identified [188]. As such, the distributions of both components are assessed before considering the pressure ratio, even though this is the quantity that is of the most interest. Consider the sample empirical PDFs of the peak and base pressures given in Figure 7.5a and 7.5b respectively. These samples are for $\dot{m}''_a = 514$ kg s^{-1} m^{-2} and $\phi = 0.6$, and the color indicates the inlet configuration. There is more significant variability for the AAI-M (red) than the AAI (blue) for each quantity. The variability/spread in the data can be a result of several factors: the imprecise nature of the algorithm to detect the base and peak pressures, thermal drift in the sensors, changes in the overall flowfield in time, and potential non-linear interactions between the primary detonation waves and secondary waves. Thermal drift can be identified in the

data as abnormally low-pressure readings since the voltage decreases as the sensor face overheats. One can correct for thermal drift by either adjusting the mean component of the signal in such regions of time or by directly removing erroneous measurements, although this is subjective. The current study takes the former approach despite the correction process being imperfect. In addition, non-linear interactions of secondary waves are detectable in spectral content as they appear as a super-cycle with a well-defined frequency. Not all tests exhibited such secondary waves, so this cannot be the sole explanation for the spread. Finally, the impact of the algorithm is unclear, so this study assumed that given enough samples, the algorithm's results would follow the central limit theorem.

Returning to the specific distributions given in Figure 7.5, the peak pressure has a larger skew (to the right). The cause of the skew is unknown since the non-linear interactions from secondary waves [45] were absent in this test. The PSD plots for the pressure measurements proved the absence of the secondary waves. Meanwhile, the base pressure more closely follows a normal distribution for AAI-M along with having a lower mean; however, this is not always the case as there are times when the distribution directly overlaps the distribution from AAI. The following section investigates this further. Both the peak and base pressures combine into the distribution for the pressure ratio (p_r) given in Figure 7.5c. The effects of the individual variability culminate with a relatively flat PDF compared to AAI. Thus, the larger error bars in Figure 7.4b stem from the increased variability of both the peak and base pressures, with the skew of the peak pressure likely having a more significant impact.

7.4.2.3 Determining Probability of Changes

The distributions discussed in the previous section are necessary to contextualize and understand the changes between the two inlets. Instead of simply comparing the most likely value of any quantities, this study now compares the distributions against one another. More specifically, this study seeks to generate the PDF of the relative change in a given quantity. This relative change is given by Π, with a subscript that gives the specific quantity considered. For instance, the relative change in pressure ratio (p_r) is given by the following,

$$\Pi_{p_\mathrm{r}} = \frac{p_{\mathrm{r,M}} - p_{\mathrm{r,B}}}{p_{\mathrm{r,B}}} \tag{7.1}$$

$$= \frac{p_{\mathrm{r,M}}}{p_{\mathrm{r,B}}} - 1 \tag{7.2}$$

The Π ratio will always be the change in a measured quantity between AAI-M (subscript "M") and AAI (subscript "B" for baseline), normalized by the baseline measurement (AAI) of said quantity.

This study found the distribution of Π for any quantity through a Monte-Carlo approach to

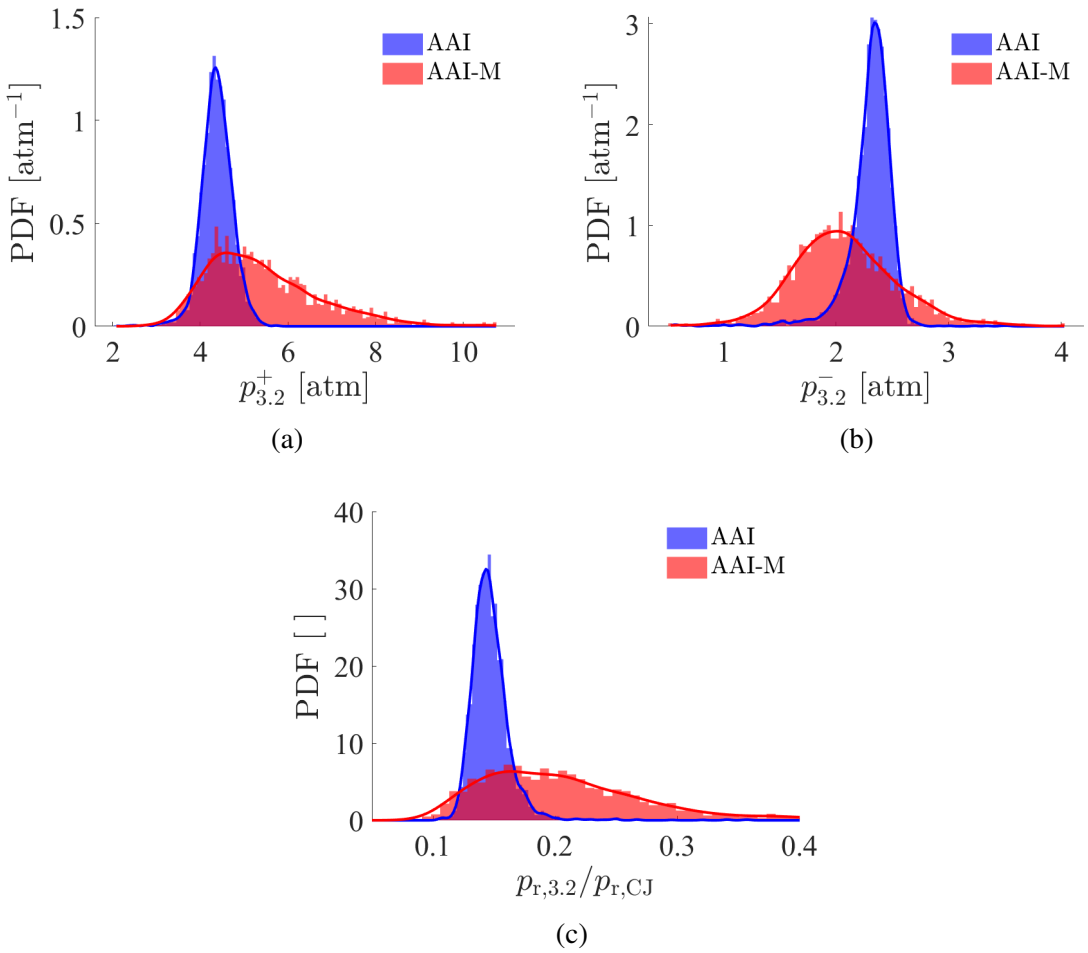

Figure 7.5: PDFs of the channel a) peak pressure, b) base pressure, and c) normalized pressure ratio across detonation wave. Data from $\dot{m}''_a = 513$ kg s^{-1} m^{-2} with $\phi = 0.6$.

avoid fitting a distribution to the data, which either will smooth the data or require applying a particular shape. The empirical distribution found with the AAI-M was assumed to be independent of the distribution of the same quantity from the AAI. The Monte-Carlo simulation independently randomly sampled both empirical Cumulative Density Function (CDF)s 5000 times and then computed Π for each pair of randomly selected values. The 5000 instances of Π then approximate the distribution of Π.

Examples of the resulting distributions for each of the quantities from the convolutions are in Figure 7.6. These are for the cases considered initially in Figure 7.5. Since Π is a ratio of two PDFs, it will inherently be right-skewed, although the skew of the peak pressure and the pressure ratio for the AAI-M also cause more skew. The dashed red line is at $\Pi = 0$, which occurs when there is no change between the inlets. Positive values of Π are when AAI-M had a larger quantity, while negative values are when the quantity is smaller for AAI-M. Using these ac PDFs, the peak

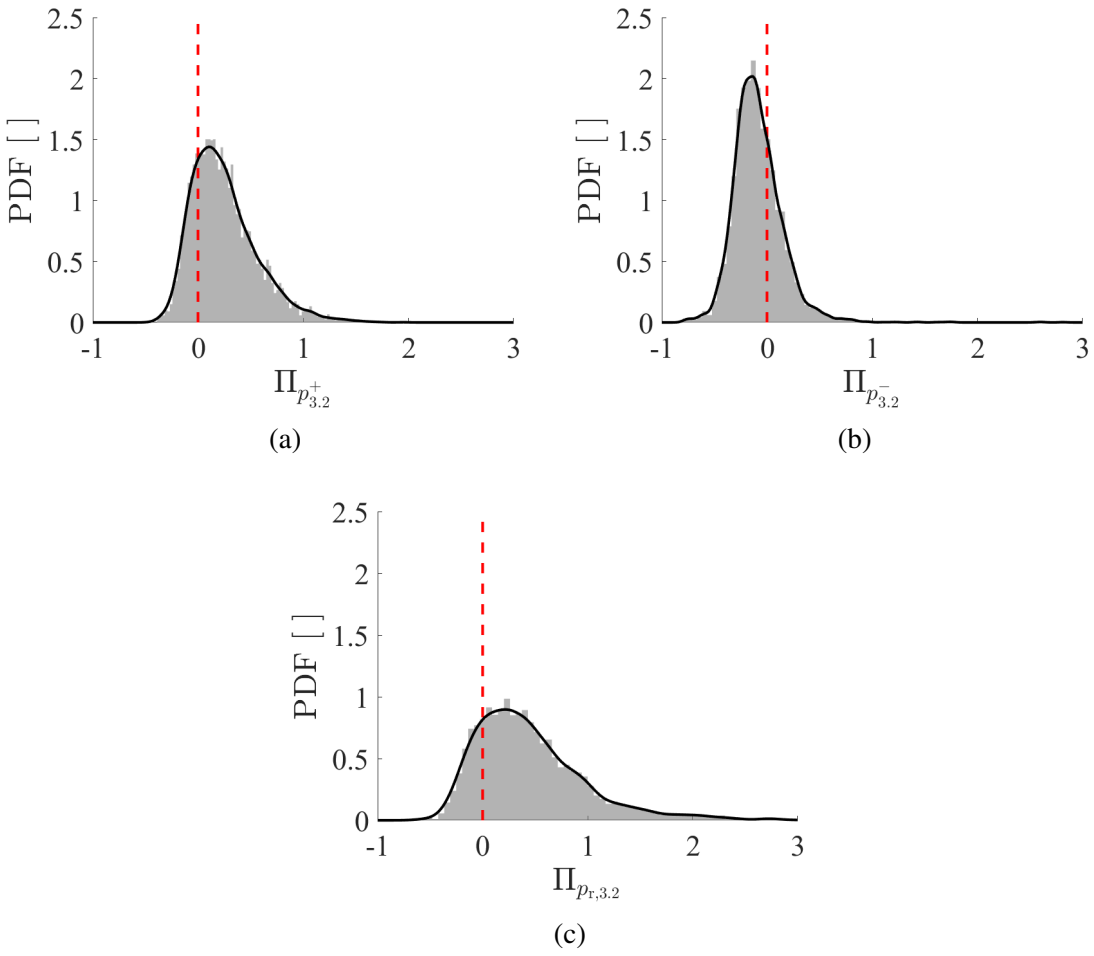

Figure 7.6: PDFs of the relative change in the channel a) peak pressure, b) base pressure, and c) normalized pressure ratio across detonation wave. Data from $\dot{m}''_a = 513$ kg s^{-1} m^{-2} with $\phi = 0.6$.

pressures and pressure ratios are more likely to be larger for AAI-M than AAI, and the base pressure is more likely to be less for AAI-M than AAI. While this could have been observed from Figure 7.5, this approach proves helpful in better quantifying the probabilistic chance that the quantity changed in a significant manner.

Due to the overlapping underlying distributions, the Π ($f(\Pi)$) distribution typically spans both positive and negative values of Π. It is desirable to define the probability (P) of the measured quantity being greater for AAI-M than for AAI. The probability comes from integrating the

empirical PDF of Π,

$$P(\Pi_{p_r} > 0) = \int_0^\infty f(\Pi_{p_r}) d\Pi \tag{7.3}$$

$$= 1 - \int_{-\infty}^0 f(\Pi_{p_r}) d\Pi \tag{7.4}$$

Equation 7.3 is equivalent to evaluating the empirical CDF at $\Pi = 0$ and subtracting that probability from one. A probability of 0% would indicate that the quantity for AAI-M is guaranteed to be less than that of AAI, even considering the experimental uncertainties/distributions. Conversely, a probability of 100% would indicate the quantity for AAI-M is guaranteed to be greater than that of AAI. Meanwhile, a normal distribution centered around $\Pi = 0$ would result in a probability of precisely 50%, making it inconclusive if the quantity is greater in either inlet. In such cases, the quantity is essentially the same between the two inlets.

This process was done for the peak and base pressures along with the pressure ratio, with the results being in Figure 7.7 for the case considered thus far. The peak pressure had the highest probability (of the three quantities) of being larger in AAI-M than AAI, with the probabilities ranging from 65% to 98% and averaging around 83%. The higher probabilities for the peak pressures likely arose from the peak pressure distributions in AAI-M being right-skewed, as displayed in Figure 7.6a. In general, as the equivalence ratio increased, so did the probability that AAI-M had a larger peak pressure. Due to the high probabilities, it is reasonable to say that it was highly likely that the peak pressures were larger in AAI-M; however, statistical significance (greater than 95% chance) is limited to only a handful of cases.

The base pressure did not follow a pattern similar to the peak pressure. The range of the probabilities was quite extensive, ranging from 10% to 79%, with the average being 45%. The equivalence ratio greatly impacted the base pressure since $\phi = 0.6$ had a high probability of AAI-M having a lower base pressure than AAI. For instance, the 10% chance that the base pressure AAI-M was larger corresponds to a 90% change it was lower than AAI. Overall, the base pressure seemed marginally lower in AAI-M at low fluxes for all ϕ and $\phi = 0.6$ for all fluxes. Then, the base pressure seemed marginally larger for AAI-M for equivalence ratios greater than 0.6 at higher fluxes. However, none of the differences were statistically significant, making the base pressure nearly the same between the inlets. This result is somewhat surprising considering that the flow would still be expanding through the area change. Yet, one could argue that slowing the expansion process lessened the viscous/turbulent losses. The net change in base pressure would be negligible as the lower losses balance the flow still expanding.

Finally, Figure 7.7c gives the pressure ratio for consideration. For every test, it was more probable that the pressure ratio was greater for AAI-M, with probabilities ranging from 61% to

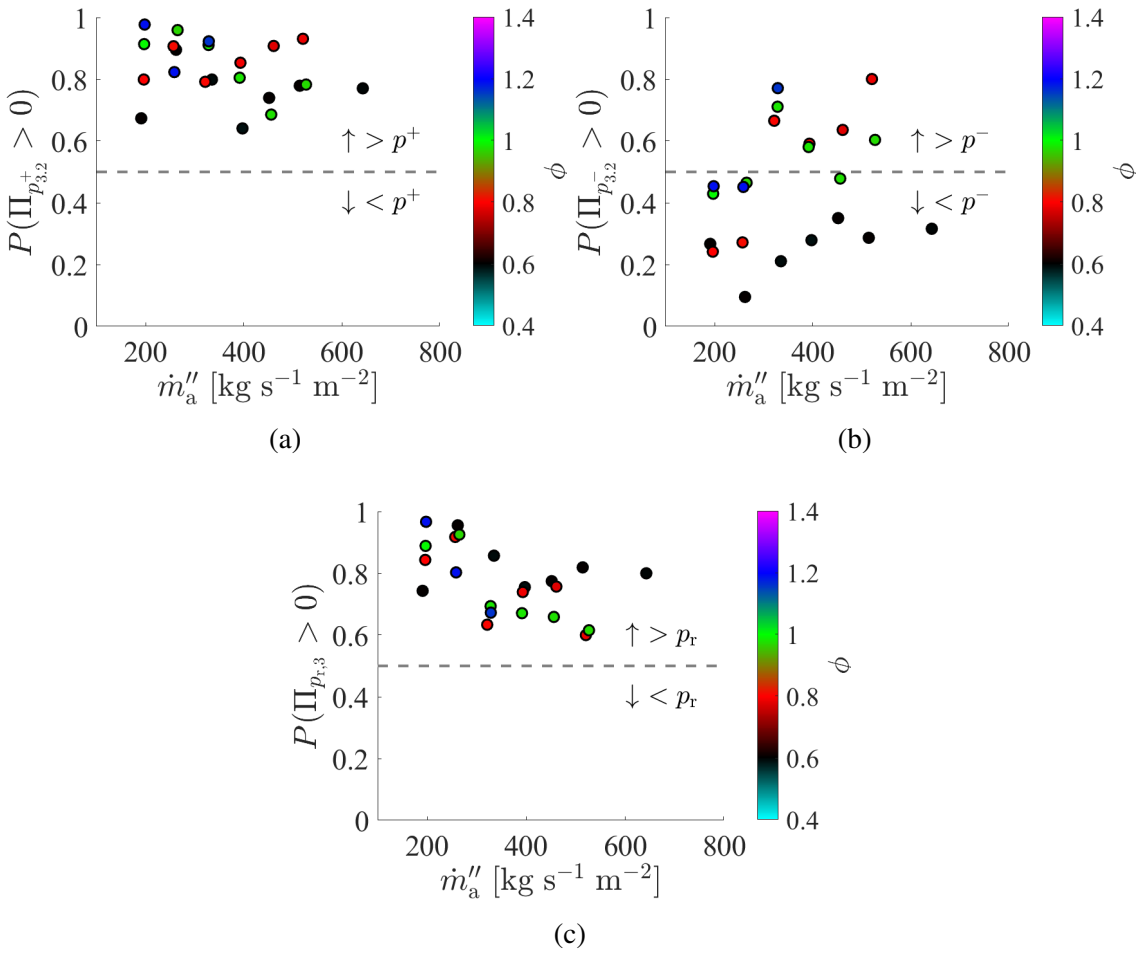

Figure 7.7: Probability that the relative change in a) peak pressure, b) base pressure, and c) normalized pressure ratio across detonation wave in the channel.

97% and averaging about 78%. This closely matches the results from the peak pressures, Figure 7.7a, although the probabilities for the pressure ratio are slightly less. Unlike the peak and base pressures, which had general trends with equivalence ratios, the pressure ratio had a less clear trend. At higher fluxes, the probabilities are the greatest for $\phi = 0.6$ from the lower base pressures. Since all the other equivalence ratios had effectively the same base pressures, the larger peak pressures for AAI-M lead to larger pressure ratios for AAI-M. Overall, while not every case is statistically significant, the trends suggest that the detonation waves were slower and likely stronger for AAI-M compared to the corresponding cases for AAI. While this matches previous results from testing AAI-M without a nozzle [58], the analysis presented here better captures the inherent spread to the data by using statistical arguments to evaluate the pressure ratios.

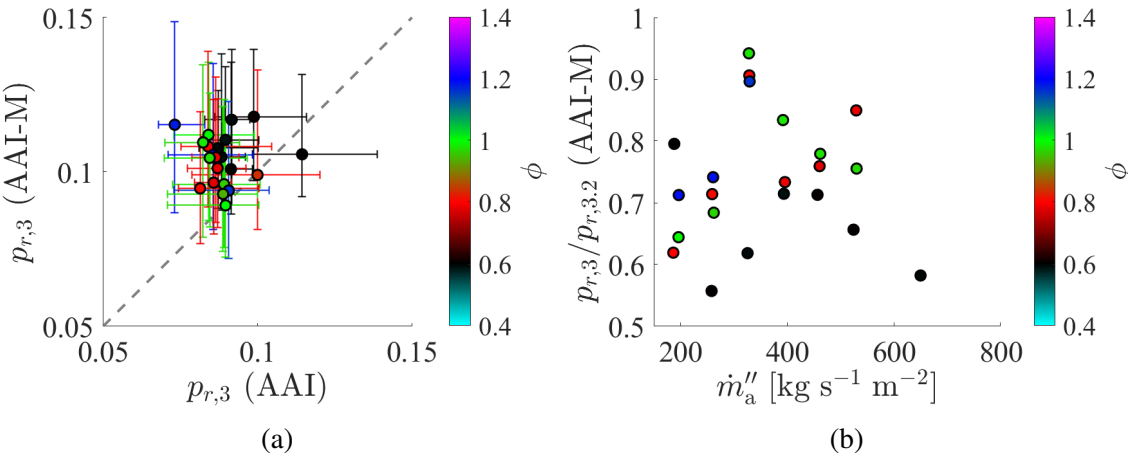

Figure 7.8: a) Direct comparison of pressure ratio across the oblique shocks in the plenum between inlets. b) The reduction in pressure ratio between the plenum and channel.

7.5 Coupling Between Detonation Channel and Plenum

This study explores the coupling between the channel and the upstream plenum in two different manners. First, a high-speed pressure measurement upstream of the inlet throat is evaluated. Such a measurement captures upstream propagating pressure disturbances (i.e., oblique shock waves). Second, the blockage fraction first discussed in the previous chapter is explored. The blockage fraction provides a sense of the global mean component of the plenum pressure.

7.5.1 Pressure Disturbances Upstream of Inlet

This study employed an additional high-speed pressure measurement 6.35 mm (0.25 in) upstream of the air inlet throat for both inlets. This measurement allows for studying the upstream propagating oblique shocks emanating from the detonation channel. Unlike the channel pressure measurement, the measurement cross-sectional area did not change from the inlet modifications. Thus, no changes in flow area influence the comparisons between the inlets of the statistics of the peak pressure, base pressure, and pressure ratios across the oblique shocks. Once again, the analysis begins with a direct comparison between the pressure ratios of the upstream propagating disturbances ($p_{r,3}$), Figure 7.8a. Note that the axis scales in Figure 7.8a are smaller than those for Figure 7.4b since the pressure ratios are lower across the oblique shock than the detonation wave(s) ($p_{r,3.2}$). For instance, there is a reduction of between 10-50% of the mean pressure ratios between the channel (③.②) and the plenum measurement (③), Figure 7.8b. The results presented in Figure 7.8b are specifically for AAI-M, although the trends are comparable between the inlets. In addition to the smaller pressure ratios, the spread in the pressure ratio measurements (i.e., the error bars) is much smaller for this

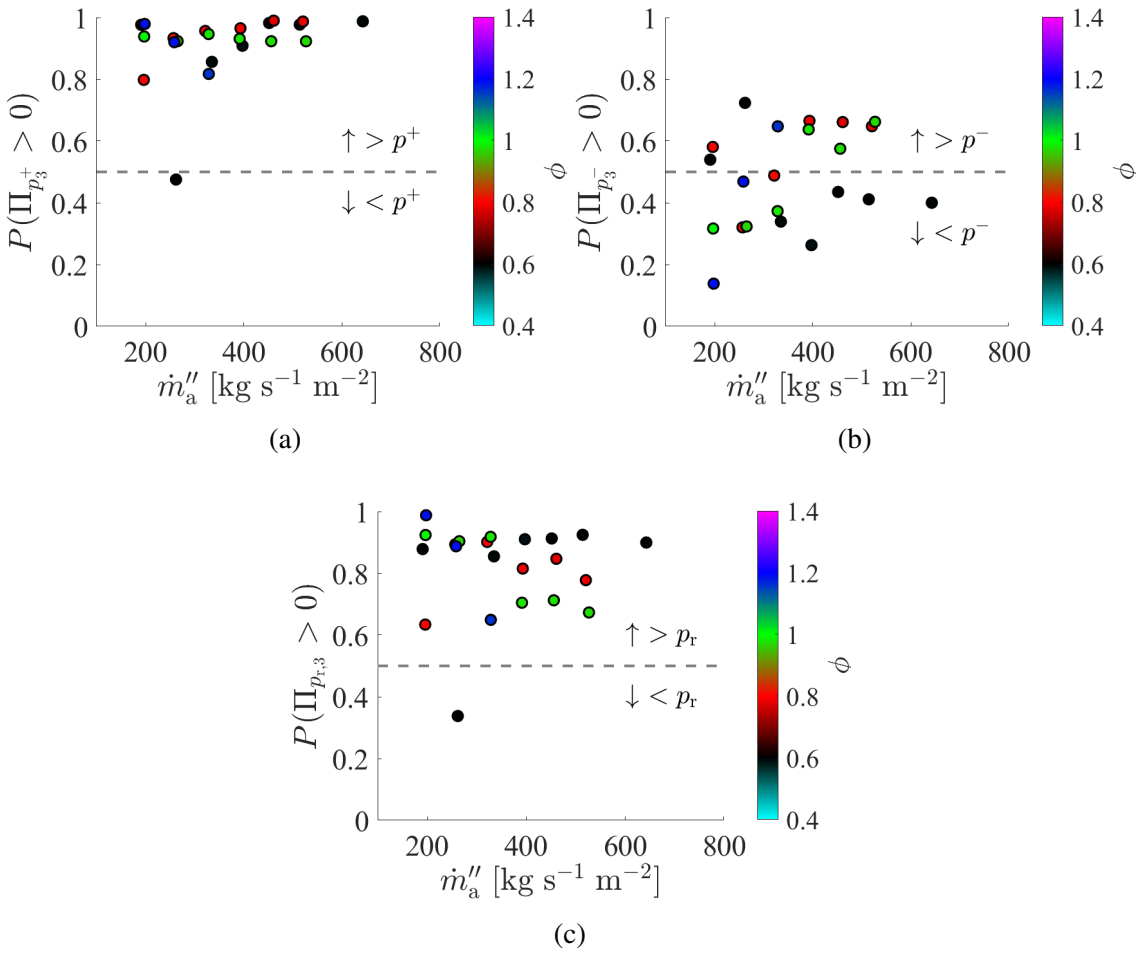

Figure 7.9: Probability that the relative change in a) peak pressure, b) base pressure, and c) pressure ratio across oblique shock wave in the inlet.

measurement than the channel measurement. Based solely on the markers, the oblique shocks were stronger in the AAI-M than AAI since all points were on or above the 1:1 line. The error bars are comparable between the inlets, unlike the channel measurement, which had the AAI-M be more skewed to the right than AAI distribution. The remainder of this section will further discuss the uncertainty caused by the error bars.

To assess if the changes in the inlet were statistically significant, the empirical PDFs of the pressure measurements were used to generate the PDF of the relative change in those measurements (Π) using Eqn. 7.2. Figure 7.9 gives the resulting probabilities based on the PDF of Π. Focusing on the peak pressures across the oblique shock (p_3^+) in Figure 7.9a, effectively all the data points had over 80% chance of the peak pressures being larger for AAI-M. Additionally, about half of the tests had statistically significant probabilities over 95%, resulting in an average probability of about 94%. The exception to this was $\dot{m}''_a$ = 300 kg s^{-1} m^{-2} and ϕ = 0.6, which had a probability

of being larger of effectively 50%; indicative of being the same between the inlets. The current measurements were insufficient to determine the cause of this abnormality, and the point was deemed an outlier. Thus, the peak pressures across the oblique shock(s) in the inlet grew larger from the modified flow path of AAI-M.

Like the channel measurement, the probability of the larger base pressure, Figure 7.9b, is evenly distributed among the center (50%) than the peak pressure, as reflected by the mean probability being 48%. Some cases were more likely to have a lower base pressure than AAI. Meanwhile, an equal number of cases had a greater likelihood of being larger, and there was no discernible pattern with either mass flux or equivalence ratio. In the context of the measurement in the inlet, the flow of fresh reactants from the plenum likely dictates the base pressure more than the upstream propagating oblique shock. The flow of fresh reactants is affected by the flow rates and the geometry upstream of the inlet throat, neither of which changed when AAI-M was implemented. Hence, the minimal changes in the base pressures and the more considerable overlap in the empirical PDFs result in the probabilities that $\Pi_{p^-} > 0$ of around 50%.

Finally, Figure 7.9c examines the strength of the oblique shocks based on the pressure ratio across it ($p_{\mathrm{r},3}$). In general, the probability that the pressure ratios are larger is less than the corresponding peak pressure probabilities ranging from as low as 65% and having an average of 84%. The lone point below the 50% line is the same test that resulted in the outlier peak pressure as discussed above. Despite the many tests in which the peak pressures were statistically greater for the AAI-M than AAI, only a single test had a pressure ratio that had a statistically significant likelihood of being greater in AAI-M. Based upon these results, the oblique shocks were likely stronger in the AAI-M, although this is not definitive.

Currently, there is no established link between the strength of these pressure events in the inlet and the strength of the detonation wave within the channel of a RDC. While somewhat inconclusive, there is reason to believe that the detonation wave(s) in the channel for AAI-M were stronger. It would be reasonable to hypothesize that the oblique shock strength would scale with the detonation wave strength, which would be consistent with the results of a detonation bounded by inert gases [36]. Still, neither an experimental nor computational demonstration of this exists in the literature. It may also be that the more gradual area change from the modified flow path is more conducive to the propagation of the oblique shock upstream, as sudden area changes can significantly disrupt a shock [193, 194]. Therefore, the oblique shock(s) can travel upstream through AAI-M without suffering as great of an induced attenuation as the baseline AAI. Regardless of the cause, the channel can seemingly communicate more with the plenum with the modified inlet for AAI-M because of the likelihood of stronger oblique shocks.

7.5.2 Blockage Fraction Measurements

Once again, the established effective blockage fraction (B_{m}) is applied to quantify the global coupling between the detonation channel and the air plenum using Eqn. 6.1. Unlike the analysis above, the blockage fraction takes a global approach as it considers the increase in the mean component of the plenum pressure. The blockage fraction, shown in Figure 7.10a, decreased with increasing air mass flux regardless of the inlet configuration. This result aligns with previous observations [139, 50]. More importantly, the results from AAI-M (triangles) are significantly larger than the results from AAI (circles). This increase is even more apparent in the direct comparisons, Figure 7.10b. No error bars are presented for B_{m} as the calculation of it relies upon an interpolation of the empirical curve relating pressure and mass flow rate, and the uncertainty of such an interpolation is challenging to quantify. Otherwise, the uncertainty would come from the pressure measurements, which are assumed to be negligible.

The geometry upstream of the inlet throat of AAI-M was identical to AAI; thus, the non-reacting flow characteristics (e.g., pressure drop, discharge coefficient, etc.) did not significantly change between the two inlets. More specifically, the flow's forward direction was undisturbed from the inlet modifications. In contrast, this study theorized that the changes made to the inlet alter the characteristics of the reversed flow direction, although this was not directly evaluated. Nevertheless, since the forward direction pressure drop did not change, a further increase in the plenum pressure indicates an increase in the fluidic blockage at the throat. Therefore, the significant increase in the blockage fraction presented in Figure 7.10 is assumed to be directly correlated to an increase in the fluidic blockage as opposed to a change in the inherent pressure losses or discharge coefficient of the inlet. Overall, the increase in fluidic blockage and the stronger upstream propagating oblique shocks provide strong evidence that the coupling between the channel and plenum significantly increased due to the modification as initially hypothesized.

7.6 Performance Analysis

7.6.1 Gross Thrust Measurements

Before considering the PG measurements, an examination of the gross thrust used in the EAP method is warranted. The evolution of the measurements with air mass flux is given in Figure 7.11a, where, once again, the thrust increases nearly linearly with increasing mass flux and also increases with increasing equivalence ratio. For most of the operating conditions, the AAI-M (triangles) are slightly below the AAI (circles). The error bars were purposely omitted from Figure 7.11a for clarity to enable better discernment between the marker shapes. Nevertheless, the error bars appear in the direct comparison between the two inlets, Figure 7.11b. In Figure 7.11b, the data

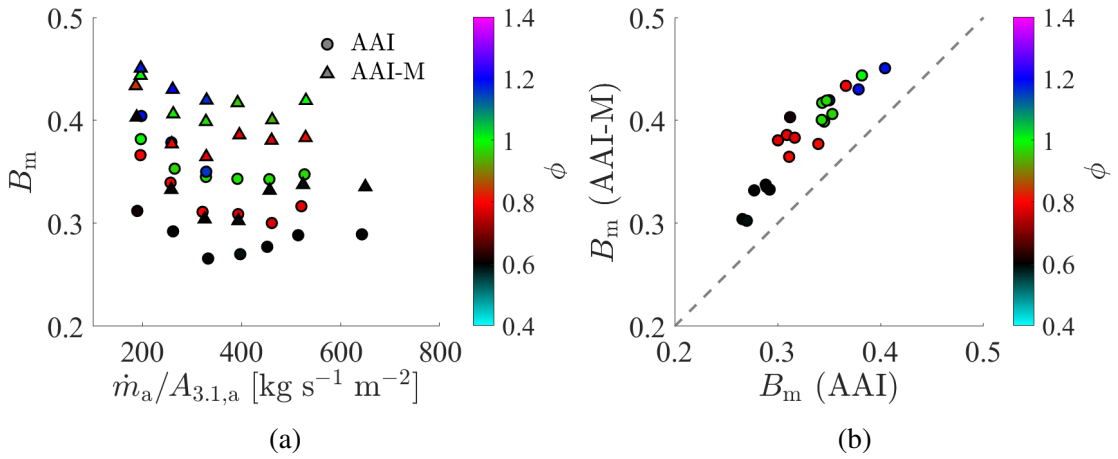

Figure 7.10: a) Blockage fraction decreases with increasing mass flux. b) Direct comparison of blockage fraction between the two inlets.

clusters around the 1:1 line, suggesting an equal thrust production between the two inlets, especially considering the error bars. However, the large span of thrust values, over 400 N, makes seeing the overlap more challenging than the other measurements simply due to the scale of the axes.

Significant changes are more identifiable by normalizing the change in thrust by the baseline results. As such, the relative change, Π from Eqn. 7.2, between the gross thrust measurements is employed. However, unlike the pressure measurements, the exact empirical PDF of F_G does not represent the full uncertainty. Instead, the uncertainty is estimated (in Chapter 5) by propagating the individual experimental uncertainties. In doing so, this work implicitly assumed that the F_G is normally distributed about the reported value, with the standard deviation relating to the uncertainty by Eqn. 3.8. A Monte-Carlo sampling process was again used, with the only difference being randomly sampling the normal distributions of F_G instead of an empirical PDF. Figure 7.11c gives the probabilities that the gross thrust produced with the AAI-M were greater than the corresponding AAI tests. Many of the points fall below the 0.5 line, which correlates to having a higher probability of having worse thrust production with the AAI-M. The maximum probability of a worse performance was around 90%, with many cases having only between 60-80% probabilities. Additionally, there were several fuel-lean tests where it was more probable that the AAI-M produced more thrust, but, again, the changes were largely insignificant. Overall, while a reduction in gross thrust output is still probable for many cases, the change is generally marginal compared to the uncertainty, making definitive claims of significant performance changes unsubstantiated.

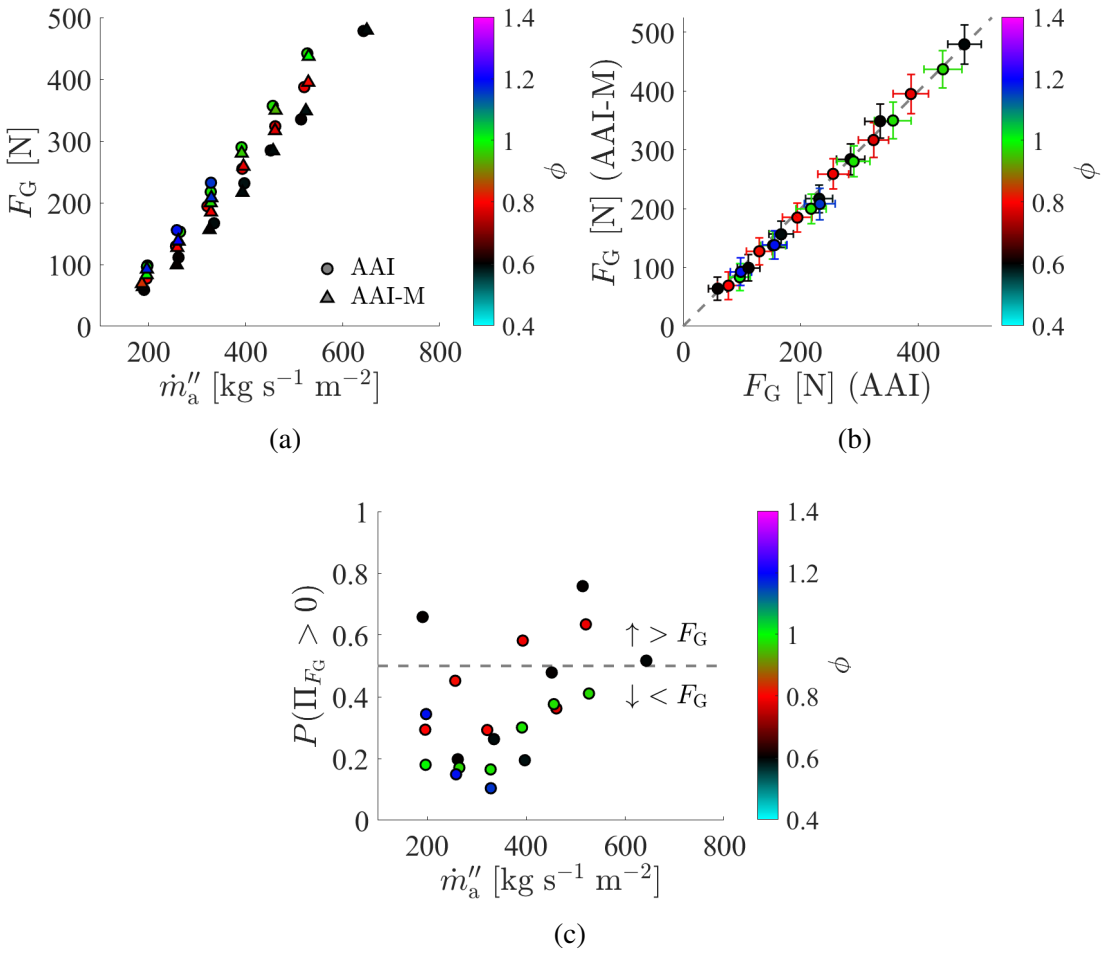

Figure 7.11: a) Gross thrust still decreased with increasing flux. b) Direct comparisons of F_G appear to fall along the 1:1 line. c) There is an insignificant probability of a worse F_G due to the large uncertainties.

7.6.2 Pressure Gain Measurements

With a probable decrease in gross thrust and a significant increase in the blockage fraction, it is no surprise that on the first pass of Figure 7.12a, the PG for the AAI-M is less (worse) than the AAI. The error bars are purposely omitted for clarity, like the gross thrust plot in Figure 7.11a. The previously observed trend of decreasing (worsening) PG with air mass flux persists since the losses across the injector will still scale with increasing flux despite the modification. In the more direct comparison between the two inlets, Figure 7.12b, all the markers are decidedly below the 1:1 line. Without the uncertainties, this indicates the PG being worse in the AAI-M compared to the AAI. As has been the case throughout this work, the larger uncertainties identified in Chapter 5 complicate the direct comparisons, as some of the error bars cross the 1:1 line, potentially leading

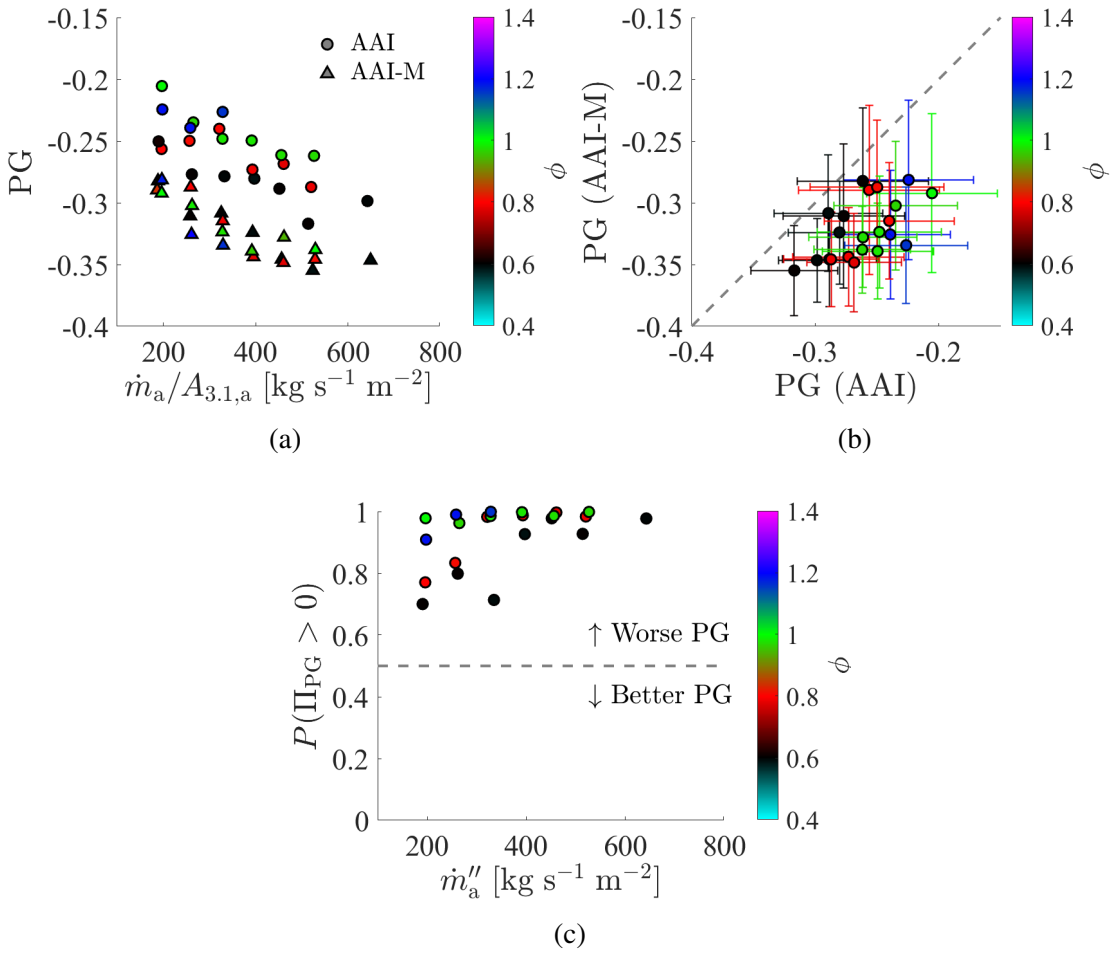

Figure 7.12: a) Pressure gain still decreased with increasing flux. b) Direct comparisons of PG suggest worse performance from AAI-M. c) There is a high probability of a worse PG despite the large uncertainties.

to no significant change in PG as a result of the relatively substantial experimental uncertainties.

The probability that the value of PG is larger (more positive) in the AAI-M is given in Figure 7.12c. Like the gross thrust, a normal distribution given by the measured uncertainty was used for the Monte-Carlo sampling in favor of an empirical PDF. Due to the negative signs of PG, a Π ratio less than zero is indicative of better (less negative) PG values for the AAI-M. The annotated text in Figure 7.12c emphasizes this. Several of the low mass flux and fuel-lean tests had less significant chances of having worse PG by being 80% or less probabilities. From Section 5.4.3, these tests had the greatest relative uncertainty, limiting the significance of the potential PG decrement. Nevertheless, a vast majority of the tests had probabilities that had a probability of being worse that was greater than 95%. Thus, even though the experimental uncertainties are relatively large, the decrement in PG from modifying the inlet can be significant. This result contrasts the

results from the previous chapter, which had no significant difference in the experimental PG.

7.7 Blockage as a Loss Mechanism

Upon examination of Figs. 7.10 and 7.12, it would appear evident that the worse performance of the modified inlet correlates with an increase in the blockage fraction. Such a correlation is seemingly intuitive as a worse blockage is a result of a greater back-pressurization of the plenum, which subsequently would reduce the computed PG if the same outlet total pressure was achieved (refer to Eqn. 5.9). However, determining whether the decrease in performance is a product of augmented blockage (backflow) or a consequence of a change in the detonation wave(s) is challenging due to the coupled nature of RDCs. Recall that in the previous chapter, the PG was invariant to the wave dynamics with the experimental uncertainties. While it is beyond the scope of this work to determine whether the results are unique to the changes caused by the combustor length, the author hypothesizes that the changes in the detonation wave(s) have a secondary and insignificant effect on the performance. Consequently, the change in performance in this study arises from the augmented blockage of the modified inlet.

However, two conflicting trends are observable if the blockage is plotted directly against the PG, as is done in Figure 7.13. First, for a fixed equivalence ratio (marker color), a negative trend in which PG decreases with increasing B_{m} across both geometries, supporting the hypothesis that more blockage is worse for performance. However, for a fixed geometry marker shape, as the equivalence ratio increases (black to blue), a positive trend is observed in which the PG increases (grows less negative) with increasing B_{m}. The positive trend seemingly conflicts with the original hypothesis and currently prevents a generalized relationship between blockage and PG; however, a direct comparison between the two may be ill-advised due to the other changes in the system, such as mass flux dependencies, that may confound the direct comparisons.

Instead of the direct approach of comparing blockage to the PG as described above, this study considered an alternative approach. The root of the analysis is the hypothetical question: what would the pressure gain be without the blockage-induced back-pressurization? This question is equivalent to: how does the estimated total pressure at the outlet of the RDC compare to the plenum pressure required to drive the flow without the back-pressurization or blockage? Such questions are purely hypothetical since the flowfield in the RDC is a result of complex coupling between the detonation wave(s) and the plenum, and removing the back-pressurization is tantamount to removing this coupling, which, at the time of writing, appears to be a necessary condition for continuous propagation of the detonation wave(s). Nevertheless, this study adopted this framework for demonstrative purposes.

An alternative version of the PG (PG′) that neglects the plenum pressure increases is here defined

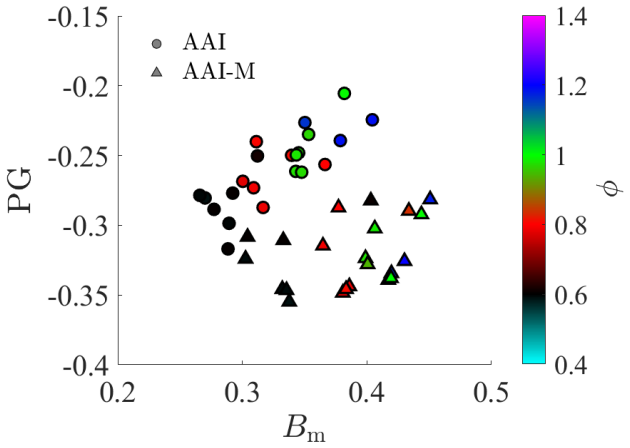

Figure 7.13: Comparing the mass-based blockage fraction to pressure gain.

as:

$$\mathrm{PG}' = \frac{\widetilde{p}_{t8}}{p_{3C|\dot{m}}} - 1 \tag{7.5}$$

The prime indication differentiates this alternative PG from the original PG. The sole difference between Eqn. 7.5 above and the original formulation of PG (Eqn. 5.9) is the pressure term in the denominator. The subscript "C" designates the pressure from the "cold" or non-reacting flow case and can be interpreted as the plenum pressure required during the non-reacting flow to drive the same mass flow rate as the reacting case. Figure 7.14a presents this hypothetical PG across the range of test conditions. Unsurprisingly, the values are larger than the actual PG (refer back to Figure 7.12), and the hypothetical PG grew with increasing mass flux before reaching an asymptote, unlike the actual PG. This reversal may reflect the outlet of RDC becoming choked at larger mass fluxes; see Section 5.5. Once the outlet becomes choked, the static pressure at the exit increases with increasing mass flux, thereby increasing the total pressure given the unity Mach number assumption.

Perhaps more important than the relationship with the flux is that the hypothetical PG values reached positive values. Thus, the total pressure at the outlet of the RDC during the operation was greater than the initial plenum pressure necessary to drive the airflow without combustion, which may be indicative of the theorized local gain from the detonation wave(s) within the channel. It is essential to highlight the distinction that the hypothetical PG is not necessarily what the performance of the RDC would be if the plenum and detonation channel were made more isolated through a higher diodicity injector [154, 148]. For this to be true, the flowfield would have to be unchanged with the higher diodicity injector, which contradicts previous experimental results [145, 156].

Whereas there was a significant difference between the resulting PG between the two inlets, the hypothetical PG (PG′) did not follow the same trend. The direct comparisons, Figure 7.14b,

fall along the 1:1, especially with the error bars. There also seems to be a random spread of some data points above the line while others are below. Both of these observations are reflected in Figure 7.14c, which is the probability that this hypothetical PG is worse with the AAI-M. The data is randomly scattered about the 0.5 line, with only a few points having a significant difference. Most of the data was between 20-80% probabilities, making the changes insignificant. Of note, when $\dot{m}''_{\mathrm{a}} \approx 200$ kg s^{-1} m^{-2} and $\phi \approx 0.6$ the PG′ was significantly better with the AAI-M for an undetermined reason. There was no significant increase in gross thrust for that test (Figure 7.11c), although there was a meaningful increase in blockage between the two inlets (see Figure 7.10). Nevertheless, the modified inlet, which had worse overall performance, produced a comparable total pressure at the outlet compared to the unmodified inlet. The comparable total pressures are mostly a direct reflection of the thrust production between the two configurations being nearly equivalent (i.e., Figure 7.11c).

While observing the increased values in the hypothetical PG provides qualitative evidence of the impact of back-pressurization, a more quantitative approach is desirable. To that end, this study casts the impact of back-pressurization in terms of a decrement in PG from this more idealized, hypothetical value.

$$\Delta\mathrm{PG} = \mathrm{PG} - \mathrm{PG}' \tag{7.6}$$

A pressure-based blockage (B_{p}) measurement [132, 139] is employed to relate the differences in the PG decrement to a measure of blockage. This blockage fraction is,

$$B_{\mathrm{p}} = 1 - \frac{p_{3\mathrm{C}|\dot{m}}}{p_{3\mathrm{H}}} \tag{7.7}$$

The pressure-based blockage is similar to the mass-based blockage fraction (B_{m}) discussed in this work (B_{m}). Yet, previous work has demonstrated that the pressure-based blockage incorrectly predicts the change in the fluidic area at lower mass fluxes [139, 50]. Nevertheless, since the pressure-based blockage is a ratio of pressures similar to the PG measurement, it allows useful analytical manipulations since the numerator in Eqn. 7.7 is identical to the denominator of Eqn. 7.5. For instance, Eqns. 5.9, 7.5, 7.6, and 7.7 can be combined to get the following,

$$\Delta\mathrm{PG} = -B_{\mathrm{p}}(1 + \mathrm{PG}') \tag{7.8}$$

$$\leq 0 \tag{7.9}$$

The B_{p} value is between 0 and 1. In contrast, the lower bound of PG′ is -1, resulting in the inequality presented above, which is merely a mathematical representation of the decrease in PG as caused by an increase in the plenum pressure.

While Eqn. 7.8 is useful for illustrative purposes, the additional dependence upon PG′ prevents

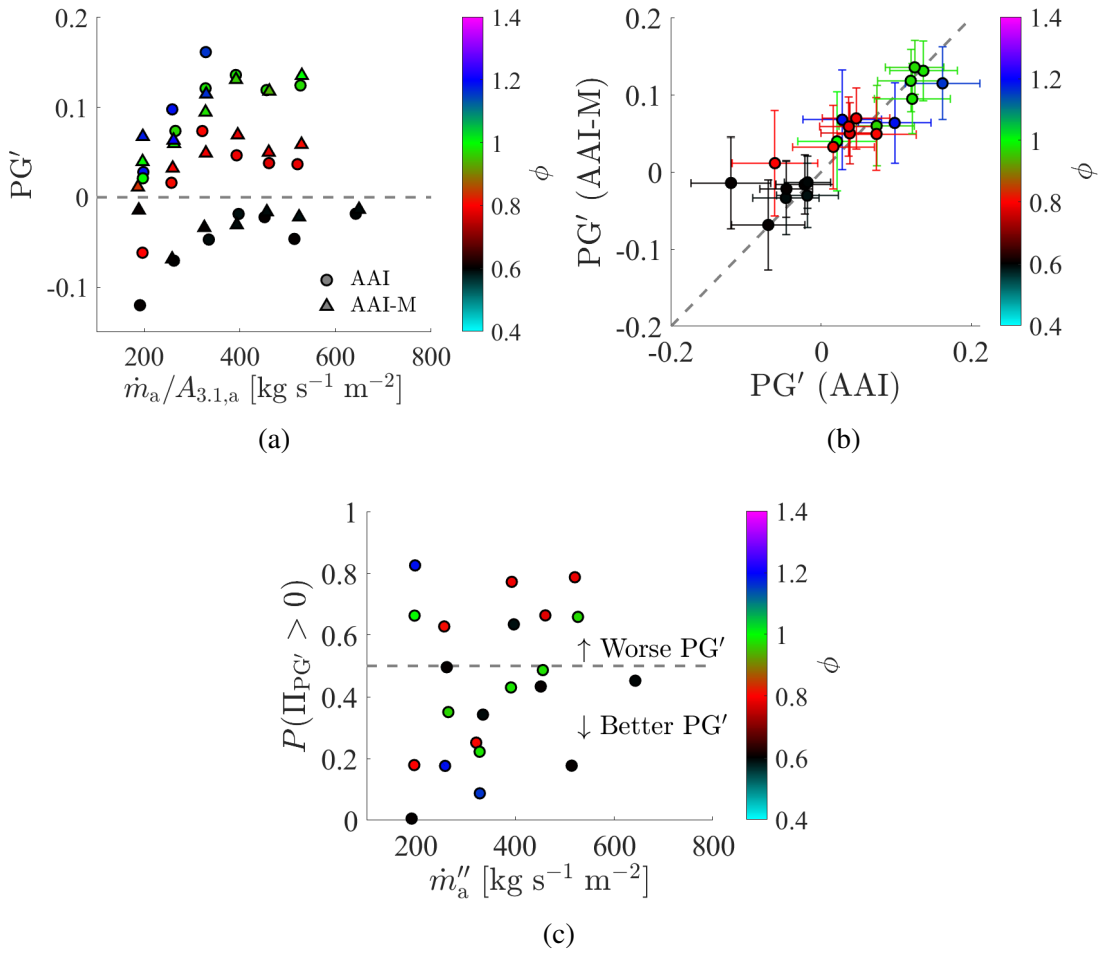

Figure 7.14: a) Pressure gain if the plenum pressure increase caused by fluidic blockage is neglected. b) Direct comparison of hypothetical pressure gain between inlets. c) Changes in the hypothetical pressure gain are insignificant.

it from being evaluated explicitly. Thus, the explicit relationship between B_p and ΔPG remains unknown a priori, necessitating an empirical relationship. The measured B_p and PG′ were plotted against one another, as shown in Figure 7.15a, to determine if there was a functional relationship between the two. Given one of the two geometries, the dashed gray lines highlight an approximately linear correlation between B_p and PG′. The two lines accentuate how the correlation is different between the two geometries. There is a significant spread in the data around the linear line, as reflected by the low R^2 values of 0.735 and 0.781 for AAI and AAI-M, respectively. Nevertheless, this study applies the following approximation since it captures the general trend in the data,

$$\mathrm{PG}' \approx mB_p + b \tag{7.10}$$

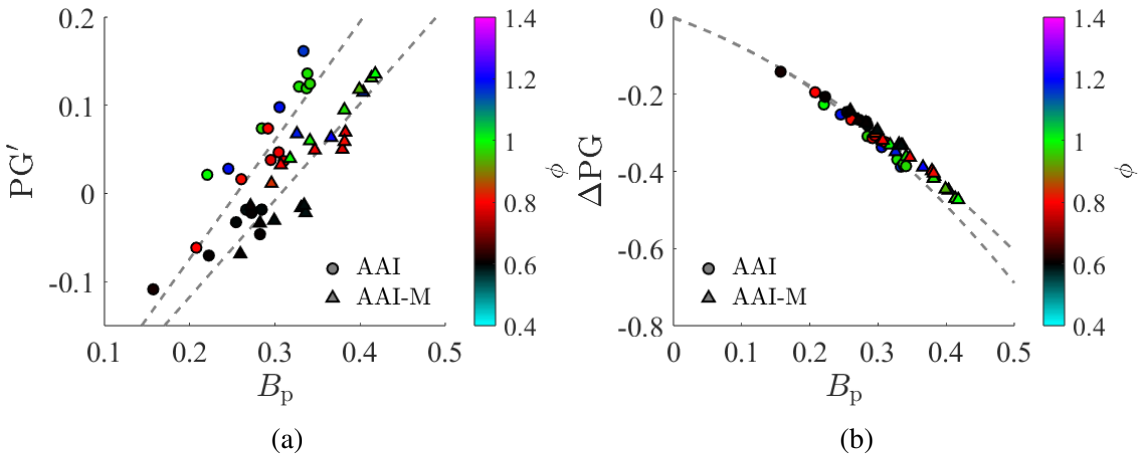

Figure 7.15: Comparing pressure-based blockage fraction to a) hypothetical PG without plenum pressure increase and b) change in PG from measured to hypothetical value.

Using Eqn. 7.10, Eqn. 7.8 can be rewritten to eliminate the dependency on PG′. This substitution gives a quadratic scaling between the decrement in PG and a measure of the blockage.

$$\Delta\text{PG} \approx -mB_p^2 - (b+1)B_p \tag{7.11}$$

$$= C_1 B_p^2 + C_2 B_p + C_3 \tag{7.12}$$

Equation 7.11 is the approximately derived relationship relating B_p and ΔPG while Eqn. 7.12 is the quadratic fit calculated from the data. The origin (0,0) point was included when calculating the fit with the experimental data to enforce that ΔPG = 0 when $B_p = 0$, which is evident from Eqn. 7.8. The resulting parameters for Eqn. 7.12 are provided in Tab. 7.1, while the fits are plotted in Figure 7.15b as the dashed gray lines. The linear fit presented in Figure 7.15a was not used; however, the high R^2 values demonstrate that a quadratic polynomial fits the data well. The quadratic fit, in turn, supports the approximation given in Eqn. 7.11. Again, there is a slight difference between the two geometries in terms of the quadratic fit. Unfortunately, the lower bound of B_p measured in this work was about 0.15, leading to a required extrapolation in the limit of $B_p \to 0$. As was seen in Figure 7.10, blockage reaches an asymptotic value that depends on the equivalence ratio and the geometry; thus, additional experiments with different geometries are necessary to confirm that the data follows the quadratic fit at even lower B_p values.

As mentioned previously, the pressure-based blockage fraction does not always accurately describe a change in fluidic area [139]. Therefore, while the decrease in PG was initially related to B_p, it is preferable to cast the results in terms of the more accurate mass-based blockage, B_m. Feleo et al. previously demonstrated that the difference between B_m and B_p is a function of a Mach

Geometry	C_1	C_2	C_3	R^2
AAI	-1.584	-0.580	-0.003	0.986
AAI-M	-1.088	-0.669	-0.001	0.993

Table 7.1: Parameters for the quadratic fits that satisfy Eqn. 7.12

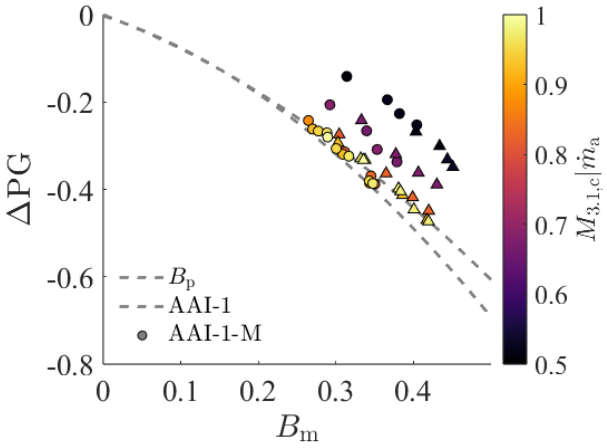

Figure 7.16: Comparing the mass-based blockage fraction to pressure gain decrease.

number during a non-reacting flow test with the same mass flux ($M_{3.1C|\dot{m}}$) [139]. In particular, this Mach number is evaluated at the inlet throat for a non-reacting flow test with the same mass flux as the reacting flow test being considered ($M_{3.1C|\dot{m}}$). Importantly, when this Mach number is unity, B_m and B_p agree, but when the Mach number is subsonic at lower mass fluxes, B_p is smaller than B_m [139]. Thus, when B_m is plotted against the PG decrement in Figure 7.16, the coloration of the markers now gives this Mach number instead of the equivalence ratio. The dashed gray curves are the quadratic fits to the B_p data. As $M_{3.1C|\dot{m}}$ approaches one, the pink markers, the data collapses along these quadratic curves since B_m becomes equivalent to B_p. When the Mach number was subsonic, an increase in blockage had less of an impact on the PG decrement as the data moves up and to the right in Figure 7.16. Regardless of the geometry, similar Mach numbers form distinct curves that relate B_m and ΔPG, suggesting a family of relationships that depend on the Mach number. Overall, the worse end-to-end performance of the modified inlet occurs due to the outlet total pressure not increasing as much as the plenum pressure increase caused by the worse blockage (larger B_m) since the inlet Mach number for the non-reacting cases was invariant to the inlet modification.

7.8 Discussion

The design of the modified inlet served two purposes: intentionally worsening the diodicity of the inlet and suppressing the toroidal re-circulation region anchored at the shoulder of the standard inlet [58]. Chacon theorized that this toroidal re-circulation region was detrimental to overall performance since it supports parasitic combustion (refer back to Section 1.5.3) by transferring thermal energy from the trapped hot products to the fresh reactants. Several modeling efforts have shown that parasitic combustion is detrimental to thrust [58, 195] or specific impulse [105]. Such a detrimental impact is a result of the heat release occurring at a lower temperature, thereby producing more overall entropy than if all the heat release occurred within the detonation wave. Chacon previously tested of AAI-M without a nozzle and demonstrated that parasitic combustion was suppressed using the OH* chemiluminescence method of Feleo et al. [58, 11]. However, in the case of the present study, the inlet modification did not completely suppress parasitic combustion. This is attributed to the back-pressurization of the nozzle, causing the reaction rates to increase such that auto-ignition kernels occur. For the sake of brevity, this work did not directly address the changes in parasitic combustion, but, generally, the heat release distribution within the cycle was altered in a manner that the parasitic combustion was reduced but not eliminated. However, the PG decreased significantly despite the reduction of a theorized loss mechanism, indicative that some other loss was more significant than the potential gains of reducing parasitic combustion.

While many aspects of the flowfield changed with the inlet modification such as the heat release distribution, the most prominent and significant of the changes is the increase in the backflow and coupling between the plenum and channel. Although this study demonstrated that both the oblique shock strength in the plenum and the overall fluidic blockage, it was not experimentally confirmed here that this was directly related to an increase in the backflow; however, Shepard tested both the AAI and AAI-M geometries along with an optically accessible outer body [50]. Iron oxide particles, approximately 50 microns in diameter, were seeded into the air stream upstream of the RDC. After the passage of the detonation wave, the iron oxide particles were visibly luminescent from blackbody radiation, enabling a high-speed camera to track them. Shepard observed that more particles flowed back up into the inlet throat when AAI-M was being tested. Likewise, the overall chemiluminescence intensity in the inlet throat increased by nearly 25% for the AAI-M [50]. While such measurements are more qualitative than quantitative, they further support the hypothesis that there was more backflow based on the measured increase in pressure coupling between the plenum and channel.

Therefore, this study attributes the significant decrease in PG to the negative impact backflow and blockage has on PG. Several theoretical processes explain this detrimental impact on PG. The flow may require work to turn the products' axial velocity back in the proper direction, which may

produce entropy. Effectively, the products that flow backward must undergo additional, potentially non-isentropic, expansion processes before exiting the combustion. Even if the expansion is isentropic, the backflow will act as both an impediment to incoming flow and additional mass that has been injected into the channel, both of which effectively increase the fluidic blockage. Another is that the hot products pre-heat the incoming fresh reactants, which would lower the peak pressure of the detonation wave, thereby causing the detonation wave to produce more entropy. Additionally, this pre-heating may be sufficient to cause auto-ignition of the fresh reactants, potentially leading to parasitic combustion [11, 10]. This is another possible explanation for the inability to suppress parasitic combustion, unlike what was observed by Chacon [58].

The theories above focus on the local physics of the losses introduced by backflow; however, a more macroscopic viewpoint is also applicable. For instance, the fluidic blockage manifests as an increase in plenum pressure, which causes a less favorable comparison to the exit total pressure. An alternative viewpoint is to interpret fluidic blockage as a reduction in the fluidic area, which is what the blockage fraction (B_{m}) tries to describe. Consider the trend observed by several researchers in which the PG became better (less negative) with more open inlets [14] originally shown in Figure 2.7. The reverse is that the PG grows worse (more negative) with more restrictive inlets. From this, the theorized smaller area (caused by blockage) would then correlate to a decrease in PG. Additionally, the mass flux through the unblocked portion of the inlet would increase with decreasing the decreasing area caused by blockage. Recall that Chapter 5 observed that total pressure losses scale with the mass flux through the throat. Thus, the increase in local mass flux may also influence the total pressure loss.

Regarding practical applications, some blockage of the injectors/inlet may be unavoidable for the continuous propagation of the detonation wave(s). Thus far, no studies have demonstrated successful operation without a plenum pressurization. The exception to this may be liquid fuels or rocket applications since the feed pressure is much greater than the channel pressure. Based on the experimental results in this work and literature, this plenum pressurization raises the threshold of total pressure needed at the outlet to demonstrate positive PG successfully. However, despite being unavoidable, the PG decrement caused by the blockage or plenum back-pressurization can be minimized by operating the RDC at fluxes with low inlet Mach numbers before the introduction of detonation waves. Currently, it is unknown what the lower bound on this Mach number is, and it is exceedingly likely that if said lower bound exists, it would be geometry-dependent. These low fluxes have the additional benefit of minimizing the turbulent losses across the inlet, making them even more preferential. In such cases, the Mach number correction to the EAP introduced in Section 5.5 would likely be necessary, as the exit Mach numbers are subsonic at flow fluxes. While low fluxes are likely ideal from a performance perspective, there is bound to the lowest flux that can achieve detonative operation [176, 38]. The current speculation is that the lower bound may

arise from too great of coupling between the inlet and channel or insufficient time for the injectors to recover [38, 43]. Therefore, there is an intrinsic tension between sustained detonative operation and better performance. This is also reflected in making the inlet throats more open [14] which Feleo and Shepard have demonstrated increases the blockage fraction [139, 50].

Finally, it is essential to highlight a significant decrease in PG occurred despite the considerable uncertainties, unlike the previous chapter. When it comes to designing better-optimized inlets and injectors as is being done currently [145, 156], the results of this chapter are promising in that potential improvements could be resolved through the EAP method. Thus, the experimental EAP can detect these significant changes for fixed inlet and outlet areas. However, the backflow and blockage correspond to fluidic changes at the inlet throat, which, from pre-existing work [114, 14], is known to impact PG significantly. Meanwhile, differences in the processes within the channel (e.g., the detonation waves, secondary waves, secondary combustion, etc.) seem to have little impact on PG based on the results from the previous chapter. The lack of sensitivity may be due to re-balancing or a hierarchy of loss mechanisms. Regardless, the agnostic nature of PG to what occurs in the channel ultimately gives the impression that the experimental PG can only resolve the pressure loss across the inlet during operation. While useful, such a measurement fundamentally neglects the titular detonation wave(s) and, therefore, is limited in assessing the processes present within RDCs.

CHAPTER 8

Conclusions and Final Discussion

This final chapter presents the conclusions of this entire work. First, the following sections explain the findings of the individual studies; each study gets an associated section. These conclusions summarize the accomplished work and contributions found in each of the preceding chapters. After such summaries, the final discussion section considers the totality of the work. Specifically, the discussion section focuses on evaluating the current global PG metric based on the results found throughout this work. The work will conclude with recommendations for future research into the performance of RDCs.

8.1 Summary of Work

8.1.1 Theoretical Analysis of Pressure Gain

The flowfield in RDCs is inherently three-dimensional and unsteady, which complicates the determination of thermodynamic gain, estimated using the total pressure ratio across the RDC, relative to standard combustors. However, various averaging procedures have been adapted in this work to reduce the dimensionality of RDC flowfields. Most of the averaging procedures end with a total pressure defined to preserve a property of the flowfield. Two such methods preserve the flow's ability to produce thrust and extractable work while maintaining the same mass-averaged total enthalpy. Likewise, averaging in a manner that preserves mass-averaged energy and entropy is considered the ideal case. All other averaging methods result in an artificial increase in entropy relative to the mass-averaged entropy, which is unavoidable due to non-uniform flow transitioning to a uniform state. In addition, this study considered the ideal and experimental EAP [113]. The ideal EAP is nearly equivalent to the thrust-averaging procedure, while the experimental EAP is roughly equivalent to the area-averaging procedure. The experimental EAP and area-averaging do not preserve the flowfield's total energy or entropy but are relevant to physical experiments. The concern then becomes whether the experimental methods for determining an average total

pressure can adequately capture the fundamental thermodynamic gain of the detonation wave(s) (less-entropy production).

This study applied the averaging procedures to high-fidelity, three-dimensional DNS simulations of a H_2/air-operated RDC with radial air injection and no exit constriction. The experimental EAP (area-average) consistently underrepresented the total pressure relative to the other averaging procedures. It was 3-15% less than the thrust-averaged, 9-20% less than the work-averaged, and 22-38% less than the entropy averaged. While experimental EAP being a conservative metric is prudent, it may be overly conservative if the trends observed in this work persist in configurations with nozzles. On the other hand, the work-averaged total pressure was greater than the ideal EAP/thrust-averaged pressure, which suggests that the process of extracting work from the outlet of a RDC may yield better performance (on the order of 4-8%) than the same RDC producing thrust.

This study also evaluated the impact of the choice in assumed static or total pressure on the averaging. The thrust-averaged pressure is more sensitive to the outlet pressure than the work-averaged pressure. Specifically, as the ambient pressure drops by several orders of magnitude, the "average" pressure also decreases despite the same exit flow. In terms of rocket applications, this would lead to a performance decrement that would worsen the lower the outlet pressure is, assuming matched pressures. Overall, PG is not an intrinsic metric as there is subjectivity in the average outlet total pressure of a RDC. The problem arises from using an "average" total pressure since any averaging procedure that reduces the flow's dimensionality results in information loss, preventing a universal solution.

Experimentally, three prominent methods exist to estimate the average total outlet pressure. These are the EAP method, NPS method, and direct measurements with Kiel probes. However, the results of these methods are consistent with one another. This study demonstrated that the consistency directly results from the convergence between area-averaged and time-averaged quantities in the periodic flowfield. Thus, physical experiments are currently limited to area-averaged total pressures, and the other methods do not resolve the issues with EAP. Correction factors that address the disagreement between experimental measures and the other averages may be beneficial to consider in the future.

8.1.2 Experimental Method to Measure Pressure Gain

8.1.2.1 Base Drag

This study presented a first-of-its-kind, in-depth analysis of the base drag acting along the truncated nozzle of a RDC. A parametric study of air mass fluxes and equivalence ratios for an experimental AAI RDC with a 50% exit area blockage operated with H_2/air provided sample base drag measurements for the analysis. This work leveraged seventeen flush-mounted pressure measurements via

CTAPs along the truncated nozzle at three equally spaced circumferential locations. Each measurement had a unique radial location. While the truncated nozzle garnered much of the focus of this work, an outer exit flange on the RDC also has base drag acting upon it. Six pressure measurements measured the base drag along the exit flange, and the lessons learned from the nozzle are readily applicable to this surface as well; however, through the judicious design of the seal, the effective area of the exit flange is minimal compared to that of the truncated nozzle.

Overall, the analysis from this study can significantly improve the measurement technique. Such improvements are essential when measuring the total pressure at the outlet of RDCs through the EAP method. Specifically, several issues with current base drag measurements were identified and addressed. Previous studies assumed that the pressure distribution along the truncated nozzles of RDCs was axisymmetric; however, the tests presented in this study revealed an observable asymmetry that invalidates said assumption. The uncertainty in the individual measurements cannot explain the asymmetry. The cause of this asymmetry is currently unknown, although it may result from the specific experimental setup (e.g., the specifics of the reactant's injection system). The base drag reported in this work, instead, is a result of a composite trapezoidal scheme in the radial direction and a standard trapezoidal scheme in the circumferential direction. The composite integration method addresses and captures the effects of the asymmetry, which alters the base drag by up to 8%. This work also discussed the impact of the lack of a pressure measurement at the edge of the surface on the resulting drag. Without a direct measurement at the proper location, previous studies assumed that the edge pressure was equivalent to the outermost pressure measurement. Based upon the radial distributions in this work, this assumption severely under-predicts the edge pressure, which artificially raises the gross thrust result by up to 8%. After addressing both assumptions, the base drag measured was reduced by up to 20%, thereby making the overall gross thrust measurement more conservative. Even more importantly, these lessons can further reduce the uncertainty in future measurements, which will be critical in having accurate and precise PG measurements if a demonstration of the gain is achievable.

Following the previous suggestion made by Fievisohn et al. [116], this work implemented a Gaussian-Kronrod scheme in conjunction with the Newton-Cotes method (e.g., trapezoidal rule) to experimentally compare the two. The implemented Gauss-Kronrod scheme was radially weighted and was order three (two points). Meanwhile, the Kronrod extension was of order seven (an additional three points). This study did not directly measure pressure at the node; however, the fine radial resolution of this study allowed for interpolation between the existing pressure locations to get the node measurements except for the node with the largest radial position, which required extrapolation. The comparison between the axis-symmetric Newton-Cotes and axis-symmetric Gauss-Kronrod schemes was quite favorable, as the differences between the two were on the order of the numerical error of the Gauss-Kronrod scheme. This numerical error was several percent of

the gross thrust; this is an improvement compared to the uncertainty in a Newton-Cotes integration when an edge pressure is not directly measured. The primary drawback of the Gauss-Kronrod scheme is having to assume the pressure distribution with potentially no a priori knowledge.

The study then provided recommendations, repeated here, based on the mentioned observations:

- One should compute the base drag using a composite, two-dimensional numerical integral. Therefore, pressure measurements must have different discrete radial and circumferential locations.

- Pressure needs to be measured at a minimum of three discrete circumferential locations evenly distributed in the circumferential direction to capture any asymmetry in the pressure distribution. The convergence rate of the trapezoidal rule in numerically integrating a periodic function is $1/N^4$; thus, three points give an error of 1.2%, although the error further reduces with a greater number of points.

- A radially-weight Gauss-Kronrod scheme is ideal for the radial integration. Based upon the approximate cubic radial pressure distribution observed in this work, a Gaussian scheme of order three (two points) with a Kronrod extension of order seven (additional three points) for five radial locations would be suitable. While the Kronrod extension does not drastically improve the accuracy of the numerical integration, it provides an invaluable estimation of the uncertainty associated with the integration.

- A Newton-Cotes integration along the radial direction instead of the recommended Gauss-Kronrod remains valid; however, the edge pressure is paramount to the numerical integration. A pressure measurement at the edge is required, or the necessary assumptions lead to significant uncertainties. The Kronrod extension typically inherently solves the edge pressure issue by having the outermost radial node be effectively at the edge of the nozzle.

- In general, low-noise pressure transducers reduce the overall base drag uncertainty. The worst pressure differential measured was about 0.08 atm (1.17 psi), which is relatively small compared to the ambient exhaust pressure. Since most pressure transducers have uncertainty/noise that scales with their full-scale value, minimizing the range of the pressure transducers while still spanning the range of expected values can provide additional uncertainty mitigation.

8.1.2.2 Thrust and EAP

The analysis of the base drag ultimately informed the concurrent detailed uncertainty analysis of the PG metric as measured by the EAP method. Just as the base drag uncertainty analysis is unprecedented in scope, the uncertainty analysis of PG is currently the most comprehensive in the

RDC literature. This work took thrust concurrently with the base drag measurements; therefore, the analysis of PG utilized the same parametric study of air mass fluxes and equivalence ratios for H_2/air operation of an experimental AAI RDC with a 50% exit area blockage. This work developed an integrated thrust stand to measure the thrust output of the RDC while still sealing against a coupled exhaust. The concept of EAP was used to estimate the PG based upon the measured gross thrust, with the estimated PG varying from -0.243 to -0.322. These values align with existing literature for an exit-to-inlet area ratio of 2.38 [14]. The highest gross thrust in this work occurred at the highest mass flux since the thrust scaled linearly with an increasing mass flow rate. Meanwhile, the highest PG happened at the lowest tested mass flux. This work theorizes that the injector's total pressure drop scales with increasing flux; thus, lower fluxes minimize the inherent total pressure drop.

This work demonstrated that the relative uncertainty in the gross thrust ranged from 5% to 30% of the nominal value, with the largest relative uncertainty at the lowest mass fluxes. The load cell measurement and the base drag on the nozzle contributed to most of the uncertainty in the gross thrust measurement, although the base drag uncertainty was more significant. The gross thrust measurement depends on both the load cell and the overall design of the thrust stand—meanwhile, the previous discussion elaborated upon the uncertainty in the base drag. Although a non-negligible amount of base drag (10% of the total gross thrust) acted upon the exit flange, this work eliminated its associated uncertainty through judicious design; a radial seal for sealing with the exhaust chamber also minimizes the effective area. Finally, the gross thrust measurement likely has no significant systematic uncertainty.

As for the PG, the random uncertainty was predominately from the gross thrust. The relative uncertainty of PG was 10-20% of the nominal value, with the greatest uncertainty being at the lowest fluxes (lowest gross thrust). In the context of the measurements presented in this study, the random uncertainty encapsulates all the changes to PG across the operating conditions. Additionally, such significant uncertainties are problematic as they could mask definitive demonstrations of PG. The PG is conservative due to the unity Mach number assumption; however, the assumption introduces a systematic uncertainty that scales proportionally to the PG, resulting in an increased uncertainty when the PG is closer to being positive.

This study also introduced a time-averaged static pressure measurement at the nozzle throat plane to get p_8 directly. There was a notable difference between the measured and EAP pressures at low mass fluxes due to subsonic average throat Mach numbers ranging from 0.4 to 0.8. The subsonic Mach numbers are demonstrated by re-arranging the simple thrust equation to solve for the Mach number given the gross thrust and measured p_8. This work then incorporated the non-unity Mach number into PG since the estimated PG under-predicts the "true" PG as a result of subsonic Mach numbers. Furthermore, using the estimated Mach number resulted in an overall decrease in the random and systematic uncertainty in PG despite the relative uncertainties in the Mach number.

Thus, the precision and accuracy of PG are improved. Overall, this study explored the concept of experimentally measured EAP and demonstrated (through rigorous uncertainty analysis) that the current implementation of EAP has a limit on both precision and accuracy that would hinder the goal of showing definitive pressure gain across RDCs.

Finally, this study discusses an alternative method of finding the exit total pressure based on the measured p_8. While similar to the NPS method [114, 120] measuring pressure at the throat circumvents the need for area-Mach relations. The modified PG introduced in this study can also be found without a thrust stand with a static pressure and temperature measurement at the exit. The uncertainty in finding the PG without thrust is comparable to the uncertainty EAP method. Further refinement of this technique could eventually lead to a significant reduction in uncertainty in the PG measurement and would replace EAP.

8.1.3 Relating Pressure Gain to Detonation Wave Properties

This work also explored the effects of changing the length of the combustor section of an RDC with an AAI operated in H_2/air. The profile of the axial air inlet and converging exit nozzle remained the same, while the combustor length alone varied from 71 mm to 137 mm. This study employed the same parametric study of air mass fluxes and equivalence ratios for four discrete combustor lengths. Spectra from high-speed pressure transducers and aft-time-resolved chemiluminescence movies identified the operating mode. The RDC exhibited rotating detonation modes of operation without any pulsing behaviors. Of the observed operating modes, two are novel: the distinguishable wave pair (2WD) and the transient super-cycle (TSC). In the case of 2WD, two waves stably propagated at the same speed but had distinct pressure ratios across the individual waves. The TSC comprised a pair of detonation waves that gradually slowed as the number of counter-propagating waves decreased and sped up. Eventually, the direction of the primary detonation waves switched, and the number of secondary waves reset. This super-cycle had a period that was many times the rotational period of one of the detonations. This study hypothesizes that the onset of this phenomenon is associated with an incomplete transition between operating modes with two and three co-rotating detonation waves.

This study presented a statistical approach to quantify the speed and pressure ratio of the detonation wave(s), specifically the empirical PDFs of both quantities. In general, the speed of the individual detonation wave(s) decreased with increasing length, assuming the multiplicity was constant. The slowing of the wave(s) may be related to the eigenfrequency of the circumferential acoustic mode, which is inversely proportional to the axial length of the annulus. Additionally, the multiplicity increased from one to two with the increase in length, which the author theorizes to be a result of a larger fill region caused by the slower waves being able to support an additional wave.

Meanwhile, the normalized pressure ratios were nearly constant configurations and test conditions, highlighting that the wave speed could significantly change without a significant change in the pressure ratio.

The methods developed earlier in this work measured the thrust and PG through the EAP method. Marginal differences in the gross thrust occurred as the length varied; any observed differences were within net thrust measurement uncertainty. Meanwhile, the plenum pressure increase caused by the detonation wave(s), as measured by an effective blockage fraction, changed significantly from the length alterations. Pressure gain compares the gross thrust to the plenum pressure, thus accounting for changes in both thrust and blockage. The pressure gain was between -0.21 and -0.32, depending on the operating condition. Despite the significantly different wave systems (speed and multiplicity) and operating modes, the total pressure loss across the RDC remained effectively constant as the length changed, with variations within the experimental uncertainty. Thus, the performance, as measured in this work, was insensitive to the combustor's length and details of the systems of multiple competing waves that result from it. This result suggests that the quality of the detonation wave does not directly translate to an increase in the overall performance of the combustor. Furthermore, the combustor length can be used as a design tool to achieve certain types of operation without sacrificing performance.

8.1.4 Detrimental Impact of Blockage on Pressure Gain

The final study intentionally modified the air inlet (AAI-M) to have a worse diodicity by streamlining the expansion downstream of the inlet throat. The inlet throat area remained unchanged, as was the 50% outlet restriction and the combustor length of 118 mm. The parametric study of air mass fluxes and equivalence ratios of H_2/air operation was repeated for the AAI-M to enable direct comparisons between AAI and AAI-M. Once again, spectra from high-speed pressure transducers and aft-time-resolved chemiluminescence movies identified the operating mode, of which no new operational modes appeared. Whereas AAI only exhibited 1W operation at a single test condition, nearly half of the test of AAI-M had 1W, indicating a meaningful change in operating mode (multiplicity) from the inlet modification.

In general, the detonation wave speeds were significantly lower for AAI-M than AAI for the same condition. Acoustic wave speeds (50% D_{CJ}) commonly occurred for AAI-M when two co-rotating detonation waves materialized within the RDC. Unlike the wave speed, more significant experimental variance complicates comparisons of the pressure ratios across the detonation wave. Thus, this study further developed the statistical analysis when considering the changes in pressure ratio by investigating the empirical PDFs of the individual components of the pressure ratio. A Monte-Carlo sampling of the PDFs resulted in the computation of the probability that the AAI-M

had a larger value of said pressure. These probabilities better enabled statistical significance arguments to be made. Thus, while AAI-M had a higher likelihood of having a greater detonation wave pressure ratio than AAI, only a handful of tests were statistically significant.

This study investigated the coupling between the detonation channel and air plenum in two ways: characterizing the upstream propagating oblique shock and measuring the effective blockage fraction. A high-speed pressure transducer upstream of the inlet throat measured the pressure across the oblique shock in the plenum. Many tests had a statistically significant likelihood that the oblique shock measured with the AAI-M was stronger than AAI, although this was not universally true. Meanwhile, the effective blockage fraction considered the mean plenum pressurization, which increased from the inlet modification. Therefore, this work concluded that the inlet modification augmented backflow/blockage, symbolic of a worse injector diodicity, as intended.

Again, the methods developed earlier in this work measured the thrust and PG through the EAP method when AAI-M was employed. Despite the large uncertainties that this work demonstrated, effectively all of the tests with AAI-M had a statistically significant worse PG than AAI, differentiating these results from those found in the length study. The PG for the AAI-M ranged from -0.28 to -0.36. Due to the correlation between more plenum coupling and worse PG, this work contextualized the PG decrement accrued by the plenum back-pressurization by considering an idealized scenario where blockage does not cause said the back-pressurization. Specifically, the relationship appears to be a negative quadratic relationship where increasing the blockage further reduces the global PG. However, the total pressure penalty imposed by the blockage reduces when the inlet throat Mach numbers during non-reacting flows are subsonic. These subsonic Mach numbers occur at low mass fluxes, which also is where the total pressure drop across the injectors is minimized, further emphasizing that the best performing RDCs from a PG perspective are those operating at loss inlet mass fluxes.

8.2 Conclusions

Good experimental metrics have four components: theoretically sound, accuracy (minimal amount of systematic errors), precision (minimal amount of random uncertainty), and practical usefulness. Through these lenses, this work evaluated the experimental global PG. The conclusions of the independent studies are summarized below in the context of the overarching evaluation.

- **Theory:** When this work evaluated the averaging procedures needed for PG, the PG was found non-unique and not intrinsic to a given flow. Thus, the value of PG is highly subjective, far from ideal for a performance metric. Averaging with any physical process in mind (thrust or work) generates entropy conflicting with the thermodynamic benefit of detonations.

Finally, the EAP is equivalent to an area-averaged total pressure, which does not satisfy any conservation equation. These combine as limitations for both PG and EAP.

- **Accuracy:** This work evaluated the accuracy of PG through the experimental methods (namely EAP) used to measure it. The primary source of systematic uncertainty in PG arises from the Mach number assumption, although accurately measuring the base drag on the nozzle is also paramount. However, one can significantly mitigate these current accuracy concerns. In doing so, the EAP method could become a sufficiently accurate representation of the area-averaged total pressure. However, the issues of the area-averaged total pressure not accurately quantities of interest, as discussed in the theory section, remains unsolved.

- **Precision:** Much of this work focused on the detailed uncertainty analysis required to appropriately estimate the random uncertainties in PG. The uncertainties culminated in requiring a measured PG greater than 0.06 for a definitive demonstration of positive gain, indicative of precision limitations. While one could reduce some of the random uncertainties, the required gross thrust measurements limit the lower bound of the relative uncertainty.

- **Usefulness:** The practical usefulness is the most subjective of established criteria and is the combination of the other metrics. Ideally, changes in the RDC flowfield from geometry changes are reflected as changes in PG to inform the next design. This work had mixed results in this regard. While a measurable decrease in PG came from an inlet modification, different detonation wave(s) and operating modes did not result in a significant change in PG for a constant inlet. The invariance result may result from poor precision in PG or a rebalancing of loss mechanisms. Regardless, PG seems limited to only measuring the inlet losses. The diodicity study, the general decrease in PG with increasing mass flux, and the compiled results in the literature all support this. Thus far, geometry changes for a given inlet have an insignificant impact on PG. with the one exception being more restrictive nozzles. Therefore, PG is limited in determining the optimal design outside the inlet and nozzle.

All told, based on these criteria, the experimental global PG is a limited metric. While PG has had its uses specifically in terms of the refinement of inlets and inclusion of nozzles, such design principles are not unique to RDCs. Further refinements to the experimental methodology may increase the accuracy and precision (thereby increasing the potential usefulness), but the theoretical limitations can never be fully overcome. Therefore, this work concludes that the fixation on PG as the be-all and end-all performance metric for RDCs has largely been unjustified. This is not to preclude the existence of a thermodynamic benefit of using RDCs; instead, this work concludes that PG may be too limited to adequately measure it.

8.3 Final Discussion

8.3.1 Concluding Remarks on Pressure Gain

One of the most perplexing elements of RDCs is the duality of simultaneously being an unsteady and steady system. Although an unsteady phenomenon (detonation wave) is *locally* contained within the system, the RDC is effectively steady *globally* due to the periodic domain within the encompassing CV. The amount of mass flown, energy added, thrust produced, and available work each are effectively steady measures owing to the periodic nature of the flowfield (Appendix A). The system must pack back the work that the detonation wave imparts upon the fresh reactants through the expansion process [37]. The steady global nature of RDCs contrasts the original PGC devices, e.g., pulse combustors and PDEs. This contrast is because the unsteady process exits the CV in the same direction as the bulk fluid motion, making it impossible to establish a steady global CV around the process. RDCs are also unique within the PGC field in that the PG occurs locally across the detonation wave but in the opposite direction of the bulk flow. However, work extraction and thrust production are global quantities; thus, somehow, the RDC needs to transfer the *local* PG from an unsteady process to a *global*, steady PG. In many aspects, this is the crux of the RDC problem.

If one considers the RDC as a globally steady system, the notion of a potential PG becomes murkier. For instance, consider a hypothetical CV around an arbitrary combustor. The properties that a traditional designer cares about, mass in/out, thrust production, extractable work, etc., are steady at the inlet and outlet of the said device while being agnostic to what occurs within the device. In such a hypothetical scenario, one would say that the total pressure in the direction of the bulk flow must go down according to the Second Law of Thermodynamics; see Section 1.4. Fundamentally, for mass to flow from the inlet to the outlet of such a system without cooling or applied *external* work, the total pressure cannot increase in the bulk flow direction. The detonation wave in a RDC is a source of *internal* work since it never crosses the CV; thus, it may not be an exception to the global decrease in total pressure. By extension, the author speculates that there must also be an axial decay of some "average" total pressure within RDCs to allow for the global steady mass flow rate. In other words, there must be a PG defined by some "average" total pressure that is negative (or at best zero) to enforce the imposed mass flow rate through the system. The *local* gain in total pressure across the detonation wave remains and is the cause of backflow and the fluidic blockage of the injectors. However, if the average total pressure within the detonation channel increases, according to this conjecture, the system will respond by increasing the inlet total pressure to a commiserate amount; otherwise, the flowfield cannot enforce the mass flow through the system on a global scale. Experimentally, this is the observable plenum back-pressurization, and this reasoning aligns with the relationship between the blockage and PG from Chapter 7.

It is not immediately apparent which "average" total pressure (e.g., thrust-average, work-average, etc.) is subject to the above conjecture; however, such knowledge is optional for this discussion's consideration. Chapter 2 demonstrated that experimental EAP/area-average consistently gave the lowest total pressure. If the theorized average total pressure that must go down is the area-average, clearly it must go down. Likewise, if the theorized total pressure that must go down is, say, the thrust-averaged total pressure, the area-average must also go down on account of being lower than the thrust-average. Thus, as long the conjecture of some hypothetical average total pressure decrease in the axial direction is true, the area-average total pressure at the outlet will always be less than the inlet. Following this line of reasoning, the corresponding experimental PG will ever be at best zero since EAP and the other experimental methods are effectively area-averaged measurements of the total pressure, which cannot increase across the device. Therefore, an experimental measurement of global PG may be an inadequate measurement of the thermodynamic benefit of the RDC since the average total pressure at the outlet will likely always be less than the inlet, according to this conjecture.

A valid counter-argument to such conjectures is the observance of positive PG in simulations, like the introductory work by Kaemming and Paxson [113]. The conservation equations are still being solved (albeit in a two-dimensional sense), and a net positive PG is demonstrated. The results of the computations are irrefutable because the numerical methods were likely appropriately implemented; however, the calculations may be correct subject to the imposed boundary conditions and models, but the boundary conditions and/or models may not reflect reality. Such simulations rely on various submodels, such as handling the detonation wave's leading shock discontinuity, the premixed mixture's reaction rates, viscous losses, etc. Perhaps the most crucial submodel Kaemming and Paxson implemented was that of the injector. They model the injection of reactants using a piecewise open boundary condition depending on the channel pressure downstream of the inlet to reduce the complexity and cost of the simulation [113, 196]. The plenum feeding the RDC is infinitely large with a fixed total pressure, thereby making the system pressure-fed as the mass through the system can modulate. This model leads to the detonation wave decoupling in some sense from the upstream plenum. Additionally, the aforementioned model does not capture the viscous/turbulent losses across the inlet. Based upon the results from this work, the model then neglects two of the more prominent losses that occur within experimental RDCs. Furthermore, if the author's conjecture of the plenum back-pressurization being a result of the system globally re-balancing to enforce a total pressure drop in the axial direction is true, neglecting the inlet coupling divorces the simulations from experiments by enabling the positive PG. Therefore, the results from Kaemming and Paxson may be misleading. In fact, the only sources in the literature that discuss an achieved PG are comparable two-dimensional simulations that model the inlet instead of simulating it (e.g., [197]).

Another valid counter-argument comes from a recent study by Brophy et al., which claimed that a positive PG has been achieved experimentally [48]. The experimental uncertainty concerns in the PG metric were not alleviated, so the demonstration was not definitive; nevertheless, this result seemingly contradicts the conjecture that PG as measured by EAP is impossible. However, the results are not contradictory but are symptomatic of PG being defined solely relative to the oxidizer plenum. Such a definition is disingenuous as it neglects the added momentum and kinetic energy of the fuel. Consider a RDC without any oxidizer flow; the total pressure at the outlet would equal the inlet. Now introduce a fuel stream into the RDC that does not undergo reaction and has an axial component. The added momentum and kinetic energy of the fuel stream, even if small, would increase the total pressure at the outlet relative to its quiescent state [198]. In doing so, an artificial increase in PG would occur as the oxidizer plenum pressure remains the same. Essentially, the fuel jet's momentum and kinetic energy are free sources with the current definition of PG. Plaehn et al. and Shepard discussed this line of reasoning when introducing the concept of an "equivalent supply pressure" [112, 50]. While this work did not examine said concept in detail, this work would nevertheless be incomplete without discussing how neglecting the introduction of fuel in the definition of PG can lead to false positives. While the discussion thus far focuses on the work of Brophy et al., it applies to all seemingly high-performing RDCs. For instance, even though Stout et al. claimed a peak PG of -0.014 [118], Shepard argued that since the fuel supply pressure was twice that of the oxidizer supply pressure, a more representative PG is -0.11 when Shepard accounted for the fuel total pressure. Therefore, even the few seemingly positive experimental PG measurements do not directly contradict (unless proven otherwise) the conjecture that the PG is at best zero when one properly accounts for all incoming momentum and energy.

All told, this is not to say that there is no thermodynamic benefit from using RDCs since less entropy production should occur within the detonation wave than a comparable deflagration. The entropy decrease is largely due to elevated temperature and pressure that the heat release is occurring at. Entropy provides the soundest thermodynamic measurement of the gain based on thermodynamics since irreversibilities (i.e., losses) directly increase entropy more than total pressure; furthermore, entropy is independent of the frame of reference, unlike the total temperature/pressure. While the detonation wave *locally* adds kinetic energy to the fluid, on a *global* scale, the release of chemical potential energy must be the only energy added to the fluid so as not to violate energy conservation; see Appendix A and the work of Zel'dovich [37]. However, given the same amount of added energy (heat), less local entropy production could still allow for more work generation or thrust production. From this, it would be *as if* there was an increase in the total pressure relative to the deflagration combustor. Consider, once again, the differences between the entropy-averaged total pressure and the area-averaged total pressure from Chapter 2. The inflated entropy-averaged total pressure is a virtual quantity since it does not describe the bulk flow and instead represents the

less entropy production. It remains to be seen if this virtual gain translates to practical applications since they may be the total pressure subject to the postulated conjecture, and any physical process considered in thrust-averaging or work-averaging lowers this hypothetical total pressure.

8.3.2 Alternative Benefits of RDCs

Ultimately, the focus of demonstrating a tangible stagnation pressure gain from using a RDC over the last few years (this work included) has not proven very successful. However, pressure losses comparable to modern aircraft engines have been observed [118, 121, 48]. In isolation, if one unfamiliar with the concept of RDCs saw that the PG promised by the PGC moniker has not been attain or is unattainable, it could mislead them into believing that RDCs do not have practical uses. However, PG alone ignores the other aspects of RDCs that can be leveraged for real-world use, such as the higher energy density, shorter combustor length, and sustaining combustion at higher flow speeds or fluxes. Thus, RDCs could result in weight savings greater than the stagnation pressure loss or could be an enabling technology such that they could maintain a flame when deflagration would otherwise blow out. It is advisable, then, that the PGC community that researches RDCs not focus solely on "pressure gain" as the only metric to be used to demonstrate whether RDCs can prove useful in applications. While further work will better optimize the designs of RDCs, in the short term, it may prove more prudent to find specific applications where the other aspects of RDCs provide a unique advantage.

8.4 Future Work

No work is ever truly finished, as there is always more to uncover, especially for flowfields as complex as RDCs. As such, this section suggests potential future work to further the community's understanding of the operation and performance of RDCs.

8.4.1 Combustion Efficiency Measurements

As alluded to in Section 1.4, the total pressure ratio is not the only performance metric for combustors. Currently, there are few to no experimental combustion efficiency measurements of experimental RDCs found in the literature. When mentioned, combustion efficiency is typically discussed in the context of assuming that complete combustion has occurred [44]. However, this has not been demonstrated, even for especially reactive mixtures like H_2. One work by Ferguson et al. addressed this by measuring the O_2 content in the exhaust of a H_2/air operated RDC. After comparisons to equilibrium calculations, they noted that the excess O_2 indicated that the RDC was not operating at peak combustion efficiency [199]. Other recent work by Cheng et al. analyzed

the CO_2 content of the exhaust of an RP-3/air operated RDC and also found that the combustion efficiency is around 60% [200, 201]. However, the short test times of RDCs (a few seconds) limit how much gas can be collected and sampled, although potential long-running water-cooled designs [202] may solve this constraint.

Other studies have compared computing the total temperature/enthalpy at the exit flow instead of analyzing the gas composition [124, 203]. Xu et al. tried adapting the EAP methodology to compute a total temperature by using the total pressure estimated through EAP [124]. However, such a method will commit the same errors as the EAP method discussed in this work. Walter et al. proposed a similar process, except particle image velocimetry measurements supplemented the process with velocity measurements [203]. An alternative approach would be to employ spectroscopic measurements at the exit plane of the device. From these, time-resolved measurements of the interrogated species' pressure, temperature, and mole fraction are possible [204, 205]. If a velocity is either assumed or inferred from a thrust measurement, the total temperature and the fraction of unreacted gases are estimable. Regardless of the method to determine the combustion efficiency, the characterization of RDC performance is incomplete without these measurements to supplement the total pressure measurements. Even if a PG value of effectively zero is demonstrated, indicating no loss in total pressure, if the combustion efficiency is poor (i.e., the total enthalpy change is less than ideal), the combustor still would be considered a poor combustor.

8.4.2 Pressure-Fed System

The laboratory test environment presents a unique divergence from real-world airbreathing devices in that the gaseous reactants' mass flow rates (and, thus, fluxes) are generally the driving parameters for individual test cases. Many studies use upstream flow metering devices to quantify flow rates; choked orifices metered the flow for this work. The orifices set the upstream pressure but do not actively control the downstream pressure (i.e., the RDC plenum pressure). As such, the plenum pressure reacts to the defined reactant mass flow rates given the boundary condition at the outlet of the RDC.

A consequence of being a mass-driven system is the plenum pressurization caused by the detonation wave blockage [139], which is detrimental to the global PG; see Chapter 6. The plenum pressurization is more prevalent for gaseous reactants since the incompressible nature of liquid reactants would inherently prevent back pressurization [206]. Thus, this may not be a concern for the liquid fuels used in airbreathing devices or the fuel and oxidizer of rockets. Regardless, in airbreathing applications outside the laboratory, the ambient conditions will dictate the inlet pressure, and the detonation wave will likely modulate the flow rate (and, thus, flux) of air based on the inlet pressure; a yet-to-be-explored scenario for air-breathing RDCs. Theoretically, if one

connected a RDC to a sufficiently large reservoir that the pressure could not vary, air mass flow would reduce once detonative operation is established. That is, if a detonative operation occurs, it seems plausible that a critical component of the continuous propagation of the detonation wave(s) is a modulation of the reactant injection. Furthermore, the author conjectures that for a given geometry, chemistry, equivalence ratio, and outlet boundary condition, the modulated mass flow rate, given the fixed pressure, will converge to the fixed mass flow rate with the same pressure. In other words, irrespective of whether the system is mass-fed or pressure-fed, a unique combination of mass flow rate and plenum pressure exists for fixed values of all other parameters. Whichever variable (mass flow or pressure) the upstream condition does not dictate will be modulated to match the unique combination.

While a pressure-fed system is an intriguing study to understand the operation of RDCs subject to different boundary conditions, there is an ulterior motive for such tests regarding the performance of RDCs. This work presented the conjecture that the pressurization of the plenum caused by blockage ensures that a global PG does not occur across the RDC. Eliminating the possibility of back-pressurization may present a means of evaluating the PG independently of fluidic blockage. Even if a fluidic blockage still existed, as hypothesized, the reduced mass flow rate through the system should not negatively impact the outlet's total pressure since total pressure is independent of the mass flow rate. Admittedly, the EAP and NPS methods discussed in this work use the mass flow rate to evaluate the Mach number when calculating the total pressure. However, the decrease in mass flow rate should not impact direct measurement through Kiel probes; thus, the other methods would also be agnostic to the changes in flow rate. Additionally, being pressure-fed would more closely match the simulations of Kaemming and Paxson, where they demonstrated positive PG. Therefore, if PG is physically possible, despite what is theorized by the author, such a test could provide a more suitable means of demonstrating a positive gain.

APPENDIX A

Unsteady Terms in Control Volume for Periodic Flows

Start with a generic fluid property (pressure, velocity, etc.) that is defined by function (f). This captures both the time and 3D variations of that variable. The time rate of change of this property within a control volume ($\mathcal{F}$) is given as,

$$\mathcal{F} = \frac{\partial}{\partial t} \iiint_V f(z, r, \theta, t) \mathrm{d}V \tag{A.1}$$

$$= \frac{\partial}{\partial t} \int_0^L \int_{R_1}^{R_2} \int_0^{2\pi} r f(z, r, \theta, t) \mathrm{d}\theta \mathrm{d}r \mathrm{d}z. \tag{A.2}$$

We want to determine if $\mathcal{F} = 0$ for RDC applications despite the traveling detonation wave(s) leading to the flowfield being unsteady in the laboratory frame. Due to the wave traveling along around the annulus, the property can be instead defined based upon it's relative position to the wave (ψ).

$$\psi = \theta + \omega t \tag{A.3}$$

For now, we assume that the rotational wavespeed (ω) is not a function of time or space,

$$\omega = \text{const.} \neq \mathrm{g}(\theta, \mathrm{t}) \tag{A.4}$$

This assumption is crucial to following derivation as it what allows the flowfield to be periodic in both space and time. This assumption leads to,

$$\mathrm{d}\theta = \mathrm{d}\psi \tag{A.5}$$

Using change of variables (integration through substitution), $\mathcal{F}$ can be rewritten as,

$$\mathcal{F} = \frac{\partial}{\partial t} \int_0^L \int_{R_1}^{R_2} \int_{\psi(\theta=0)}^{\psi(\theta=2\pi)} r f(z, r, \psi) \mathrm{d}\psi \mathrm{d}r \mathrm{d}z. \tag{A.6}$$

It is assumed that the separation of variables can be employed to break up the directional dependencies in f:

$$\mathcal{F} = \frac{\partial}{\partial t}\int_0^L \int_{R_1}^{R_2} \int_{\psi(\theta=0)}^{\psi(\theta=2\pi)} rF(z)G(r)H(\psi)\mathrm{d}\psi\mathrm{d}r\mathrm{d}z. \tag{A.7}$$

It is desirable to bring the time derivative into the integral for reasons that will be seen later. Since F and G do not depend on time by construction, the partial derivative only operates on H since it has a functional dependence on time through ψ. However, the bounds $\psi(\theta = 0)$ and $\psi(\theta = 2\pi)$ also depend on time, necessitating the Leibniz integral rule.

$$\frac{\partial}{\partial t}\int_{\psi(\theta=0)}^{\psi(\theta=2\pi)} H(\psi)\mathrm{d}\psi = \int_{\psi(\theta=0)}^{\psi(\theta=2\pi)} \frac{\partial H}{\partial t}\mathrm{d}\psi + \frac{\partial[\psi(\theta=2\pi)]}{\partial t}H[\psi(\theta=2\pi)] - \frac{\partial[\psi(\theta=0)]}{\partial t}H[\psi(\theta=0)] \tag{A.8}$$

$$\frac{\partial}{\partial t}\int_{\psi(\theta=0)}^{\psi(\theta=2\pi)} H(\psi)\mathrm{d}\psi = \int_{\psi(\theta=0)}^{\psi(\theta=2\pi)} \frac{\partial H}{\partial t}\mathrm{d}\psi + (\omega)H[\psi(\theta=2\pi)] - (\omega)H[\psi(\theta=0)] \tag{A.9}$$

$$= \int_{\psi(\theta=0)}^{\psi(\theta=2\pi)} \frac{\partial H}{\partial t}\mathrm{d}\psi + \omega(H[\psi(\theta=2\pi)] - H[\psi(\theta=0)]) \tag{A.10}$$

Up this point, we have not assumed that the flowfield is periodic as what can be found in ideal RDCs. Thus far, we have only assumed that the fluid property depends on the relative position of the detonation wave(s), ψ, and that the wave-speed is constant, ω = constant. Imposing that the flowfield is periodic in the circumferential direction (θ) and in time (the period is related to ω), results in,

$$H[\psi(\theta=2\pi)] = H[\psi(\theta=0)], \tag{A.11}$$

at every instance in time. That is to say that in the θ and t domain, H is constant along lines that are perpendicular to the line given by ψ. Now $\mathcal{F}$ can be re-written as,

$$\mathcal{F} = \int_0^L \int_{R_1}^{R_2} \int_{\psi(\theta=0)}^{\psi(\theta=2\pi)} rF(z)G(r)\frac{\partial H(\psi)}{\partial t}\mathrm{d}\psi\mathrm{d}r\mathrm{d}z. \tag{A.12}$$

The chain rule is used to get the partial derivative of H with respect to time,

$$\frac{\partial H(\psi)}{\partial t} = \frac{\mathrm{d}H}{\mathrm{d}\psi}\frac{\partial \psi}{\partial t} \tag{A.13}$$

$$= \omega H'. \tag{A.14}$$

Substituting back in gives,

$$\mathcal{F} = \int_0^L \int_{R_1}^{R_2} \int_{\psi(\theta=0)}^{\psi(\theta=2\pi)} r\omega F(z)G(r)H'(\psi)\mathrm{d}\psi\mathrm{d}r\mathrm{d}z. \tag{A.15}$$

Integrating with respect to ψ results in,

$$\mathcal{F} = \omega\left(H[\psi(\theta = 2\pi)] - H[\psi(\theta = 0)]\right) \int_0^L \int_{R_1}^{R_2} rF(z)G(r)\mathrm{d}r\mathrm{d}z. \tag{A.16}$$

Again, due to the imposed periodic nature of the flowfield, the first term is identically zero. Thus,

$$\mathcal{F} = 0, \tag{A.17}$$

which means that the unsteady term in the control analysis can be neglected due the periodic nature of the flowfield.

APPENDIX B

Inequality within Experimental EAP

This appendix gives the mathematical differences between the experimental EAP and the area-averaged total pressure. The differences arise from the resulting non-linear terms that arise in trying to commute the area-averaging procedure to the product of several terms.

A simple decomposition of Q can be made such that it is expressed in terms of a mean component and a variation, which depends on $\mathbf{x}$, from that mean.

$$Q(\mathbf{x}) = \langle Q \rangle_{\mathrm{A}} + Q'(\mathbf{x}) \tag{B.1}$$

where, by definition,

$$\langle Q \rangle_{\mathrm{A}} = \frac{1}{\iint_A \mathrm{d}A} \iint_A Q(\mathbf{x}) \mathrm{d}A = \frac{1}{A} \iint_A Q \mathrm{d}A \tag{B.2}$$

$$\langle Q'(\mathbf{x}) \rangle_{\mathrm{A}} = 0 \tag{B.3}$$

$$\langle \langle Q \rangle_{\mathrm{A}} \rangle_{\mathrm{A}} = \langle Q \rangle_{\mathrm{A}} \tag{B.4}$$

Consider the area-averaging procedure as applied to the basic gross thrust equation (Eqn. 2.19), as given by,

$$\left\langle p_8 (1 + \gamma_8 M_{8,\mathrm{z}}^2) \right\rangle_{\mathrm{A}} = \frac{1}{A_8} \iint_{A_8} p_8(\mathbf{x}) \left[1 + \gamma_8(\mathbf{x}) M_{8,\mathrm{z}}^2(\mathbf{x}) \right] \mathrm{d}A \tag{B.5}$$

The decomposition introduced above is applied to the right-hand side integral. For simplicity, we will neglect the variations of γ_8 around the annulus ($\gamma_8' \approx 0$), although in reality there will be additional terms that appear.

$$\iint_{A_8} p_8(\mathbf{x})(1 + \gamma_8(\mathbf{x}) {M_{8,\mathrm{z}}}^2(\mathbf{x})) \mathrm{d}A = \iint_{A_8} \left[\langle p_8 \rangle_{\mathrm{A}} + p_8'(\mathbf{x}) \right] \Big(1 + \langle \gamma_8 \rangle_{\mathrm{A}} \left[\left\langle M_{8,\mathrm{z}} \right\rangle_{\mathrm{A}} + M_{8,\mathrm{z}}'(\mathbf{x}) \right]^2 \Big) \mathrm{d}A \tag{B.6}$$

$$\iint_{A_8} p_8(\mathbf{x})(1+\gamma_8(\mathbf{x}){M_{8,z}}^2(\mathbf{x}))\mathrm{d}A = A_8\left\langle p_8\right\rangle_{\mathrm{A}}\left(1+\left\langle\gamma_8\right\rangle_{\mathrm{A}}\left\langle M_{8,z}\right\rangle_{\mathrm{A}}^2\right)+$$
$$A_8\left\langle\gamma_8\right\rangle_{\mathrm{A}}\left(\left\langle p_8\right\rangle_{\mathrm{A}}\left\langle (M'_{8,z})^2\right\rangle_{\mathrm{A}}+2\left\langle M_{8,z}\right\rangle_{\mathrm{A}}\left\langle p'_8M'_{8,z}\right\rangle_{\mathrm{A}}+\left\langle p'_8(M'_{8,z})^2\right\rangle_{\mathrm{A}}\right) \quad \text{(B.7)}$$

Note the terms that arise from the variations ($'$). The average of the product of two or more variations is not necessarily zero since the averaging is not commutative. Thus, it has been demonstrated that Eq. 2.20 (shown below) is true,

$$\left\langle p_8(1+\gamma_8M_{8,z}^2)\right\rangle_{\mathrm{A}} \neq \left\langle p_8\right\rangle_{\mathrm{A}}\left(1+\left\langle\gamma_8\right\rangle_{\mathrm{A}}\left\langle M_{8,z}\right\rangle_{\mathrm{A}}^2\right) \quad \text{(B.8)}$$

APPENDIX C

Ideal Equivalent Available Pressure Derivation

C.1 Overview

In this appendix, a derivation of the ideal EAP (EAP_i) as originally proposed by Kaemming and Paxson [113] is given, while extending it to include the effect of variable gas composition and properties in the spatial domain. One of the underlying assumptions of the original derivation is that it assumes constant properties (e.g., c_p and γ). This has been identified as a possible source of errors as shown by Klopsch et al. [207] and the following derivation highlights where this assumption affects the result.

C.2 Derivation

First, the ideal Mach number after expanding to ambient pressure is solved using isentropic relations. In other words,

$$\frac{p_{t,8}(\mathbf{x})}{p_0} = \left(1 + \frac{\gamma_8(\mathbf{x}) - 1}{2} M_{9i}^2(\mathbf{x})\right)^{\frac{\gamma_8(\mathbf{x})}{\gamma_8(\mathbf{x})-1}} \tag{C.1}$$

is solved for M_{9i} since $p_{t,8}$ is known from the simulations. Using this Mach number, the ideal velocity can be found.

$$T_{9i}(\mathbf{x}) = T_{t,8}(\mathbf{x}) \left(1 + \frac{\gamma_8(\mathbf{x}) - 1}{2} M_{9i}^2(\mathbf{x})\right)^{-1} \tag{C.2}$$

$$u_{9i}(\mathbf{x}) = M_{9i}(\mathbf{x}) \sqrt{\gamma_8(\mathbf{x}) R_8(\mathbf{x}) T_{9i}(\mathbf{x})} \tag{C.3}$$

Again, $T_{t,8}$ is known from the simulations. The above three equations when combined are equivalent to Eqn. 2.21 without the nozzle efficiency term. I.e.,

$$u_{9i}(\mathbf{x}) = \sqrt{2 c_{p,8}(\mathbf{x}) T_{t,8}(\mathbf{x}) \left[1 - \left(\frac{p_0}{p_{t,8}(\mathbf{x})}\right)^{\frac{\gamma_8(\mathbf{x})-1}{\gamma_8(\mathbf{x})}}\right]} \tag{C.4}$$

The axial component of the ideal velocity is isolated by subtracting the circumferential component from state 8 (which is assumed to not change across the nozzle) from the total velocity.

$$u_{\mathrm{z},9\mathrm{i}}(\mathbf{x}) = \sqrt{u_{9\mathrm{i}}^2(\mathbf{x}) - u_{\theta,9\mathrm{i}}^2(\mathbf{x})} \tag{C.5}$$

This velocity is in the examination of the kinetic energy component of the total enthalpy. As such, the total enthalpy/temperature needs to be defined. Kaemming and Paxson assume that $c_{p,8}$ is a constant (or varies negligibly) such that a mass-averaged total temperature can be defined similarly. [113]

$$\left\langle T_{\mathrm{tz},8} \right\rangle_{\mathrm{M}} = \frac{1}{\dot{m}_8} \iint_{A_8} T_{\mathrm{tz},8}(\mathbf{x}) \mathrm{d}\dot{m}_8(\mathbf{x}) \tag{C.6}$$

The nozzle is assumed to conserve total temperature (enthalpy),

$$h_{\mathrm{tz},8}(\mathbf{x}) = c_{p,8}(\mathbf{x}) T_{9\mathrm{i}}(\mathbf{x}) + \frac{1}{2} u_{\mathrm{z},9\mathrm{i}}^2(\mathbf{x}) \tag{C.7}$$

$$= c_{p,8}(\mathbf{x}) T_{\mathrm{tz},8}(\mathbf{x}) \tag{C.8}$$

The mass-averaging procedure is then applied to the above equation, while still assuming that $c_{p,8}$ is a constant.

$$\left\langle c_{p,8} T_{\mathrm{tz},8} \right\rangle_{\mathrm{M}} = c_{p,8} \left\langle T_{9\mathrm{i}} \right\rangle_{\mathrm{M}} + \frac{1}{2} \left\langle u_{\mathrm{z},9\mathrm{i}}^2 \right\rangle_{\mathrm{M}} \tag{C.9}$$

$$= c_{p,8} \left\langle T_{\mathrm{tz},8} \right\rangle_{\mathrm{M}} \tag{C.10}$$

This can be manipulated into the following expression for the ideal mass-averaged exit static temperature,

$$\left\langle T_{9\mathrm{i}} \right\rangle_{\mathrm{M}} = \left\langle T_{\mathrm{tz},8} \right\rangle_{\mathrm{M}} - \frac{\left\langle u_{\mathrm{z},9\mathrm{i}}^2 \right\rangle_{\mathrm{M}}}{2 c_{p,8}} \tag{C.11}$$

This result is very similar to the EAP-related average static temperature which is given as,

$$\widetilde{T}_{9\mathrm{i}} = \left\langle T_{\mathrm{tz},8} \right\rangle_{\mathrm{M}} - \frac{\left\langle u_{\mathrm{z},9\mathrm{i}} \right\rangle_{\mathrm{M}}^2}{2 c_{p,8}} \tag{C.12}$$

However, the square cannot be brought out of the averaging procedure, as there is a variation term

($\prime$) that would be ignored. I.e.,

$$\left\langle u_{\mathrm{z,9i}}^2 \right\rangle_{\mathrm{M}} \neq \left\langle u_{\mathrm{z,9i}} \right\rangle_{\mathrm{M}}^2 \tag{C.13}$$

$$= \left\langle u_{\mathrm{z,9i}} \right\rangle_{\mathrm{M}}^2 + \left\langle (u'_{\mathrm{z,9i}})^2 \right\rangle_{\mathrm{M}} \tag{C.14}$$

The velocity variations are likely too large to be neglected. The relation between the EAP equivalent temperature ($\widetilde{T}_{9\mathrm{i}}$) and the mass-averaged temperature ($\langle T_{9\mathrm{i}} \rangle_{\mathrm{M}}$) as derived here is,

$$\widetilde{T}_{9\mathrm{i}} = \langle T_{9\mathrm{i}} \rangle_{\mathrm{M}} + \frac{\left\langle (u'_{\mathrm{z,9i}})^2 \right\rangle_{\mathrm{M}}}{2c_{p,8}} \tag{C.15}$$

The final step to determining the total pressure is to utilize isentropic relationships to relate the total temperature and pressure,

$$\frac{p_{\mathrm{tz},8}(\mathbf{x})}{p_0} = \left(\frac{T_{\mathrm{tz},8}(\mathbf{x})}{T_9(\mathbf{x})} \right)^{\frac{\gamma_8(\mathbf{x})}{\gamma_8(\mathbf{x})-1}} \tag{C.16}$$

Substituting the averaged total and static pressures while assuming a constant γ_8 (or using some average value), the final equation for $\mathrm{EAP_i}$ is recovered,

$$\mathrm{EAP_i} = \widetilde{p}_{\mathrm{tz,8i}} = p_0 \left(\frac{\left\langle T_{\mathrm{tz},8} \right\rangle_{\mathrm{M}}}{\widetilde{T}_{9\mathrm{i}}} \right)^{\frac{\gamma_8}{\gamma_8 - 1}} \tag{C.17}$$

Since the derivation of ideal EAP assumes constant gas properties (c_p and γ), some ambiguity arises as to which gas property to use since they vary around the annulus. Typically mass-averaged gas properties are used, although area-averages have been shown to be more conservative [207]. On the other hand, the thrust-averaging procedure presented in the main body of this work can more readily incorporate the variations in gas properties and eliminate ambiguity. Any discrepancies between the thrust-averaging and the ideal EAP come from two sources, the variations in $c_{p,8}$ and the variations in γ_8. The thrust-averaging can also be thought of as an extension of the ideal EAP to capture those effects.

APPENDIX D

Work-Averaged Extended Derivation

This appendix presents the remainder of the derivation of the work-averaged total pressure. The two expressions for the theoretical work output ($\dot{W}$), Eqns. 2.43 and 2.44, are equated and subsequently manipulated.

$$\eta_t \dot{m}_4 \left\langle c_{p,4} T_{\mathrm{tz},4} \right\rangle_{\mathrm{M}} \left[1 - \left(\frac{p_{\mathrm{tz},5}}{\left\langle p_{\mathrm{tz},4} \right\rangle_{\mathrm{W}}} \right)^{\frac{\langle \gamma_4 \rangle_{\mathrm{M}} - 1}{\langle \gamma_4 \rangle_{\mathrm{M}}}} \right] = \iint_{A_4} \eta_t c_{p,4}(\mathbf{x}) T_{\mathrm{tz},4}(\mathbf{x}) \left[1 - \left(\frac{p_{\mathrm{tz},5}}{p_{\mathrm{tz},4}(\mathbf{x})} \right)^{\frac{\gamma_4(\mathbf{x}) - 1}{\gamma_4(\mathbf{x})}} \right] \mathrm{d}\dot{m}_4(\mathbf{x}) \quad \text{(D.1)}$$

$$\eta_t \dot{m}_4 \left\langle c_{p,4} T_{\mathrm{tz},4} \right\rangle_{\mathrm{M}} \left[1 - \left(\frac{p_{\mathrm{tz},5}}{\left\langle p_{\mathrm{tz},4} \right\rangle_{\mathrm{W}}} \right)^{\frac{\langle \gamma_4 \rangle_{\mathrm{M}} - 1}{\langle \gamma_4 \rangle_{\mathrm{M}}}} \right] = \iint_{A_4} \eta_t c_{p,4}(\mathbf{x}) T_{\mathrm{tz},4}(\mathbf{x}) \mathrm{d}\dot{m}_4(\mathbf{x}) - \iint_{A_4} \eta_t c_{p,4}(\mathbf{x}) T_{\mathrm{tz},4}(\mathbf{x}) \left[\left(\frac{p_{\mathrm{tz},5}}{p_{\mathrm{tz},4}(\mathbf{x})} \right)^{\frac{\gamma_4(\mathbf{x}) - 1}{\gamma_4(\mathbf{x})}} \right] \mathrm{d}\dot{m}_4 \quad \text{(D.2)}$$

The first term on the right-hand side can be simplified by identifying that it is effectively the mass-averaged total enthalpy as long as η_t is constant.

$$\eta_t \dot{m}_4 \left\langle c_{p,4} T_{\mathrm{tz},4} \right\rangle_{\mathrm{M}} = \iint_{A_4} \eta_t c_{p,4}(\mathbf{x}) T_{\mathrm{tz},4}(\mathbf{x}) \mathrm{d}\dot{m}_4(\mathbf{x}) \quad \text{(D.3)}$$

Next, both sides are divided by the $\dot{m}_4 \eta_t \left\langle c_{p,4} T_{\mathrm{tz},4} \right\rangle_{\mathrm{M}}$:

$$1 - \left(\frac{p_{\mathrm{tz},5}}{\left\langle p_{\mathrm{tz},4} \right\rangle_{\mathrm{W}}} \right)^{\frac{\langle \gamma_4 \rangle_{\mathrm{M}} - 1}{\langle \gamma_4 \rangle_{\mathrm{M}}}} = 1 - \frac{\iint_{A_4} \eta_t c_{p,4}(\mathbf{x}) T_{\mathrm{tz},4}(\mathbf{x}) \left(\frac{p_{\mathrm{tz},5}}{p_{\mathrm{tz},4}(\mathbf{x})} \right)^{\frac{\gamma_4(\mathbf{x})-1}{\gamma_4(\mathbf{x})}} \mathrm{d}\dot{m}_4(\mathbf{x})}{\eta_t \iint_{A_4} c_{p,4}(\mathbf{x}) T_{\mathrm{tz},4}(\mathbf{x}) \mathrm{d}\dot{m}_4(\mathbf{x})} \tag{D.4}$$

$$\left(\frac{\left\langle p_{\mathrm{tz},4} \right\rangle_{\mathrm{W}}}{p_{\mathrm{tz},5}} \right)^{\frac{\langle \gamma_4 \rangle_{\mathrm{M}} - 1}{\langle \gamma_4 \rangle_{\mathrm{M}}}} = \frac{\eta_t \iint_{A_4} c_{p,4}(\mathbf{x}) T_{\mathrm{tz},4}(\mathbf{x}) \mathrm{d}\dot{m}_4(\mathbf{x})}{\iint_{A_4} \eta_t c_{p,4}(\mathbf{x}) T_{\mathrm{tz},4}(\mathbf{x}) \left(\frac{p_{\mathrm{tz},5}}{p_{\mathrm{tz},4}(\mathbf{x})} \right)^{\frac{\gamma_4(\mathbf{x})-1}{\gamma_4(\mathbf{x})}} \mathrm{d}\dot{m}_4(\mathbf{x})} \tag{D.5}$$

$$\left\langle p_{\mathrm{tz},4} \right\rangle_{\mathrm{W}} = \left(\frac{\eta_t (p_{\mathrm{tz},5})^{\frac{\langle \gamma_4 \rangle_{\mathrm{M}} - 1}{\langle \gamma_4 \rangle_{\mathrm{M}}}} \iint_{A_4} c_{p,4}(\mathbf{x}) T_{\mathrm{tz},4}(\mathbf{x}) \mathrm{d}\dot{m}_4(\mathbf{x})}{\iint_{A_4} \eta_t c_{p,4}(\mathbf{x}) T_{\mathrm{tz},4}(\mathbf{x}) \left(\frac{p_{\mathrm{tz},5}}{p_{\mathrm{tz},4}(\mathbf{x})} \right)^{\frac{\gamma_4(\mathbf{x})-1}{\gamma_4(\mathbf{x})}} \mathrm{d}\dot{m}_4(\mathbf{x})} \right)^{\frac{\langle \gamma_4 \rangle_{\mathrm{M}}}{\langle \gamma_4 \rangle_{\mathrm{M}} - 1}} \tag{D.6}$$

Above is the proper form for the work-averaged total pressure. Due to the variations in γ_4, the total pressure post turbine ($p_{\mathrm{tz},5}$) cannot be directly eliminated. Re-arranging the above equation, to find how $\left\langle p_{\mathrm{tz},4} \right\rangle_{\mathrm{W}}$ depends on $p_{\mathrm{tz},5}$, results in the following,

$$\left\langle p_{\mathrm{tz},4} \right\rangle_{\mathrm{W}} \propto \left[\iint_{A_4} (p_{\mathrm{tz},5})^{\frac{\gamma_4(\mathbf{x})-1}{\gamma_4(\mathbf{x})}} (p_{\mathrm{tz},5})^{-\frac{\langle \gamma_4 \rangle_{\mathrm{M}} - 1}{\langle \gamma_4 \rangle_{\mathrm{M}}}} \mathrm{d}\dot{m}_4(\mathbf{x}) \right]^{-1} \tag{D.7}$$

$$\propto \left[\iint_{A_4} (p_{\mathrm{tz},5})^{\frac{\gamma_4(\mathbf{x}) - \langle \gamma_4 \rangle_{\mathrm{M}}}{\langle \gamma_4 \rangle_{\mathrm{M}} \gamma_4(\mathbf{x})}} \mathrm{d}\dot{m}_4(\mathbf{x}) \right]^{-1} \tag{D.8}$$

$$\propto \left[\iint_{A_4} (p_{\mathrm{tz},5})^{\frac{\gamma_4'(\mathbf{x})}{\langle \gamma_4 \rangle_{\mathrm{M}} \gamma_4(\mathbf{x})}} \mathrm{d}\dot{m}_4(\mathbf{x}) \right]^{-1} \tag{D.9}$$

If it is assumed that the variations in γ_4 are small compared to the mean ($\gamma_4' \ll \langle \gamma_4 \rangle_{\mathrm{M}}$), the exponent term becomes approximately zero. Thus, $p_{\mathrm{tz},5}$ is effectively eliminated, resulting in an insignificant dependence on the value of the chosen $p_{\mathrm{tz},5}$. Overall, the following approximation is valid within

a percent deviation,

$$\langle p_{\mathrm{tz},4} \rangle_{\mathrm{W}} \approx \left(\frac{\eta_t \iint_{A_4} c_{p,4}(\mathbf{x}) T_{\mathrm{tz},4}(\mathbf{x}) \mathrm{d}\dot{m}_4(\mathbf{x})}{\iint_{A_4} \eta_t c_{p,4}(\mathbf{x}) T_{\mathrm{tz},4}(\mathbf{x}) \left(\frac{1}{p_{\mathrm{tz},4}(\mathbf{x})} \right)^{\frac{\gamma_4(\mathbf{x})-1)}{\gamma_4(\mathbf{x})}} \mathrm{d}\dot{m}_4(\mathbf{x})} \right)^{\frac{\langle \gamma_4 \rangle_{\mathrm{M}}}{\langle \gamma_4 \rangle_{\mathrm{M}^{-1}}}} \tag{D.10}$$

APPENDIX E

Equating Time-Average to Area-Average Quantities in Periodic Flowfields

E.1 Overview

This appendix has two goals. First, is to demonstrate the validity of equating the average over a period of a point measurement and area-averaging of any quantity in a periodic flowfield, like what is seen in RDCs. While this has been previously discussed and alluded to extensively in the RDC community [113, 208], this paper seeks to directly support previous analysis and discussions through a rigorous mathematical demonstration. The required assumptions/constraints are discussed, and the equality is extended to averaging over a generic period of time (time-averaging) and for an arbitrary number of wave systems. The second goal of this paper is to assert that the consistency between the different total pressure measurement techniques is a direct consequence of the periodic nature of the flowfield. By virtue of EAP being an effective area-average quantity and the flowfield being periodic in space and time, the EAP would then be equal to time-averaged measures of the total pressure (either from Kiel probes or the NPS method).

E.2 Proof

Consider an arbitrary thermodynamic or fluidic quantity Q within the RDC. Let us assume that the spatiotemporal variation of Q is given by a generic function f; thus:

$$Q = f(r, \theta, z, t) \tag{E.1}$$

$$\approx f(\theta, z, t) \tag{E.2}$$

Cylindrical coordinates are used for convenience since many RDC geometries are cylindrical, but the analysis that follows is not dependent on the choice of coordinate system. Additionally, the

radial dependence is assumed to be negligible. The validity of this assumption has been evaluated for small channel widths [106, 107] and with radial stratification of the fuel [166].

This work seeks to demonstrate that during the operation of a RDC, the time and area averages of Q are equal, i.e., we seek to demonstrate that the following equality holds:

$$\left\langle Q|_{t_\mathrm{i},z_\mathrm{i}} \right\rangle_\mathrm{A} = \left\langle Q|_{\theta_\mathrm{i},z_\mathrm{i}} \right\rangle_\mathrm{t} \tag{E.3}$$

where $\langle\cdot\rangle$ is the averaging operator which is defined below.

Area-averaging procedure requires the definition of the plane over which the averaging procedure is applied. For cylindrical RDCs, the simplest plane would be the cross-section at a given axial (z_i) location. As such, for an axial plane given by z_i and at time t_i, the area-average ($\left\langle Q|_{t_\mathrm{i},z_\mathrm{i}} \right\rangle_\mathrm{A}$) is given by:

$$\left\langle Q|_{t_\mathrm{i},z_\mathrm{i}} \right\rangle_\mathrm{A} = \left(\iint_A \mathrm{d}A \right)^{-1} \iint_A f(r, \theta; z_\mathrm{i}, t_\mathrm{i}) \mathrm{d}A \tag{E.4}$$

$$= \frac{1}{2\pi} \int_{\theta=0}^{\theta=2\pi} f(\theta; z_\mathrm{i}, t_\mathrm{i}) \mathrm{d}\theta \tag{E.5}$$

Meanwhile, the time-averaging procedure is performed at a single spatial location. Thus, at a given circumferential, θ_i, and axial location z_i, the time-average ($\left\langle Q|_{\theta_\mathrm{i},z_\mathrm{i}} \right\rangle_\mathrm{t}$) is given by:

$$\left\langle Q|_{\theta_\mathrm{i},z_\mathrm{i}} \right\rangle_\mathrm{t} = \left(\int_{t_1}^{t_2} \mathrm{d}t \right)^{-1} \int_{t_1}^{t_2} f(t; \theta_\mathrm{i}, z_\mathrm{i}) \mathrm{d}t \tag{E.6}$$

The averaging procedure is over the time interval given by $[t_1, t_2]$ where $t_2 > t_1$. The bounds of this time-averaging will be assigned later in this section.

E.2.1 Single Mode Operation

First, we limit the analysis to the case when the RDC has a single wave system (mode) during operation. This wave system is comprised of one or more detonation wave(s) rotating in the same direction. The number, strength, and position of the detonation wave(s) relative to one another are irrelevant. For instance, the wave system can consist of a single detonation wave propagating with an angular velocity of ω or multiple co-rotating detonation waves that are each propagating at ω. The multiple co-rotating waves do not need to be identical in terms of pressure ratio, heat release profile, etc. (see Section 6.3.2); however, they must maintain the same angular speed (ω). This is equivalent to saying that the flowfield is steady in the rotating (detonation) frame of reference given by the angular speed ω.

With this framework, the functional dependence of Q on θ and t in Q (f) can be described by a periodic function (g) that only depends on the relative position of the detonation wave system (ψ) given by,

$$\psi = \theta + \omega t \tag{E.7}$$

For now, we impose that ω does not vary in space or time and can be treated as a constant throughout the operation. This corresponds to imposing the following condition on ω:

$$\frac{\partial \omega}{\partial \theta} = \frac{\partial \omega}{\partial t} = 0 \tag{E.8}$$

or alternatively,

$$\mathrm{d}\psi = \mathrm{d}\theta \tag{E.9}$$

$$= \omega \mathrm{d}t \tag{E.10}$$

E.2.1.1 Area-Average

Performing a change of variables on Eqn. E.5 utilizing Eqns. E.7 and E.9 gives,

$$\left\langle Q|_{t_\mathrm{i},z_\mathrm{i}} \right\rangle_\mathrm{A} = \frac{1}{2\pi} \int_{\psi(\theta=0,t=t_\mathrm{i})}^{\psi(\theta=2\pi,t=t_\mathrm{i})} g(\psi; z_\mathrm{i}) \mathrm{d}\psi \tag{E.11}$$

The bounds of integration are evaluated to be,

$$\psi(\theta = 0, t = t_\mathrm{i}) = \omega t_\mathrm{i} \tag{E.12}$$

$$\psi(\theta = 2\pi, t = t_\mathrm{i}) = 2\pi + \omega t_\mathrm{i} \tag{E.13}$$

where ωt_i can be treated as a constant.

The function, $g(\psi)$, is constructed to be periodic over the ψ domain since the flowfield is assumed to be steady in the detonation frame of reference. If a real function $F(x)$ is periodic and integrable over its period ($\mathcal{T}$), the following relation is always true:

$$\int_0^{\mathcal{T}} F(x) \mathrm{d}x = \int_a^{\mathcal{T}+a} F(x) \mathrm{d}x \tag{E.14}$$

for every $a \in \mathbb{R}$. Since ψ describes a full cycle of the detonation wave(s), it has a period of 2π.

Using Eqns. E.11-E.14 the area-average can be rewritten as,

$$\langle Q|t_{\mathrm{i}}\rangle_{\mathrm{A}} = \frac{1}{2\pi}\int_{\omega t_{\mathrm{i}}}^{2\pi+\omega t_{\mathrm{i}}} g(\psi; z_{\mathrm{i}})\mathrm{d}\psi \tag{E.15}$$

$$= \frac{1}{2\pi}\int_{0}^{2\pi} g(\psi; z_{\mathrm{i}})\mathrm{d}\psi \tag{E.16}$$

No further simplifications can be made; thus, this is the final form for the area-average.

E.2.1.2 Time-Average over One Period

Now, we turn our focus to the time-averaging procedure. Before addressing the full form of the time-averaging procedure, we consider the case where the averaging occurs over a single period (τ) according to:

$$\left\langle Q|_{\theta_{\mathrm{i}},z_{\mathrm{i}}}\right\rangle_{\tau} = \left(\int_{t_{\mathrm{j}}}^{t_{\mathrm{j}}+\tau}\mathrm{d}t\right)^{-1}\int_{t_{\mathrm{j}}}^{t_{\mathrm{j}}+\tau} f(t;\theta_{\mathrm{i}}, z_{\mathrm{i}})\mathrm{d}t \tag{E.17}$$

The time-averaging procedure begins at time, t_{j}, which is arbitrary. The subscript "j" is to differentiate from the instantaneous time that the area-averaging is performed on. It is possible that subsequent time-averaged measurements are taken in series and the "j" gives its position within the series.

Again, a change of variables is performed on Eqn. E.17 utilizing Eqns. E.7 and E.10.

$$\left\langle Q|_{\theta_{\mathrm{i}},z_{\mathrm{i}}}\right\rangle_{\tau} = \left(\int_{\psi(\theta=\theta_{\mathrm{i}},t=t_{\mathrm{j}})}^{\psi(\theta=\theta_{\mathrm{i}},t=t_{\mathrm{j}}+\tau)}\frac{1}{\omega}\mathrm{d}\psi\right)^{-1}\int_{\psi(\theta=\theta_{\mathrm{i}},t=t_{\mathrm{j}})}^{\psi(\theta=\theta_{\mathrm{i}},t=t_{\mathrm{j}}+\tau)}\frac{g(\psi; z_{\mathrm{i}})}{\omega}\mathrm{d}\psi \tag{E.18}$$

The bounds of integration of the above equation are evaluated to be,

$$\psi(\theta=\theta_{\mathrm{i}}, t=t_{\mathrm{j}}) = \theta_{\mathrm{i}} + \omega t_{\mathrm{j}} \tag{E.19}$$

$$\psi(\theta=\theta_{\mathrm{i}}, t=t_{\mathrm{j}}+\tau) = \theta_{\mathrm{i}} + \omega(t_{\mathrm{j}}+\tau) \tag{E.20}$$

This can be further simplified by using the definition of the angular speed, $\omega = 2\pi/\tau$. Using the bounds of integration, the additive property of definite integrals, and recalling Eqn. E.14, the period-averaged quantity can then be expressed as:

$$\left\langle Q|_{\theta_{\mathrm{i}},z_{\mathrm{i}}}\right\rangle_{\tau} = \frac{1}{\omega\tau}\int_{0}^{\omega\tau} g(\psi; z_{\mathrm{i}})\mathrm{d}\psi \tag{E.21}$$

$$= \frac{1}{2\pi}\int_{0}^{2\pi} g(\psi; z_{\mathrm{i}})\mathrm{d}\psi \tag{E.22}$$

Equations E.16 and E.22 are equivalent, thus proving that Eqn. E.3 is valid if there is a single wave system uniformly propagating at a constant angular speed. The time-averaging, thus far, must be performed over time-intervals equal to the period of the wave system.

E.2.1.3 Convergence of Time-Average

While averaging over a singular period is possible for time-resolved measurements, other measurements can be taken at a sample rate significantly smaller than the detonation wave(s). One such measurement are the CTAPs that are frequently in the experimental setup of RDC testing [169]. Thus, the analysis presented in the preceding section must be expanded to account for longer intervals of time-averaging.

Now consider averaging the quantity, Q, over an arbitrary length of time ($\mathfrak{T}$). The arbitrary length of time can be expressed in terms of the period of the wave system (τ) as:

$$\mathfrak{T} = n\tau + \delta t \tag{E.23}$$

where $n \in \mathbb{Z}$ and δt is the remainder after factoring out the n periods from $\mathfrak{T}$. From this, the time-average can be defined as:

$$\left\langle Q|_{\theta_\mathrm{i},z_\mathrm{i}} \right\rangle_\mathrm{t} = \left(\int_{t_\mathrm{j}}^{t_\mathrm{j}+\mathfrak{T}} \mathrm{d}t \right)^{-1} \int_{t_\mathrm{j}}^{t_\mathrm{j}+\mathfrak{T}} f(t;\theta_\mathrm{i},z_\mathrm{i})\mathrm{d}t \tag{E.24}$$

Again, the time interval begins at the arbitrary t_j.

Using the same definition of ψ given in Eqn. E.7, a replacement of variables is employed to convert everything to be in terms of ψ,

$$\left\langle Q|_{\theta_\mathrm{i},z_\mathrm{i}} \right\rangle_\mathrm{t} = \left(\int_{\psi(\theta=\theta_\mathrm{i},t=t_\mathrm{j})}^{\psi(\theta=\theta_\mathrm{i},t=t_\mathrm{j}+\mathfrak{T})} \frac{1}{\omega}\mathrm{d}\psi \right)^{-1} \int_{\psi(\theta=\theta_\mathrm{i},t=t_\mathrm{j})}^{\psi(\theta=\theta_\mathrm{i},t=t_\mathrm{j}+\mathfrak{T})} \frac{g(\psi;z_\mathrm{i})}{\omega}\mathrm{d}\psi \tag{E.25}$$

The bounds of integration are now evaluated to be,

$$\psi(\theta=\theta_\mathrm{i}, t=t_\mathrm{j}) = \theta_\mathrm{i} + \omega t_\mathrm{j} \tag{E.26}$$

$$\psi(\theta=\theta_\mathrm{i}, t=t_\mathrm{j}+\mathfrak{T}) = \theta_\mathrm{i} + \omega(t_\mathrm{j} + n\tau + \delta t) \tag{E.27}$$

Substituting these bounds and utilizing the additive property of definite integrals to break up the

integral gives the following,

$$\left\langle Q|_{\theta_\mathrm{i},z_\mathrm{i}}\right\rangle_\mathrm{t} = \frac{1}{2\pi n+\omega\delta t}\left[\int_{\theta_\mathrm{i}+\omega t_\mathrm{j}}^{\theta_\mathrm{i}+\omega t_\mathrm{j}+2\pi n} g(\psi;z_\mathrm{i})\mathrm{d}\psi + \int_{\theta_\mathrm{i}+\omega t_\mathrm{j}+2\pi n}^{\theta_\mathrm{i}+\omega t_\mathrm{j}+2\pi n+\omega\delta t} g(\psi;z_\mathrm{i})\mathrm{d}\psi\right] \tag{E.28}$$

$$= \frac{1}{2\pi n+\omega\delta t}\left[\sum_{k=1}^{n}\int_{\theta_\mathrm{i}+\omega t_\mathrm{j}+2\pi(k-1)}^{\theta_\mathrm{i}+\omega t_\mathrm{j}+2\pi k} g(\psi;z_\mathrm{i})\mathrm{d}\psi + \int_{\theta_\mathrm{i}+\omega t_\mathrm{j}+2\pi n}^{\theta_\mathrm{i}+\omega t_\mathrm{j}+2\pi n+\omega\delta t} g(\psi;z_\mathrm{i})\mathrm{d}\psi\right] \tag{E.29}$$

Note that Eqn. E.14 can be applied to the integral within the summation, since the difference in the upper and lower bounds is 2π. The $\theta_\mathrm{i}+\omega t_\mathrm{j}$ term, which is treated as a constant, can be thus eliminated from the summed integral. Likewise, the $2\pi n$ term can also be eliminated in the bounds for the second integral. The additional simplification results in the following,

$$\left\langle Q|_{\theta_\mathrm{i},z_\mathrm{i}}\right\rangle_\mathrm{t} = \frac{1}{2\pi n+\omega\delta t}\left[\sum_{k=1}^{n}\int_{2\pi(k-1)}^{2\pi k} g(\psi;z_\mathrm{i})\mathrm{d}\psi + \int_{\theta_\mathrm{i}+\omega t_\mathrm{j}}^{\theta_\mathrm{i}+\omega t_\mathrm{j}+\omega\delta t} g(\psi;z_\mathrm{i})\mathrm{d}\psi\right] \tag{E.30}$$

$$= \frac{n}{2\pi n+\omega\delta t}\int_0^{2\pi} g(\psi;z_\mathrm{i})\mathrm{d}\psi + \frac{1}{2\pi n+\omega\delta t}\int_{\theta_\mathrm{i}+\omega t_\mathrm{j}}^{\theta_\mathrm{i}+\omega t_\mathrm{j}+\omega\delta t} g(\psi;z_\mathrm{i})\mathrm{d}\psi \tag{E.31}$$

From this equation, it can be seen that this time-average not only depends on where in the detonation cycle the measurement began, as given by ωt_j, but also where in the detonation cycle the measurement ended, as given by $\omega t_\mathrm{j}+\omega\delta t$.

It is desirable to express Eqn. E.31 in a more compact form and evaluate the potential error introduced by integrating over a non-integer multiple of the period. To do this, the quantity α is introduced as the ratio between the two integrals in Eqn. E.31 as follows,

$$\alpha(\delta t;t_\mathrm{j}) = \frac{\displaystyle\int_{\theta_\mathrm{i}+\omega t_\mathrm{j}}^{\theta_\mathrm{i}+\omega t_\mathrm{j}+\omega\delta t} g(\psi;z_\mathrm{i})\mathrm{d}\psi}{\displaystyle\int_0^{2\pi} g(\psi;z_\mathrm{i})\mathrm{d}\psi} \tag{E.32}$$

For the properties considered in this work (e.g., pressure, temperature, etc.), $g(\psi)>0$ for all values of ψ. Thus, α has to be strictly positive and cannot be larger than one.

$$0 \le \alpha(\delta t;t_\mathrm{j}) \le 1 \tag{E.33}$$

Using α, Eqn. E.31 can be manipulated in the following manner,

$$\left\langle Q|_{\theta_i,z_i}\right\rangle_t = \frac{n}{2\pi n+\omega\delta t}\int_0^{2\pi} g(\psi;z_i)\mathrm{d}\psi + \frac{\alpha(\delta t;t_j)}{2\pi n+\omega\delta t}\int_0^{2\pi} g(\psi;z_i)\mathrm{d}\psi \tag{E.34}$$

$$= \left(\frac{n+\alpha(\delta t;t_j)}{n+\frac{\omega\delta t}{2\pi}}\right)\left(\frac{1}{2\pi}\int_0^{2\pi} g(\psi;z_i)\mathrm{d}\psi\right) \tag{E.35}$$

Other than the additional term in the first set of parentheses, Eqn. E.35 looks identical to that of the area-average as given by Eqn. E.16. Due to not integrating over an exact integer number of periods, an error (ϵ) is going to be introduced relative to the area-average. This is given by,

$$\epsilon = \left|\left\langle Q|_{\theta_i,z_i}\right\rangle_t - \left\langle Q|_{t_i,z_i}\right\rangle_A\right| \tag{E.36}$$

$$= \left|\frac{n+\alpha(\delta t;t_j)}{n+\frac{\omega\delta t}{2\pi}} - 1\right|\left\langle Q|_{t_i,z_i}\right\rangle_A \tag{E.37}$$

While there is no direct means to evaluate the error, as that would require knowing the shape of $g(\psi)$, the worst case scenario can be taken to find the rate of convergence. The worst-case scenario is $\alpha = 1$ when $\delta t = 0$. This gives the rate of convergence as,

$$\epsilon = \left|\frac{n+1}{n} - 1\right|\left\langle Q|_{t_i,z_i}\right\rangle_A \tag{E.38}$$

$$= \left|\frac{1}{n}\right|\left\langle Q|_{t_i,z_i}\right\rangle_A \tag{E.39}$$

This provides the maximum difference between averaging Q over an arbitrary period of time at a single point ($\left\langle Q|_{\theta_i,z_i}\right\rangle_t$) and averaging Q over the area at a single instance of time ($\left\langle Q|_{t_i,z_i}\right\rangle_A$). If $\mathfrak{T} \gg \tau$ such that $n \gg 1$, the error will converge to zero. Thus, the following approximation can be made for a sufficiently long integration time scale,

$$\epsilon \approx 0 \tag{E.40}$$

$$\left\langle Q|_{t_i,z_i}\right\rangle_A \approx \left\langle Q|_{\theta_i,z_i}\right\rangle_t \tag{E.41}$$

From this analysis, the time-averaged and area-averaged quantities can be equated for a single mode of operation as long as the angular velocity is constant, and the time-integration is over a single period or many periods.

E.2.2 Multiple Modes

Thus far, we have limited our discussion to a single wave system (mode) that rotates about a single constant period. An extension can be made for when multiple wave systems (modes) exist simultaneously in the RDC. This has practical applications since secondary waves and/or counter-rotating detonation waves are common occurrences in RDCs [209, 45, 210, 211].

The quantity, Q, can still be described by the general spatiotemporal function, f, given by Eqn. E.1. That being said, unlike the previous section, f cannot be cast in terms of a single phase variable (i.e., ψ) since the flowfield would also depend on the relative position of the multiple wave modes at any given instance in time. Instead, Q depends on the relative positioning of all the modes simultaneously. For instance, assuming that there are two independent wave systems propagating continuously in the RDC, the phase variables that describe their propagation are given by the following,

$$\psi = \theta + \omega_1 t \tag{E.42}$$

$$\phi = \theta + \omega_2 t + \delta\theta \tag{E.43}$$

where ω_1 and ω_2 represent the rotational speed of the two different wave systems. The additional $\delta\theta$ term is added to allow for the different waves to be spaced apart by an arbitrary amount at $t = 0$ (i.e., it represents the phase delay between the two wave systems). Although this process can be done for any number of modes, the demonstration provided in this work will focus on two modes for simplicity. It is again assumed that both ω_1 and ω_2 are constant, similar to Eqn. E.8. The periods for the two wave systems are τ_1 and τ_2 for ψ and ϕ respectively.

An assumption is required about the interaction between the different modes. In the interest of proving the equality in Eqn. E.3, it is assumed that the wave systems are *linearly* superimposed upon one another. That is to say, the waves do not non-linearly interact and the overall flowfield can be described by,

$$f(\theta, z, t) = g(\psi, z) + h(\phi, z) \tag{E.44}$$

As we will discuss further below, this is an approximation that is in general not true, but it is necessary to provide a convenient solution to the problem. However, this assumption does not preclude us from drawing conclusions from the results presented next which also informs us of the properties of averaging when non-linear wave interactions are present.

E.2.2.1 Area-Average

To process to evaluate the area-averaging procedure begins by directly combining Equations E.5 and E.44. A separation of the functions g and h is performed using the additive property of definite

integrals. After the separation, a change of variables for each integral is done to get the integrals in terms of the phase variables. These steps are expressed in the following equations,

$$\left\langle Q|_{t_\mathrm{i},z_\mathrm{i}}\right\rangle_\mathrm{A} = \frac{1}{2\pi}\int_{\theta=0}^{\theta=2\pi}\left[g(\psi;z_\mathrm{i})+h(\phi;z_\mathrm{i})\right]\mathrm{d}\theta \tag{E.45}$$

$$= \frac{1}{2\pi}\left[\int_{\theta=0}^{\theta=2\pi} g(\psi;z_\mathrm{i})\mathrm{d}\theta + \int_{\theta=0}^{\theta=2\pi} h(\phi;z_\mathrm{i})\mathrm{d}\theta\right] \tag{E.46}$$

$$= \frac{1}{2\pi}\left[\int_{\psi(\theta=0,t=t_\mathrm{i})}^{\psi(\theta=2\pi,t=t_\mathrm{i})} g(\psi;z_\mathrm{i})\mathrm{d}\psi + \int_{\phi(\theta=0,t=t_\mathrm{i})}^{\phi(\theta=2\pi,t=t_\mathrm{i})} h(\phi;z_\mathrm{i})\mathrm{d}\phi\right] \tag{E.47}$$

The need for the linear superposition is immediately evident in allowing for the phase variables to be separated in the manner described above. Following the defintion of Eqn. E.43, the bounds of integration for ϕ are evaluated to be,

$$\phi(\theta=0,t=t_\mathrm{i}) = \omega_2 t_\mathrm{i} + \delta\theta \tag{E.48}$$

$$\phi(\theta=2\pi,t=t_\mathrm{i}) = 2\pi + \omega_2 t_\mathrm{i} + \delta\theta \tag{E.49}$$

where $\omega_2 t_\mathrm{i}$ and $\delta\theta$ can both be treated as constants. Meanwhile, the bounds of integration for ψ remain Eqns. E.12 and E.13.

Both phase variables, ψ and ϕ, are periodic between values of 0 and 2π by construction. Thus, the property of periodic functions (Eqn. E.14) can be applied to both integrals in Eqn. E.47 like what was done for the single-mode operation in the previous section. This gives the following final simplification,

$$\left\langle Q|_{t_\mathrm{i},z_\mathrm{i}}\right\rangle_\mathrm{A} = \frac{1}{2\pi}\left[\int_0^{2\pi} g(\psi;z_\mathrm{i})\mathrm{d}\psi + \int_0^{2\pi} h(\phi;z_\mathrm{i})\mathrm{d}\phi\right] \tag{E.50}$$

Note how the above equation is very similar to the result of area-averaging for the single mode given in Eqn. E.16. This is a direct result of the linear superposition assumption.

E.2.2.2 Time-Average over One Period

A similar process of separating the phase variables in the time-average integral before applying the change of variables is possible. First, the time-averaging process is applied over the period of the first mode, τ_1, which is associated with the ψ variable. The time average quantity then becomes:

$$\left\langle Q|_{\theta_\mathrm{i},z_\mathrm{i}}\right\rangle_\tau = \left(\int_{\psi(\theta=\theta_\mathrm{i},t=t_\mathrm{j})}^{\psi(\theta=\theta_\mathrm{i},t=t_\mathrm{j}+\tau_1)} \frac{1}{\omega_1}\mathrm{d}\psi\right)^{-1}\left[\int_{\psi(\theta=\theta_\mathrm{i},t=t_\mathrm{j})}^{\psi(\theta=\theta_\mathrm{i},t=t_\mathrm{j}+\tau_1)} \frac{g(\psi;z_\mathrm{i})}{\omega_1}\mathrm{d}\psi + \int_{\phi(\theta=\theta_\mathrm{i},t=t_\mathrm{j})}^{\phi(\theta=\theta_\mathrm{i},t=t_\mathrm{j}+\tau_1)} \frac{h(\phi;z_\mathrm{i})}{\omega_2}\mathrm{d}\phi\right] \tag{E.51}$$

The bounds of integration for ϕ are evaluated to be,

$$\phi(\theta = \theta_\mathrm{i}, t = t_\mathrm{j}) = \theta_\mathrm{i} + \omega_2 t_\mathrm{j} + \delta\theta \tag{E.52}$$

$$\phi(\theta = \theta_\mathrm{i}, t = t_\mathrm{j} + \tau_1) = \theta_\mathrm{i} + \omega_2 (t_\mathrm{j} + \tau_1) + \delta\theta \tag{E.53}$$

where $\omega_2 t_\mathrm{j}$ and $\delta\theta$ can both be treated as constants. Meanwhile, the bounds of integration for ψ remain Eqns. E.19 and E.20. Recall that $\omega_1 \tau_1 = 2\pi$ and is the period of the periodic function g. Equation E.51 can then be manipulated in the following way,

$$\left\langle Q|_{\theta_\mathrm{i}, z_\mathrm{i}} \right\rangle_\tau = \left(\int_{\theta_\mathrm{i}+\omega_1 t_\mathrm{j}}^{\theta_\mathrm{i}+\omega_1(t_\mathrm{j}+\tau_1)} \mathrm{d}\psi \right)^{-1} \left[\int_{\theta_\mathrm{i}+\omega_1 t_\mathrm{j}}^{\theta_\mathrm{i}+\omega_1(t_\mathrm{j}+\tau_1)} g(\psi; z_\mathrm{i}) \mathrm{d}\psi + \frac{\omega_1}{\omega_2} \int_{\theta_\mathrm{i}+\omega_2 t_\mathrm{j}+\delta\theta}^{\theta_\mathrm{i}+\omega_2(t_\mathrm{j}+\tau_1)+\delta\theta} h(\phi; z_\mathrm{i}) \mathrm{d}\phi \right] \tag{E.54}$$

$$= \frac{1}{\omega_1 \tau_1} \left[\int_0^{\omega_1 \tau_1} g(\psi; z_\mathrm{i}) \mathrm{d}\psi + \frac{\omega_1}{\omega_2} \int_{\theta_\mathrm{i}+\omega_2 t_\mathrm{j}+\delta\theta}^{\theta_\mathrm{i}+\omega_2(t_\mathrm{j}+\tau_1)+\delta\theta} h(\phi; z_\mathrm{i}) \mathrm{d}\phi \right] \tag{E.55}$$

$$= \frac{1}{2\pi} \int_0^{2\pi} g(\psi; z_\mathrm{i}) \mathrm{d}\psi + \frac{1}{\omega_2 \tau_1} \int_{\theta_\mathrm{i}+\omega_2 t_\mathrm{j}+\delta\theta}^{\theta_\mathrm{i}+\omega_2(t_\mathrm{j}+\tau_1)+\delta\theta} h(\phi; z_\mathrm{i}) \mathrm{d}\phi \tag{E.56}$$

The second integral cannot be simplified further as $\omega_2 \tau_1$ does not necessarily equal an integer multiple 2π. A similar result would arise if the time-averaging was performed over τ_2 instead of τ_1. Since Eqn. E.56 does not match Eqn. E.50, it cannot be said that time-averaging over the period of one of the wave systems is equivalent to the area-averaging over an instance in time. In the context of RDCs, if either a secondary wave system or counter-propagating detonation wave(s) exists, averaging a time-resolved measurement over the detonation period is not the same as an area-integrated or area-averaged measurement. This is true for the case where modes are linearly superimposed upon one another, as well as non-linearly superimposed.

E.2.2.3 Convergence of Time-Average

Similar to what was done in Section E.2.1.3 for the single mode, the averaging procedure is now performed over an arbitrary time ($\mathfrak{T}$). Expressing this time relative to the two relevant periods gives,

$$\mathfrak{T} = n\tau_1 + \delta t_1 \tag{E.57}$$

$$= m\tau_2 + \delta t_2 \tag{E.58}$$

where $n, m \in \mathbb{Z}$ and the δt terms are again the remainders. Changing the bounds of Eqn. E.51 to reflect the new integration length and performing some simplifications results in the following,

$$\left\langle Q|_{\theta_i,z_i}\right\rangle_t = \frac{1}{\omega_1\mathfrak{T}}\int_{\psi(\theta=\theta_i,t=t_j)}^{\psi(\theta=\theta_i,t=t_j+\mathfrak{T})} g(\psi;z_i)\mathrm{d}\psi + \frac{1}{\omega_2\mathfrak{T}}\int_{\phi(\theta=\theta_i,t=t_j)}^{\phi(\theta=\theta_i,t=t_j+\mathfrak{T})} h(\phi;z_i)\mathrm{d}\phi \tag{E.59}$$

The integration bounds for ψ are the same as seen in Eqns. E.26 and E.27. Meanwhile, the integration bounds for ϕ are evaluated as,

$$\phi(\theta=\theta_i, t=t_j) = \theta_i + \omega_2 t_j + \delta\theta \tag{E.60}$$

$$\phi(\theta=\theta_i, t=t_j+\mathfrak{T}) = \theta_i + \omega_2(t_j + m\tau_2 + \delta t_2) + \delta\theta \tag{E.61}$$

Again, θ_i, $\omega_2 t_j$, and $\delta\theta$ can all be treated as constants within the bounds. The same process as elaborated in the single mode analysis is applied; the definite integrals are broken apart using the additive property and the property of periodic functions is utilized. Doing so will result in a summation of both g and h over their periods with the remainder of the integration time being left as a separate integral (see Eqn. E.31). After manipulation, the final equation is given as,

$$\begin{aligned}\left\langle Q|_{\theta_i,z_i}\right\rangle_t =& \frac{n}{2\pi n+\omega_1\delta t_1}\int_0^{2\pi} g(\psi;z_i)\mathrm{d}\psi + \frac{1}{2\pi n+\omega_1\delta t_1}\int_{\theta_i+t_j+2\pi n}^{\theta_i+t_j+2\pi n+\delta t_1} g(\psi;z_i)\mathrm{d}\psi \\ &+ \frac{m}{2\pi m+\omega_2\delta t_2}\int_0^{2\pi} h(\phi;z_i)\mathrm{d}\phi + \frac{1}{2\pi m+\omega_2\delta t_2}\int_{\theta_i+t_j+2\pi m}^{\theta_i+t_j+2\pi m+\delta t_2} h(\phi;z_i)\mathrm{d}\phi\end{aligned} \tag{E.62}$$

If both δt_1 and δt_2 are set to be zero in the above equation, it can be reduced into the following form.

$$\left\langle Q|_{\theta_i,z_i}\right\rangle_t = \frac{1}{2\pi}\left[\int_0^{2\pi} g(\psi;z_i)\mathrm{d}\psi + \int_0^{2\pi} h(\phi;z_i)\mathrm{d}\phi\right] \tag{E.63}$$

This is the same result from the area-averaging as seen in Eqn. E.50. From this, it can be seen that a super-period, τ^*, can be defined such that the time-average and area-average are equivalent. This super-period is defined as the least common multiple (lcm) of the two periods since both n and m are integers ($n, m \in \mathbb{Z}$).

$$\tau^* = \mathrm{lcm}(\tau_1, \tau_2) \tag{E.64}$$

In other words, τ^* satisfies the condition with the smallest values of n and m possible.

$$\tau^* = n\tau_1 = m\tau_2 \tag{E.65}$$

While useful, the averaging procedure may not always be an integer multiple of the super-period.

It is therefore useful to reduce the number of integrals in a manner similar to what was done in Section E.2.1.3. As such the following quantities indicating the fraction of the integration length with respect to the period are used to simplify Eqn. E.62:

$$\alpha(\delta t_1; t_\mathrm{j}) = \frac{\displaystyle\int_{\theta_\mathrm{i}+\omega_1 t_\mathrm{j}}^{\theta_\mathrm{i}+\omega_1 t_\mathrm{j}+\omega_1\delta t} g(\psi; z_\mathrm{i})\mathrm{d}\psi}{\displaystyle\int_0^{2\pi} g(\psi; z_\mathrm{i})\mathrm{d}\psi} \tag{E.66}$$

$$\beta(\delta t_2; t_\mathrm{j}) = \frac{\displaystyle\int_{\theta_\mathrm{i}+\omega_2 t_\mathrm{j}+\delta\theta}^{\theta_\mathrm{i}+\omega_2 t_\mathrm{j}+\delta\theta+\omega_2\delta t} h(\phi; z_\mathrm{i})\mathrm{d}\phi}{\displaystyle\int_0^{2\pi} h(\phi; z_\mathrm{i})\mathrm{d}\phi} \tag{E.67}$$

Using these definitions, Eqn. E.62 can be re-written as,

$$\left\langle Q|_{\theta_\mathrm{i},z_\mathrm{i}}\right\rangle_\mathrm{t} = \frac{n+\alpha(\delta t_1; t_\mathrm{j})}{2\pi n+\omega_1\delta t_1}\int_0^{2\pi} g(\psi; z_\mathrm{i})\mathrm{d}\psi + \frac{m+\beta(\delta t_2; t_\mathrm{j})}{2\pi m+\omega_2\delta_2}\int_0^{2\pi} h(\phi; z_\mathrm{i})\mathrm{d}\phi \tag{E.68}$$

$$= \left(\frac{n+\alpha(\delta t_1; t_\mathrm{j}}{n+\frac{\omega_1\delta t_1}{2\pi}}\right)\left(\frac{1}{2\pi}\int_0^{2\pi} g(\psi; z_\mathrm{i})\mathrm{d}\psi\right) + \left(\frac{m+\beta(\delta t_2; t_\mathrm{j})}{m+\frac{\omega_2\delta t_2}{2\pi}}\right)\left(\frac{1}{2\pi}\int_0^{2\pi} h(\phi; z_\mathrm{i})\mathrm{d}\phi\right) \tag{E.69}$$

Using the result of the area-averaging procedure discussed previously (Eqn. E.50), the difference between the time-averaged and area-averaged serves as the error that is committed in approximating the two averaged values as being equivalent. Thus, the error is defined as:

$$\epsilon = \left|\left\langle Q|_{\theta_\mathrm{i},z_\mathrm{i}}\right\rangle_\mathrm{t} - \left\langle Q|_{t_\mathrm{i},z_\mathrm{i}}\right\rangle_\mathrm{A}\right| \tag{E.70}$$

$$= \left|\left(\frac{\alpha(\delta t_1; t_\mathrm{j}) - \frac{\omega_1\delta t_1}{2\pi}}{n+\frac{\omega_1\delta t_1}{2\pi}}\right)\left(\frac{1}{2\pi}\int_0^{2\pi} g(\psi; z_\mathrm{i})\mathrm{d}\psi\right) + \left(\frac{\beta(\delta t_2; t_\mathrm{j}) - \frac{\omega_2\delta t_2}{2\pi}}{m+\frac{\omega_2\delta t_2}{2\pi}}\right)\left(\frac{1}{2\pi}\int_0^{2\pi} h(\phi; z_\mathrm{i})\mathrm{d}\phi\right)\right| \tag{E.71}$$

Like with the single mode, the worst possible disagreement between the time-average and area-average can be found by taking the limit as $\delta t_1 \to 0, \delta t_2 \to 0$ and enforcing that $\alpha \to 1, \beta \to 1$. In such a limit, the error becomes,

$$\epsilon = \left|\frac{1}{n}\frac{1}{2\pi}\int_0^{2\pi} g(\psi; z_\mathrm{i})\mathrm{d}\psi + \frac{1}{m}\frac{1}{2\pi}\int_0^{2\pi} h(\phi; z_\mathrm{i})\mathrm{d}\phi\right| \tag{E.72}$$

Unsurprisingly, each term convergences by one over the number of periods within the averaging window. This matches what was found for the single mode. Consider the case of two wave

systems that propagate at the same speed but in the opposite direction to one another; the so-called "slapping" or "clapping" mode of operation [13]. By moving at the same speed, $n = m$ which causes Eqn. E.72 to reduce to the result from the single mode analysis (Eqn. E.39). Outside of this specific situation, if $\mathfrak{T} \gg \tau_1, \tau_2$ such that $n, m \gg 1$, the error will converge to zero. Thus, the time-average and area-average can be equated under the assumption of the linear superposition of the different modes.

The conclusions for the two-mode operation presented here can be readily extended to scenarios with more than two wave systems. If the overall flowfield remains subject to the linear superposition assumption, Eqn. E.44 can describe any number of modes with an equivalent amount of phase variables. A super-period can be defined regardless of the number of wave modes and if the time-average is over that super-period, the result would match the area-averaged. Likewise, the error between the area-averaged and time-average over an arbitrary time (Eqn. E.72) would be the summation of the integrals of the functional representation of the wave systems (g, h, ...) scaled by the inverse in the number of periods associated with each wave system ($1/n$, $1/m$, ...).

E.3 Discussion

The validity of the assumptions made throughout this work warrants further discussion. One of the key assumptions was neglecting any variations in the wavespeed. The detonation wave(s) can continuously propagate in a stable manner while simultaneously having varying wave speeds [212]. Likewise, modal transitions can occur during experimentation in which the wavespeed can oscillate before the transition [213]. Even during stable operation, there exists some cycle-to-cycle variability in the measured detonation wavespeed (for example, [214, 215]. The analysis presented here best applies when the averaging occurs when the wave multiplicity remains the same, as the unsteady nature of modal transitions and step-changes in velocity from a change in multiplicity invalidates the demonstrated equality (Eqn. E.3). As for the cases when the multiplicity remains constant but the waves change speed, as long as the distribution of wavespeeds are normally distributed about a mean, all the methods will converge if the time-average is taken over a period much longer than the time over which changes in wavespeed occurs.

Another implicit assumption that was made is that the time-average at any point does not depend on the circumferential location of that measurement point (Eqns. E.6 and E.71). Codoni et al. provided evidence that this is incorrect [120]. CTAP measurements taken at the same axial location but different circumferential locations revealed that there is a non-uniformity in the "average" static pressure about the annulus. Thus, while a single measurement point may be able to resolve the full spatial variations caused solely by the detonation wave in an idealistic system, any additional spatial variations caused by misaligned geometry, upstream components, etc., limit the usefulness

of a single measurement point. Currently, there is no means of knowing a priori if such additional spatial variations exist; taking measurements in experiments at different circumferential locations is required to address this. In the case of disagreements in the time-averaged quantities, quantities then have to be averaged over the area to be more consistent with the EAP metric [120].

Finally, in regards to the multiple modes analysis, it has been established in the literature that counter-propagating detonation/secondary wave systems non-linearly interact when the waves are co-located in space [211, 45]. For example, the peak pressure at the local interaction is larger than the summation of the peak pressures of the individual waves. The non-linear interactions then lead to the area-average quantities varying in time since the average would depend on the relative positions of the wave systems. This contrasts the results presented in this work where the area-averaged is invariant with time. At the time of writing a link between non-linear interactions and performance metrics at the outlet has yet to be established. Furthermore, there has yet to be a demonstration that the local intersection of downstream propagating oblique shocks results in non-linear interactions at the exit throat. Such interactions are theorized to exist and thus, they would result in time-variation of thrust and subsequently EAP produced by RDCs even if the speeds of the wave systems are constant. That being said, since the experimental EAP is oftentimes averaged over time windows that are significantly larger than the period of interactions, it is likely that the effects of the non-linear interaction on the steady state value are mitigated.

APPENDIX F

Sensor Positions for Base Drag Correction

This appendix contains a detailed description of the different pressure measurements used to measure the base drag of the RDC. The sensor name, radial position (r), circumferential location (θ), and pressure sensor range are provided in Table F.1.

Sensor Position	r [cm]	θ [°]	Sensor Range [atm]
p_{cb} 1	0	-	2.04
p_{cb} 2	0.386	0	13.6
p_{cb} 3	0.770	120	13.6
p_{cb} 4	1.16	240	13.6
p_{cb} 5	1.54	0	13.6
p_{cb} 6	1.93	120	13.6
p_{cb} 7	2.31	240	13.6
p_{cb} 8	2.70	0	13.6
p_{cb} 9	3.08	120	2.04
p_{cb} 10	3.47	240	2.04
p_{cb} 11	3.85	0	2.04
p_{cb} 12	4.24	120	2.04
p_{cb} 13	4.62	240	2.04
p_{cb} 14	5.00	0	2.04
p_{cb} 15	5.39	120	2.04
p_{cb} 16	5.78	240	2.04
p_{cb} 17	6.16	0	2.04
p_{fl} 1	7.82	-5	2.04
p_{fl} 2	7.82	5	2.04
p_{fl} 3	7.82	115	2.04
p_{fl} 4	7.82	125	2.04
p_{fl} 5	7.82	235	2.04
p_{fl} 6	7.82	245	2.04

Table F.1: Position and sensor range for CTAP measurements taken for base drag correction.

APPENDIX G

Pressure Gain Uncertainty Sensitivity Coefficients

As a part of the sensitivity analysis of the PG measurement, the partial derivatives of pressure gain with respect to the other variables are required. These partial derivatives are the sensitivity coefficients in the uncertainty propagation equations; they determine the impact of the individual variable's uncertainty on the overall PG uncertainty. Presented in this appendix are the partial derivatives of Eqn. 5.10 and an order of magnitude analysis to provide a sense of scale. The equations for the EAP and PG are repeated here for simplicity. Recall that the equation for the EAP for any Mach number is as follows:

$$\mathrm{EAP}(M_{8,\mathrm{z}}) = \widetilde{p}_8 \left(1 + \frac{\gamma_8 - 1}{2} M_{8,\mathrm{z}}^2\right)^{\frac{\gamma_8}{\gamma_8 - 1}} \tag{G.1}$$

$$= \left(\frac{F_\mathrm{G}}{A_8} + p_\infty\right) \frac{\left(1 + \frac{\gamma_8 - 1}{2} M_{8,\mathrm{z}}^2\right)^{\frac{\gamma_8}{\gamma_8 - 1}}}{\left(1 + \gamma M_{8,\mathrm{z}}^2\right)} \tag{G.2}$$

From which a modified pressure gain that includes a non-unity $M_{8,\mathrm{z}}$ can then be defined according to:

$$\mathrm{PG_M} = \frac{\mathrm{EAP}(M_{8,\mathrm{z}})}{p_3} - 1 \tag{G.3}$$

The random uncertainty is given as the following

$$\delta\mathrm{PG}^2 = \left(\frac{\partial \mathrm{PG}}{\partial F_\mathrm{G}} \delta F_\mathrm{G}\right)^2 + \left(\frac{\partial \mathrm{PG}}{\partial p_\infty} \delta p_\infty\right)^2 + \left(\frac{\partial \mathrm{PG}}{\partial p_3} \delta p_3\right)^2 \tag{G.4}$$

Additionally, the systematic uncertainty in PG is given as follows:

$$\delta\mathrm{PG_{sys}} = \pm \frac{\partial \mathrm{PG}}{\partial A_8} \delta A_8 \pm \frac{\partial \mathrm{PG}}{\partial \gamma_8} \delta\gamma_8 \pm \frac{\partial \mathrm{PG}}{\partial M_{8,\mathrm{z}}} \delta M_{8,\mathrm{z}} \tag{G.5}$$

Note, that in this formulation, the Mach number is treated as an independent variable that is measurable. If instead the choked assumption is invoked, the partial derivative of PG with respect

to the Mach number should be moved from the random uncertainty equation to the systematic uncertainty equation. In addition, since the Mach number is then treated as a constant, its derivative with respect to any other variable would then be zero. The systematic error can be then approximated as (see the main text body):

$$\frac{\partial \mathrm{PG}}{\partial M_{8,\mathrm{z}}}\delta M_{8,\mathrm{z}} = \frac{\partial \mathrm{PG}}{\partial \mathrm{EAP}}\frac{\partial \mathrm{EAP}}{\partial M_{8,\mathrm{z}}}\delta M_{8,\mathrm{z}} \approx \frac{1}{p_3}(\epsilon_{\mathrm{M}}\mathrm{EAP}) = \epsilon_{\mathrm{M}}(\mathrm{PG}+1) \tag{G.6}$$

$$\mathrm{PG}+1 = O\left(10^{0}\right) \tag{G.7}$$

The remaining partial derivatives are:

$$\frac{\partial \mathrm{PG}}{\partial p_3} = -\frac{\widetilde{p}_{\mathrm{t}8}}{p_3^2} \tag{G.8}$$

$$= \frac{\mathrm{PG}+1}{p_3} \tag{G.9}$$

$$= O\left(10^{-5}\right)\mathrm{Pa}^{-1} \tag{G.10}$$

$$\frac{\partial \mathrm{PG}}{\partial F_{\mathrm{G}}} = \frac{\left(1+\frac{\gamma_8-1}{2}M_{8,\mathrm{z}}^2\right)^{\frac{\gamma_8}{\gamma_8-1}}}{A_8 p_3(1+\gamma_8 M_{8,\mathrm{z}}^2)} + \frac{\partial \mathrm{PG}}{\partial M_{8,\mathrm{z}}}\frac{\partial M_{8,\mathrm{z}}}{\partial F_{\mathrm{G}}} \tag{G.11}$$

$$= \frac{1}{F_{\mathrm{G}}}\left[\mathrm{PG}+1-\frac{p_\infty}{p_3(1+\gamma_8 M_{8,\mathrm{z}}^2)}\left(1+\frac{\gamma_8-1}{2}M_{8,\mathrm{z}}^2\right)^{\frac{\gamma_8}{\gamma_8-1}}\right] + \frac{\partial \mathrm{PG}}{\partial M_{8,\mathrm{z}}}\frac{\partial M_{8,\mathrm{z}}}{\partial F_{\mathrm{G}}} \tag{G.12}$$

$$= O\left(10^{-3}\right)\mathrm{N}^{-1} + \frac{\partial \mathrm{PG}}{\partial M_{8,\mathrm{z}}}\frac{\partial M_{8,\mathrm{z}}}{\partial F_{\mathrm{G}}} \tag{G.13}$$

$$\frac{\partial \mathrm{PG}}{\partial p_\infty} = \frac{\left(1+\frac{\gamma_8-1}{2}M_{8,\mathrm{z}}^2\right)^{\frac{\gamma_8}{\gamma_8-1}}}{p_3(1+\gamma_8 M_{8,\mathrm{z}}^2)} + \frac{\partial \mathrm{PG}}{\partial M_{8,\mathrm{z}}}\frac{\partial M_{8,\mathrm{z}}}{\partial p_\infty} \tag{G.14}$$

$$= \frac{1}{p_\infty}\left[\mathrm{PG}+1-\frac{F_{\mathrm{G}}}{A_8 p_3(1+\gamma_8 M_{8,\mathrm{z}}^2)}\left(1+\frac{\gamma_8-1}{2}M_{8,\mathrm{z}}^2\right)^{\frac{\gamma_8}{\gamma_8-1}}\right] + \frac{\partial \mathrm{PG}}{\partial M_{8,\mathrm{z}}}\frac{\partial M_{8,\mathrm{z}}}{\partial p_\infty} \tag{G.15}$$

$$= O\left(10^{-6}\right)\mathrm{Pa}^{-1} + \frac{\partial \mathrm{PG}}{\partial M_{8,\mathrm{z}}}\frac{\partial M_{8,\mathrm{z}}}{\partial p_\infty} \tag{G.16}$$

$$\frac{\partial \mathrm{PG}}{\partial A_8} = -\frac{F_\mathrm{G}(1+\frac{\gamma_8-1}{2}M_{8,\mathrm{z}}^2)^{\frac{\gamma_8}{\gamma_8-1}}}{A_8^2 p_3(1+\gamma_8 M_{8,\mathrm{z}}^2)} + \frac{\partial \mathrm{PG}}{\partial M_{8,\mathrm{z}}}\frac{\partial M_{8,\mathrm{z}}}{\partial A_8} \tag{G.17}$$

$$= \frac{1}{A_8}\left[\frac{p_\infty}{p_3(1+\gamma_8 M_{8,\mathrm{z}}^2)}\left(1+\frac{\gamma_8-1}{2}M_{8,\mathrm{z}}^2\right)^{\frac{\gamma_8}{\gamma_8-1}} - \mathrm{PG} - 1\right] + \frac{\partial \mathrm{PG}}{\partial M_{8,\mathrm{z}}}\frac{\partial M_{8,\mathrm{z}}}{\partial A_8} \tag{G.18}$$

$$= \mathcal{O}\left(10^2\right)\mathrm{m}^{-2} + \frac{\partial \mathrm{PG}}{\partial M_{8,\mathrm{z}}}\frac{\partial M_{8,\mathrm{z}}}{\partial A_8} \tag{G.19}$$

$$\frac{\partial \mathrm{PG}}{\partial \gamma_8} = \frac{(F_\mathrm{G}/A_8 + p_\infty)\left(1+\frac{\gamma_8-1}{2}M_{8,\mathrm{z}}^2\right)^{\frac{\gamma_8}{\gamma_8-1}}}{p_3(1+\gamma_8 M_{8,\mathrm{z}}^2)}\left[\frac{\gamma_8 M_{8,\mathrm{z}}^2}{2(\gamma_8-1)(1+\frac{\gamma-1}{2}M_{8,\mathrm{z}}^2)} - \frac{M_{8,\mathrm{z}}^2}{1+\gamma_8 M_{8,\mathrm{z}}^2}\right. \tag{G.20}$$

$$\left. + \left(\frac{1}{\gamma_8-1} - \frac{\gamma_8}{(\gamma_8-1)^2}\right)\ln\left(1+\frac{\gamma_8-1}{2}M_{8,\mathrm{z}}^2\right)\right] + \frac{\partial \mathrm{PG}}{\partial M_{8,\mathrm{z}}}\frac{\partial M_{8,\mathrm{z}}}{\partial \gamma_8}$$

$$= (\mathrm{PG}+1)\left[\frac{\gamma_8 M_{8,\mathrm{z}}^2}{2(\gamma_8-1)(1+\frac{\gamma-1}{2}M_{8,\mathrm{z}}^2)} - \frac{M_{8,\mathrm{z}}^2}{1+\gamma_8 M_{8,\mathrm{z}}^2}\right. \tag{G.21}$$

$$\left. + \left(\frac{1}{\gamma_8-1} - \frac{\gamma_8}{(\gamma_8-1)^2}\right)\ln\left(1+\frac{\gamma_8-1}{2}M_{8,\mathrm{z}}^2\right)\right] + \frac{\partial \mathrm{PG}}{\partial M_{8,\mathrm{z}}}\frac{\partial M_{8,\mathrm{z}}}{\partial \gamma_8}$$

$$= \mathcal{O}\left(10^{-1}\right) + \frac{\partial \mathrm{PG}}{\partial M_{8,\mathrm{z}}}\frac{\partial M_{8,\mathrm{z}}}{\partial \gamma_8} \tag{G.22}$$

$$\frac{\partial \mathrm{PG}}{\partial M_{8,\mathrm{z}}} = \frac{(F_\mathrm{G}/A_8 + p_\infty)\left(1+\frac{\gamma_8-1}{2}M_{8,\mathrm{z}}^2\right)^{\frac{\gamma_8}{\gamma_8-1}}}{p_3(1+\gamma_8 M_{8,\mathrm{z}}^2)}\left[\frac{M_{8,\mathrm{z}}\gamma_8(M_{8,\mathrm{z}}^2-1)}{\left(1+\frac{\gamma_8-1}{2}M_{8,\mathrm{z}}^2\right)\left(1+\gamma_8 M_{8,\mathrm{z}}^2\right)}\right] \tag{G.23}$$

$$= (\mathrm{PG}+1)\left[\frac{M_{8,\mathrm{z}}\gamma_8(M_{8,\mathrm{z}}^2-1)}{\left(1+\frac{\gamma_8-1}{2}M_{8,\mathrm{z}}^2\right)\left(1+\gamma_8 M_{8,\mathrm{z}}^2\right)}\right] \tag{G.24}$$

$$= \mathcal{O}\left(10^{-1}\right) \tag{G.25}$$

$$\frac{\partial \mathrm{PG}}{\partial p_8} = \frac{\partial \mathrm{PG}}{\partial M_{8,\mathrm{z}}}\frac{\partial M_{8,\mathrm{z}}}{\partial p_8} \tag{G.26}$$

BIBLIOGRAPHY

[1] Lijuan Liu and Qi Zhang. Numerical study of cellular structure in detonation of a stoichiometric mixture of vapor jp-10 in air using a quasi-detailed chemical kinetic model. *Aerospace Science and Technology*, 91:669–678, August 2019.

[2] Rafa l Porowski and Andrzej Teodorczyk. Cellular structure of detonation wave in hydrogen-methane-air mixtures. *Journal of Power Technologies*, 91(3):130–135, 2011.

[3] Qiaofeng Xie, Zifei Ji, Haocheng Wen, Zhaoxin Ren, Piotr Wolanski, and Bing Wang. Review on the rotating detonation engine and it's typical problems. *Transactions on Aerospace Research*, 2020(4):107–163, December 2020.

[4] E Wintenberger and John E Shepherd. Thermodynamic cycle analysis for propagating detonations. *Journal of propulsion and power*, 22(3):694–698, 2006.

[5] Richard Dyer and Thomas Kaemming. The thermodynamic basis of pulsed detonation engine thrust production. In *38th AIAA/ASME/SAE/ASEE Joint Propulsion Conference*. AIAA, July 2002.

[6] Kazuki Ishihara, Ken Matsuoka, Jiro Kasahara, Akiko Matsuo, and Ikkoh Funaki. Performance evaluation of a rotating detonation engine with conical-shape tail. In *53rd AIAA Aerospace Sciences Meeting*. Paper No. AIAA-2015-0630, January 2015.

[7] Joseph E Shepherd and J Kasahara. Analytical models for the thrust of a rotating detonation engine. *Technical Report FM2017.001*, 2017.

[8] T. Sato, F. Chacon, M. Gamba, and V. Raman. Mass flow rate effect on a rotating detonation combustor with an axial air injection. *Shock Waves*, 31(7):741–751, February 2021.

[9] Riley Huff, Marc D. Polanka, Michael J. McClearn, Frederick R. Schauer, Matthew L. Fotia, and John L. Hoke. Design and operation of a radial rotating detonation engine. *Journal of Propulsion and Power*, 35(6):1143–1150, November 2019.

[10] Fabian Chacon and Mirko Gamba. Study of parasitic combustion in an optically accessible continuous wave rotating detonation engine. In *AIAA Scitech 2019 Forum*. Paper No. 2019-0473, 2019.

[11] Alexander Feleo, Fabian Chacon, and Mirko Gamba. Effects of heat release distribution on detonation properties in a H2/air rotating detonation combustor from OH* chemiluminescence. In *AIAA Propulsion and Energy 2019 Forum*. Paper No. AIAA-2019-4045, 2019.

[12] Craig Nordeen, Douglas Schwer, Fredrick Schauer, John Hoke, Baki Cetegen, and Thomas Barber. Thermodynamic modeling of a rotating detonation engine. In *49th AIAA Aerospace Sciences Meeting including the New Horizons Forum and Aerospace Exposition*. Paper No. AIAA-2011-803, January 2011.

[13] Eric Bach, Panagiotis Stathopoulos, Christian Oliver Paschereit, and Myles D. Bohon. Performance analysis of a rotating detonation combustor based on stagnation pressure measurements. *Combustion and Flame*, 217:21–36, July 2020.

[14] Eric Bach, Bhavraj S Thethy, Daniel Edgington-Mitchell, Mohammad Rezay Haghdoost, Christian Oliver Paschereit, Panagiotis Stathopoulos, and Myles D Bohon. Kiel probes for stagnation pressure measurement in rotating detonation combustors. *AIAA Journal*, pages 1–12, June 2022.

[15] Stephen R. Turns. *Introduction to combustion*. McGraw-Hill Companies, third edition, 1996.

[16] Takuma Sato, Caleb Van Beck, and Venkat Raman. Numerical and boundary condition effects on the prediction of detonation engine behavior using detailed numerical simulations. *Frontiers in Aerospace Engineering*, 2:1123249, April 2023.

[17] Caleb Van Beck and Venkat Raman. Nox formation processes in rotating detonation engines. *Frontiers in Aerospace Engineering*, 3, 2024.

[18] Piotr Wolański. Detonative propulsion. *Proceedings of the combustion Institute*, 34(1):125–158, 2013.

[19] David Leonard Chapman. Vi. on the rate of explosion in gases. *The London, Edinburgh, and Dublin Philosophical Magazine and Journal of Science*, 47(284):90–104, 1899.

[20] Emile Jouguet. On the propagation of chemical reactions in gases. *J. de mathematiques Pures et Appliquees*, 1(347-425):2, 1905.

[21] Wildon Fickett and William C. Davis. *Detonation: Theory and Experiment*. Dover Books on Physics. Dover Publications, 2012.

[22] Irvin Glassman. *Combustion*. Elsevier, second edition, 1987.

[23] Sanford Gordon and Bonnie J McBride. Computer program for calculation of complex chemical equilibrium compositions and applications. Part 1: Analysis. *NASA RP 1311*, 1994.

[24] Yakov Borissovich Zeldovich. On the theory of the propagation of detonation in gaseous systems. *Zh. eksp. teoret. fiz.*, 10:542–568, 1940.

[25] John Von Neuman. Theory of detonation waves. Technical report, Institute for Advanced Study Princeton NJ, 1942.

[26] Werner Döring. Über den detonationsvorgang in gasen. *Annalen der Physik*, 435(6-7):421–436, 1943.

[27] John HS Lee. Dynamic parameters of gaseous detonations. *Annual review of fluid mechanics*, 16(1):311–336, 1984.

[28] Roger A Strehlow. Gas pase detonations: recent developments. *Combustion and Flame*, 12(2):81–101, 1968.

[29] Reta Knystautas, JH Lee, and CM Guirao. The critical tube diameter for detonation failure in hydrocarbon-air mixtures. *Combustion and Flame*, 48:63–83, 1982.

[30] Fedor A. Bykovskii, Sergey A. Zhdan, and Evgenii F. Vedernikov. Continuous spin detonations. *Journal of Propulsion and Power*, 22(6):1204–1216, 2006.

[31] Hisahiro Nakayama, Takahiro Moriya, Jiro Kasahara, Akiko Matsuo, Yuya Sasamoto, and Ikkoh Funaki. Stable detonation wave propagation in rectangular-cross-section curved channels. *Combustion and Flame*, 159(2):859–869, February 2012.

[32] Yuta Sugiyama, Yoshio Nakayama, Akiko Matsuo, Hisahiro Nakayama, and Jiro Kasahara. Numerical investigations on detonation propagation in a two-dimensional curved channel. *Combustion Science and Technology*, 186(10–11):1662–1679, September 2014.

[33] SIGMUND J Jacobs. The energy of detonation. *NAVORD report*, 4366:17, 1956.

[34] William H. Heiser and David T. Pratt. Thermodynamic cycle analysis of pulse detonation engines. *Journal of Propulsion and Power*, 18(1):68–76, January 2002.

[35] K. Kailasanath. Recent developments in the research on pulse detonation engines. *AIAA Journal*, 41(2):145–159, 2003.

[36] M. Sichel and J.C. Foster. The ground impulse generated by a plane fuel-air explosion with side relief. *Acta Astronautica*, 6(3-4):243–256, March 1979.

[37] Ya B Zeldovich. To the question of energy use of detonation combustion. *Journal of Propulsion and Power*, 22(3):588–592, 2006.

[38] Frank K. Lu and Eric M. Braun. Rotating detonation wave propulsion: Experimental challenges, modeling, and engine concepts. *Journal of Propulsion and Power*, 30(5):1125–1142, 2014.

[39] Gordon C. Oates. *Aerothermodynamics of Gas Turbine and Rocket Propulsion*. American Institute of Aeronautics and Astronautics, January 1997.

[40] H I H Saravanamuttoo, G F C Rogers, H Cohen, and Paul Straznicky. *Gas Turbine Theory*. Prentice Hall, Philadelphia, PA, 6 edition, September 2008.

[41] Ionio Q. Andrus, Paul King, Matthew Fotia, Frederick Schauer, and John Hoke. Experimental analogue of a pre-mixed rotating detonation engine in plane flow. In *53rd AIAA Aerospace Sciences Meeting*. Paper No. AIAA-2015-1105, jan 2015.

[42] Jian Sun, Jin Zhou, Shijie Liu, and Zhiyong Lin. Numerical investigation of a rotating detonation engine under premixed/non-premixed conditions. *Acta Astronautica*, 152:630–638, November 2018.

[43] Vijay Anand and Ephraim Gutmark. Rotating detonation combustors and their similarities to rocket instabilities. *Progress in Energy and Combustion Science*, 73:182–234, 2019.

[44] Brent A. Rankin, Daniel R. Richardson, Andrew W. Caswell, Andrew Naples, John Hoke, and Frederick Schauer. Imaging of OH* chemiluminescence in an optically accessible nonpremixed rotating detonation engine. In *53rd AIAA Aerospace Sciences Meeting*. Paper No. AIAA-2015-1604, January 2015.

[45] F. Chacon, A. D. Feleo, and M. Gamba. Secondary waves dynamics and their impact on detonation structure in rotating detonation combustors. *Shock Waves*, 31(7):675–702, October 2021.

[46] Blaine Bigler, John W. Bennewitz, Stephen A. Danczyk, and William A. Hargus. Injector mixing effects in rotating detonation rocket engines. In *AIAA Propulsion and Energy 2019 Forum*. Paper No. AIAA-2019-3869, August 2019.

[47] Joshua Shepard, Alexander Feleo, and Mirko Gamba. Effects of inlet area ratio on operability of an axial air inlet rotating detonation combustor. In *AIAA Propulsion and Energy 2021 Forum*. Paper No. AIAA 2021-3676, 2021.

[48] Christopher M. Brophy and Alexis Thoeny. Geometry impact on the operability and delivered pressure gain characteristics of a rotating detonation combustor. In *AIAA SCITECH 2024 Forum*. Paper No. AIAA-2024-2609, January 2024.

[49] Craig A. Nordeen, Douglas Schwer, Andrew T. Corrigan, and Baki Cetegen. Radial effects on rotating detonation engine swirl. In *51st AIAA/SAE/ASEE Joint Propulsion Conference*. Paper No. AIAA-2015-3781, July 2015.

[50] J. Shepard, Joshua. *Experimental Characterization of Rotating Detonation Engine Loss Mechanisms*. PhD thesis, University of Michigan, 2023.

[51] Riley Huff and Mirko Gamba. Effects on non-zero azimuthal velocity on the performance of rotating detonation engines. In *AIAA SciTech 2024 Forum*. Paper No. AIAA-2024-1658, January 2024.

[52] Douglas Schwer and Kailas Kailasanath. Effect of inlet on fill region and performance of rotating detonation engines. In *47th AIAA/ASME/SAE/ASEE Joint Propulsion Conference & Exhibit*, 2011.

[53] Vijay Anand, Andrew St. George, and Ephraim Gutmark. Amplitude modulated instability in reactants plenum of a rotating detonation combustor. *International Journal of Hydrogen Energy*, 42(17):12629–12644, apr 2017.

[54] Alexander Feleo, Joshua Shepard, and Mirko Gamba. Prediction of detonation-induced disturbances propagating upstream into inlets of rotating detonation combustors. In *AIAA Propulsion and Energy 2021 Forum*. Paper No. AIAA-2021-3687, 2021.

[55] Xingkui Yang, Feilong Song, Yun Wu, Shanguang Guo, Shida Xu, Jianping Zhou, and Hao Liu. Suppression of pressure feedback of the rotating detonation combustor by a tesla inlet configuration. *Applied Thermal Engineering*, 216:119123, 2022.

[56] Supraj Prakash and Venkat Raman. The effects of mixture preburning on detonation wave propagation. *Proceedings of the Combustion Institute*, 38(3):3749–3758, 2021.

[57] Fabian Chacon and Mirko Gamba. Development of an optically accessible continuous wave rotating detonation engine. In *2018 Joint Propulsion Conference*. Paper No. AIAA-2018-4779, jul 2018.

[58] Fabian Chacon. *Non-Ideal Phenomena in Rotating Detonation Combustors*. PhD thesis, University of Michigan, 2020.

[59] Evan C. Unruh, Michaela Spaulding, David M. Lineberry, Kunning G. Xu, and Robert A. Frederick. Development of an optically accessible racetrack-type rotating detonation rocket engine. In *AIAA Propulsion and Energy 2020 Forum*. Paper No. AIAA-2020-3868, August 2020.

[60] Fabian Chacon and Mirko Gamba. Study of parasitic combustion in an optically accessible continuous wave rotating detonation engine. *AIAA Scitech 2019 Forum*, jan 2019.

[61] Xin-Meng Tang, Jian-Ping Wang, and Ye-Tao Shao. Three-dimensional numerical investigations of the rotating detonation engine with a hollow combustor. *Combustion and Flame*, 162(4):997–1008, April 2015.

[62] Vijay Anand, Andrew C. St. George, and Ephraim J. Gutmark. Hollow rotating detonation combustor. In *54th AIAA Aerospace Sciences Meeting*, 2016.

[63] Regan Hencel, John Hoke, Matthew Fotia, and Stephen A. Schumaker. Experimental testing of a single airstream centerbodiless rotating detonation engine with a hollow core. In *AIAA SCITECH 2023 Forum*. Paper No. AIAA-2023-2392, January 2023.

[64] Soma Nakagami, Ken Matsuoka, Jiro Kasahara, Yoshiki Kumazawa, Jumpei Fujii, Akiko Matsuo, and Ikkoh Funaki. Experimental visualization of the structure of rotating detonation waves in a disk-shaped combustor. *Journal of Propulsion and Power*, pages 80–88, 2017.

[65] J A C. Kentfield and M. O'Blenes. Methods for achieving a combustion-driven pressure gain in gas turbines. *Journal of Engineering for Gas Turbines and Power*, 110(4):704–711, October 1988.

[66] Hans Holzwarth and W Schule. Thyseen-holzwarth oil and gas turbines. *Journal of the American Society for Naval Engineers*, 34(3):453–457, August 1922.

[67] Carroll D. Porter. Valveless-gas-turbine combustors with pressure gain. In *ASME 1958 Gas Turbine Power Conference and Exhibit*, GT1958. American Society of Mechanical Engineers, March 1958.

[68] A. A. Putnam, F. E. Belles, and J. A. C. Kentfield. Pulse combustion. *Progress in Energy and Combustion Science*, 12(1):43–79, January 1986.

[69] L. Narayanaswami and G. A. Richards. Pressure-gain combustion: Part i—model development. *Journal of Engineering for Gas Turbines and Power*, 118(3):461–468, July 1996.

[70] G. A. Richards and R. S. Gemmen. Pressure-gain combustion: Part ii—experimental and model results. *Journal of Engineering for Gas Turbines and Power*, 118(3):469–473, July 1996.

[71] Xiangmei Meng, Wiebren de Jong, and Tadeusz Kudra. A state-of-the-art review of pulse combustion: Principles, modeling, applications and r and d issues. *Renewable and Sustainable Energy Reviews*, 55:73–114, March 2016.

[72] J. A. C. Kentfield. Pressure-gain combustion, a review of recent progress. In *Proceedings of the Symposium on Pulse Combustion Technology for Heating Applications*. Argonne National Laboratory, November 1979.

[73] J. A. C. Kentfield, M. Rehman, and E. S. Marzouk. A simple pressure-gain combustor for gas turbines. *Journal of Engineering for Power*, 99(2):153–158, April 1977.

[74] D. Helman, R. Shreeve, and S. Eidelman. Detonation pulse engine. In *AIAA 22nd Joint Propulsion Conference*. Paper No. AIAA-86-1683, June 1986.

[75] B. V. Voitsekhovskii. Stationary spin detonation. *Sov J Appl Mech Tech Phys*, 3(1):157–164, 1960.

[76] J. Nicholls, H. Wilkinson, and R. Morrison. Intermittent detonation as a thrust-producing mechanism. *Journal of Jet Propulsion*, 27(5):534–541, 1957.

[77] JA Nicholls, RE Cullen, and KW Ragland. Feasibility studies of a rotating detonation wave rocket motor. *Journal of Spacecraft and Rockets*, 3(6):893–898, 1966.

[78] F. A. Bykovskii and V. V. Mitrofanov. Detonation combustion of a gas mixture in a cylindrical chamber. *Combustion, Explosion, and Shock Waves*, 16(5):570–578, 1981.

[79] F. A. Bykovskii, V. V. Mitrofanov, and E. F. Vedernikov. Continuous detonation combustion of fuel-air mixtures. *Combustion, Explosion, and Shock Waves*, 33(3):344–353, May 1997.

[80] FA Bykovskii and VV Mitrofanov. A continuous spin detonation in liquid fuel sprays. *Control of Detonation Processes*, pages 209–211, 2000.

[81] F. A. Bykovskii, S. A. Zhdan, and E. F. Vedernikov. Continuous spin detonation in annular combustors. *Combustion, Explosion, and Shock Waves*, 41(4):449–459, July 2005.

[82] Shmuel Eidelman and William Grossmann. Pulsed detonation engine experimental and theoretical review. In *28th Joint Propulsion Conference and Exhibit*, page 3168, 1992.

[83] T. Bussing and G. Pappas. An introduction to pulse detonation engines. In *32nd Aerospace Sciences Meeting and Exhibit*. American Institute of Aeronautics and Astronautics, January 1994.

[84] K. Kailasanath. Review of propulsion applications of detonation waves. *AIAA Journal*, 38(9):1698–1708, September 2000.

[85] Fred Schauer, Jeff Stutrud, and Royce Bradley. Detonation initiation studies and performance results for pulsed detonation engine applications. In *AIAA39th Aerospace Sciences Meeting and Exhibit*. Paper No. AIAA-2001-1129, January 2001.

[86] J. A. C. Kentfield. Thermodynamics of airbreathing pulse-detonation engines. *Journal of Propulsion and Power*, 18(6):1170–1175, November 2002.

[87] Larine Barr. Pulse detonation engine flies into history. *Press Release, Air Force Material Command*, 2008.

[88] G.D. Roy, S.M. Frolov, A.A. Borisov, and D.W. Netzer. Pulse detonation propulsion: challenges, current status, and future perspective. *Progress in Energy and Combustion Science*, 30(6):545–672, January 2004.

[89] Piotr Wolański. Rotating detonation wave stability. In *Proceedings of the 23rd International Colloquium on the Dynamics of Explosions and Reactive Systems*, pages 1–6, 2011.

[90] Douglas Schwer and Kailas Kailasanath. Numerical investigation of rotating detonation engines. In *46th AIAA/ASME/SAE/ASEE Joint Propulsion Conference & Exhibit*, 2010.

[91] James Suchocki, Sheng-Tao Yu, John Hoke, Andrew Naples, Frederick Schauer, and Rachel Russo. Rotating detonation engine operation. In *50th AIAA Aerospace Sciences Meeting including the New Horizons Forum and Aerospace Exposition*. Paper No. AIAA-2012-119, January 2012.

[92] Daniel Paxson. A simplified model for detonation based pressure-gain combustors. In *46th AIAA/ASME/SAE/ASEE Joint Propulsion Conference and Exhibit*. Paper No. AIAA-2010-6717, July 2010.

[93] K. Kailasanath. Research on pulse detonation combustion systems: A status report. In *47th AIAA Aerospace Sciences Meeting including The New Horizons Forum and Aerospace Exposition*. Paper No. AIAA-2009-631, January 2009.

[94] Suhan Lee, Deok-Rae Cho, and Jeong-Yeol Choi. Effect of curvature on the detonation wave propagation characteristics in annular channels. In *46th AIAA Aerospace Sciences Meeting and Exhibit*. Paper No. AIAA-2008-988, January 2008.

[95] Venkat Athmanathan, James Braun, Zachary M. Ayers, Christopher A. Fugger, Austin M. Webb, Mikhail N. Slipchenko, Guillermo Paniagua, Sukesh Roy, and Terrence R. Meyer. On the effects of reactant stratification and wall curvature in non-premixed rotating detonation combustors. *Combustion and Flame*, 240:112013, June 2022.

[96] Venkat Raman, Supraj Prakash, and Mirko Gamba. Nonidealities in rotating detonation engines. *Annual Review of Fluid Mechanics*, 55(1):639–674, 2023.

[97] Robert Burke, Taha Rezzag, Ian Dunn, Wilmer Flores, and Kareem Ahmed. The effect of premixed stratification on the wave dynamics of a rotating detonation combustor. *International Journal of Hydrogen Energy*, 46(54):27816–27826, August 2021.

[98] Takuma Sato and Venkat Raman. Detonation structure in ethylene/air-based non-premixed rotating detonation engine. *Journal of Propulsion and Power*, 36(5):752–762, 2020.

[99] Fabian Chacon and Mirko Gamba. OH PLIF visualization of an optically accessible rotating detonation combustor. In *In proceedings AIAA Propulsion and Energy Forum*, 2019.

[100] Brent A. Rankin, Daniel R. Richardson, Andrew W. Caswell, Andrew G. Naples, John L. Hoke, and Frederick R. Schauer. Chemiluminescence imaging of an optically accessible non-premixed rotating detonation engine. *Combustion and Flame*, 176:12–22, 2017.

[101] Supraj Prakash, Romain Fiévet, Venkat Raman, Jason Burr, and Kenneth H. Yu. Analysis of the detonation wave structure in a linearized rotating detonation engine. *AIAA Journal*, 58(12):5063–5077, 2020.

[102] Takuma Sato, Fabian Chacon, Logan White, Venkat Raman, and Mirko Gamba. Mixing and detonation structure in a rotating detonation engine with an axial air inlet. *Combustion Institute*, 38(3):3769–3776, 2021.

[103] Alexander Feleo, Jacob France, Logan W. White, and Mirko Gamba. Evaluation of OH emission for determining operation of a rotating detonation engine. In *AIAA Scitech 2019 Forum*. Paper No. AIAA-2019-2252, jan 2019.

[104] Robert T. Fievisohn, John L. Hoke, and Adam Holley. Thermodynamic and operability implications of product recirculation in rotating detonation engines. *AIAA Propulsion and Energy Forum and Exposition, 2019*, 2019.

[105] Jason R. Burr and Eric Paulson. Thermodynamic performance results for rotating detonation rocket engine with distributed heat addition using cantera. In *AIAA Propulsion and Energy 2021 Forum*. Paper No. AIAA-2021-3682, 2021.

[106] R. Zhou and J.-P. Wang. Numerical investigation of shock wave reflections near the head ends of rotating detonation engines. *Shock Waves*, 23(5):461–472, March 2013.

[107] Manabu Hishida, Toshi Fujiwara, and Piotr Wolanski. Fundamentals of rotating detonations. *Shock Waves*, 19(1):1–10, February 2009.

[108] N. A. Cumpsty and J. H. Horlock. Averaging nonuniform flow for a purpose. *Journal of Turbomachinery*, 128(1):120–129, 02 2005.

[109] C. A. Nordeen, D. Schwer, F. Schauer, J. Hoke, T. Barber, and B. M. Cetegen. Role of inlet reactant mixedness on the thermodynamic performance of a rotating detonation engine. *Shock Waves*, 26(4):417–428, apr 2015.

[110] Craig A Nordeen, Douglas Schwer, Fredrick Schauer, John Hoke, Th Barber, and B Cetegen. Thermodynamic model of a rotating detonation engine. *Combustion, Explosion, and Shock Waves*, 50(5):568–577, 2014.

[111] Tom Kaemming, Matthew L. Fotia, John Hoke, and Fred Schauer. Thermodynamic modeling of a rotating detonation engine through a reduced-order approach. *Journal of Propulsion and Power*, 33(5):1170–1178, September 2017.

[112] Ethan W. Plaehn, Rohan M. Gejji, Ian V. Walters, and Carson D. Slabaugh. Equivalent supply pressure for pressure gain estimation in rotating detonation engines. *Journal of Propulsion and Power*, 39(1):141–145, January 2023.

[113] Thomas A. Kaemming and Daniel E. Paxson. Determining the pressure gain of pressure gain combustion. In *2018 Joint Propulsion Conference*. Paper No. AIAA-2018-4567, January 2018.

[114] Christopher M. Brophy and Joshua Codoni. Experimental performance characterization of an RDE using equivalent available pressure. In *AIAA Propulsion and Energy 2019 Forum*. Paper No. AIAA-2019-4212, August 2019.

[115] A. TenEyck, Joshua. Determination of effective available pressure of a rotating detonation engine. Master's thesis, Naval Postgraduate School, 2019.

[116] Robert T. Fievisohn, John Hoke, and Adam T. Holley. Equivalent available pressure measurements on a laboratory rde. In *AIAA Scitech 2020 Forum*. Paper No. AIAA-2020-2285, January 2020.

[117] John W. Bennewitz, Blaine Bigler, Stephen Danczyk, William A. Hargus, and Richard D. Smith. Performance of a rotating detonation rocket engine with various convergent nozzles. In *AIAA Propulsion and Energy 2019 Forum*. Paper No. AIAA-2019-4299, August 2019.

[118] Jeffrey B. Stout and Alexander Baratta. Demonstrated low loss and low equivalence ratio operation of a rotating detonation engine for power generation. In *AIAA Scitech 2020 Forum*. Paper No. AIAA-2020-1173, January 2020.

[119] Ian V Walters, Aaron Lemcherfi, Rohan M Gejji, Stephen D Heister, and Carson D Slabaugh. Performance characterization of a natural gas–air rotating detonation engine. *Journal of Propulsion and Power*, 37(2):292–304, 2021.

[120] Joshua R. Codoni, Grant Birindelli, Alexis Thoeny, and Christopher M. Brophy. Experimental approaches for obtaining a temporally- and spatially-averaged representative static pressure for rotating detonation engines. In *AIAA Scitech 2022 Forum*. Paper No. AIAA-2022-2369, January 2022.

[121] Christopher M. Brophy, Joshua R. Codoni, and Alexis Thoeny. Channel width impact on rde performance with fuel injection parity. In *AIAA SciTech 2022 Forum*. Paper No. AIAA-2022-1877, January 2022.

[122] Alexis J. Harroun, Stephen D. Heister, and Joseph H. Ruf. Computational and experimental study of nozzle performance for rotating detonation rocket engines. *Journal of Propulsion and Power*, 37(5):660–673, September 2021.

[123] Tim Kayser, Hongyi Wei, Eric Bach, Christian O. Paschereit, and Myles Bohon. Experimental comparison of different pressure gain measurement techniques for RDCs. In *AIAA Scitech 2023 Forum*. Paper No. AIAA 2023-0929, January 2023.

[124] Shida Xu, Feilong Song, Yun Wu, Jianping Zhou, Peng Cheng, Xingkui Yang, and Xin Chen. Experimental investigation on combustion efficiency of a partially premixed kerosene-air rotating detonation combustor. *Fuel*, 329:125418, December 2022.

[125] Sotirios E Notaris. Gauss-kronrod quadrature formulae–a survey of fifty years of research. *Electron. Trans. Numer. Anal*, 45:371–404, 2016.

[126] David P Stechmann, Stephen D Heister, and Alexis J Harroun. Rotating detonation engine performance model for rocket applications. *Journal of Spacecraft and Rockets*, 56(3):887–898, 2019.

[127] Blaine R Bigler, John W Bennewitz, Stephen A Danczyk, and William A Hargus. Rotating detonation rocket engine operability under varied pressure drop injection. *Journal of Spacecraft and Rockets*, 58(2):316–325, 2021.

[128] Joint Committee for Guides in Metrology. Evaluation of measurement data - guide to the expression of uncertainty in measurement - jcgm 100:2008. Technical report, Joint Committee for Guides in Metrology, 2008.

[129] Robert T. Fievisohn, John Hoke, and Adam T. Holley. Experimental measurements of equivalent available pressure - lessons learned. In *AIAA Scitech 2022 Forum*. Paper No. AIAA-2022-0833, 2022.

[130] J. Shank. *Development and Testing of a Rotating Detonation Engine Run on Hydrogen and Air*. PhD thesis, Air Force Institute of Technology, 2012.

[131] Li Deng, Hu Ma, Can Xu, Xiao Liu, and Changsheng Zhou. The feasibility of mode control in rotating detonation engine. *Applied Thermal Engineering*, 129:1538–1550, 2018.

[132] Li Deng, Hu Ma, Xiao Liu, and Changsheng Zhou. Secondary shock wave in rotating detonation combustor. *Aerospace Science and Technology*, 95:105517, December 2019.

[133] Richard Bluemner, Ephraim J. Gutmark, Christian Oliver Paschereit, and Myles D. Bohon. Stabilization mechanisms of longitudinal pulsations in rotating detonation combustors. *Proceedings of the Combustion Institute*, 38(3):3797–3806, 2021.

[134] Douglas Schwer and Kailas Kailasanath. Feedback into mixture plenums in rotating detonation engines. *50th AIAA Aerospace Sciences Meeting including the New Horizons Forum and Aerospace Exposition*, 2012.

[135] Tae-Hyeong Yi, Jing Lou, Cary Turangan, Jeong-Yeol Choi, and Piotr Wolanski. Propulsive performance of a continuously rotating detonation engine. *Journal of Propulsion and Power*, 27(1):171–181, January 2011.

[136] John W. Bennewitz, Blaine R. Bigler, Mathias C. Ross, Stephen A. Danczyk, William A. Hargus, and Richard D. Smith. Performance of a rotating detonation rocket engine with various convergent nozzles and chamber lengths. *Energies*, 14(8):2037, April 2021.

[137] Ryuya Yokoo, Keisuke Goto, Jiro Kasahara, Venkat Athmanathan, James Braun, Guillermo Paniagua, Terrence R. Meyer, Akira Kawasaki, Ken Matsuoka, Akiko Matsuo, and Ikkoh Funaki. Experimental study of internal flow structures in cylindrical rotating detonation engines. *Proceedings of the Combustion Institute*, 38(3):3759–3768, 2021.

[138] Kazuki Ishihara, Kentaro Yoneyama, Hiroaki Watanabe, Noboru Itouyama, Akira Kawasaki, Ken Matsuoka, Jiro Kasahara, Akiko Matsuo, Ikkoh Funaki, and Kazuyuki Higashino. Thrust performance of converging rotating detonation engine compared with steady rocket engine. *Journal of Propulsion and Power*, 39(3):297–307, May 2023.

[139] Alexander Feleo, Joshua Shepard, and Mirko Gamba. Evaluation of reaction-induced effective inlet blockage of rotating detonation combustors. In preparation, 2024.

[140] Matthew Fotia, John Hoke, and Fred Schauer. Propellant plenum dynamics in a two-dimensional rotating detonation experiment. *52nd Aerospace Sciences Meeting*, January 2014.

[141] R Driscoll, V Anand, A St George, and E Gutmark. Investigation on RDE operation by geometric variation of the combustor annulus and nozzle exit area. In *9th US National Combustion Meeting*, 2015.

[142] Li Deng, Hu Ma, Can Xu, Changsheng Zhou, and Xiao Liu. Investigation on the propagation process of rotating detonation wave. *Acta Astronautica*, 139:278–287, 2017.

[143] Ken Matsuoka, Masaya Tanaka, Tomoyuki Noda, Akira Kawasaki, and Jiro Kasahara. Experimental investigation on a rotating detonation cycle with burned gas backflow. *Combustion and Flame*, 225:13–19, March 2021.

[144] K. Goto, R. Yokoo, A. Kawasaki, K. Matsuoka, J. Kasahara, A. Matsuo, I. Funaki, and H. Kawashima. Investigation into the effective injector area of a rotating detonation engine with impact of backflow. *Shock Waves*, 31(7):753–762, March 2021.

[145] Xingkui Yang, Feilong Song, Yun Wu, Jianping Zhou, Zhao Yang, and Yitao Kou. Experimental study on tesla valve and bypass manifold to suppress feedback of rotating detonation engine fuel by kerosene. *Acta Astronautica*, 211:755–763, October 2023.

[146] Tomoyuki Noda, Ken Matsuoka, Keisuke Goto, Akira Kawasaki, Hiroaki Watanabe, Noboru Itouyama, Jiro Kasahara, and Akiko Matsuo. Impact of mixture mass flux on hydrodynamic blockage ratio and mach number of rotating detonation combustor. *Acta Astronautica*, 207:219–226, June 2023.

[147] Jian Sun, Jin Zhou, Shijie Liu, Zhiyong Lin, and Jianhua Cai. Effects of injection nozzle exit width on rotating detonation engine. *Acta Astronautica*, 140:388–401, November 2017.

[148] Daniel E. Paxson and Kenji Miki. Computational assessment of inlet backflow effects on rotating detonation engine performance and operability. In *AIAA SCITECH 2022 Forum*. Paper No. AIAA-2022-1263, January 2022.

[149] Jie Lu, Longxi Zheng, Zhiwu Wang, Lingyi Wang, and Chuanjun Yan. Experimental investigation on interactions between a two-phase multi-tube pulse detonation combustor and a centrifugal compressor. *Applied Thermal Engineering*, 113:426–434, February 2017.

[150] Zhiwu Wang, Yuxuan Yang, Jingjing Huang, and Lisi Wei. Effect of back-propagation pressure on axial flow compressor in a pulse detonation turbine engine. *Aerospace Science and Technology*, 141:108525, October 2023.

[151] F. Gnani, H. Zare-Behtash, and K. Kontis. Pseudo-shock waves and their interactions in high-speed intakes. *Progress in Aerospace Sciences*, 82:36–56, April 2016.

[152] Robin Hunt, Louis M. Edelman, and Mirko Gamba. Scaling of pseudoshock length and pressure rise. In *2018 AIAA Aerospace Sciences Meeting*. American Institute of Aeronautics and Astronautics, January 2018.

[153] Saravanan R., S. L. N. Desikan, and Muruganandam T. M. Isolator characteristics under steady and oscillatory back pressures. *Physics of Fluids*, 32(9), September 2020.

[154] Thomas A Kaemming, Matthew L Fotia, John L Hoke, and Stephen A Schumacker. Quantification of the loss mechanisms of a ram rotating detonation engine. In *AIAA Scitech 2020 Forum*. Paper No. AIAA-2020-0927, 2020.

[155] Andrew T. Sisler. Experimental investigation for characterizing and improving inlet designs in rotating detonation engines. Master's thesis, West Virginia University, 2016.

[156] Provence Barnoiun, Eric Bach, Christian Oliver Paschereit, and Mylese D. Bohon. Rdc operation with varying air injector diodicity. In *AIAA Scitech 2024 Forum*. Paper No. AIAA-2024-1830, January 2024.

[157] Daniel E. Paxson and Tom Kaemming. Influence of unsteadiness on the analysis of pressure gain combustion devices. *Journal of Propulsion and Power*, 30(2):377–383, March 2014.

[158] Christian Frey, Graham Ashcroft, Michael Müller, and Jens Wellner. Analysis of turbomachinery averaging techniques. *Journal of Turbomachinery*, 145(5), November 2022.

[159] R. A. Baurle and R. L. Gaffney. Extraction of one-dimensional flow properties from multi-dimensional data sets. *Journal of Propulsion and Power*, 24(4):704–714, July 2008.

[160] Daniel Paxson and Thomas Kaemming. Foundational performance analyses of pressure gain combustion thermodynamic benefits for gas turbines. In *50th AIAA Aerospace Sciences Meeting including the New Horizons Forum and Aerospace Exposition*. American Institute of Aeronautics and Astronautics, January 2012.

[161] Andrew Naples, John Hoke, Ryan Battelle, and Fred Schauer. T63 turbine response to rotating detonation combustor exhaust flow. *Journal of Engineering for Gas Turbines and Power*, 141(2), October 2018.

[162] Bonnie J McBride. *NASA Glenn coefficients for calculating thermodynamic properties of individual species*. National Aeronautics and Space Administration, John H. Glenn Research Center, 2002.

[163] David G Goodwin, Raymond L Speth, Harry K Moffat, and Bryan W Weber. Cantera: An object-oriented software toolkit for chemical kinetics, thermodynamics, and transport processes. https://www.cantera.org, 2021.

[164] Ral Bielawski, Shivam Barwey, Supraj Prakash, and Venkat Raman. Highly-scalable GPU-accelerated compressible reacting solver for shock-containing flows. *Comput. Fluids*, 2022. In review.

[165] Brent A Rankin, Matthew L Fotia, Daniel E Paxson, John L Hoke, and Frederick R Schauer. Experimental and numerical evaluation of pressure gain combustion in a rotating detonation engine. In *53rd AIAA Aerospace Sciences Meeting*, 2015.

[166] Kyle A. Schau and Joseph C. Oefelein. Numerical analysis of wave characteristics in a methane-oxygen rotating detonation engine. *AIAA Journal*, 61(1):97–111, January 2023.

[167] M Pianko and Friedricb Wazelt. Propulsion and energetics panel working group 14 on suitable averaging techniques in non-uniform internal flows. AGARD Advisory Report 182, Advisory Group for Aerospace Research and Development, 1982.

[168] Keisuke Goto, Ken Matsuoka, Koichi Matsuyama, Akira Kawasaki, Hiroaki Watanabe, Noboru Itouyama, Kazuki Ishihara, Valentin Buyakofu, Tomoyuki Noda, Jiro Kasahara, Akiko Matsuo, Ikkoh Funaki, Daisuke Nakata, Masaharu Uchiumi, Hiroto Habu, Shinsuke Takeuchi, Satoshi Arakawa, Junichi Masuda, Kenji Maehara, Tatsuro Nakao, and Kazuhiko Yamada. Space flight demonstration of rotating detonation engine using sounding rocket s-520-31. *Journal of Spacecraft and Rockets*, pages 0–0, October 2022.

[169] Matthew Fotia, John Hoke, and Frederick Schauer. Experimental study of the response of capillary tube attenuated pressure measurements to high amplitude, non-linear forcing. In *2018 AIAA Aerospace Sciences Meeting*. Paper No. AIAA-2018-0634, January 2018.

[170] Eric Bach, C.O. Paschereit, Panagiotis Stathopoulos, and Myles D. Bohon. An empirical model for stagnation pressure gain in rotating detonation combustors. *Proceedings of the Combustion Institute*, 38(3):3807–3814, 2021.

[171] Ian V. Walters, Christopher Journell, Aaron I. Lemcherfi, Rohan Gejji, Stephen D. Heister, and Carson D. Slabaugh. Performance characterization of a natural gas-air rotating detonation engine at elevated pressure. In *AIAA Propulsion and Energy 2019 Forum*. Paper No. AIAA-2019-4214, August 2019.

[172] Sergey M Frolov, Viktor S Aksenov, Vladislav S Ivanov, Sergey N Medvedev, and Igor O Shamshin. Flow structure in rotating detonation engine with separate supply of fuel and oxidizer: Experiment and cfd. *Detonation control for propulsion: Pulse detonation and rotating detonation engines*, pages 39–59, 2018.

[173] Christopher Lietz, Yogin Desai, William A. Hargus, and Venke Sankaran. Parametric investigation of rotating detonation rocket engines using large eddy simulations. In *AIAA Propulsion and Energy 2019 Forum*. Paper No. AIAA-2019-4129, August 2019.

[174] Supraj Prakash, Venkat Raman, Christopher F. Lietz, William A. Hargus, and Stephen A. Schumaker. Numerical simulation of a methane-oxygen rotating detonation rocket engine. *Proceedings of the Combustion Institute*, 38(3):3777–3786, 2021.

[175] Peter Strakey and Donald H. Ferguson. Validation of a computational fluid dynamics model of a methane-oxygen rotating detonation engine. In *AIAA Scitech 2022 Forum*. Paper No. AIAA-2022-1113, January 2022.

[176] Fabian Chacon, Alexander Feleo, and Mirko Gamba. Impact of inlet area ratio on the operation of an axial air inlet configuration rotating detonation combustor. In *AIAA Propulsion and Energy 2019 Forum*. Paper No. AIAA 2019-4450, August 2019.

[177] Matthew L. Fotia, Fred Schauer, Tom Kaemming, and John Hoke. Experimental study of the performance of a rotating detonation engine with nozzle. *Journal of Propulsion and Power*, 32(3):674–681, May 2016.

[178] Arnab Roy, Donald H. Ferguson, Todd Sidwell, Bridget O'Meara, Peter Strakey, Clinton Bedick, and Andrew Sisler. Experimental study of rotating detonation combustor performance under preheat and back pressure operation. In *55th AIAA Aerospace Sciences Meeting*. Paper No. AIAA-2017-1065, January 2017.

[179] Joshua Shepard, Alexander Feleo, and Mirko Gamba. The effect of facility induced backpressure on rotating detonation combustor operation. In *AIAA Scitech 2022 Forum*. Paper No. AIAA 2022-0517, 2022.

[180] Yasin M. Abul-Huda and Mirko Gamba. Flow characterization of a hypersonic expansion tube facility for supersonic combustion studies. *Journal of Propulsion and Power*, 33(6):1504–1519, November 2017.

[181] John R. Taylor. *An Introduction to Error Analysis: The Study of Uncertainties in Physical Measurements*. University Science Books, Sausalito, CA, 2nd ed. edition, 1996.

[182] E. T. Jaynes. Information theory and statistical mechanics. *Physical Review*, 106(4):620–630, May 1957.

[183] Enrico Zio. *Monte carlo simulation: The method*. Springer, 2013.

[184] J. A. C. Weideman. Numerical integration of periodic functions: A few examples. *The American Mathematical Monthly*, 109(1):21–36, January 2002.

[185] Venkat Athmanathan, K. Arafat Rahman, Daniel K. Lauriola, James Braun, Guillermo Paniagua, Mikhail N. Slipchenko, Sukesh Roy, and Terrence R. Meyer. Femtosecond/picosecond rotational coherent anti-stokes raman scattering thermometry in the exhaust of a rotating detonation combustor. *Combustion and Flame*, 231:111504, September 2021.

[186] Z. . Luan, Y. Huang, S. . Liu, and H. . Jiang. Interaction between detonation and non-premixed fuel jets. *Tuijin Jishu/Journal of Propulsion Technology*, 42(4):883–891, 2021.

[187] John W. Bennewitz, Blaine R. Bigler, William A. Hargus, Stephen A. Danczyk, and Richard D. Smith. Characterization of detonation wave propagation in a rotating detonation rocket engine using direct high-speed imaging. In *2018 Joint Propulsion Conference*. Paper No. AIAA-2018-4688, 2018.

[188] Fabian Chacon, James Duvall, and Mirko Gamba. Evaluation of pressure rise and oscillation in a rotating detonation engine. In *2018 AIAA Aerospace Sciences Meeting*. Paper No. AIAA-2018-0405, jan 2018.

[189] G. Walz, W. Krebs, S. Hoffmann, and H. Judith. Detailed analysis of the acoustic mode shapes of an annular combustion chamber. *Journal of Engineering for Gas Turbines and Power*, 124(1):3–9, March 1999.

[190] Nikola Tesla. Valvular conduit, February 1920. U.S. Patent No. 1329559.

[191] Fred K Forster, Ronald L Bardell, Martin A Afromowitz, Nigel R Sharma, and Alan Blanchard. Design, fabrication and testing of fixed-valve micro-pumps. *Asme-Publications-Fed*, 234:39–44, 1995.

[192] A. St. George, R. Driscoll, V. Anand, and E. Gutmark. On the existence and multiplicity of rotating detonations. *Proceedings of the Combustion Institute*, 36(2):2691–2698, 2017.

[193] R. F. Chisnell. The motion of a shock wave in a channel, with applications to cylindrical and spherical shock waves. *Journal of Fluid Mechanics*, 2(3):286–298, May 1957.

[194] G. B. Whitham. On the propagation of shock waves through regions of non-uniform area or flow. *Journal of Fluid Mechanics*, 4(04):337, August 1958.

[195] Riley Huff and Mirko Gamba. Effects of non-idealities on gain in a detonation cycle. *Proceedings of the 29th International Colloquium on the Dynamics of Explosions and Reactive Systems*, 29(236), 2023.

[196] Daniel Paxson and Jack Wilson. An improved numerical model for wave rotor design and analysis. In *31st Aerospace Sciences Meeting*. Paper No. AIAA-93-0482, January 1993.

[197] Xiang-Yang Liu, Ming-Yi Luan, Yan-Liang Chen, and Jian-Ping Wang. Flow-field analysis and pressure gain estimation of a rotating detonation engine with banded distribution of reactants. *International Journal of Hydrogen Energy*, 45(38):19976–19988, July 2020.

[198] Ascher H Shapiro. *The dynamics and thermodynamics of compressible fluid flow, volume 1*. The Ronald Press Company, New York, May 1953.

[199] Donald H. Ferguson, Bridget O'Meara, Arnab Roy, and Kristyn Johnson. Experimental measurements of NOx emissions in a rotating detonation engine. In *AIAA Scitech 2020 Forum*. Paper No. AIAA-2020-0204, January 2020.

[200] Peng Cheng, Feilong Song, Shida Xu, Jianping Zhou, and Yun Wu. Experimental study on combustion efficiency and gas analysis of rdc with different blockage ratio. *Combustion Science and Technology*, 195(16):4166–4185, April 2022.

[201] Peng Cheng, Feilong Song, Shida Xu, Jianping Zhou, Fang Feng, Kexin Song, and Xu Qiao. Experimental study on combustion efficiency and pressure gain characteristic of rdc with guide vanes. *Combustion Science and Technology*, page 1–16, November 2023.

[202] Kristyn B. Johnson, Donald H. Ferguson, Justin M. Weber, and Andrew C. Nix. Consideration of nonideal detonation regimes influenced by wave modes in a water-cooled rotating detonation engine using oh* chemiluminescence. *Journal of Engineering for Gas Turbines and Power*, 145(11), September 2023.

[203] Ian V. Walters, Rohan M. Gejji, Stephen D. Heister, and Carson D. Slabaugh. Flow and performance analysis of a natural gas-air rotating detonation engine with high-speed velocimetry. *Combustion and Flame*, 232:111549, October 2021.

[204] Christopher S Goldenstein, Christopher A Almodóvar, Jay B Jeffries, Ronald K Hanson, and Christopher M Brophy. High-bandwidth scanned-wavelength-modulation spectroscopy sensors for temperature and h2o in a rotating detonation engine. *Measurement Science and Technology*, 25(10):105104, 2014.

[205] Garrett C. Mathews, Matthew G. Blaisdell, Aaron I. Lemcherfi, Carson D. Slabaugh, and Christopher S. Goldenstein. High-bandwidth absorption-spectroscopy measurements of temperature, pressure, co, and h2o in the annulus of a rotating detonation rocket engine. *Applied Physics B*, 127(12), November 2021.

[206] Micha l Kawalec, Piotr Wolański, Witold Perkowski, and Adam Bilar. Development of a liquid-propellant rocket powered by a rotating detonation engine. *Journal of Propulsion and Power*, 39(4):554–561, July 2023.

[207] Roman Klopsch, Niclas Garan, Eric Bach, Christian O. Paschereit, and Myles Bohon. Investigation of geometric RDC dependencies using a fast reactive euler solver. In *AIAA SCITECH 2023 Forum*. American Institute of Aeronautics and Astronautics, January 2023.

[208] Roman Klopsch, Niclas Garan, Myles Bohon, Eric Bach, Majid Asli, and Panagiotis Stathopoulos. 2d euler modeling of rotating detonation combustion in preparation for turbomachinery matching. In *AIAA Scitech 2022 Forum*. Paper No. AIAA-2022-0836, January 2022.

[209] M.D. Bohon, R. Bluemner, C.O. Paschereit, and E.J. Gutmark. High-speed imaging of wave modes in an RDC. *Experimental Thermal and Fluid Science*, 102:28–37, April 2019.

[210] R. Bluemner, M.D. Bohon, C.O. Paschereit, and E.J. Gutmark. Counter-rotating wave mode transition dynamics in an RDC. *International Journal of Hydrogen Energy*, 44(14):7628–7641, March 2019.

[211] Alexander Zahn, Ethan Knight, Vijay Anand, Justas Jodele, and Ephraim J. Gutmark. Examination of counter-rotating detonation waves using cross-correlation. In *2018 Joint Propulsion Conference*. Paper No. AIAA 2018-4568, July 2018.

[212] James Koch and J. Nathan Kutz. Modeling thermodynamic trends of rotating detonation engines. *Physics of Fluids*, 32(12):126102, December 2020.

[213] John W Bennewitz, Blaine R Bigler, Jessica J Pilgram, and William A Hargus Jr. Modal transitions in rotating detonation rocket engines. *International Journal of Energetic Materials and Chemical Propulsion*, 18(2):91–109, March 2019.

[214] Qiaofeng Xie, Bing Wang, Haocheng Wen, and Wei He. Thermoacoustic instabilities in an annular rotating detonation combustor under off-design condition. *Journal of Propulsion and Power*, 35(1):141–151, January 2019.

[215] Shengbing Zhou, Hu Ma, Shuai Li, Daokun Liu, Yu Yan, and Changsheng Zhou. Effects of a turbine guide vane on hydrogen-air rotating detonation wave propagation characteristics. *International Journal of Hydrogen Energy*, 42(31):20297–20305, August 2017.